

AD-A187 336

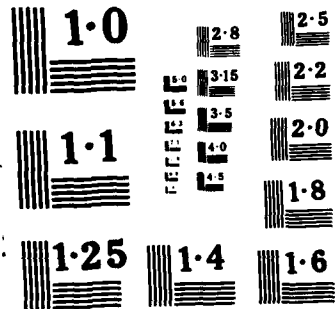
ADVANCED ENERGY CONVERSION CONCEPT FOR BEAMED-ENERGY
PROPULSION(U) RENSSELAER POLYTECHNIC INST TROY NY DEPT
OF MECHANICAL ENGINEERING L N WYBICKO 21 AUG 87

1/3

UNCLASSIFIED

RPI-5-24178 AFOSR-YN-87-1387 AFOSR-84-0361 F/C 9/3

ML



**ADVANCED ENERGY CONVERSION CONCE
FOR BEAMED-ENERGY PROPULSION**

FINAL TECHNICAL REPORT

August 21, 1987

2
AFOSR-TR- 87 - 1387

**ADVANCED ENERGY CONVERSION CONCEPT
FOR BEAMED-ENERGY PROPULSION**

FINAL TECHNICAL REPORT

August 21, 1987

**Prepared under Contract No. RPI-5-24170
for the Air Force Office of Scientific Research**

Approved for public release;
distribution unlimited.

**Rensselaer Polytechnic Institute
Dept. of Mech. Engrg., Aero. Engrg. and Mechanics
Troy, NY 12180-3590**

AIR FORCE OFFICE OF SCIENTIFIC RESEARCH (AFSC)
NOTICE OF TRANSMISSION TO DTIC
This technical report has been reviewed and is
approved for public release (AW AFIR 190-12).
Distribution is unlimited.
STEPHEN J. KERPNER
Chief, Technical Information Division

AD 87-1387

REPORT DOCUMENTATION PAGE				Form Approved OMB No. 0704-0188	
1a REPORT SECURITY CLASSIFICATION Unclassified			1b RESTRICTIVE MARKINGS		
2a SECURITY CLASSIFICATION AUTHORITY			3 DISTRIBUTION/AVAILABILITY OF REPORT Approved for public release; distribution is unlimited		
2b DECLASSIFICATION/DOWNGRADING SCHEDULE					
4 PERFORMING ORGANIZATION REPORT NUMBER(S)			5. MONITORING ORGANIZATION REPORT NUMBER(S) AFOSR-TR- 87-1387		
6a NAME OF PERFORMING ORGANIZATION Rensselaer Polytechnic Institute		6b OFFICE SYMBOL (if applicable)	7a. NAME OF MONITORING ORGANIZATION AFOSR/NA		
6c. ADDRESS (City, State, and ZIP Code) Troy, New York 12180-3590			7b. ADDRESS (City, State, and ZIP Code) Building 410, Bolling AFB DC 20332-6448		
8a NAME OF FUNDING/SPONSORING ORGANIZATION AFOSR/NA		8b OFFICE SYMBOL (if applicable)	9 PROCUREMENT INSTRUMENT IDENTIFICATION NUMBER AFOSR-84-0361		
8c ADDRESS (City, State, and ZIP Code) Building 410, Bolling AFB DC 20332-6448			10 SOURCE OF FUNDING NUMBERS		
		PROGRAM ELEMENT NO 61102F	PROJECT NO 2308	TASK NO A1	WORK UNIT ACCESSION NO.
11. TITLE (Include Security Classification) (U) ADVANCED ENERGY CONVERSION CONCEPT FOR BEAMED-ENERGY PROPULSION (u)					
12 PERSONAL AUTHOR(S) Myrabo, L.N., et. al. (see cover page)					
13a. TYPE OF REPORT Final Technical		13b. TIME COVERED FROM 9/84 TO 11/86		14. DATE OF REPORT (Year, Month, Day) 1987, August 21	
15. PAGE COUNT 184					
16. SUPPLEMENTARY NOTATION					
17. COSATI CODES			18. SUBJECT TERMS (Continue on reverse if necessary and identify by block number)		
FIE	GROUP	SUB-GROUP	Advanced Airbreathing Propulsion, Beamed Energy Propulsion, External Radiation Heated (ERH) Thruster. ←		
19 ABSTRACT (Continue on reverse if necessary and identify by block number)					
<p>The principal objective of this study was to perform basic research investigations into an innovative power conversion concept for transatmospheric, beamed energy propulsion: a new class of External Surface Impulse (ESI) thrusters. This advanced thruster principle could be used for atmospheric VTOL, high acceleration, and lateral flight (e.g., short-term "cruise") propulsion of Single-Stage-To-Orbit (SSTO) beam-powered shuttlecraft of the next century.</p> <p>Three classes of ESI thrusters were initially examined: 1) simple thermal, 2) electrostatic and 3) electromagnetic. Beam power wavelengths from 10cm (microwave) to 0.3um (laser) were considered. The subsequent research effort concentrated on the simple thermal repetitively-pulsed ESI thrusters, energized with laser power and using air as the working fluid. Laser frequencies were selected because of the relative wealth of experimental data and theoretical research on "laser impulse coupling" which exists in the literature.</p> <p>The first year analytical effort has proven conclusively that such an engine can deliver</p>					
20 DISTRIBUTION/AVAILABILITY OF ABSTRACT <input checked="" type="checkbox"/> UNCLASSIFIED/UNLIMITED <input checked="" type="checkbox"/> SAME AS RPT <input type="checkbox"/> DTIC USERS			21 ABSTRACT SECURITY CLASSIFICATION Unclassified		
22a NAME OF RESPONSIBLE INDIVIDUAL Dr Mitat Birkan			22b TELEPHONE (Include Area Code) (202) 767-4937		22c OFFICE SYMBOL AFOSR/NA

ADVANCED ENERGY CONVERSION CONCEPT FOR BEAMED- ENERGY PROPULSION

TABLE OF CONTENTS

LIST OF FIGURES	iv
LIST OF TABLES	vii
ABSTRACT	viii
I. INTRODUCTION	1
A) Electrostatic ESI Thruster	1
B) Electromagnetic ESI Thruster	1
C) Simple Thermal Thruster	4
D) Report Organization	6
II. FLIGHT PLATFORM REFERENCE CONFIGURATION	8
A) Reference Platform	8
B) Engine, Vehicle and Power System Architecture	10
C) Analysis of Primary Receptive Optics Area	64
III. LASER ENERGY ABSORPTION INTO GASES	76
A) Introduction	76
B) Earlier Models of LSD wave Propagation	76
C) Results of the Earlier Models	83
D) Summary	84
IV. INSTANTANEOUS LINE-SOURCE ERH THRUSTER MODEL (Static)	85
A) Impulse Generation Model for LSD Waves Propagating Parallel to a Surface	85
B) Results of the Line Source Model	94
C) Summary	98
V. PROPAGATING LSD-WAVE ERH THRUSTER MODEL	102
A) Basic Operating Principles	102
B) LSD Blast Wave Analysis	103
C) Static Thrust Model	109
D) Dynamic Thruster Model	112
E) Results	115
VI. LSC WAVE ERH THRUSTER MODEL (Static)	124
A) Description of the Model	124
B) Analytical Results	129
C) Summary	132
VII. TEMPERATURE HISTORY OF AN ERH THRUSTER SURFACE (Static)	135
A) Radiation Model	135
B) Conduction Model	138
C) Analytical Results	139
D) Future Extensions	143
VIII. FAR-FIELD SOUND LEVELS PRODUCED BY ERH THRUSTER	145
A) Introduction	145
B) Blast Wave Characteristics	146
C) Blast Wave Approximation	147
D) Blast Wave Spectrum	149
E) Far-Field Sound Spectrum Level	154

TABLE OF CONTENTS

F) Overall Far-Field Sound Level	155
G) Summary	156
IX. SIMULATION OF ERH THRUSTER NOISE SIGNATURES	158
A) Introduction	158
B) Model Description	158
C) Model Implementation	159
D) Digital Simulation Constraints	162
E) Reduction of Undesired Modulation Effects	166
F) Model for Acoustic Transmission Path H_2	168
G) Single Relay Satellite Trajectory Simulation	169
H) Summary	176
X. CONCLUSIONS	181
XI. REFERENCES	182

LIST OF FIGURES

Figure I-1. Pulsed electrostatic ESI thruster	2
Figure I-2. Pulsed electromagnetic ESI thruster	3
Figure I-3. Electrical model of pulsed inductive thruster	5
Figure I-4. Simple thermal ESI thruster	5
Figure II-1. Reference platform for ERH thruster	9
Figure II-2. Secondary optics and ERH thruster geometry	9
Figure II-3. Methods for incorporating variable geometry in radially-symmetric supersonic inlets	17
Figure II-4. Shroud/cowl flow-turning options	18
Figure II-5. Flow-turning by LSD wave "jet"	20
Figure II-6. Options for Receptive Optical Trains a) shrouded (ref. config.) b) unshrouded	22
Figure II-6. Options for Receptive Optical Trains, cont'd. c) mini-shroud (side view), d) mini-strut (top view)	23
Figure II-6. Options for Receptive Optical Trains, cont'd. e) shroud configuration with Tertiary Optics (side view), f) shroud configuration with Tertiary Optics (bottom view)	25
Figure II-7. Top view of PO surface for ref. point design	26
Figure II-8. Partial-internal/Partial-external expansion type nozzle	27
Figure II-9. Nozzle contours vs. percent internal expansion	29
Figure II-10. 2-D Prandtl-Meyer expansions (constant area ratio, constant thrust)	30
Figure II-11. Outline of a 50% internal expansion plug nozzle	31
Figure II-12. Effect of base angle	32
Figure II-13. Extreme area ratio plug nozzle	34
Figure II-14. Relationship of individual "line source" thrust vector and vehicle C.G. (center of gravity)	37
Figure II-15. Thrust vector control relationships	37
Figure II-16. Wavelength scaling relationship	39
Figure II-17. Normal equal loudness contours for pure tones	41
Figure II-18. ERH thrust vector geometry for rotating line source(s)	42
Figure II-19. Energy deposition modes - bottom view (unpowered cylindrical and planar sources)	44
Figure II-19. Energy deposition modes - bottom view (unpowered cylindrical and planar sources), cont'd.	45
Figure II-20. Rotating Detonation Wave Engine (RDWE)	47
Figure II-21. ERH thruster energy deposition modes - bottom view (powered cylindrical and powered spherical modes)	49
Figure II-22. Measurements of air breakdown in the presence of particulate matter	51
Figure II-23. Basic thruster "refresh" modes (shown for line/cylindrical source)	53
Figure II-24. Mechanisms for active refresh enhancement	55
Figure II-24. Mechanisms for active refresh enhancement, cont'd.	57
Figure II-24. Mechanisms for active refresh enhancement, cont'd.	59
Figure II-24. Mechanisms for active refresh enhancement, cont'd.	60
Figure II-25. Infra-sound levitation: ground effect	62
Figure II-26. PRF vs. Vehicle diameter and Hover height	63
Figure II-27. Amplitude-shaped macro pulses	65
Figure II-28. General layout of Engine/Optics/Vehicle configuration	66

LIST OF FIGURES, cont'd.

Figure II-29. Geometry for receptive optics	68
Figure II-30. Active area fraction vs. nose cone angle ($\alpha = 0^\circ$)	71
Figure II-31. Active area fraction vs. nose cone angle ($\alpha = 30^\circ$)	72
Figure II-32. Active area fraction vs. nose cone angle ($\alpha = 45^\circ$)	73
Figure II-33. Active area fraction vs. nose cone angle ($\alpha = 60^\circ$)	74
Figure II-34. Active area fraction vs. nose cone angle ($\alpha = 90^\circ$)	75
Figure III-1 The LSD wave for the case in point	78
Figure III-2 The LSD wave geometry considered by Raizer (see ref. [15])	78
Figure III-3 Shock adiabat of a laser energy absorption wave (see ref. [15])	80
Figure IV-1 Envisioned structure of the parallelly propagating LSD wave	87
Figure IV-2 Perspective view of the blast wave structure for the line source model	87
Figure IV-3 Peak surface (reference) pressure, p_{LSD} , vs. Incident laser intensity	88
Figure IV-4a Cylindrical blast wave surface pressure vs. time, $p(t)$	91
Figure IV-4b Cylindrical blast wave radius vs time, $r(t)$	91
Figure IV-4c Cylindrical blast wave pressure-radius relationship, $p(r)$	92
Figure IV-5 Single pulse impulse, I , imparted to the plate	95
Figure IV-6 Time-averaged thrust, T , applied to the plate	96
Figure IV-7 Peak laser power supplied to the LSD wave for the plasma generation	96
Figure IV-8 Laser pulse energy supplied to generate the line source	96
Figure IV-9 Maximum time-averaged power, \bar{P} , vs. incident laser flux	97
Figure IV-10 Coupling efficiency of the impulse exchange between the blast wave and the plate	97
Figure IV-11 Maximum cylindrical blast wave radius, r_0	99
Figure IV-12 Pulse Repetition Frequency, PRF, vs. flux level	99
Figure IV-13 Laser pulse duration, t_p , vs. flux level	100
Figure IV-14 Duty factor, DF, vs laser flux	100
Figure V-1. ERH thruster engine configuration.	105
Figure V-2. LSD wave Lagrangian view.	105
Figure V-3. Cylindrical blast wave geometry.	108
Figure V-4. LSD/Blast wave expansion.	110
Figure V-5. Supersonic air expansion over thruster plate.	114
Figure V-6. Dynamic model control volume.	116
Figure V-7 Max Expansion Time - 10 km, Mach 3	118
Figure V-8 Time Average Thrust - 48 Beams	119
Figure V-9. PRF - 48 Beams	119
Figure V-10. Time Average Power - 48 Beams	121
Figure V-11. Coupling Coefficient - 48 Beams	121
Figure V-12. Time Average Thrust - 12 Beams	122
Figure V-13. PRF - 12 Beams	122
Figure V-14. Time Averaged Power - 12 Beams	123
Figure V-15. Coupling Coefficient - 12 Beams	123
Figure VI-1 Sketch of LSC wave structure	126
Figure VI-2 Surface pressure due to LSC wave, p_{LSD} , vs. intensity	126
Figure VI-3 Time-averaged thrust vs. Intensity for the LSC wave based-ERH-thruster	130
Figure VI-4 PRF vs. intensity for the LSC wave based-ERH-thruster	130
Figure VI-5 Coupling coefficient vs. intensity for the LSC wave based-ERH-thruster	131
Figure VI-6 Laser pulse energy, E_p	131

LIST OF FIGURES, cont'd.

Figure VI-7 Time-averaged laser power required by the LSC-wave-based ERH thruster . . .	133
Figure VI-8 Laser pulse duration, t_p	133
Figure VI-9 Cylindrical LSC wave's radius at time t_p	134
Figure VI-10 Radius of the wave at the end of the expansion	134
Figure VII-1. ERH Thruster Configuration	136
Figure VII-2. LSC-wave Expansion	136
Figure VII-3a. RR vs. T/T_s , Surface Emissivity of 0.1	141
Figure VII-3b. RR vs. T/T_s , Surface Emissivity of 0.6	141
Figure VII-4a. t/t_s vs. z/r , Surface Emissivity of 0.1	142
Figure VII-4b. t/t_s vs. z/r , Surface Emissivity of 0.6	142
Figure VII-5a. t/t_s vs. T/T_s , Surface Emissivity of 0.1	144
Figure VII-5b. t/t_s vs. T/T_s , Surface Emissivity of 0.6	144
Figure VIII-1. Typical Pressure for Successive Times After Explosion	148
Figure VIII-2. Plot of Peak Blast Wave Pressure vs. Distance from the Source	150
Figure VIII-3. Pressure Signature of ERH Thruster	152
Figure IX-1. Instrumentation Setup	160
Figure IX-2. Computer code flowchart	160
Figure IX-3(a). Theoretical Acoustic Impulse Response - $PRF = 500Hz$	161
Figure IX-3(b). Theoretical Acoustic Impulse Response - $PRF = 1135Hz$	161
Figure IX-4(a). Aliasing and Sampling-Induced Modulation - (analog signal)	163
Figure IX-4(b). Aliasing and Sampling-Induced Modulation - (sampling $f_1(t)$ at a rate of 1 sample/sec)	163
Figure IX-4(c). Aliasing and Sampling - (analog signal $\sin(2.8\pi t)$)	165
Figure IX-4(d). Aliasing and Sampling - Induced Modulation - (sampling $f_2(t)$ at a rate of 1 sample/sec)	165
Figure IX-5. Drag Coefficient vs. Flight Mach number	171
Figure IX-6. Geometry for Horizontal Fly-by at constant thrust, 50 ft altitude, 100 MPH and 41.67 Hz PRF	171
Figure IX-7. Acoustic Signature for 100 MPH Fly-by at 50 ft altitude, a) Distance from observer in feet, b) Normalized amplitude c) Doppler-shifted frequency, d) vehicle pulsing frequency	173
Figure IX-8. Key Trajectory Parameters	174
Figure IX-9. Initial Liftoff Geometry	174
Figure IX-10. Trajectory/Forcing function for Constant 3 G Launch from 0° Initial Zenith Angle	176
Figure IX-11. Acoustic Signature for Constant 3 G Launch from 0° Initial Zenith Angle	177
Figure IX-12. Trajectory/Forcing function for Constant 3 G Launch from 45° Initial Zenith Angle	178
Figure IX-13. Acoustic Signature for Constant 3 G Launch from 45° Initial Zenith Angle	179

LIST OF TABLES

Table II-1. Sedov's Scaling Laws (see Sedov [22])	42
Table III-1. Sedov's Scaling Laws (see Sedov [22])	82
Table VII-1. Parameters Utilized for Input into Numerical Solution	140
Table VIII-1. Predicted Noise Levels	146
Table VIII-2. SPL Values for the First Ten Spectral Components	153
Table VIII-3. SPL vs. Distance From Vehicle	156

ABSTRACT

The principal objective of this study was to perform basic research investigations into an innovative power conversion concept for trans-atmospheric, beamed-energy propulsion: a new class of External Surface Impulse (ESI) thrusters. This advanced thruster principle could be used for atmospheric VTOL, high acceleration, and lateral flight (e.g., short-term "cruise") propulsion of Single-Stage-To-Orbit (SSTO) beam-powered shuttlecraft of the next century.

Three classes of ESI thrusters were initially examined: 1) simple thermal, 2) electrostatic, and 3) electromagnetic. Beam power wavelengths from 10cm (microwave) to 0.3um (laser) were considered. The subsequent research effort concentrated on the simple thermal repetitively-pulsed ESI thrusters, energized with laser power and using air as the working fluid. Laser frequencies were selected because of the relative wealth of experimental data and theoretical research on "laser impulse coupling" which exists in the literature.

The first year analytical effort has proven conclusively that such an engine can deliver high levels of thrust-to-beam-power at liftoff (e.g., at least an order-of-magnitude greater than beam-powered hydrogen-fueled rockets), with infinite specific impulse (decreased only, perhaps, by ablation of the thruster surface). Later along an orbital trajectory, the primary propulsion function would transition to other modes; upon leaving the atmosphere, the SSTO vehicle would continue in a pure rocket mode with a specific impulse (I_{sp}) of 1000 seconds or more. The principal motivation behind this variety of "combined-cycle" transatmospheric propulsion is the potential for "more payload to orbit" for a given laser power level - than given by beam-powered rockets alone.

CHAPTER I

INTRODUCTION

The first year effort began with an initial investigation of several alternative approaches to External Surface Impulse (ESI) thrusters: 1) simple thermal, 2) electrostatic, and 3) electromagnetic varieties. The primary focus of the subsequent investigation was on the simple thermal class of thrusters: specifically, the External Radiation-Heated (ERH) thruster. For the purpose of comparison, the latter two thruster types will be described first.

A) Electrostatic ESI Thruster

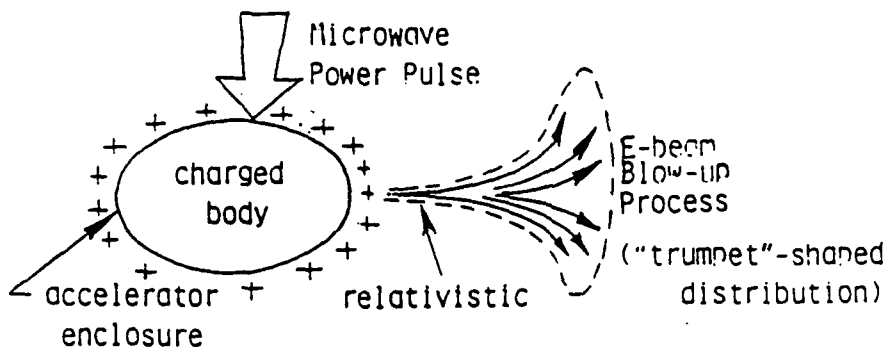
The electrostatic ESI thruster concept (shown in Fig. I-1) utilizes a remote projected microwave or laser power beam to accelerate and eject relativistic streams of electrons to some remote location away from the thruster surface. This leaves the vehicle exterior with a large resultant positive charge. The ejected electrons preferentially attach to previously neutral oxygen or water molecules (in the ambient air) thereby creating a negatively charged cloud. Impulse is then generated by electrostatic forces occurring between the charged cloud and vehicle surface. As the vehicle moves through the negative ion cloud, its surface charge is neutralized; then the entire process is repeated.

B) Electromagnetic ESI Thruster

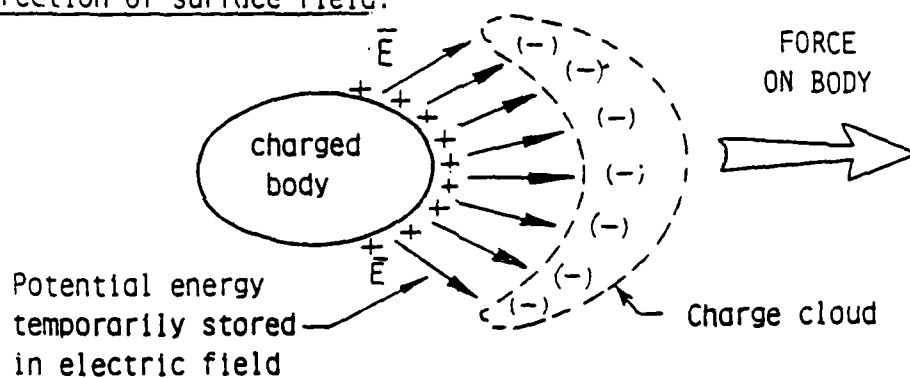
The electromagnetic type of ESI thruster uses microwave or laser energy to first ionize the ambient air working fluid near the thruster surface (e.g., see Fig. I-2). Once ionized, the driver loop (an electromagnet) is pulsed and an electric field is induced in the gas. The gas is then repelled from the thruster surface by means of electromagnetic forces, (i.e., $F = J \times B$), thereby generating thrust. Presumably, a powerful and lightweight on-board electric power supply would be required, one which could be recharged with beamed energy. Refer to Fig. I-3 which shows the electrical circuit model for one exemplary electromagnetic ESI thruster.

Both electrostatic and electromagnetic ESI thrusters are technologically complex and require additional onboard power conversion equipment - with which simple thermal engines would not be burdened. For such complicated thrusters, it is presently unclear as to which flight velocities and altitudes would yield superior performance, and how they could be integrated into energetic

a) Charge emitted near body surface:



b) Creation of surface field:



c) Acceleration of "Charge Cloud" Reaction Mass:

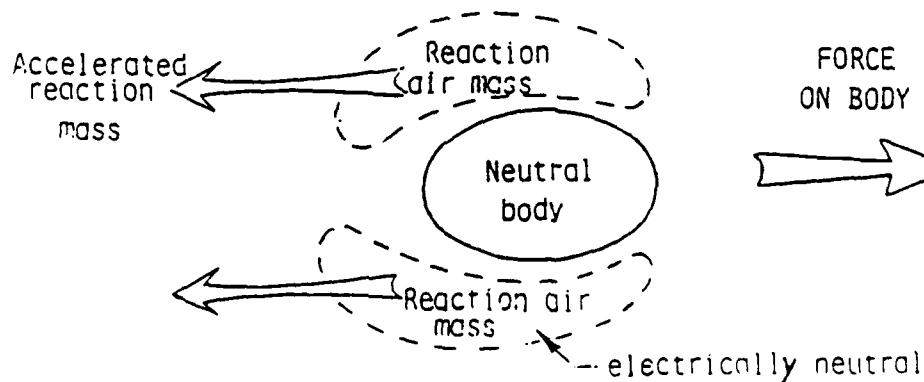


Figure I-1 Pulsed Electrostatic ESI Thruster

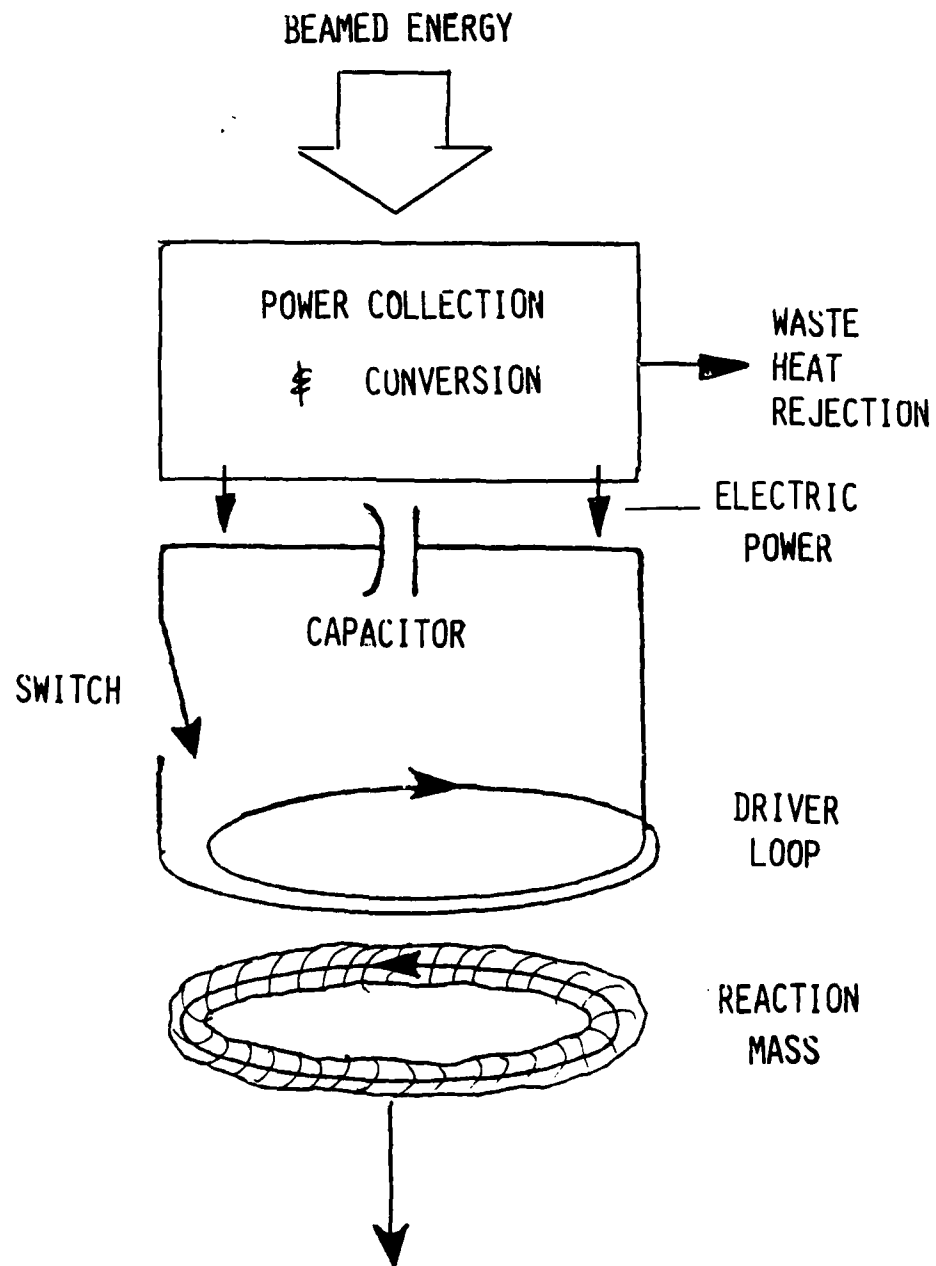


Figure I-2 Pulsed Electromagnetic ESI Thruster

combined-cycle engines.

On the other hand, the results of the present study have shown that simple thermal ESI thrusters are ideally suited for the initial liftoff boost period (e.g. Mach 0 to 3) of advanced air-breathing shuttlecraft, are easily integrated into a variety of combined-cycle engine concepts, and require minimal energy conversion (on-board) equipment. For these reasons, the engine holds much promise for use with beam-powered transatmospheric vehicles of more-or-less "conventional" design (i.e., heavier-than-air, and relatively compact in size).

C) Simple Thermal ESI Thruster

The External Radiation-Heated (ERH) thruster concept is pictured in Fig. I-4. The reaction surface is integrated with the underside exterior structure of the vehicle. The actual thruster geometry can vary greatly depending upon the desired vehicle configuration. ERH surface shapes considered here were circular frustrums and flat circular plates, which are appropriate for vehicles of radial symmetry (e.g., the Apollo Command Module). Other shapes would be more suitable for delta-winged shuttlecraft, like the space shuttle orbiter.

To create thrust, high intensity electromagnetic radiation (either microwave or laser frequencies) must be projected radially inward from the vehicle's perimeter, and brought to focus near the geometric center of the ERH thruster surface. This radiation ignites and sustains a number of air-plasma "waves" which propagate radially outward (and parallel to) the thruster surface as shown in Fig. I-4. These laser-sustained plasmas produce blast waves which subsequently expand over the ERH surface - generating impulsive thrust.

The process of thrust production is described more thoroughly in the following sequence:

- i) Depending on the frequency and intensity of focused radiation, either a Laser Supported Detonation (LSD) or Combustion (LSC) wave is initiated by the mechanism of inverse Bremsstrahlung. In these radiation-sustained plasma waves, electromagnetic energy (e.g., laser light) is converted to thermal energy - resulting in a high temperature zone with elevated pressure. In the case of an LSD wave, a very high pressure blast wave is formed. However if an LSC wave is used, the resultant blast wave pressure is several orders of magnitude lower, but furthermore the plasma temperature is much higher.
- ii) As the blast wave decays to the local ambient pressure, a reaction impulse is transmitted to the thruster surface. Some portion of this impulse is converted to usable upward thrust, depending on the inclination of the ERH thruster surface to the flight axis.
- iii) Once the blast wave has decayed, the region adjacent to the thruster surface still contains

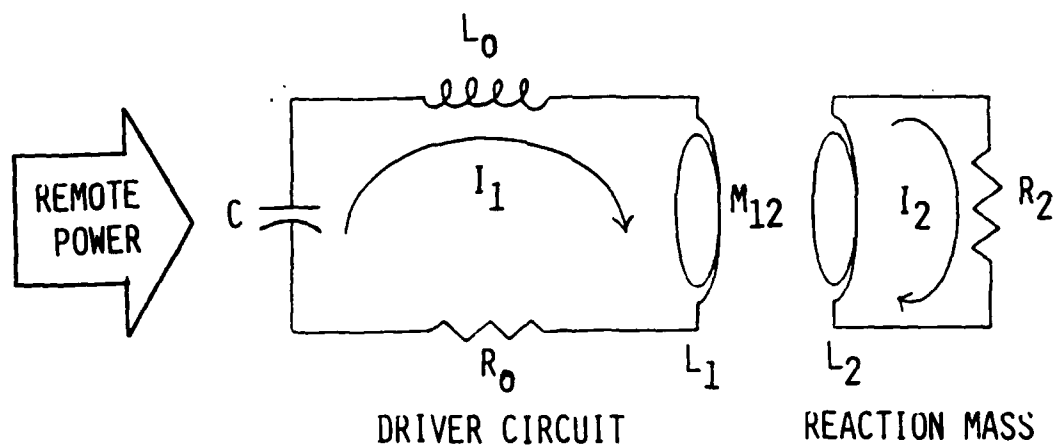


Figure I-3 Electrical Model of Pulsed Inductive Thruster
(after Mileci, Ref. 24)

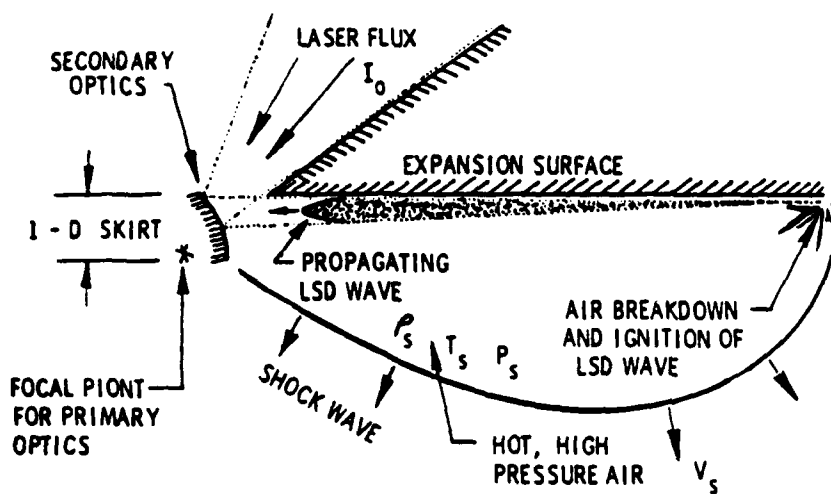


Figure I-4 Simple Thermal ESI Thruster

hot gases. These "spent" gases must be removed and replaced with unprocessed ambient air before a new thrust cycle can be started. Expressed another way, the surface must be "refreshed". This process is equivalent to the heat rejection part of a conventional thermodynamic cycle. Unlike most current propulsive engines which utilize "pulsejet" heat addition in a Brayton cycle, the ERH thruster is closest to the "constant volume" class of engines (e.g., like the V-1 "Buzz Bomb" used by Germany against England in World War II).

Note that the ERH thruster is a repetitively-pulsed engine. Its Pulse Repetition Frequency (PRF) is governed by the blast wave decay time and the thruster surface refresh time. Therefore, the total cycle time is dependent on the ambient air pressure and density in which the ERH thruster operates. This implies that the thruster performance varies with both altitude and flight velocity. The maximum engine PRF varies throughout the entire flight envelope; a typical cycle time is on the order of a millisecond.

Although not specifically examined in the first year, it is important to consider the use of microwave frequencies with the "simple thermal class" of ESI thrusters. Less literature exists on microwave-sustained plasmas, but sufficient understanding has now been accumulated to begin research on microwave beam energized ESI thermal engines.

These long wavelengths (microwave) are critically important for the future beamed-powered SSTO shuttlecraft. Air Force scenarios generally dictate all-weather operation, and only microwave beams can penetrate clouds/rain/fog (all forms of precipitation) without significant attenuation. By contrast, laser beams must "burn-through" clouds, exploding and evaporating water droplets - a brute force solution that is highly wasteful of beamed power. A preferred solution is for the shuttlecraft to perform a "pop-up" maneuver, wherein it climbs vertically through the cloud layers (e.g., up to 30-40,000 ft) under a low-power microwave beam, then rotates to engage a high power laser beam link for the final boost. It has become apparent that both modes will be important for future SSTO beam-powered vehicles.

D) Report Organisation

Chapter II covers the reference vehicle/platform configuration assumed in the present research effort. Since the method of heating the engine working fluid (air) requires the use of optics and an air refresh scheme (lateral and/or axial modes), it is clearly platform dependent.

Chapter III reviews the basic phenomenology of inverse bremsstrahlung absorption of laser energy into the air working fluid.

Chapters IV and V introduce two models for LSD-wave heated ERH thrusters. These models are of the "static" variety, in that they do not directly take into account a particular "refresh" scheme for convecting new air into the active thruster volume. Chapter V also analyzes the "dynamic" performance of a conical-frustrum thruster surfaces.

Chapters VI and VII describe analyses of an LSC wave heated ERH thruster. Chapter VI reviews the impulse generation model, and suggests additional refinements which are necessary. A radiation heat transfer model was also created, and used to assess the severity of the surface heating problem. The temperature history results are presented in Chapt. VII.

Chapter VIII provides an analysis of the far-field sound levels produced by the reference ERH thruster configuration. In Chapt. VIII, this analytical model is used to simulate the sound patterns (i.e., frequency, amplitude, doppler shift, etc.) produced by an ERH thruster as it accelerates along representative boost trajectories - as perceived by observers on the Earth's surface.

Finally, Chapt. X gives a summary of principal conclusions reached in the first year funding segment.

II FLIGHT PLATFORM REFERENCE CONFIGURATION

The primary task of this "basic research" investigation was to develop and exercise analytical models for estimating the performance of advanced beamed-energy propulsion concepts. However, a reference flight platform geometry was adopted in order to introduce the combined requirements for primary and secondary optics, impulse generation, surface contours, and "refresh" modes for the ERH thruster. In addition, the pursuit of a reference configuration helped to clarify how the ERH thruster concept might be incorporated into variable-cycle engines optimized for acceleration along an Earth-to-orbit trajectory, wherein rockets are used for final orbit injection.

These innovative airbreathing engines must incorporate the functions provided by conventional inlet and nozzle (exhaust) components. It is interesting to note that for hypersonic speeds, airbreathing inlets can become very large - large enough to house the entire payload. Hence, the following discussion uses the terms "vehicle" and "engine" almost interchangeably.

A) Reference Platform

The reference engine/vehicle shape is that of a five meter diameter axis-symmetric body largely composed of conic frustrums, as illustrated in Fig. II-1. The body can be divided into three basic components: forebody, cowl and afterbody.

The forebody consists of an external isentropic "spike" diffuser with a conical tip of 15 degrees (semi-vertex angle) and a 35 degree turn into the cowl. It provides the dual role of an external compression inlet and, equally as important, the parabolic primary receiver optics for the incoming power beam. Roughly half of the cross-sectional area represented by the inlet centerbody is covered with the primary receptor mirror.

The forward inner rim of the cowl contains twelve small circular secondary optics (ref. config.) which are positioned close to the focal point of the large parabolic primary receiver mirror. These secondary mirrors then project the high power beam(s) parallel to the afterbody external surface - at an intensity of $5 \times 10^8 \text{ W/cm}^2$ (see Fig. II-2). The cowl itself provides the function of directing the compressed inlet airflow so that it "blows" across the afterbody - for the purpose of "refreshing" the spent air in the detonation zone. The cowl is assumed able to translate axially so that optimal inlet flow characteristics can be maintained throughout the flight envelope; the cowl may also have a deformable forward lip and trailing edge. This variable-geometry cowl would ideally keep the conical bow shock always attached at the cowl lip - above some design mach number (e.g., mach 3).

The afterbody forms the base of the vehicle and behaves as an external-expansion conical plug nozzle of 45° half angle. It is here that the LSC/LSD waves deliver their impulse, since the plug also serves as the ERH thruster surface. In the reference configuration, twelve propagating LSD waves (semi-circular cross-section, 1 cm radius) produce twelve high pressure (800 atm), 2.5 m long cylindrical plasma volumes (hereafter called "fingers"), which subsequently expand laterally over the plug nozzle surface to generate thrust. Fresh air is fed axially to the nozzle afterbody, as directed by the cowl; the lateral refresh mechanism also serves an important role.

As mentioned above, a base angle of 45° was selected for the LSD mode in the reference configuration. A base angle of 0° was picked for the LSC mode since most of the impulse may be transmitted to a nearly horizontal surface area represented by the lower (hemi-spherical) end of the truncated cone afterbody.

B) Engine, Vehicle and Power System Architecture

As mentioned above, the central thrust of this investigation is a basic research effort into the physics of ERH thrusters. However, in order to compute the performance of the device one must specify in detail a number of "boundary conditions" - which are intimately related to the energy deposition mode (e.g., LSD vs LSC wave), optical focusing, and gasdynamic assumptions (including "refresh"). In other words the investigation is built upon, or defined around, a specific "reference configuration".

In the pursuit of research on CW beamed-energy rockets, one must specify the beam power, degree of focusing, focal geometry (e.g., point vs line), absorption chamber dimensions, nozzle geometry and working fluid conditions (pressure, temperature and mass flow rate). All these "system-related" considerations have an impact on basic research investigations. On the other hand, such issues as the size of propellant tankage or dimensions of receiving optics are of little concern to the propulsion researcher. Obviously, all the propellant is carried onboard for the rockets, and optic dimensions are driven by the mission.

In contrast, an airbreathing engine has a somewhat different set of "driving issues". Perhaps the dominant one is the need for an efficient inlet since the engine working fluid is collected from the atmospheric environment, through which the engine propels itself. For high mach numbers (e.g., high supersonic and hypersonic), the inlet size often dwarfs the rest of the engine. Why? Because of the need to maximize total pressure recovery within the inlet. In fact, for hypersonic engines proposed for the "Orient Express" (e.g., scramjets), the inlet/nozzle considerations dictate the entire lower airframe geometry. In essence, all the payload and much of the fuel will be housed

within the external compression inlet volume.

This fact gives great incentive for future "designers" of beam-powered transatmospheric aerospacecraft to integrate the primary receptive optics with the engine inlet, vehicle airframe, or exhaust nozzle. Depending on the choice of beam wavelength, transmitting antenna diameter and range-to-the-power source (or relay), the receiving antenna size can be a significant issue. The reference engine/platform configuration adopted for the present study, assumes that the primary optic is integrated with a radially-symmetric isentropic spike inlet; an external-expansion nozzle also doubles as the vehicle afterbody. Furthermore, it is assumed that the intake is sufficiently large to contain the payload; the engine and vehicle are merged into a single entity. The following discussion attempts a broad discussion of the choices in engine/optics/airframe integration which face future designers of beam-boosted transatmospheric shuttlecraft - that utilize ERH thrusters.

Ten basic "platform considerations" have been identified (there may be more) which influence the detailed design aspects of ERH thrusters. In turn, these considerations affect the choice of "boundary conditions" that must be specified in order to analyze the performance of any given ERH thruster concept. They are:

- 1) Power source location (ground-based vs. space based)
- 2) Power beam wavelengths (frequency-switching)
- 3) Overall vehicle/airframe configuration
- 4) Flight vector orientation (relative to beam)
- 5) Airbreathing inlet geometry
- 6) Shroud/cowl configuration
- 7) Receptive optical train geometry
- 8) Thruster surface/nozzle geometry
- 9) Thrust vectoring control
- 10) Energy deposition modes for thrust generation
- 11) Air "refresh" schemes

Each of these ERH thruster-related considerations will now be discussed in more detail.

1. Power Source Location (GB vs. SB)

The beam power source may be based either in space (SB) or on the ground (GB), and utilize low altitude relay stations. The present reference system assumes 5 to 10 GW satellite solar powerstations in geostationary orbit and multiple low altitude relay satellites (e.g., at 185 km). The system assumes the use of "cross-links" and "down-links", but no "up-links" of beam power from

the ground.

2. Power Beam Wavelengths (frequency switching)

A single wavelength for the power beam is usually invoked in beamed-energy propulsion studies. The capability for frequency switching has been mentioned on occasion, usually in connection with enhancing the efficiency of power beam transmission, or conversion to propulsive thrust. For example, shorter (i.e. laser) wavelengths are advantageous for longer transmission links between receiver and transmitter antennae of a given size. Laser power transmission is usually limited to fair weather, but a high power beam could also "burn through" clouds, evaporating all moisture in the path. Ultraviolet wavelengths shorter than $0.3 \mu\text{m}$ are too badly dissipated by molecular and particulate scattering - to be of much use at the bottom of the atmosphere. However, if "down-linked" from space, ultraviolet beams could still be used to advantage (by a beam-powered vehicle) in the upper reaches of the atmosphere and of course, throughout the vacuum space environment. In contrast, microwave and millimeter radiation exhibit the lowest atmospheric attenuation through weather (clouds and all forms of precipitation), but wavelengths much longer than 10 cm yield transmitter/receiver apertures that become unwieldy.

The present reference system assumes that frequency switching is available in the bandwidth from 10cm through $0.3 \mu\text{m}$. Microwave wavelengths (10cm-0.1cm) are used for near-vertical "popup" maneuvers, wherein the shuttlecraft climbs (at low acceleration) up through weather. A low altitude (185km) transmissive fresnel-type microwave relay satellite may be used to refocus a large diameter microwave beam (e.g., 7 km), down to the small dimensions of a shuttlecraft. Once above the clouds, the shuttle (and primary optic) is rotated to engage a "laser-link" - by way of another laser relay satellite at 185km - which it chases all the way into orbit (the final transatmospheric acceleration run).

The characteristics of microwave radiation sharply restrict the maximum beam intensity level which can be collected upon the vehicle/engine primary optics. This "plasma maintenance" intensity threshold scales directly with wavelength to the negative 0.45 power. As a result, microwaves frequencies are only good for low power accelerations; alternately laser frequencies can easily enable vehicle accelerations beyond human tolerance.

It is known that, radiation-sustained plasmas produced by optical wavelengths (i.e., laser) region have two distinct structures, depending on the incident radiation flux density. These structures resemble conventional detonation and deflagration waves generated by chemical reactions. High beam intensities create laser-supported detonation (LSD) waves; lower intensities, laser-supported

combustion (LSC) waves. A critical question is: "Do similar absorption wave structures exist with microwave radiation?"

The analytical expressions derived for laser-supported detonation wave velocity and peak pressure (by Raizer) show no frequency dependence. As a result, one might expect that "detonation" waves could also be sustained by microwave power. However, the electric breakdown threshold of air appears to scale with the inverse square of the beam wavelength, so the threshold is much lower for the microwave frequencies than for optical. In the microwave region, breakdown at atmospheric pressure occurs at a flux density of $1-2 \text{ MW/cm}^2$, as compared with $4-5 \text{ GW/cm}^2$ for $10.6 \text{ }\mu\text{m}$ radiation. Raizer indicates out that microwave-triggered breakdown normally occurs before a detonation wave can be generated at sea level pressure. The breakdown threshold is simply lower than that intensity which can maintain a detonation-type structure.

However, as will be demonstrated in Chapt. VII, laser-sustained "deflagration-type" waves can indeed produce blast waves, the essential ingredient for generating propulsive forces with ERH thrusters. So there is good reason to suspect that microwave-sustained "deflagration" waves can successfully be used as well. Microwave radiation can sustain plasma temperatures which are much lower than those generated by optical frequencies. For microwaves, resultant air plasma temperatures can be on the order of 2000 to 4000K, whereas can it exceed 10000 to 20000 K for optical frequencies. Therefore, radiation heat transfer to ERH thruster surfaces might be reduced by using microwave power during low acceleration maneuvers (i.e., lift-off and landing) and hover.

One must be careful, however, not to compare apples and oranges. As noted above, the ERH thruster is a repetitively pulsed engine which generates thrust by expanding blast waves off the impulse-coupling surface. The pulse repetition frequency and duty cycle obviously must enter into this heat transfer problem. Hence one cannot just examine peak microwave- and laser-heated plasma temperatures, but should carefully assess the convective, conductive and radiative heat transfer to the ERH thruster surface.

3. Overall Vehicle/Airframe Configuration

Clearly there should exist an infinite variety of airframe choices for transatmospheric aerospacecraft. Historically, however, there have been only two broad categories: i) delta-wing, and ii) axi-symmetric. The first category is exemplified by the space shuttle orbiter, and perhaps by several earlier lifting-body research vehicles (glide re-entry mission). Of more recent vintage are numerous delta-winged concepts for the "Orient Express", propelled by hypersonic scramjet engines.

The other major class is exemplified by the radially symmetric Apollo, Gemini and Mercury

space capsules, and certain axi-symmetric experimental engines like the NASA Hypersonic Research Engine (HRE). The present reference configuration is assumed to be axi-symmetric, and has a parabolic primary receptive optics intimately integrated with the large external-compression inlet centerbody.

4. Flight Vector Orientation (relative to beam)

In theory, a beam-powered shuttlecraft could be propelled in any flight direction relative to the projected energy beam. For transatmospheric missions, some fixed-geometry laser-heated rocket schemes have been proposed to utilize a large range of beam intercept angles (e.g., up to 60°); these concepts do not require focusing optics in the propulsion converter, however. For those that do require precision receptive optics, two alternatives exist: i) fixed geometry, and ii) variable geometry.

A good example of the second class is the articulated "telescope" receptive optical train proposed by TRW for their laser-heated H_2 rocket-powered orbit transfer vehicle (OTV) concept. Clearly, in the vacuum of space, this telescope arrangement gives complete freedom in the flight vector orientation ($\pm 180^\circ$). With no atmospheric drag penalty in a zero "G" environment, these structures could be both large and light-weight.

Worlds apart from the OTV mission is that of an airbreathing TAV powered by beamed energy. In the TAV mission, articulated primary optic geometries for beam reception must be abandoned, unless small enough to be placed beneath a transparent high-power dome/window - that also has low drag. The remaining fixed-geometry alternative leaves two options for flight/beam vector orientation: i) axial, or ii) lateral. In the former, the vehicle flight axis is aligned with the beam, and the engine "swallows" the beam as it climbs to orbit. In the latter option, the vehicle accelerates at right angles to the beam (or at some fixed angle).

Both options might need to invoke a low altitude relay satellite in order to negotiate the pitch change schedule required along the boost trajectory. A viable alternative is to switch through several relay stations in strategically placed orbits, to accomplish a series of greater vehicular pitch changes. It should be noted that a large primary optic which is permanently affixed to a TAV shuttlecraft can probably not sustain a beam misalignment (pointing accuracy) of more than 1-3 degrees. However, most studies of rocket engine thrust vector data gathered on current launch vehicles (including the space shuttle orbiter) indicate that 2-3 degrees is typically what is demonstrated.

The present study assumes that the vehicle axis of symmetry is aligned with the flight direction to an "accuracy of ± 2 or 3 degrees" - to permit thrust vector control of the flight path

angle.

5. Airbreathing Inlet Geometry

There is no guarantee that a revolutionary airbreathing engine concept such as the ERH thruster would necessarily derive benefit from the addition of a supersonic inlet of conventional design (or geometry). This issue is especially worth considering because it is the low supersonic and subsonic mach numbers where the ERH thruster is expected to excel (e.g., Mach 0 to 3 for the reference configuration). However, other factors related to multi-mode or combined-cycle operation can be expected to enter into the requirements for defining the ultimate airbreathing inlet geometry. For example, in the reference configuration the primary propulsive role may transition from ERH thruster to ramjet at Mach 3, then to scramjet at Mach 6 (or quite possibly into scramjet at Mach 3, skipping the ramjet mode altogether). These latter cycles may require a cowl for best performance, and the ERH thruster should benefit from the additional air supply for axial "refresh".

Early studies by Billig [3], and others have proven that scramjets with conventional inlets and cowls to contain the "combustor" section, yielded superior propulsive efficiencies to un-cowled or "external-burning ramjet" concepts. However these studies examined the use of conventional chemical fuels in hypersonic cruise modes. Hence, the conclusions may require some interpretation when applied to radically different advanced engine concepts designed for the acceleration role - utilizing beamed energy. Furthermore, one must consider that a beam-powered TAV engine will be in this propulsive mode for a very short time (e.g., less than 60 seconds).

Similar statements could be made for the ERH thruster since it is an unusual repetitively-pulsed engine, and falls in a completely different class than the more familiar ones using Brayton "constant pressure" cycles. One should note that the compression process (in the ERH thruster) is provided by a propagating LSD or LSC wave, and not a mechanical compressor. Also, the spent air must be vented and replaced with new air, and two mechanisms have been identified that could provide this function: i) axial refresh, and ii) lateral refresh (discussed below, in another section). Hence, the unusual engine cycle exhibited by the ERH thruster concept demands that one take a completely new look at the available options for air inlet, power-injection, and exhaust mechanisms.

As is commonly known, all fixed-geometry supersonic inlets have a design Mach number (M_D) whereupon the bow shock is exactly attached at the inlet cowl lip. Off-design operation forces the inlet into a sub-critical or super-critical condition wherein the total pressure recovery can be expected to decline.

Variable-geometry inlets attempt to extend the range of optimum performance beyond just

M_D . Clearly, the approaches to varying the inlet geometry are different, depending upon whether the configuration has 2-dimensional (2-D) or radial symmetry (isentropic spike, bi-conic, tri-conic, etc.). The present study will focus will be upon the latter, since it is used on the reference platform.

There appear to be at least six methods (see Fig. II-3) which (singly or jointly) have the potential for preventing a conical bow shock from becoming lodged (or swallowed) into the inlet cowl: i) translating the shroud fore and aft (e.g., like NASA's HRE scramjet), ii) deforming the cowl leading edge (i.e., like retractable "high lift slats" on wings), iii) replacing the conical tip with an ogive shape, iv) extending a pointed spike forward out the cone tip, scheduled with increasing flight mach number, v) "kicker plates", and vi) blunted hemispherical nose caps.

The first option has a potential problem in that the secondary optic may be forced to translate fore and aft with the shroud, thereby removing them from the primary optics focal region. (Alternatively, shroud translation can be used to engage a sequential series of secondary optics.) The second option may increase the mechanical complexity of the cowl, but should be feasible for cowls having a large diameter and relatively short length. The third option may spill a lot of air, causing increased "spillage drag" for the inlet. It is not clear whether or not the fourth option, extending a spike, will deflect enough air at supersonic speeds to do any good. The fifth option, kicker plates, has been successfully employed with 2-D inlets in almost all current Mach 2^+ jets. The sixth option of blunting the nose on the conical tip (e.g., with a hemisphere), would result in a detached shock forming just off the nose. Although the flow could be expected to re-attach later on the ogive or conical inlet surface, some loss in total pressure recovery would be incurred.

6. Shroud/Cowl configuration

At least three mechanisms (see Fig. II-4) can be invoked for turning the engine air working fluid around a large external-compression inlet centerbody - so that the ERH thruster surface maybe "refreshed" axially: i) a physical shroud with a variable exit area nozzle, ii) a shroudless configuration that leaves Prandtl-Meyer expansion fans to turn the flow, and iii) a thin mini-shroud "ring" which solely consists of a small annular secondary (reflective) optics.

The first option is the traditional approach (most conservative), and could be counted upon for enabling good total pressure recovery throughout the entire Mach 0-3 envelope (required of the ERH thruster in the reference platform). Clearly, this jet of pressurized air leaving the shroud could supply most of the ERH thruster surface with "refreshed" air at densities much above ambient. It would also permit the engine to develop thrust levels beyond that which could be demonstrated in the static (i.e., motionless) condition at any given altitude. However, this favorable situation is not

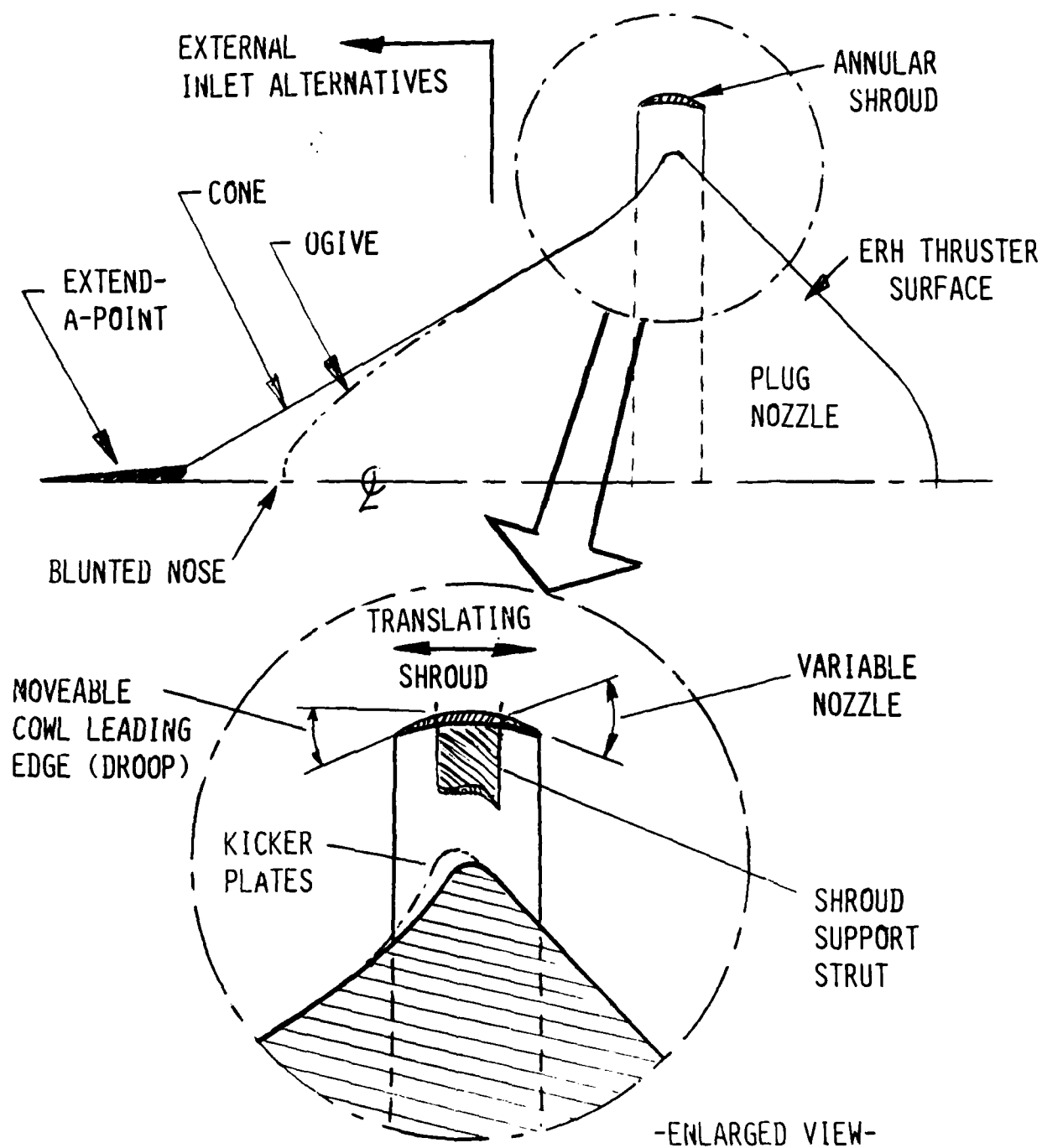
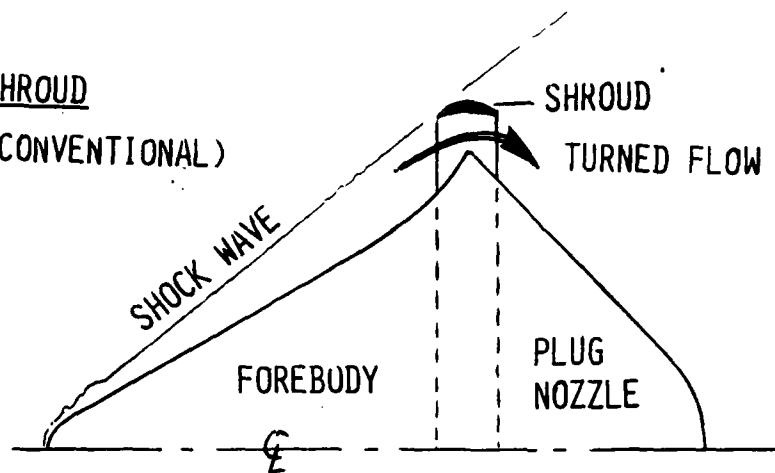
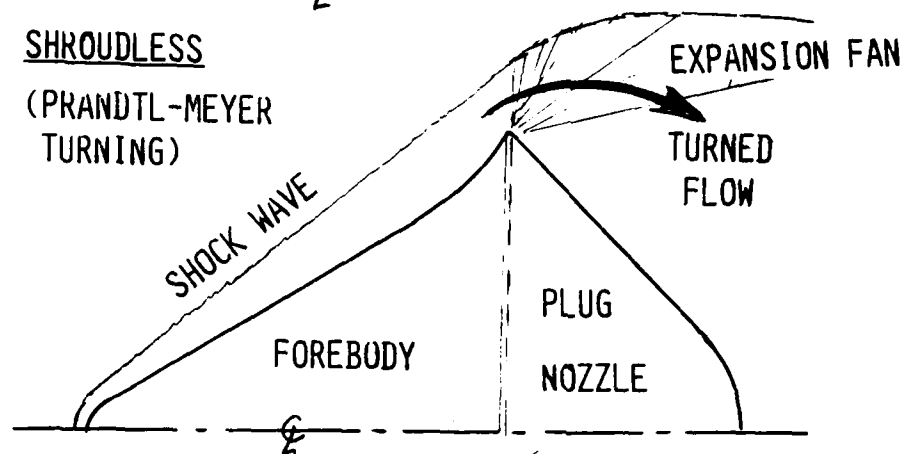


Figure II-3 Methods for incorporating variable geometry in radially-symmetric supersonic inlets

A) SHROUD
(CONVENTIONAL)



B) SHROUDLESS
(PRANDTL-MEYER TURNING)



C) MINI-SHROUD
(SO-RING)

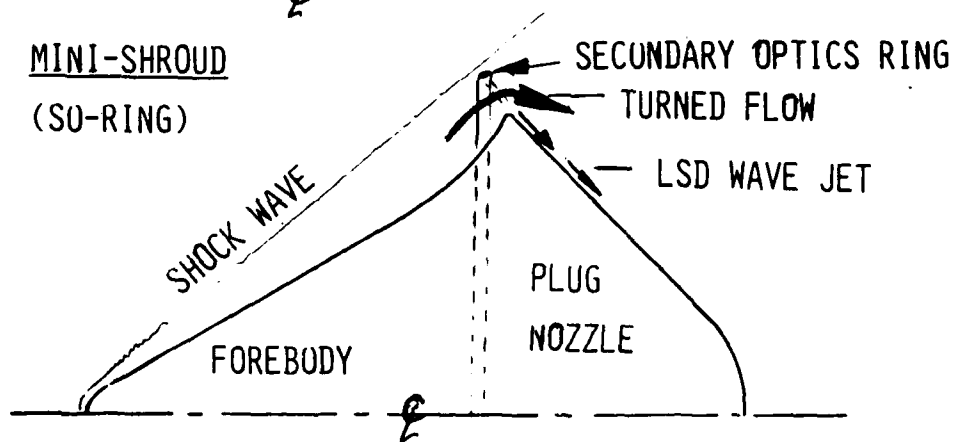


Figure II-4 Shroud/Cowl Flow-turning options

secured without suffering the penalties of increased drag produced by the annular shroud and radial support struts, and spilled ram air.

The second option avoids shroud drag altogether, by eliminating the shroud itself. However, the penalties for this approach will appear in several other areas. During high supersonic speeds, the ERH thruster surface will be immersed in "refresh air" at a lower density than with the shrouded option. This condition translates into a reduction in maximum attainable thrust. Also, with small " α " plug nozzles (i.e., nearly flat-bottomed configurations), flow separation could occur immediately aft of the maximum engine/vehicle cross-section. Hence, the resultant low densities behind the vehicle would not only produce greatly increased drag, but adversely affect thrust generation as well. Another potential problem is the complex flow field that would result from separation and vortex shedding, off the aft ERH thruster surface. This may have a deleterious effect on the LSD wave ignition and propagation processes. Finally, there may be other significant losses due to vorticity in the exiting flow as it expands away from the vehicle.

In the third option, the mini-shroud is simply a small annular secondary mirror, having an aspect ratio not much different from a "hula-hoop" - only with a bi-convex cross-section. Although this thin miniature airfoil could induce some "aerodynamic lift" flow-turning, the bulk of the work would be accomplished by high velocity jet flow fields which trail behind propagating LSD waves [2] - as shown in Fig. II-5. Pre-compressed air that enters the "cowl" will have been turned outward (e.g., 35° to 40° from axial) by the external inlet forebody. Next, hypersonic LSD waves would chop repeatedly through this annular "duct" flow. After much turbulent mixing, the annular cowl air flow would be vectored back past the axial direction (perhaps aided by an "ejector" process), and expanded against the engine/vehicle afterbody plug nozzle.

The obvious penalty incurred here, will be due to the additional beam-power invested in longer laser pulses (i.e., to turn the flow with LSD waves). Normally, the laser pulse would be terminated just as the LSD waves reach the uppermost perimeter of the ERH thruster "plug", right before they enter the annular shroud air gap. Clearly, this type of flow-turning mechanism would be accessible only to receptive optical trains which incorporate "ring-type" secondary optics. In contrast, a slightly-scalloped primary optics which links to a set of small circular-type secondary optics, could obviously not invoke the LSD wave flow-turning mechanism.

7. Receptive Optical Train Geometry

Taken as a whole, the receptive optical train comprises the receiving "antenna" which collects the remote-beamed power and delivers it to the ERH thruster surface. In general, the train requires

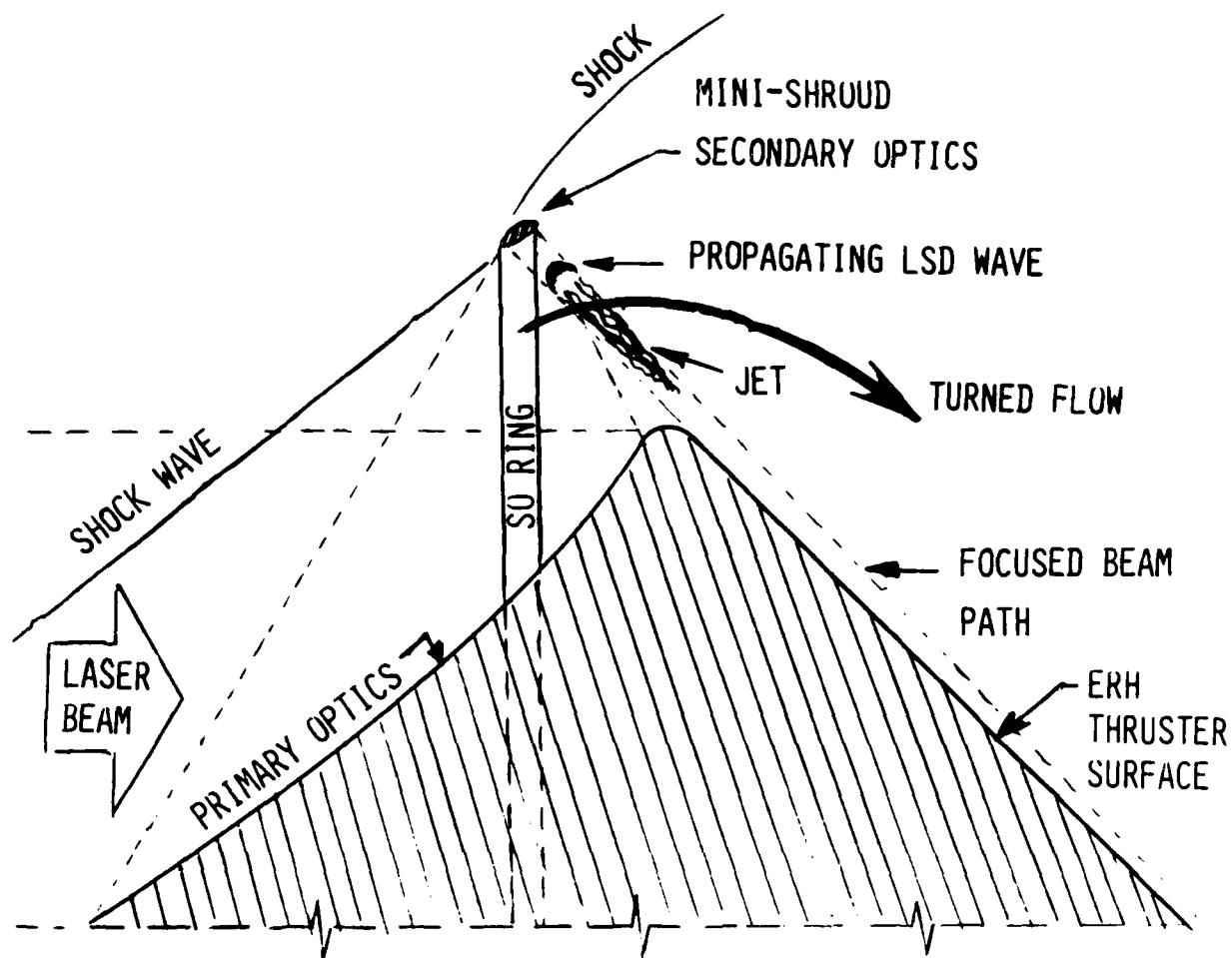


Figure II-5 Flow-turning by LSD-wave "Jet"

only Primary Optics (PO) and Secondary Optics (SO), but in some cases may include Tertiary Optics (TO). For brevity, the following discussion is restricted to engine/vehicle configurations with radial symmetry.

As mentioned in the previous section, radially-symmetric engines can: i) be shrouded, ii) be shroud-less, or iii) use a mini-shroud. Figure II-6 displays representative receptive optical trains which are compatible with these three categories; it is not meant to be an exhaustive treatment of the subject. For the purpose of comparison, the reference platform is shown in Fig. II-6a. The large receptive primary optic is a paraboloid of revolution. If, for example, an annular high-intensity beam must be delivered across the ERH thruster surface, then the secondary optic must also be a continuous ring mounted to the inner surface of the shroud, just short of the annular line focus (i.e., of the parabolic PO). If a large number of cylindrical detonation wave sources (i.e., "fingers") is desired across the ERH thruster, the primary optic surface must be slightly scalloped. This will concentrate and split the power beam onto a series of small circular-shaped secondary optics - which, in turn, will reflect the beam in a multi-fingered fashion. This option may be referred to as a multi-point focus.

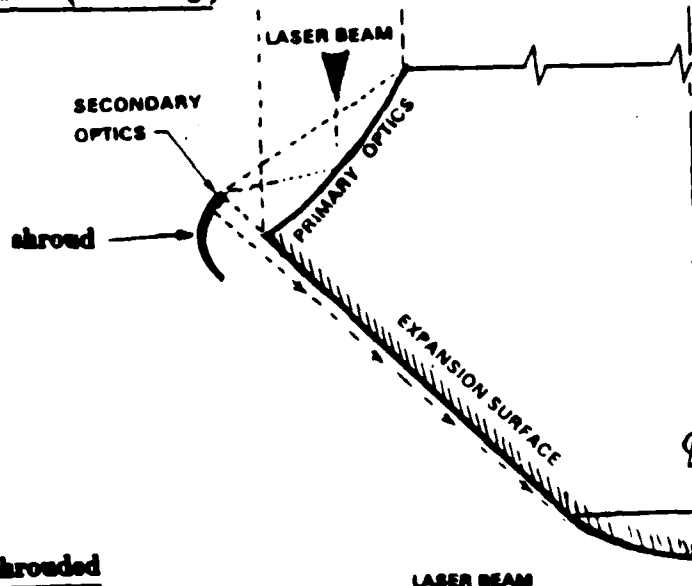
Finally, it should be mentioned that if the shroud is allowed to translate fore and aft, several sets of the small, lightweight SO mirrors could be engaged - either at discrete increasing flight Mach no.'s (perhaps during transitions to different engine modes), or possibly as a result of power beam frequency-shifting. In the latter case, larger SO apertures may be required with longer beam wavelengths in order to counteract diffraction effects. In general, the SO's may be designed to project collimated beams with roughly constant intensity along the ERH thruster plug.

The unshrouded engine/vehicle configuration shown in Fig. II-6b takes a slightly different approach to the optical train design. Here, a high power window is placed over the parabolic reflective primary optic. Clearly, there will be losses suffered by the beam as it passes through this transparent aeroshell. Upon reflecting off the PO, the beam is focused towards the SO, then travels onward to the ERH thruster surface. Either annular-line or multi-point foci can be invoked for use with truncated plug nozzles. Alternately, one might use transmissive primary lenses instead of the reflective variety, and eliminate one set of optical surfaces (i.e., the high power "planar" window).

Figures II-6c and 6d portray the mini-strut geometry, which is a variation of the mini-shroud theme shown earlier in Figs. II-4c and II-5. If the reflective PO is slightly scalloped, then the annular SO may be replaced by a set of circular SO's affixed to the end of radial mini-struts. Incidentally, these external struts could be incorporated into other engine modes and thereby serve multiple functions.

Fig. II-6e illustrates one final option for the receptive optical train geometry, one which

a) shrouded (ref. config.)



Note:
PO can be parabolic
surface to produce
annular line focus,
or "scaloped" to
produce multi-point
focus - at the site
of the secondary
optic(s).

b) unshrouded

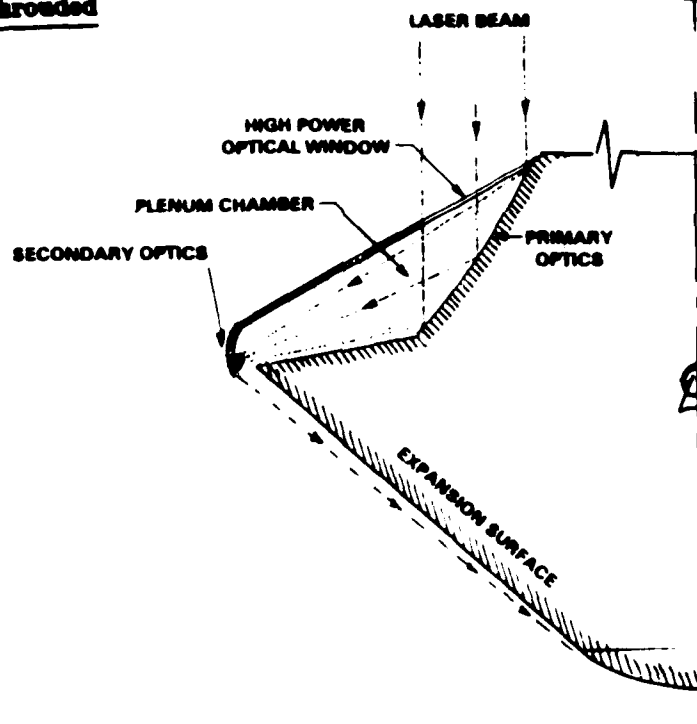
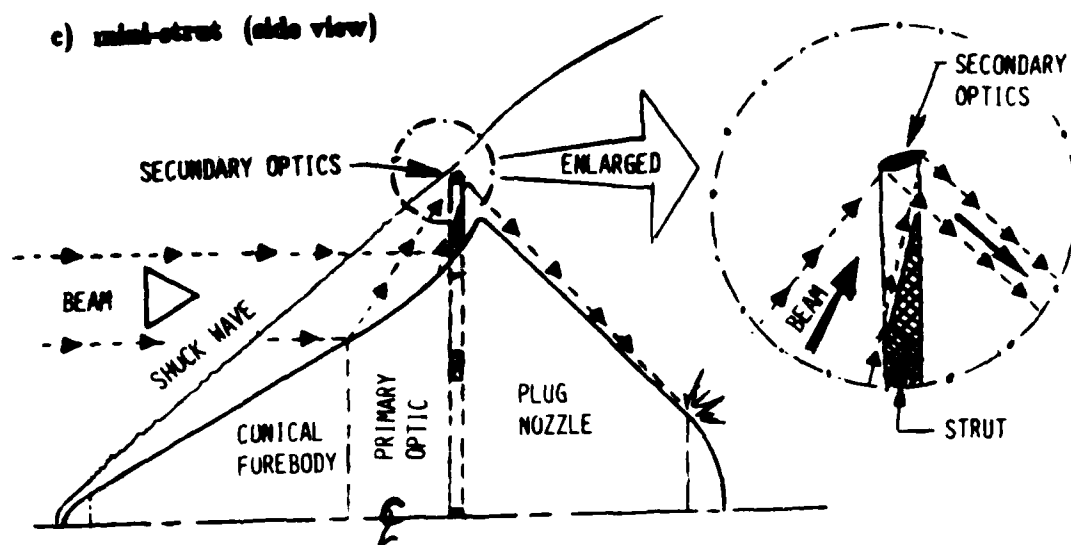


Figure II-6 Options for Receptive Optical Trains



d) mini-strut (top view)

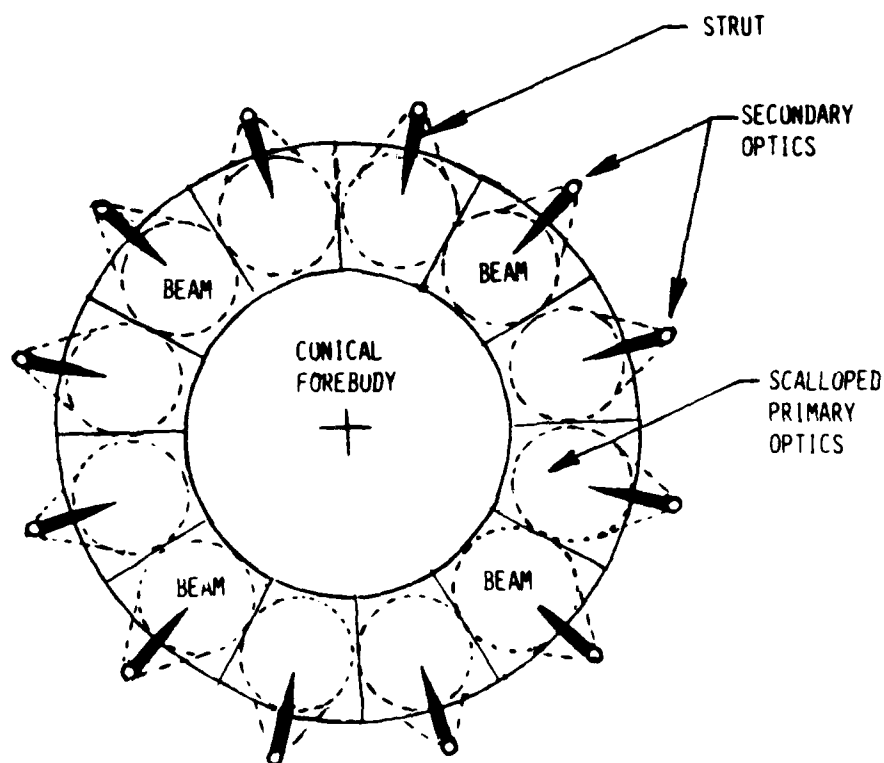


Figure II-6 Options for Receptive Optical Trains, cont'd.

demonstrates the use of tertiary optics. In this example, the parabolic PO first throws the power beam out towards an annular line focus; then a scalloped annular SO intercepts the beam and reflects it towards a set of small grazing-incidence TO's. As indicated in Fig. II-6a, the fan-shaped beam between each SO and TO (see Fig. II-6f) would be concentrated in only one direction. Each TO would be of approximately cylindrical contour and reflect a circular beam across the ERH thruster plug.

This geometry would enable the use of multiple detonation- line sources (i.e., "plasma fingers"), yet not demand the use of a scalloped PO surface. Why use this three element optical train when it appears more complicated than the two-element system? Because other combined-cycle engine modes may require a different combination of lenses - necessitating an optical train with variable-geometry. For example, the TO's in Fig. II-6b are sufficiently small to be easily retracted.

Finally, Fig. II-7 portrays a top view of the PO surface for the reference point design. Figure II-7a shows the laser illumination pattern used to generate the simultaneous 12 line ("finger") source, and Fig. II-7b for the rotating single line source.

8. Thruster Surface/Nozzle Geometry

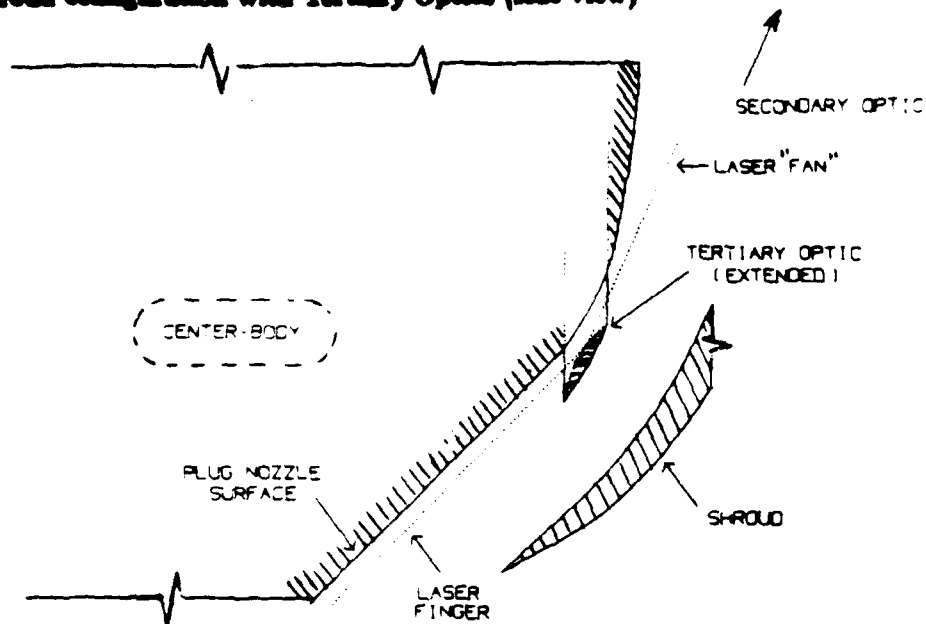
In general, the vehicle afterbody on future beam-powered reusable SSTO shuttlecraft will need to serve multiple functions. In the reference radially-symmetric engine/vehicle, the afterbody is used as a plug nozzle type of external-expansion surface for the entire combined-cycle engine. This multi-mode propulsion system is composed of the ERH thruster from Mach 0 to 3, several other airbreathing modes from Mach 3 to 25, and finally rockets for orbit insertion. The afterbody also acts as a re-entry heat shield. Hence it is likely to be an uncooled surface, and probably fabricated from advanced refractory materials like the carbon/carbon composites used on the Space Shuttle Orbiter nose and leading edges.

a) Plug nozzle variation

It is logical to assume that the plug nozzle should be combined with the ERH thruster surface itself because of the need for "axial refresh" - a replenishment of the 'spent' air heated by the previous LSD wave. The specific variety of plug nozzle used in the reference design is shown in Fig. II-8: i.e., a partial-internal/partial-external expansion type. For this geometry, a portion of the flow expansion will occur within the cowl; the minimum cross-sectional duct area would be upstream of the cowl exit station.

Figure II-9 graphically demonstrates the effect on nozzle (and cowl) contours as the per-

e) shroud configuration with Tertiary Optics (side view)



f) shroud configuration with Tertiary Optics (bottom view)

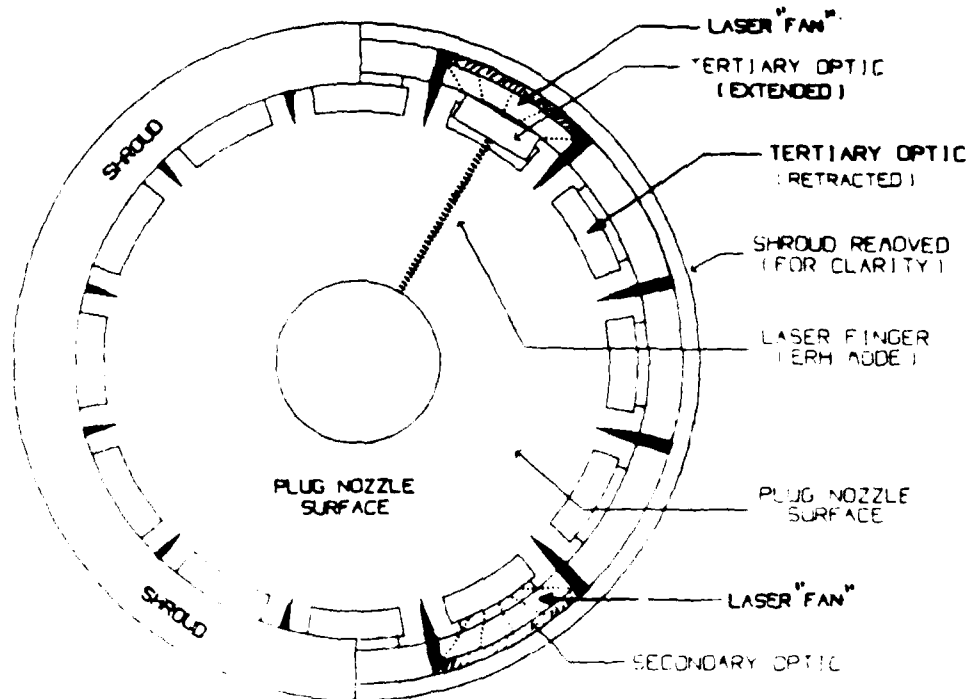
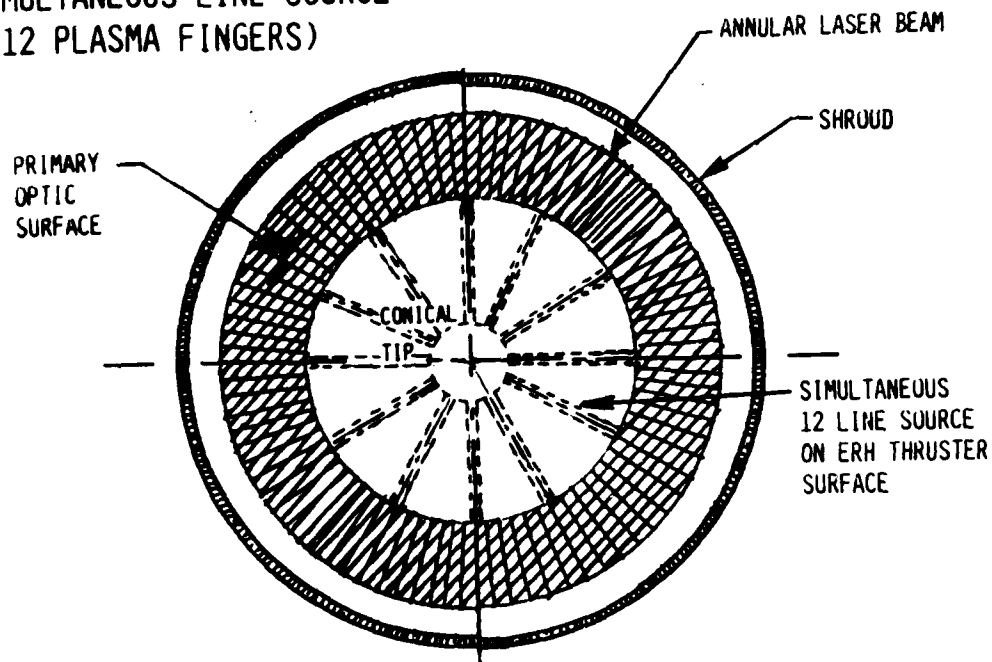


Figure II-6 Options for Receptive Optical Trains, cont'd.

A) SIMULTANEOUS LINE SOURCE
(12 PLASMA FINGERS)



B) SINGLE LINE SOURCE
(1 PLASMA FINGER)

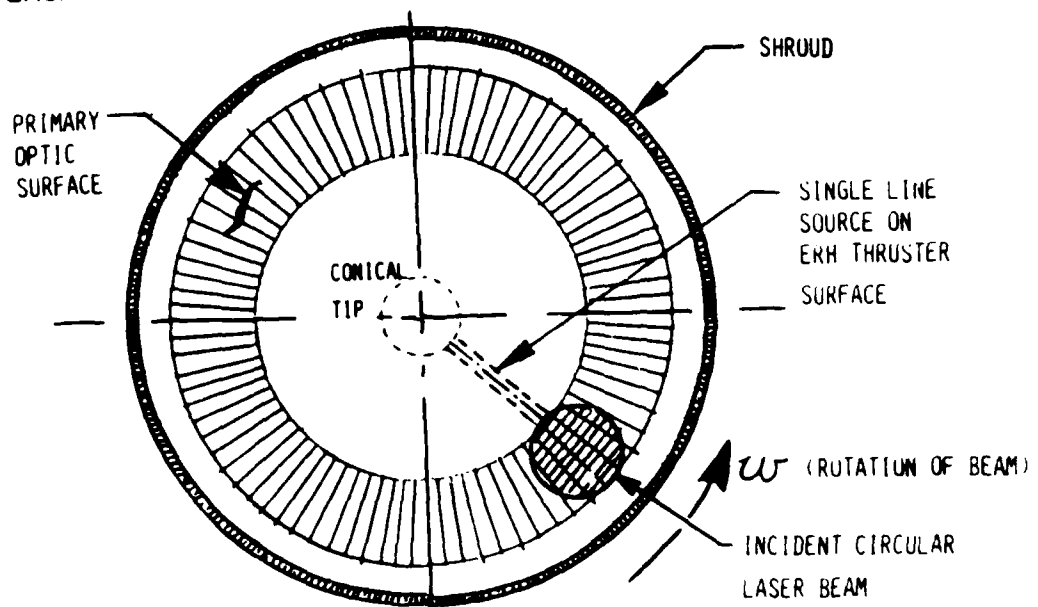


Figure II-7 Top view of PO surface for ref. point design

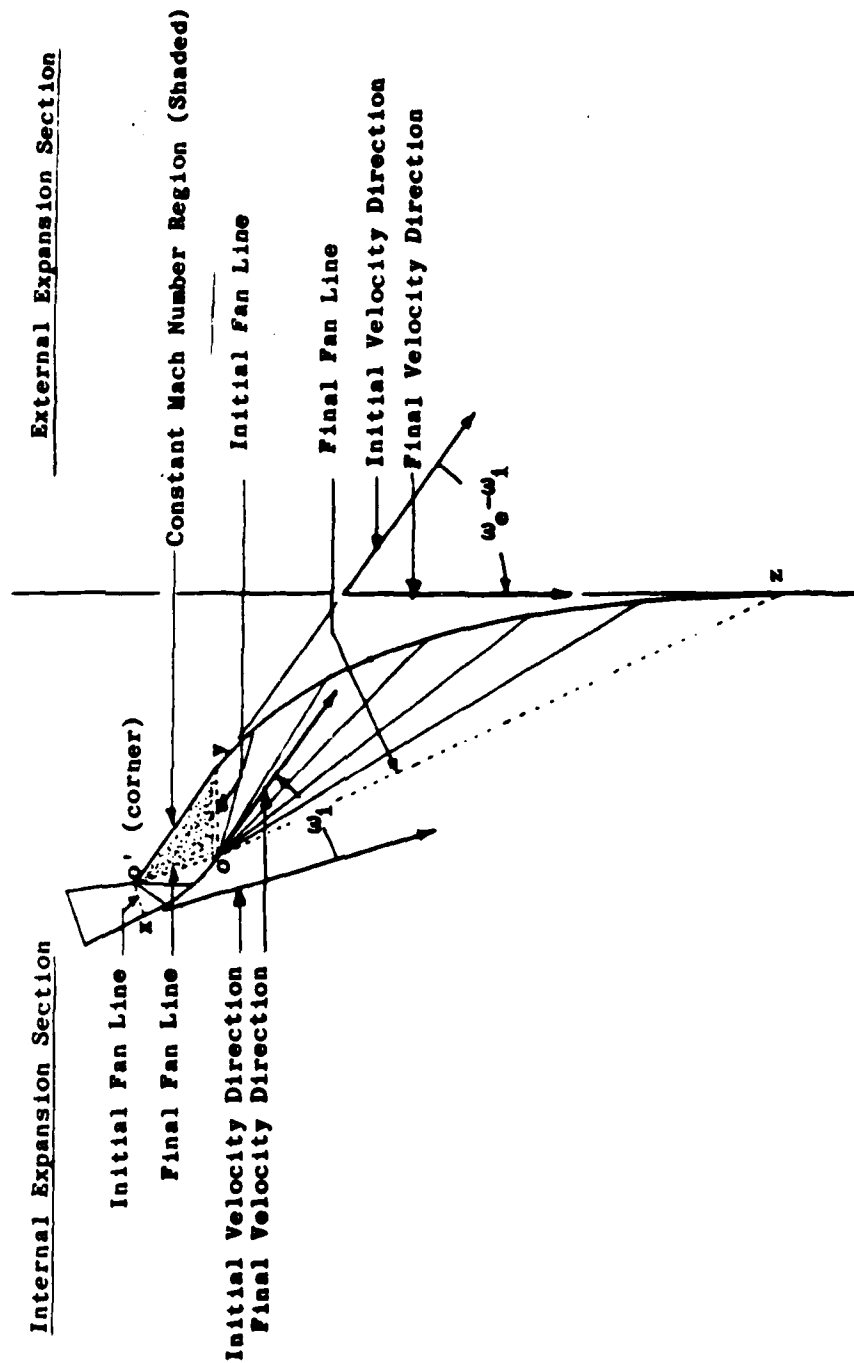


Figure II-8 Partial-internal/Partial-external expansion type nozzle
 (From Graham, Ref. #6)

centage of internal expansion is increased. Note that the initial angle which the flow makes with the central axis of symmetry (i.e., α) gets larger with increased internal expansion. Eventually, with 100 % internal expansion, the nozzle becomes 'inverted', and all flow expansion takes place against the inner surface (see Fig. II-10). This variety of nozzle is sometimes referred to as an Expansion-Deflection (ED) nozzle.

Since laser power can only be projected along straight lines, the external plug nozzle surface must be approximated by a simple cone. For example, Fig. II-11 shows the outline of a 50% internal expansion plug nozzle and demonstrates how the complex isentropic spike contour can be replaced with a variety of conical surfaces. Upon further examination, it becomes obvious that one must select the largest indicated cone apex angle, in order to prevent high intensity laser beams (projected by the SO mirrors) from impinging upon the plug nozzle surface. For the case given in Fig. II-11, " α " would roughly equal 40° , which is also the angle that cowl-ducted gas would emerge upon the plug nozzle. (Incidentally, since the reference engine/vehicle has an α of 45° , one might expect that 25% to 50% of the flow expansion would take place within the shroud.)

b) Importance of base angle

One important parameter to consider in the design of such conical plug nozzles (i.e., for use as ERH thruster surfaces), is the base angle α indicated in Fig. II-12. As the base α is increased so does the length " L " of the conical ERH thruster surface (i.e., $L = r / \cos \alpha$). This creates a longer "blast zone" for the input of energy, as well as additional surface area over which the blast wave can expand. However, the additional area does not always produce more propulsive force, because only the vector component aligned with the vehicle flight direction results in "thrust" (i.e., usable thrust = $T \cos \alpha$). By increasing the base angle α the efficiency of the ERH thruster will actually decrease, since more laser-generated impulse is required for an equivalent propulsive thrust.

Nevertheless, when designing the overall engine/vehicle configuration, many compromises come into play, and the above discussion is just one example. One should note that a decrease in thruster efficiency (due to large α) may to some extent be offset by a decrease in aerodynamic drag, and an improvement in "refresh" function.

In the search for an ideal thruster base angle, α , one should also consider plug nozzle performance in the rocket mode - which is an important issue for combined-cycle engines. Note that the extreme area ratio plug nozzle shown in Fig. II-13 would give excellent expansion characteristics for rocket engines initiated above 200,000 ft altitude. Shallow thruster angles (e.g., $\alpha = 30^\circ$) would give exceptional performance in the ERH thruster mode as well. Throughout the intervening airbreathing modes from Mach 3 to 25, ducted air flow must be prevented from separating at the

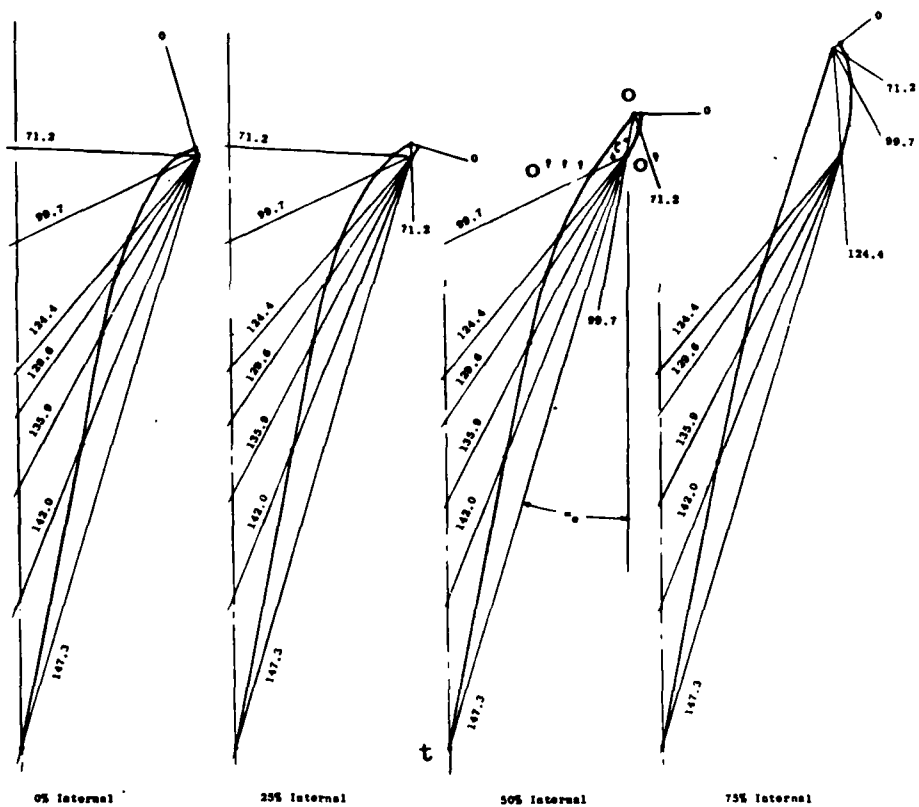


Figure II-9 Nozzle contours vs. percent internal expansion
 (From Graham, Ref. #6)

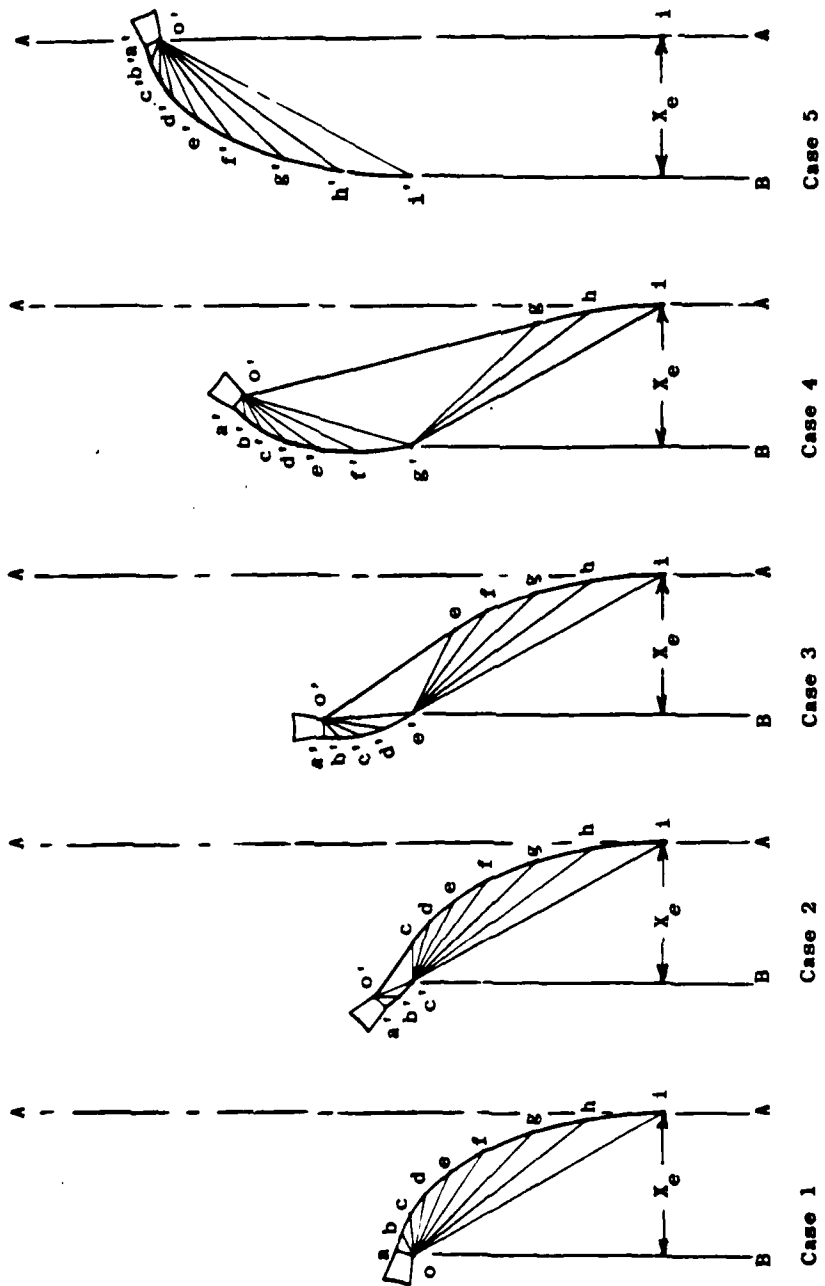


Figure II-10 2-D Prandtl-Meyer expansions (constant area ratio, constant thrust)
(From Graham, Ref. #6)

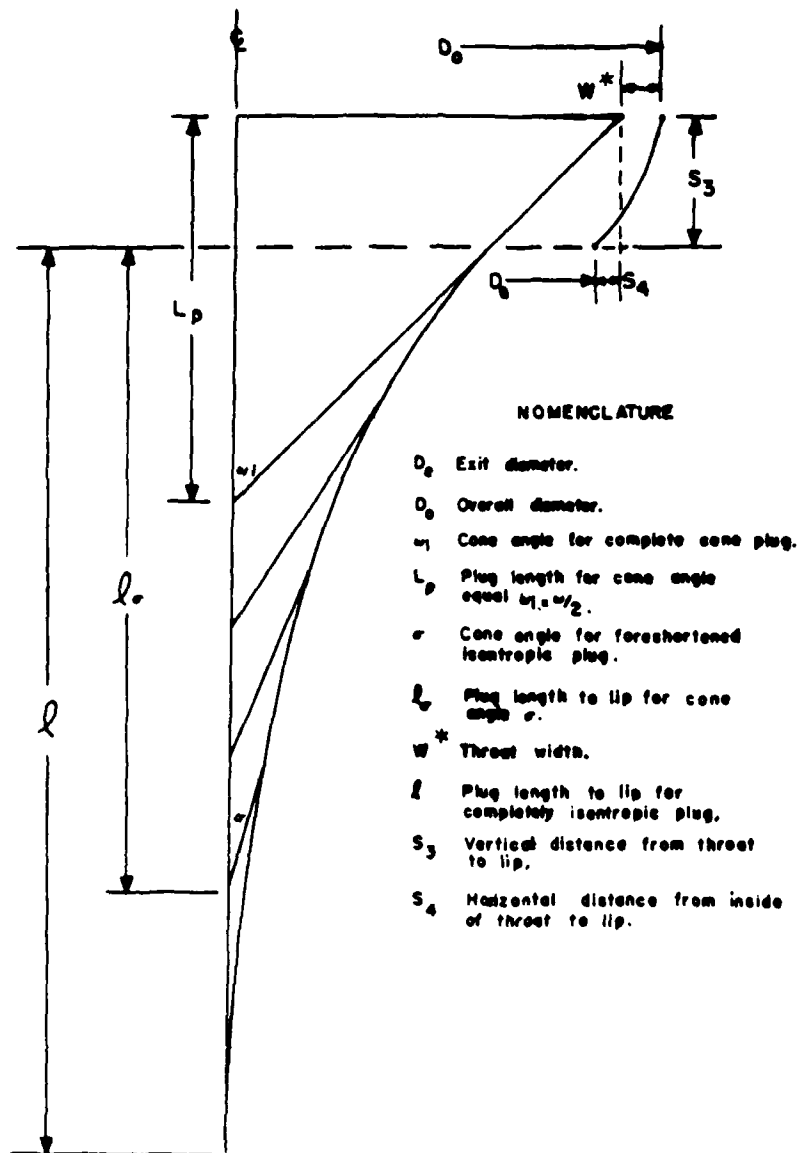


Figure II-11 Outline of a 50 % internal expansion plug nozzle
(From Graham, Ref. #6)

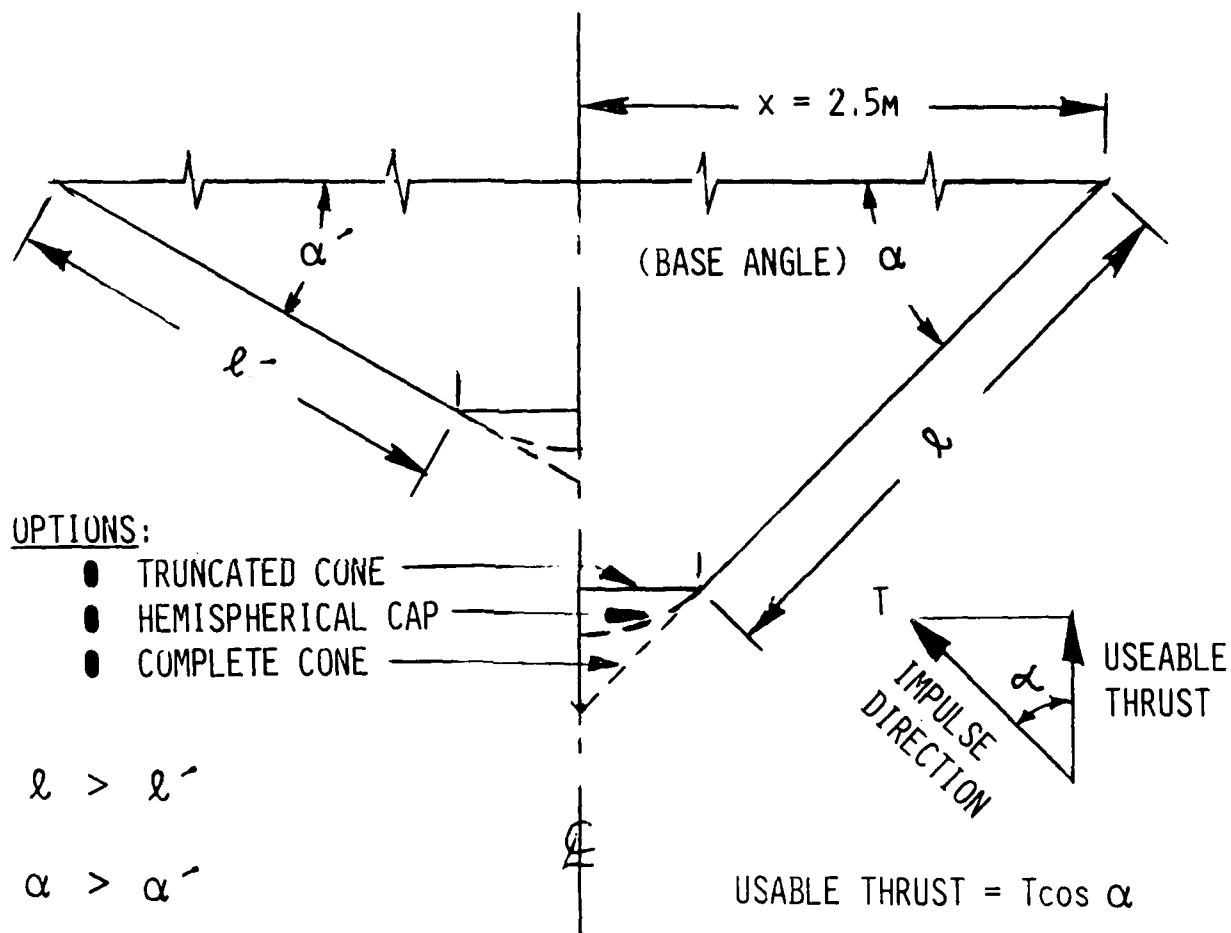


Figure II-12 Effect of base angle

extreme cowl exit angles, of course.

c) Blast wave overlap problem

In the aerothermodynamic design of ERH thruster surfaces, it is important to consider the degree of overlap by adjacent cylindrical blast waves as they expand down to local ambient pressure, against the conical plug. Expressed another way, one must consider the ratio of "active" to "passive" thruster area available over the entire thruster plug. Here, "active" area is defined as that plug area which lies immediately above an LSD wave as it races up the entire length of the nozzle. "Passive" area is that lateral area over which the resultant cylindrical blast wave expands, in the process of delivering impulse to the plug.

The maximum lateral radius to which a cylindrical blast wave expands (when the pressure within it reaches ambient) is a critical design parameter for efficient "lateral refresh". If significant overlap of adjacent blast waves occurs, then the lateral refresh process will become impaired.

As the engine/vehicle climbs in altitude, this lateral "refresh impairment" will first occur at the lower point of a complete conical plug nozzle. Hence, ERH thruster efficiency can be enhanced by truncating the cone. Incidentally, if the ERH thruster surface must also serve as a re-entry heat shield, the cone tip must be rounded to a large spherical radius anyway (see Fig. II-12).

One logical way to prevent the lateral refresh impairment problem, (even for truncated cone plugs) would be to utilize a conically focused "multi-finger" beam geometry across the ERH thruster face - instead of the cylindrical "multi-finger" beam geometry used in the reference design. This means that the plasma fingers will actually be tapered; hence, the plasma will relax to ambient pressure faster at the lower end of the plug (i.e., at the finger tips), than at the top. Since more room exists for lateral expansion at the top of the truncated plug than at the bottom, this would seem to be an optimum solution.

Then in order to maintain a constant beam intensity upon propagating LSD waves (required for a homogeneous detonation pressure), beam power must be increased (i.e., ramped upward) during the laser pulse. This will result in a "sawtooth-shaped" pulse energy distribution vs. time. Since the primary receptive optics has a fixed area over which to receive the power beam, a "saw-toothed" laser pulse would more severely load the PO at the end of the laser pulse, than at the beginning. This condition might necessitate a reduction in received time-averaged beam power, below that which is assumed for the reference design. (Incidentally, a homogeneous detonation pressure field might be advantageous from an engineering design perspective, because the entire plug surface would have the same load per unit area.)

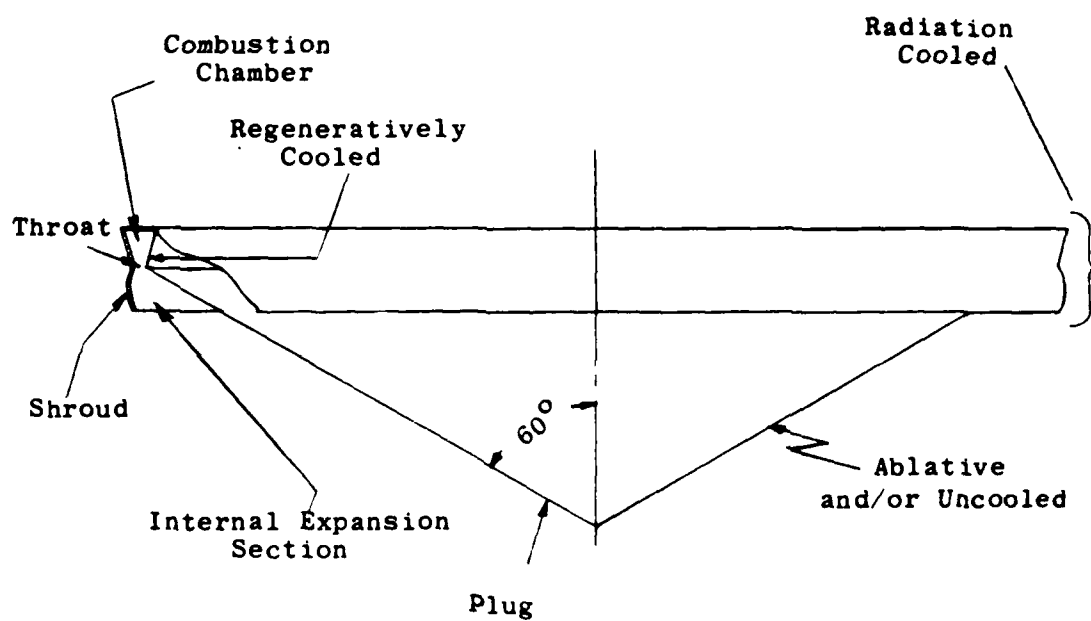


Figure II-13 Extreme area ratio plug nozzle
(From Graham, Ref. #6)

d) Miscellaneous issues

The available receptive PO mirror area and peak beam power can be easily computed for a given ERH thruster plug - once the entire engine/vehicle geometry has been defined. (This subject is treated thoroughly in Section C below, and will not be repeated here.) It bears mentioning, though, that the available PO area can be directly related to the choice of forebody inlet geometry (i.e., as dominated by inlet the cone apex angle), inlet design Mach number (M_D), and angle α of the afterbody plug nozzle.

In designing an ERH thruster, one would be ill-advised to ignore the relationship of the shroud to the expanding blast waves shed by the ERH thruster plug. With some thought, one could imagine a shroud/plug geometry wherein the shroud helps to direct the rapidly expanding plasma aft, yielding increased thruster efficiency.

As a final note, ERH thruster surfaces will be exposed to radiation-sustained plasmas at temperatures of roughly 4000 K with LSD waves, and greater than 10,000 K with LSC waves. Such elevated temperatures may cause the thruster surface to ablate (a potential materials problem). Furthermore, LSD waves will produce very high peak pressures (e.g., 600 atm in the reference design) upon very localized areas, resulting in extremely high stresses. Most conventional high temperature materials (e.g., ceramics) are unable to withstand such high localized stresses. In contrast, ductile materials (refractory metals) which can survive large non-uniform stress distributions, lose strength when heated to extreme temperatures.

Actual material selection for the reference ERH thruster configuration was not attempted. However, such advanced materials are likely to become available in the foreseeable future, if they are not already present: e.g., carbon/carbon re-entry heat shields, or whisker-reinforced ceramic composites.

9. Thrust Vectoring Control

The final topic of this section involves the need for "thrust vectoring", a necessary element in the control of vehicle flight path angle. The ERH thruster utilizes a "segmented" type of operation, which automatically offers a unique mechanism for thrust vector control - without the need of a gimbal system. By increasing and decreasing the time-averaged pressure across various segments, the necessary forces for controlling the thrust vector may be generated. The time-averaged pressure over any segment angle of the plug may be varied simply by changing the laser intensity delivered to the LSD waves propagating across that segment. This, in turn, varies the detonation pressure (p_{DW}), and therefore impulse delivery.

The thrust-vectoring control process can be accomplished in three additional ways. First, the radial symmetry of the blast waves may be disrupted to asymmetrically push one side of the plug more often than the other. Second, as indicated in Fig. II-14, the LSD wave ignition point may be varied up or down the plug to decrease or increase the cylindrical length of the blast waves. Third, the laser pulse duration could be shortened in order to restrict impulse delivery (preferentially) to the lower end of the thruster plug.

It may be necessary to configure the plug geometry such that the impulse generated by a single full-length "line source" blast wave is directed along a vector that passes exactly through the vehicle center-of-gravity. This condition would enable the vehicle to propel itself at right angles to the laser power beam, perhaps a necessary control-related function for a beam-riding engine/vehicle.

In Fig. II-15, it is seen that the time-averaged pressure across the high pressure side of the plug is defined as p_{ch} and that on the low pressure side as p_{cl} , which acts over the segment angle " ϕ " of the plug. In general, when p_{ch} is increased, p_{cl} is decreased in such a way as to maintain constant total thrust. In normal flight, the entire thruster plug would operate with the same time-averaged pressure, defined as p_{cs} .

When thrust vector control is obtained by this technique, the vector can be made to tilt over through the angle " δ " and also shift laterally through a distance " d ". Normally, the direction of vector angle and vector shift would be additive, in so far as generating a turning moment about the vehicle center of gravity. Finally, the vector angle can be expected to depend upon at least three parameters: i) the percent overpressure, $(p_{ch} - p_{cs})/p_{cs}$; ii) operating pressure ratio, p_{cs}/p (where p_a = ambient atmospheric pressure), and iii) plug nozzle geometry itself.

10. Energy Deposition Modes for Thrust Generation

This section offers a broad perspective of the various energy deposition modes which can be used by ERH thrusters. In describing these modes, the following physical principles come into play:

- a) Performance vs. incident beam intensity
- b) Noise generation
- c) Asymmetric thrust considerations
- d) Scaling laws for various blast wave geometries
- e) Absorption-wave/thruster geometry
- f) Passive refresh of planar vs. line sources
- g) Wavelength scaling effects (LSC/MSP regime)
- h) Ignition requirements for radiation-sustained plasmas

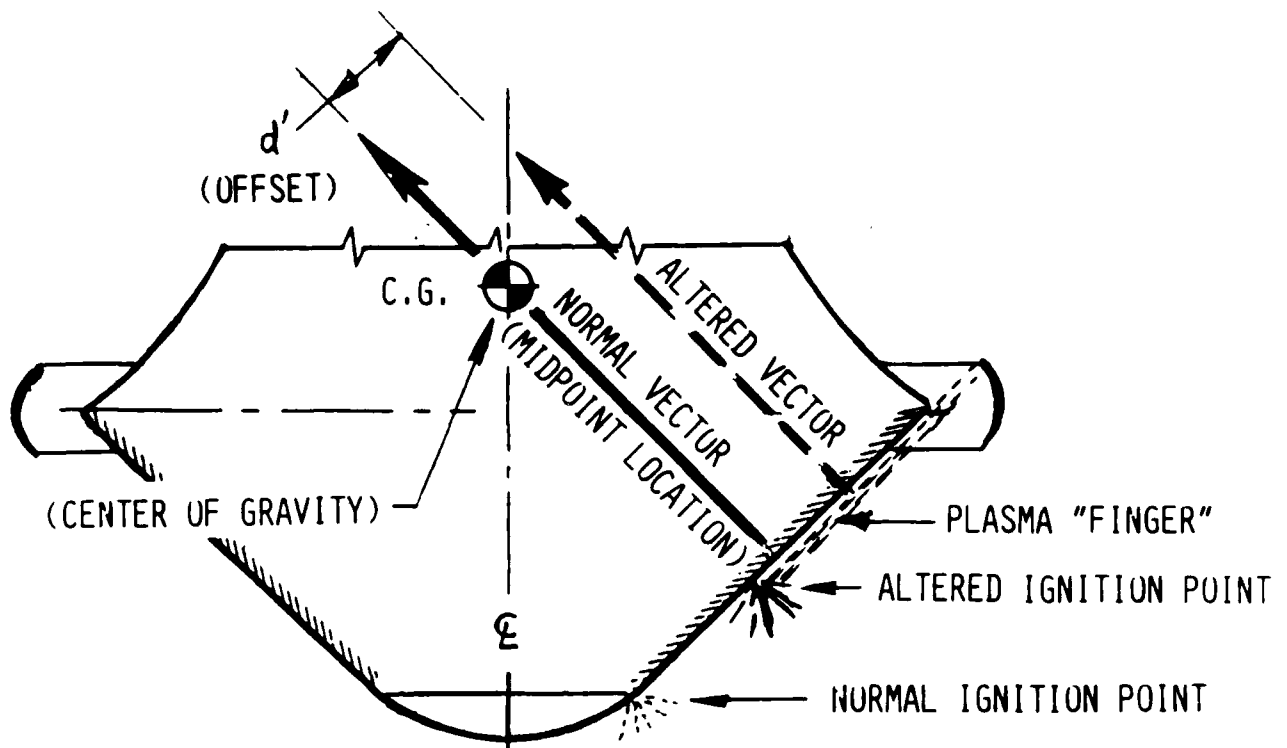


Figure II-14 Relationship of individual "line source" thrust vector and vehicle C.G. (center of gravity)

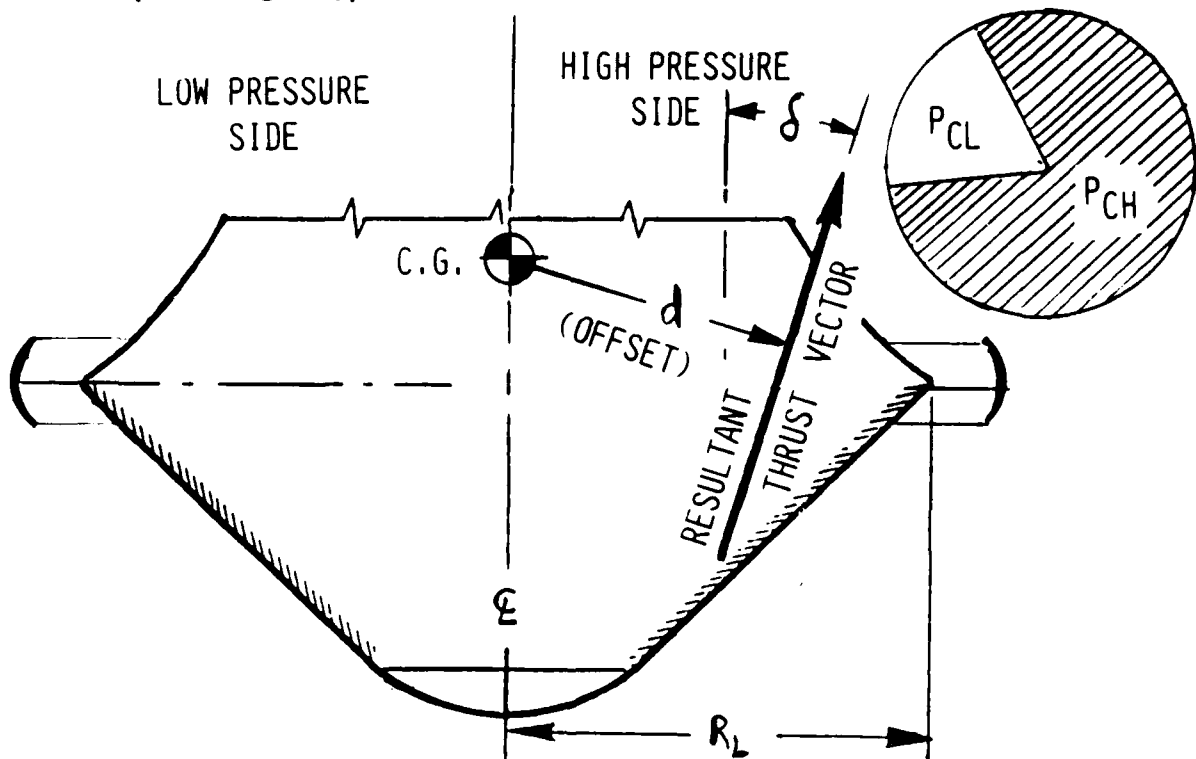


Figure II-15 Thrust vector control relationships

i) Atmospheric aerosol/particulate contamination

a) Performance vs. Incident beam intensity

The ERH thruster is a repetitively-pulsed engine which produces thrust by expanding blast waves over an impulse-coupling surface especially designed for that role. These blast waves are, of course, created by pulsed radiation-sustained plasmas ignited below the reaction surface. As will be demonstrated in a later chapter, maximum coupling coefficients (Newtons of thrust per megawatt of beam power) are realized for the greatest beam intensities delivered to the propagating absorption waves. Why? Because the highest intensities create the largest blast wave overpressures.

Clearly, this relationship has a strong wavelength dependence, which also limits the clear air electrical breakdown threshold. As indicated in Fig. II-16, the highest beam intensities are accessible only for the shortest wavelengths. The shortest wavelength of interest is 0.3 microns, for two reasons. First, it is difficult to construct a mirror which will be highly reflective in the ultraviolet regime. Second, much below 0.35 microns, atmospheric (molecular and particulate) scattering losses become intolerable. Hence, one must confine ERH thruster operation to "atmospheric window" wavelengths between 0.3 microns and 10 cm.

This is not meant to imply that lower beam intensities and lower blast wave overpressures typical of the LSC wave regime are not of real interest. Quite to the contrary, this regime may be ideally suited to low vehicle accelerations and VTOL flight with reduced noise levels. It is apparent though, that the highest vehicle accelerations are attainable only with the shortest practical beam wavelengths.

b) Noise generation

Since the greatest blast wave overpressures yield the highest coupling coefficients, much attention should be given to mechanisms for noise suppression/attenuation/alleviation - especially when addressing human payloads. The problem of noise generation by an ERH thruster goes beyond considerations of environmental impact to the immediate external surroundings. One must also consider health and safety issues, especially with regard to the crew who must reside within close proximity to an extremely powerful noise source.

We should note, here, that the human ear is sensitive to regular compression waves in the range of 40Hz to 20 kHz; and for young people, 16 Hz to 20 kHz. In contrast, dogs can hear up to 30 kHz - 40 kHz and bats up to 100 kHz. Regular compression waves at frequencies below those which we perceive as sound can often be perceived as vibration; one can still sense frequencies lower than those which we consider 'hearing'. Ordinarily, one can distinguish three characteristic

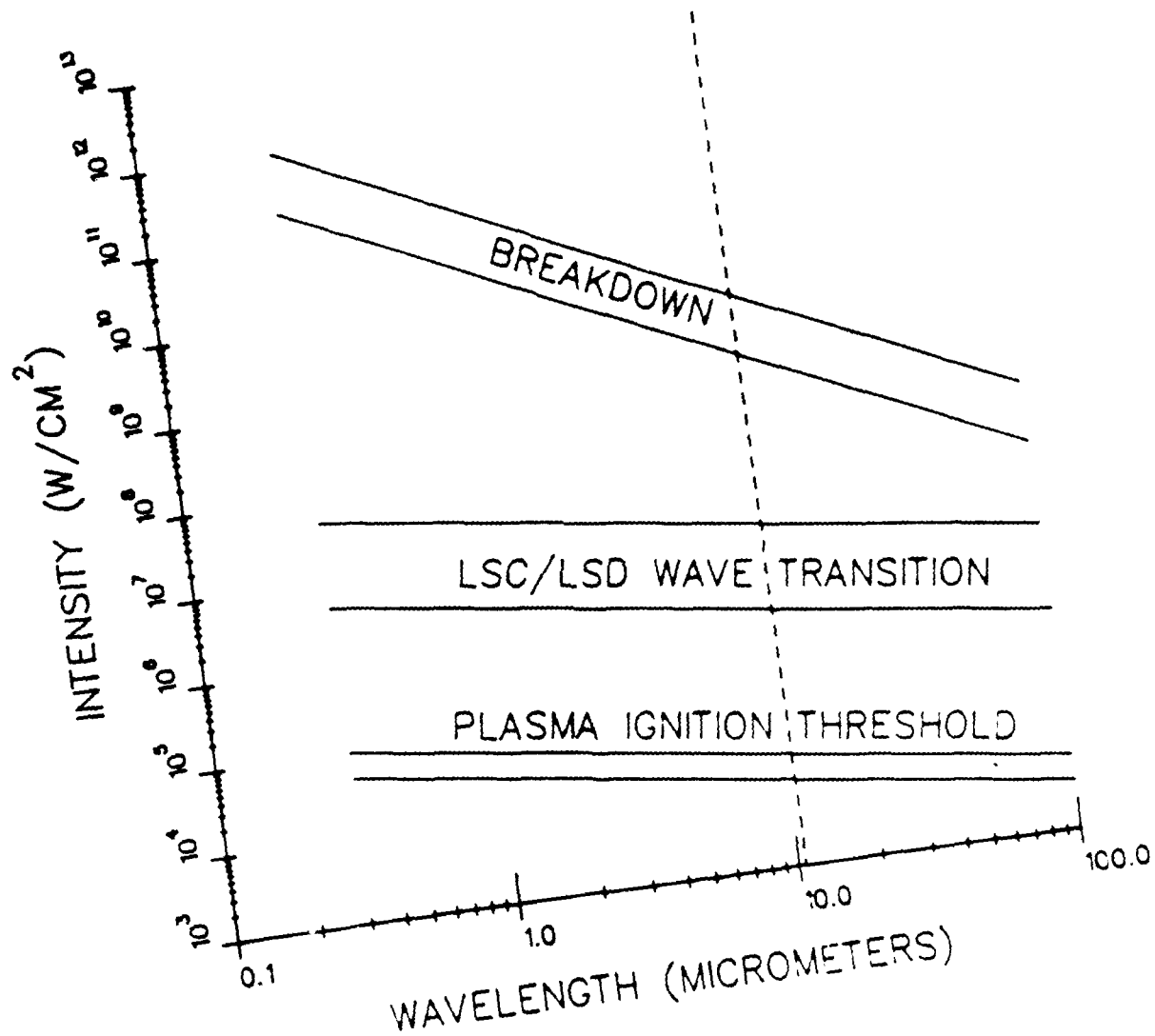


Figure II-16 Wavelength scaling relationship

audible sound: pitch, volume (intensity), and tone quality. For example, regular sinusoidal varying compression waves will have a different tone quality than a sawtooth shaped wave.

Figure II-17 illustrates the normal equal loudness contours for pure tones. Note that if ERH thruster operation is restricted to either the infra-sonic regime (for low acceleration, PRF = 40 kHz), or the ultra-sonic regime (for maximum acceleration, PRF = 15 kHz), the apparent impact on human hearing can be minimized. Incidentally, when operating an ERH thruster within the infra-sonic regime, one should avoid the potentially damaging resonant frequencies of the heart, lungs and nerve synapses.

Another obvious way to reduce thruster noise is to minimize energy delivered in a single laser pulse. The required thrust level and time-averaged power can be maintained simply by increasing the frequency of laser pulses. This approach would result in LSD- wave-heating of the smallest possible volume of air, with the minimum feasible laser pulse energy; then this "detonation" source would be rotated sequentially about the thruster surface. More details on this concept will be given below in another section devoted to the "Rotating Detonation Wave Engine" (RDWE).

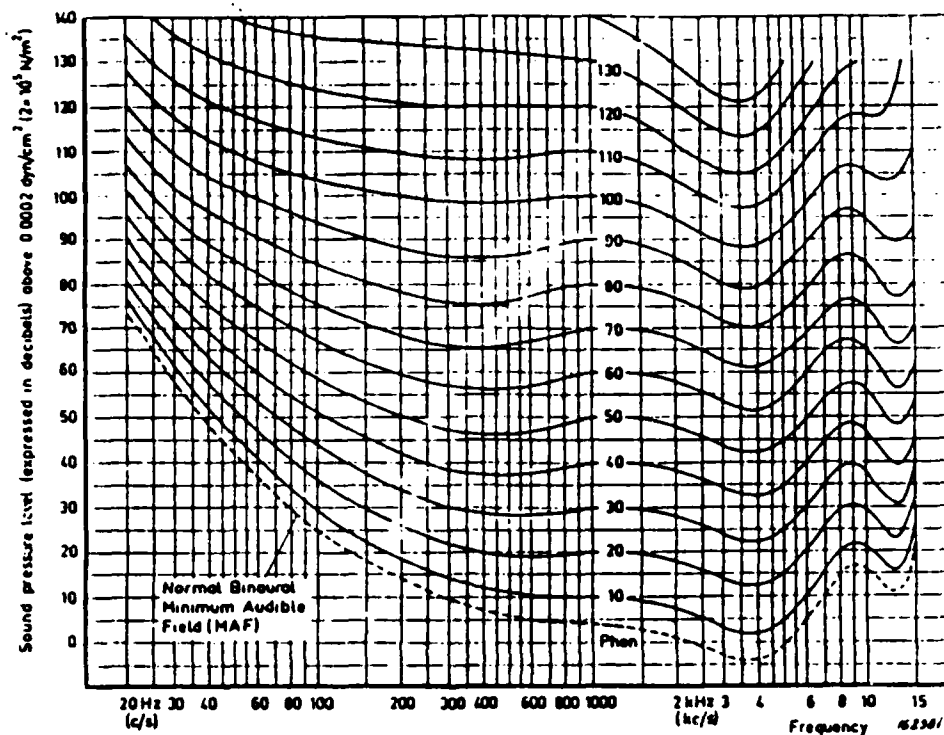
Incidentally, the reference ERH thruster energy deposition mode of 12 LSD waves (pulsed simultaneously with a total beam energy of approximately 1.6 MJ) was chosen without regard to noise generation. A more ideal "source" would utilize 48 smaller LSD waves, each one pulsed individually (with an energy of about 34 kJ each) to create a rotating line source. This would result in a pulsing frequency 48 times greater than the reference design. When producing maximum thrust with a time-averaged beam power of 2 GW, the ideal thruster could accelerate a 5555 kg spacecraft at 30 G's, noiselessly, at an ultra-sonic frequency of 60,000 Hz. In hover (above "ground effect" altitude), when all 48 waves are pulsed simultaneously at 40 Hz, the thruster will operate almost silently within the infra-sonic regime.

c) Asymmetric thrust considerations

During low PRF hover operation, caution must be exercised to avoid unstable rotation rates for offset thrust vectors, of course. This situation could be alleviated by using symmetric thrust geometries of two, three or four "lift points", which rotate over the thruster surface (at the cost of increased noise generation). Figure II-18 shows these options.

d) Scaling laws for particular blast wave geometries

Table III-1 contains a listing of the various available blast wave geometries and applicable scaling laws (e.g., planar, powered planar, cylindrical, powered cylindrical, spherical and powered spherical). First order estimates of the impulse coupling efficiency for a given ERH thruster model



Normal equal loudness contours for pure tones. They can be applied when:

- The source of sound is directly ahead of the listener.
- The sound reaches the listener in the form of a free progressive plane wave.
- The sound pressure level is measured in the absence of the listener.
- The listening is binaural.
- The listeners are otologically normal persons in the age group 18 to 25 years inclusive.

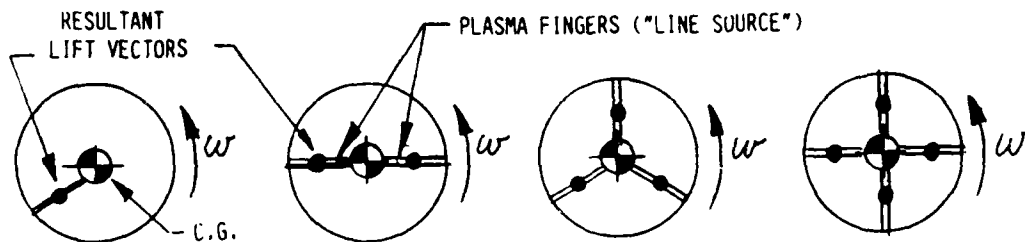
Figure II-17 Normal equal loudness contours for pure tones (from Ref.35)

Table II-1-Sedov's Scaling Laws, (See Sedov [22])

	UNPOWERED	POWERED
<u>PLANAR</u>	$P/P_{ref} = (t/t_{ref})^{-2/3}$ $z/z_{ref} = (t/t_{ref})^{2/3}$	$P/P_{ref} = \text{const}$ $z/z_{ref} = (t/t_{ref})$
<u>CYLINDRICAL</u>	$P/P_{ref} = (t/t_{ref})^{-1}$ $r/r_{ref} = (t/t_{ref})^{1/2}$	$P/P_{ref} = (t/t_{ref})^{-1/2}$ $r/r_{ref} = (t/t_{ref})^{3/4}$
<u>SPHERICAL</u>	$P/P_{ref} = (t/t_{ref})^{-6/5}$ $r/r_{ref} = (t/t_{ref})^{2/5}$	$P/P_{ref} = (t/t_{ref})^{-4/5}$ $r/r_{ref} = (t/t_{ref})^{3/5}$

A) BOTTOM VIEW:

(NOTE: " ω " INDICATES LINE SOURCE ROTATION)



B) SIDE VIEW:

(NOTE: " N " IS NUMBER OF LINE SOURCES)

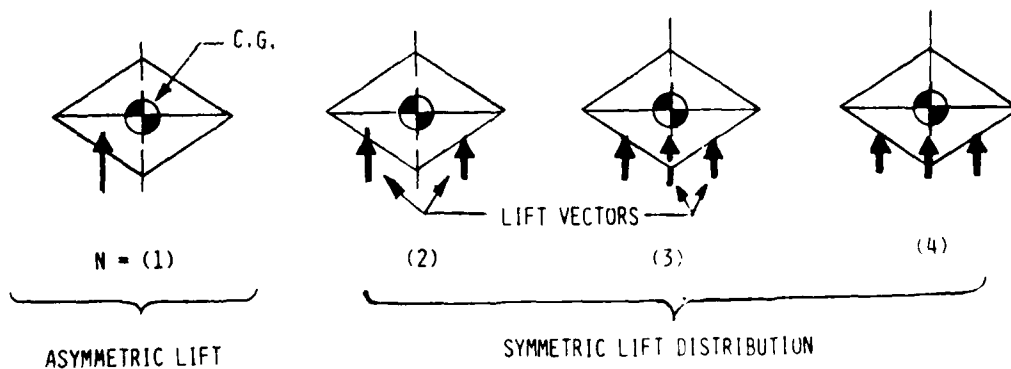


Figure II-18 ERH thrust vector geometry for rotating line source(s)

can be derived by application of these scaling laws, once the detailed "source" geometry and energy deposition mode have been established.

e) Absorption-wave/thruster geometry

Figure II-19 displays seven representative energy deposition modes for radially-symmetric thrusters utilizing truncated conical plugs (like the point design). Variations-on-a-theme for the line/cylindrical source are presented in Figs. II-19a and II-19b; whereas, similar modes for the planar source are given in Figs. II-19c through II-19g. These illustrations present bottom views of the ERH thruster plug with the secondary optics (SO) wrapped about the upper plug circumference. Ignition of the radiation-sustained plasma wave is assumed to take place around the lower end of the truncated plug. For the "line source" cases, the SO's are assumed to project high intensity power beams towards a point focus; for the "planar source", a line focus.

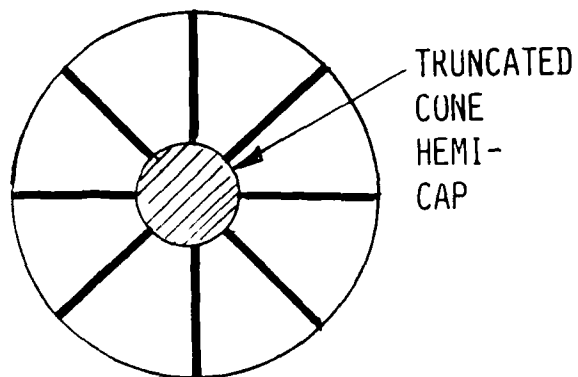
All the modes displayed in Fig. II-19 assume the use of rapidly-propagating (i.e., hypersonic velocity) LSD waves, probably falling in the "super detonation wave regime" (according to the nomenclature of Raizer [2]). The plasma expansion time is generally a factor of 10 longer than the laser pulse duration (i.e., the beam energy "deposition" time).

The following describes the process of pulsed energy deposition for each mode in Fig. II-19. (Note that the basic principles behind the "simultaneous-line" source and the "rotating-line" source were already covered in Fig. II-18.) Two choices for PO/SO/TO optical train geometries exist: i) annular PO with a scalloped annular SO linked to a set of small grazing-incidence TO's, or, ii) scalloped PO and a set of circular SO's. For the simultaneous-line source, the entire PO must be illuminated at once, with a bar beam (i.e., having a hollow center). For the rotating-line source, discrete portions of the PO are exposed. This is accomplished with a single (smaller) circular beam, or with multiple circular beams, distributed around the annular PO surface. After delivery of a laser pulse, the power beam must then be slewed to the next "targeted" location on the PO, as indicated earlier in Fig. II-7.

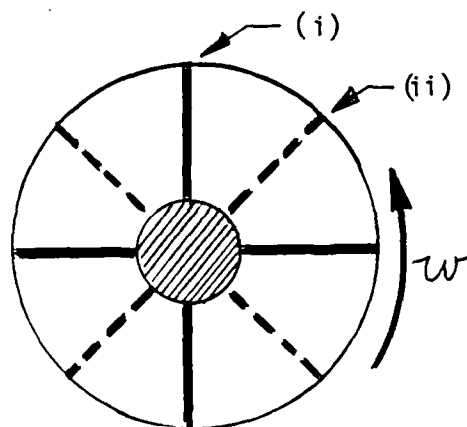
The other modes portrayed in Figs. II-19c through II-19g would use continuous annular PO and SO optical trains. The Fig. II-19c mode pulses the whole engine lower surface at once; hence, the entire plug surface is "active" and the only unilluminated surface results from shadows cast by the shroud support struts.

Figures II-19d and II-19e show the concept of a "rotating-wedge" planar source, an alternative mode obtained by illuminating some smaller portion of the PO (i.e., during a given laser pulse). A sequence of pulses is delivered to adjacent segments of the annular PO "race track". Figure II-19f indicates a variation on the Fig. II-19d mode, wherein the laser beam placement on the PO "race

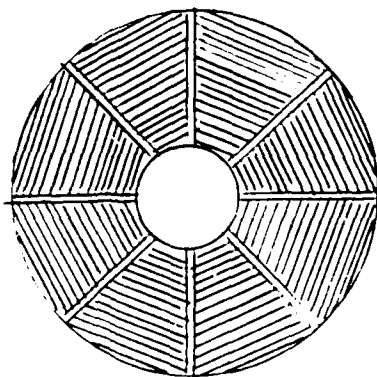
A) SIMULTANEOUS LINE



B) ROTATING LINE



C) SIMULTANEOUS PLANAR



D) ROTATING "WEDGE" PLANAR

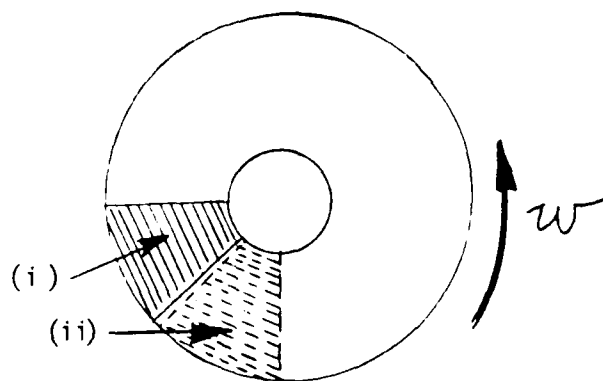
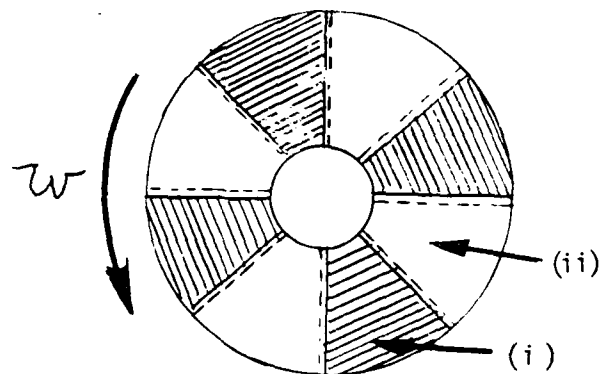
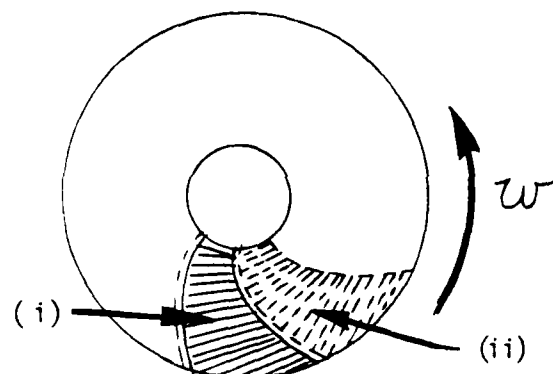


Figure II-19 Energy deposition modes - bottom view (unpowered cylindrical and planar sources)

E) ROTATING "MULTI-WEDGE"



F) ROTATING SPIRAL WEDGE



G) ROTATING SPIRAL MULTI-WEDGE

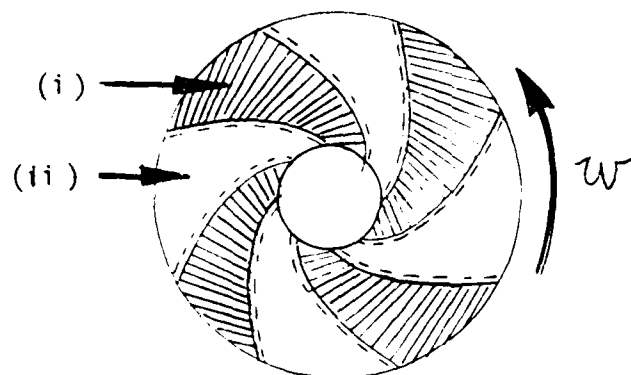


Figure II-19 Energy deposition modes - bottom view (unpowered cylindrical and planar sources), cont'd.

track" is slewed during the laser pulse -- yielding a spiral-shaped plasma wedge. The spiral mode may enable a reduction in the time-averaged heat load sustained by an annular SO mirror, by spreading the incident beam 'foot-print' over a larger SO surface area (i.e., during a given laser pulse). One additional advantage may occur from simplifying the pointing/tracking requirements for the laser transmitter. The transmitter antenna can be slewed constantly in a circular pattern about the PO "race track" without having to start and stop (i.e., re-target) between laser pulses.

One additional comment should be made with regard to the "rotating-line" energy deposition mode of Fig. II-19b. If pulsed at sufficiently frequent intervals, the thruster could operate as a continuous Rotating Detonation Wave Engine (RDWE) mode as shown in Fig. II-20. In this mode, fresh air which resides just ahead of the advancing blast wave front would be "detonated" just prior to the arrival of the front. Hence, in a time-averaged sense, the energy deposition process would simulate that of a detonating line source that rapidly wipes around the thruster plug.

f) Passive refresh of planar vs line sources

One final point should be made with regard to the "lateral refresh" mechanism and its suitability for use with line (finger) source and planar source geometries. The line source seems ideally suited to this refresh mechanism. However, the planar source does not appear as appropriate, especially when the entire lower surface is pulsed (see Fig. II-19c). Why? Because with the planar source, the ratio of active to passive thruster surface is so small (i.e., roughly equal to 1), that the most expedient "refresh" must take place at right angles to the thruster surface -- as one would expect with a 1-D planar source. As a result, the maximum frequency at which planar sources can be pulsed will be different than that for multi-line sources. The implications of this on ERH thruster performance has yet to be examined in any detail.

g) Wavelength scaling effects (LSC/MSP regime)

Up to now, energy deposition modes suitable for high intensity LSD-waves have been emphasized largely because of their greater impulse coupling efficiency. However, thrust can also be generated using lower intensities typical of the LSC wave regime (albeit with reduced efficiency), if the plasma is still ignited within close proximity to the impulse surface. Figure II-21 indicates two feasible energy deposition modes: i) powered cylindrical, and ii) powered spherical. In the first case (Fig. II-21a), an annular power beam is projected by a ring-type SO mirror towards a line focus -- which is oriented perpendicular to the thruster surface. (This thruster mode is analyzed in Chapt. VII.) Figure II-21b shows a variation of this theme, wherein the annular power beam is again projected by a "ring-type" SO mirror towards a central focal region -- but this time a point focus is

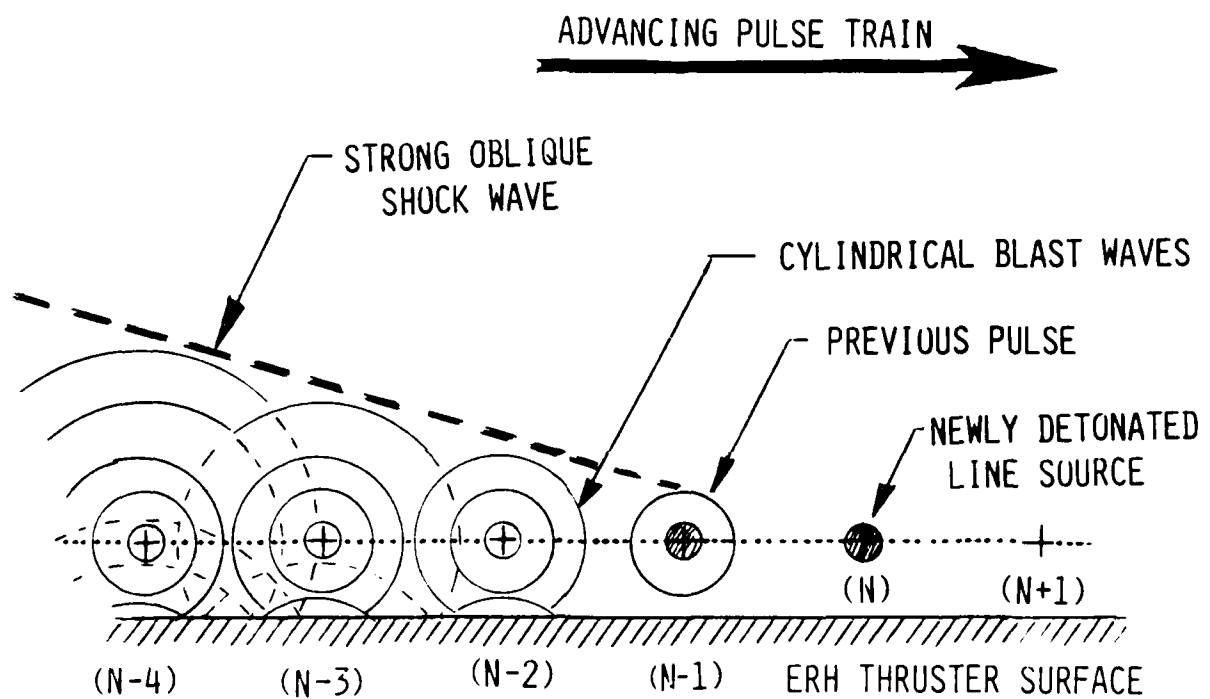


Figure II-20 Rotating Detonation Wave Engine (RDWE)

assumed, not a line. The resultant optical geometry can perhaps create a powered spherical blast wave below the ERH thruster surface.

For the geometries displayed in Fig. II-21, microwave radiation could have a significant advantage; it can produce plasma temperatures which are much lower than those generated by optical frequencies. Whereas electron temperatures will still be 10000 to 15000 K, ions and neutrals can be as low as 2000 to 4000 K - so the resultant air plasmas can be in a non-equilibrium condition. In contrast, LSC wave plasmas will produce equilibrium temperatures of 10,000 - 30,000 K. Since radiant heat transfer to the ERH thruster is proportional to σT^4 , a factor of 3 reduction in plasma temperature (T) can lower overall heat transfer rates by several orders of magnitude. Subsequently, the thermal stress problem (for ERH thruster materials) should be greatly alleviated by using microwave-sustained plasmas for low acceleration, "pop-up" maneuvers and hover flight modes. During these times, the plug surface would be exposed to potential "overheat" conditions caused by ingestion (i.e., undesired recirculation) of hot exhaust gases.

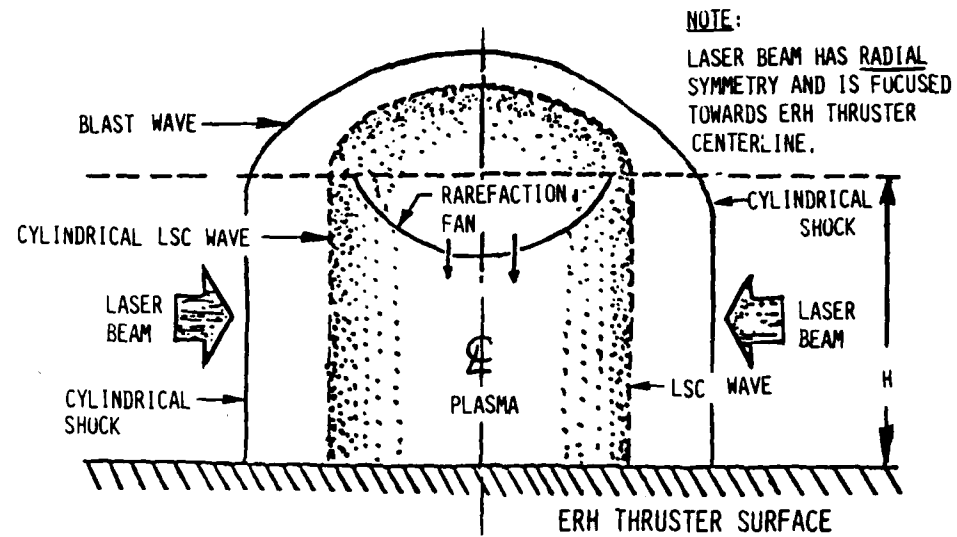
It should be noted that microwave-induced electrical air breakdown normally occurs before detonation waves can be produced: e.g., flux densities of 1 - 2 MW/cm² at sea level pressure. However, radiation-sustained plasmas typical of the "deflagration" regime are easily ignited. Hence, all evidence points favorably to the potential for thrust production with repetitively-pulsed microwave power. Since inverse bremsstrahlung absorption coefficients for microwave radiation are exceedingly low, the physical size of powered cylindrical and spherical plasmas (shown in Fig. II-20) can grow to be much larger than with laser wavelengths. Significant blast wave overpressures (10 atm or more) could be generated over a sizeable portion of the ERH thruster surface.

h) Ignition requirements for radiation-sustained plasmas

In all the above mentioned energy deposition modes, inverse bremsstrahlung absorption is invoked as the radiation absorption mechanism. However, a "breakdown" mechanism is needed to start the cascade process in which enough free electrons are available to ignite an LSC wave, LSD wave, or Microwave-Supported Plasma (MSP) wave. Several breakdown mechanisms exist: i) laser-induced clean air breakdown, ii) particulate "seeding", iii) aerosol or molecular "seeding", iv) electric spark, v) metallic target, and vi) thermionic or field emission. Options ii) and v) present potential optical fouling problems. Option iii) is limited to absorption over a finite wavelength range. Options iv) and vi) require an on-board electric power source; of these, option iv) would probably consume the least power.

Overall, option i) is the preferred breakdown mechanism. However, if the PO/SO optical focusing geometry is not able to produce sufficient intensity to induce electrical breakdown, an elec-

A. POWERED CYLINDRICAL



B. POWERED SPHERICAL

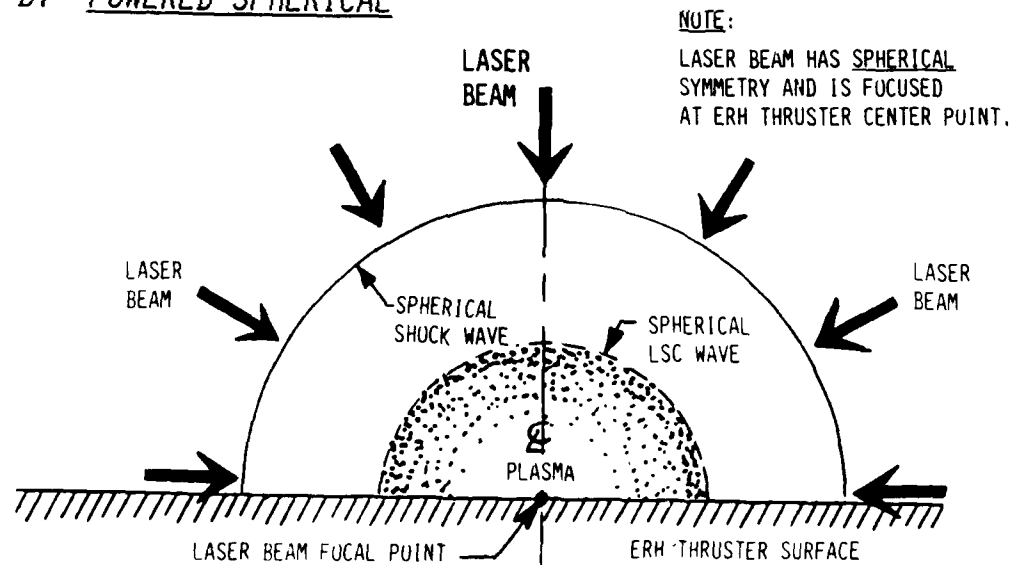


Figure II- 21 ERH thruster energy deposition modes - bottom view (powered cylindrical and powered spherical modes)

tric spark device would be a useful alternative. As mentioned earlier, several strategically-located "spark plugs" distributed along the "detonation-line" sources would have the valuable ability to trigger breakdown at numerous locations; this mechanism should enable a thrust-vectoring capability.

i) Atmospheric aerosol/particulate contamination

Several final comments should be made regarding the data presented in Fig. II-22. Note that the clean air breakdown threshold is beyond $10^9 W/cm^2$. For the reference design which uses a uniform intensity of $5 \times 10^8 W/cm^2$, breakdown can be triggered upon a metal target in roughly 20 nanoseconds - with an energy cost of $10 J/cm^2$ integrated over the beam cross-section. Ignition on contaminating particles (0.3 micron diameter) would be triggered in 100 nanoseconds, or an energy cost of 5X larger. Clean air breakdown cannot be triggered at all for the reference system intensity of $5 \times 10^8 W/cm^2$. Hence, the metallic igniter plug or the electric spark would be the preferred ignition mechanism.

Let us now examine another optical train and ERH thruster design that incorporates a multi-point focus SO (i.e., tapered plasma "fingers"), and uses the laser-induced breakdown mechanism. With $5 \times 10^9 W/cm^2$ at the ignition point, it is evident that roughly 40 nanoseconds must be invested at an energy cost of $200 J/cm^2$ - but of course, the focused beam area (at the ignition point) would be reduced very much below the afore-mentioned example. However, as seen in Fig. II-22, ignition on contaminating particles (which accidentally enter the beam) could occur at even earlier times - and perhaps at an undesired location along the ERH thruster plug, with potentially hazardous results. This may cause a severe vectoring of the thrust in an unpredictable fashion. Hence, the super high thrust/acceleration abilities of the ERH thruster should probably not be invoked immediately at liftoff. The certainty of encountering particulate contamination near the ground may necessitate low acceleration pop-up maneuvers, wherein the engine/vehicle climbs to a safe altitude (perhaps as low as tree-top level) - before really "blasting off" at high rates of acceleration.

11. Air "Refresh" Schemes

During normal repetitively-pulsed ERH thruster operation, there comes a time when the heated, high pressure air resulting from a given radiation-sustained plasma ("detonation" or "deflagration") wave eventually decays to ambient pressure. This volume of hot, ambient-pressure, "spent" air must be convected out of the actively-irradiated thruster region - before it can be "pulsed" again. The entire cyclic process can be likened to the intake/compression/ignition/exhaust mechanisms in conventional 4-cycle internal combustion engines. Clearly, if the time required to resupply the "deto-

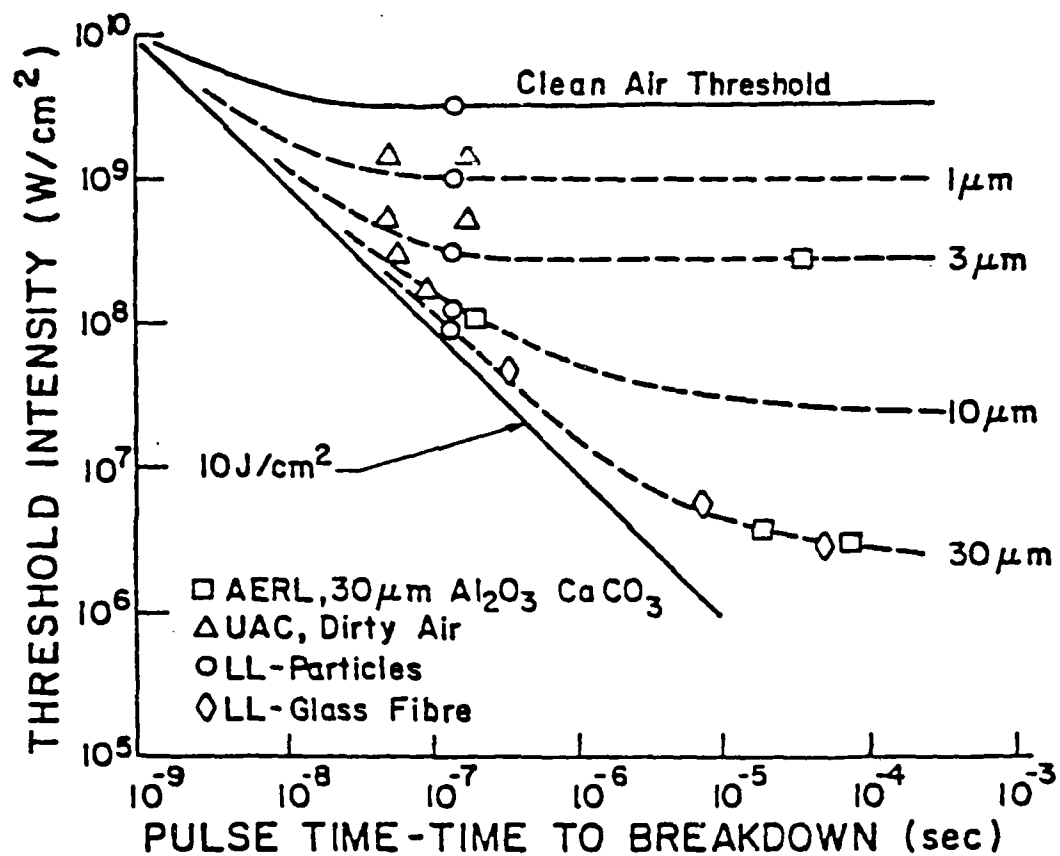


Figure II-22 Measurements of air breakdown in the presence of particulate matter. (from Refs. 37 - 39)

detonation zone" can somehow be reduced, then it will be possible to increase the engine pulse repetition frequency and hence, time-averaged thrust.

a) Basic modes for refreshment

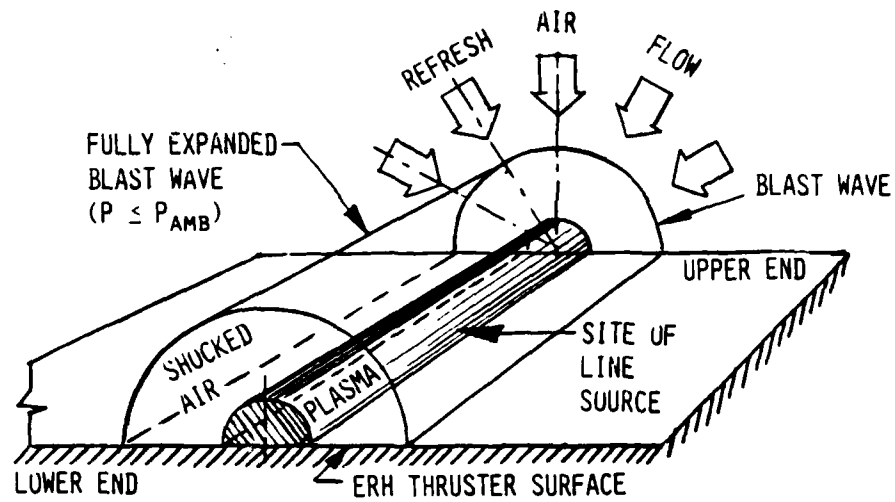
It is useful to examine the mechanisms by which this "refresh" process might be enhanced. The reference platform utilizes an LSD wave-heated (line/cylindrical) source, so it will serve as the exemplary "straw-man" ERH thruster in this section. Note in Fig. II-23 that there are only two basic modes for "refreshment" of the ERH thruster surface: i) passive, or ii) active. In the former "passive" mode, sufficient time must be allowed for the heated cylindrical hot plasma "bubble" to "burst", then collapse back upon itself - allowing cool ambient air to rush back into the "detonation zone". For the latter "active" mode, some type of forced convection mechanism is employed to drive fresh air back into the "detonation zone" - often in less time than that required for a complete "passive refresh" of the surface.

b) Passive refresh enhancement

The various mechanisms available for "passive" refresh enhancement can be incorporated into a given thruster simply by making judicious "design decisions" in the overall engine geometry. A number of these principles were first introduced earlier in this chapter. For example, the total time required for refresh of the reference ERH thruster (with its twelve line source and truncated conical plug) is the sum total of: i) LSD wave ignition time, ii) time for LSD waves to propagate across the entire plug length, iii) time for blast waves to expand laterally to the local static pressure, and iv) time for plasma bubbles to cool and collapse back, so that fresh air can rush in. Clearly, the first two time intervals can be minimized by selecting the maximum beam intensity (within some safety margin) that can be projected upon the propagating LSD waves by the SO mirrors; this in turn, minimizes the necessary laser pulse duration.

The third time interval can be minimized in two ways. First, for a given incident beam intensity (upon the LSD wave), one can minimize the blast wave expansion time by selecting the smallest "detonation" volume. For a given thruster plug, one would then select the minimum laser beam diameter consistent with the limits of diffraction, turbulence, thermal blooming and jitter of the SO (or TO) mirrors. This small diameter, high pressure cylindrical volume of plasma can certainly relax more quickly to the local static pressure than a larger volume. Secondly, there are ways to immerse the entire thruster plug (and its detonation zones) in static pressure levels significantly above ambient; hence, less time elapses during the plasma expansion process. Finally, as mentioned earlier for the multi-fingered reference thruster, care must be taken to minimize the

A. PASSIVE REFRESH



B. ACTIVE REFRESH (FORCED CONVECTION)

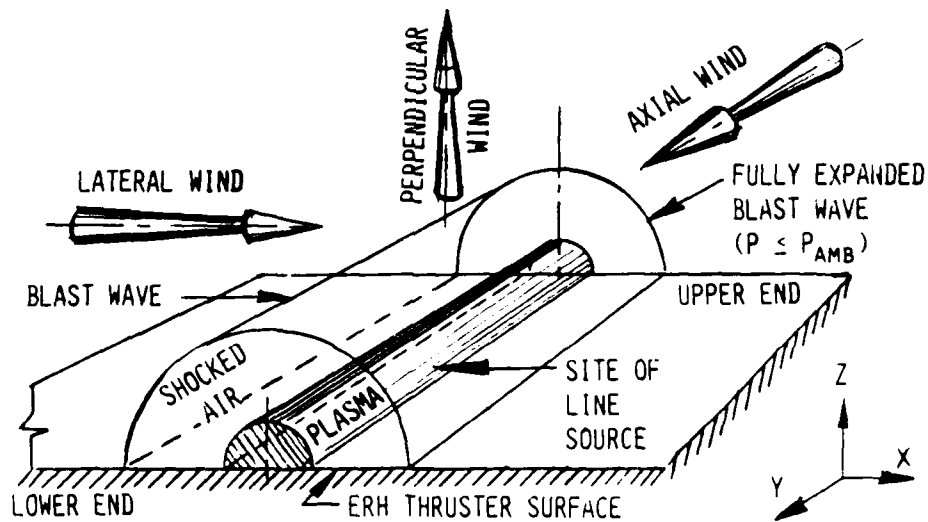


Figure II-23 Basic thruster "refresh" modes (shown for line/cylindrical source)

overlapping of adjacent cylindrical blast waves. This condition will hinder the subsequent passive refresh process, as well as optimum thrust production.

Similar comments can be made with regard to the fourth time interval, which is proportional to the maximum blast wave expansion radius (i.e., when plasma pressure first equals local static), and the sonic velocity. Since cool air can rush in only at the speed of sound, one would want to minimize the expanded plasma volume, and maximize the local sound speed. The local sound speed can be increased to some extent, with the aid of compressed cowl air, as will be discussed later.

c) Active refresh enhancement

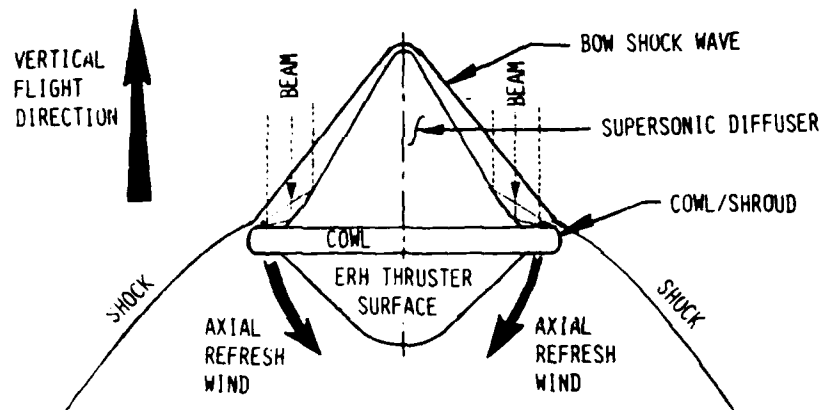
Figure II-24 displays eight schemes for "active" refresh enhancement. Over half have already been introduced. In Fig. II-24a, the engine/vehicle is shown in supersonic axial flight, utilizing the mechanism of forced axial convection for "active refresh" of the ERH thruster plug. The degree to which fresh air can be convected across the plug surface is dictated by the specifics of engine/vehicle configuration: i.e., inlet forebody shape, shroud contour (if not shroudless), and nozzle/afterbody geometry. As will be analyzed more thoroughly in Chapt. VI, a properly designed cowl and inlet forebody enables the plug to be "immersed" in axial-refresh air with a local pressure (and sound speed) quite above ambient.

Depending on the inlet design Mach number (M_D) and flight speed, airflow emerging from the annular cowl duct can either be subsonic or supersonic. If ducted air expands at supersonic velocity across the plug nozzle, it can be most effective in the "active" refresh process. Even so, during the time interval required to clear the entire length of the ERH thruster plug of hot spent air, several new detonations will have been triggered. However, note that blast waves ignited at the lower end of the plug have the most time to expand (i.e., as the LSD wave races up the plug surface), so the plug aft end will be refreshed first, passively. Hence, it is the upper end that needs the active refresh enhancement most urgently, and gets it. Incidentally, the fully expanded plasma "fingers" should not obstruct a significant fraction of the internal cowl cross-section - so as to cause a reduction in the mass flow rate of axial refresh air.

Figure II-24b shows another forced convection refresh mode that could occur in subsonic lateral flight. In this case, the local wind vector would "blow" at right angles to the plasma fingers - helping to clear out spent hot air. In subsonic flight, this mode may not accomplish anything more significant than to prevent the local static temperatures (of "passive refresh" air) from becoming too large.

d) "RDWE" active refresh mechanism

A. SUPERSONIC AXIAL FLIGHT
(FORCED AXIAL "REFRESH")



B. SUBSONIC/SUPERSONIC LATERAL FLIGHT
(FORCED LATERAL "REFRESH")

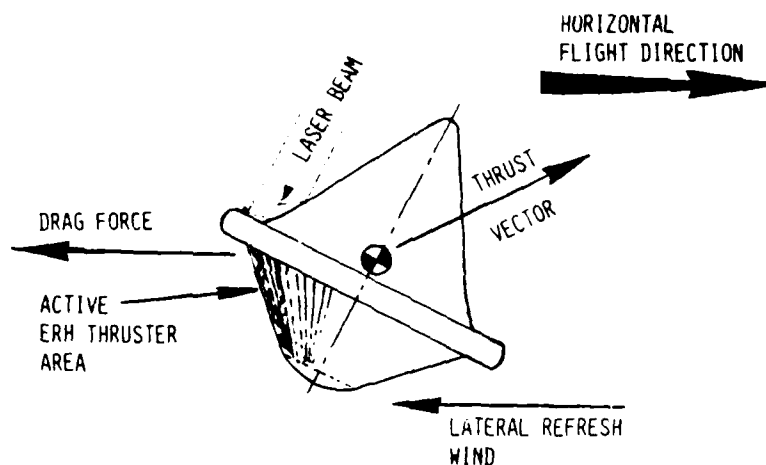


Figure II-24 Mechanisms for active refresh enhancement

The active refresh mechanism displayed in Fig II-24c, may enhance the performance of Rotating Detonation Wave Engines (RDWE) using a symmetric, multi-line ERH thruster geometry. Beneficial interaction is anticipated between two adjacent, sequentially-pulsed sources. One possibility is that the pre-cursor cylindrical shock wave shed by a given detonating line could convect "refresh" gases laterally into the site of the next "line" to be pulsed. It might even be able to produce a pre-pressurizing effect. A second possibility involves a similar beneficial exchange between adjacent detonations, but only for the first and last line sources - as the RDWE "overlaps" after a complete 360° sweep of the ERH thruster plug. A third possibility involves beneficial interaction between the trailing jet behind one spiral-source LSD wave, and the adjacent spiral detonation zone (e.g., see the engine geometry in Fig. II-24g). These opportunities for refresh enhancement, have yet to be explored in any depth.

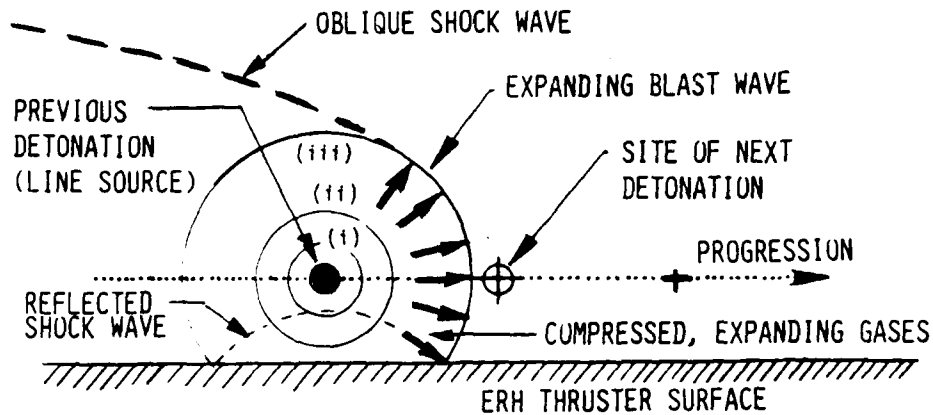
e) "porous plate" active refresh mechanism

Figure II-24d portrays another scheme for active refresh enhancement, one which forcibly convects "refresh" gases in a direction perpendicular to the ERH surface. This concept assumes that the thruster "plate" is porous and that the refresh fluid is pumped out with an on-board auxiliary power supply. The refresh "fluid" would be stored internally in a liquid state, then evaporate through the ERH thruster as it emerges from the gaseous plate. (Note that a similar function could be provided by an ablatively-cooled ERH thruster surface.)

Two technical problems are evident for such a scheme. First is the mass loss due to refresh-fluids, which would penalize the ERH thruster with a finite specific impulse. Clearly, one would want to minimize both the refresh-fluid mass flow rate and the total porous plate surface area. Perhaps the only porous regions could be restricted to just the actively-irradiated plug nozzle areas (i.e., immediately below the line sources). The second problem area relates to the pressure ratios which must be applied across the porous plates, remembering that peak blast wave pressures reach 600 atm. in the ref. platform. Also, it is not obvious that the refresh gases should be admitted continuously: perhaps a repetitively-pulsed mode would give better performance. If the former is chosen, the porous plate surface might act as a self-operated acoustic "valve", anyway.

One final note should be made regarding the porous plate option. This mechanism might permit the thruster surface to perform as a rocket within a near vacuum environment. However, the gaseous working fluid must be carefully expelled and uniformly heated to a high temperature before the rocket expansion process is completed. This sequence of events might present a technical problem with the rocket-mode scheme.

C. ROTATING DETONATION WAVE ENGINE (RDWE)
(BLAST WAVES CONVECT "REFRESH" GASES Laterally)



D. POROUS PLATE (OR ABLATION)
(PERPENDICULAR "REFRESH")

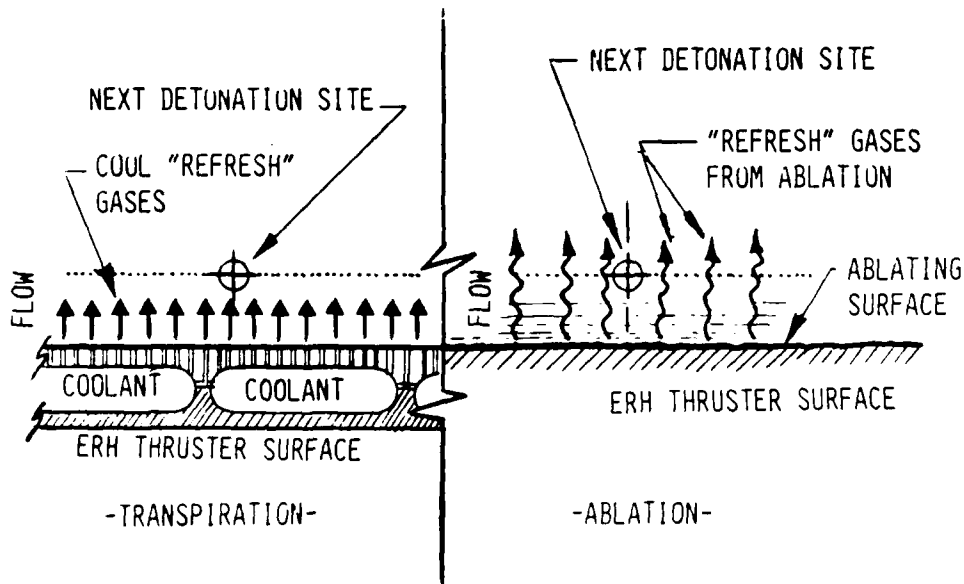


Figure II-24 Mechanisms for active refresh enhancement, cont'd.

f) "Rotating plate" active refresh mechanism

Illustrated in Fig. II-24e is another concept for active refresh of an ERH thruster, which invokes a rapid rotation of the radially-symmetric plug nozzle. In this scheme, the thruster surface is spun up to a maximum velocity of Mach 1 (or 2) at the outermost rim of the conical plug; high subsonic velocities might also be useful. The goal would be to "drag" local refresh air laterally through the detonation- zones (line source sites), by means of viscous forces within the turbulent boundary layer. As shown in Fig. II-24e, the detonation zones must be placed extremely close to the thruster surface anyway, in order to maximize impulse coupling. Hence, line sources would be located completely inside the boundary layer, probably within one centimeter (or less) from the ERH thruster surface. It is evident that the resultant blast wave would cause separation of the boundary layer, and sufficient time must be allowed for it to re-attach before the thruster could be pulsed again.

This refresh mechanism could possibly be enhanced by increasing surface roughness, and perhaps a well-used ablatively-cooled re-entry heat shield might just make the perfect ERH thruster surface. Exaggerated surface roughness will certainly produce additional aerodynamic drag, and require more power for "spin up". However, this may be worth the trouble.

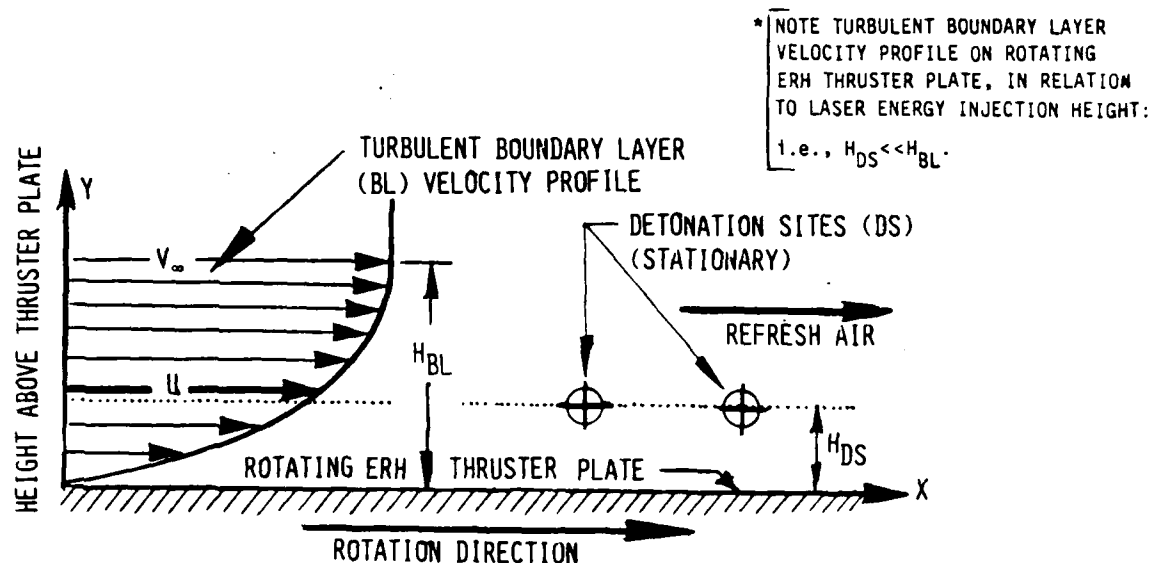
Azimuthal flow circulation might be further enhanced by the attachment of "flow fences" to the ERH thruster surface (as indicated in Fig. II-24f). Flow fences would be high enough to efficiently pump fresh air into the detonation zones, yet not so high as to trigger separation of the boundary layer. With such devices attached, plug nozzle rotation could generate significant centrifugal forces within the immediate boundary layer air flows, as shown in Fig. 24g. The effect of these forces upon the resultant spiraling air flow patterns and the refresh process should eventually be examined in subsequent research.

All the above mentioned "active refresh" mechanisms would require the ERH thruster plug to be spun up slowly on the ground, just prior to launch, using an auxilliary on- board power supply. Following liftoff, no on-board power would be needed during the 20 - 30 second boost period when the ERH thruster is accelerated from Mach 0 to 3. The massive rotational inertia (stored in the engine/vehicle) would be gradually be released and dissipated by aerodynamic drag, along the orbital trajectory.

g) "Axial fan-driven" active refresh mechanism

Figure II-24h portrays another active refresh mechanism which invokes rotating components. In this engine/vehicle configuration, a supersonic axial (or perhaps centrifugal) fan is housed within the annular shroud volume. In preparation for liftoff, a small auxiliary power supply would (again)

E. ROTATING PLATE (WITH NORMAL SURFACE ROUGHNESS)



F. ROTATING PLATE WITH FLOW FENCES (VANES)

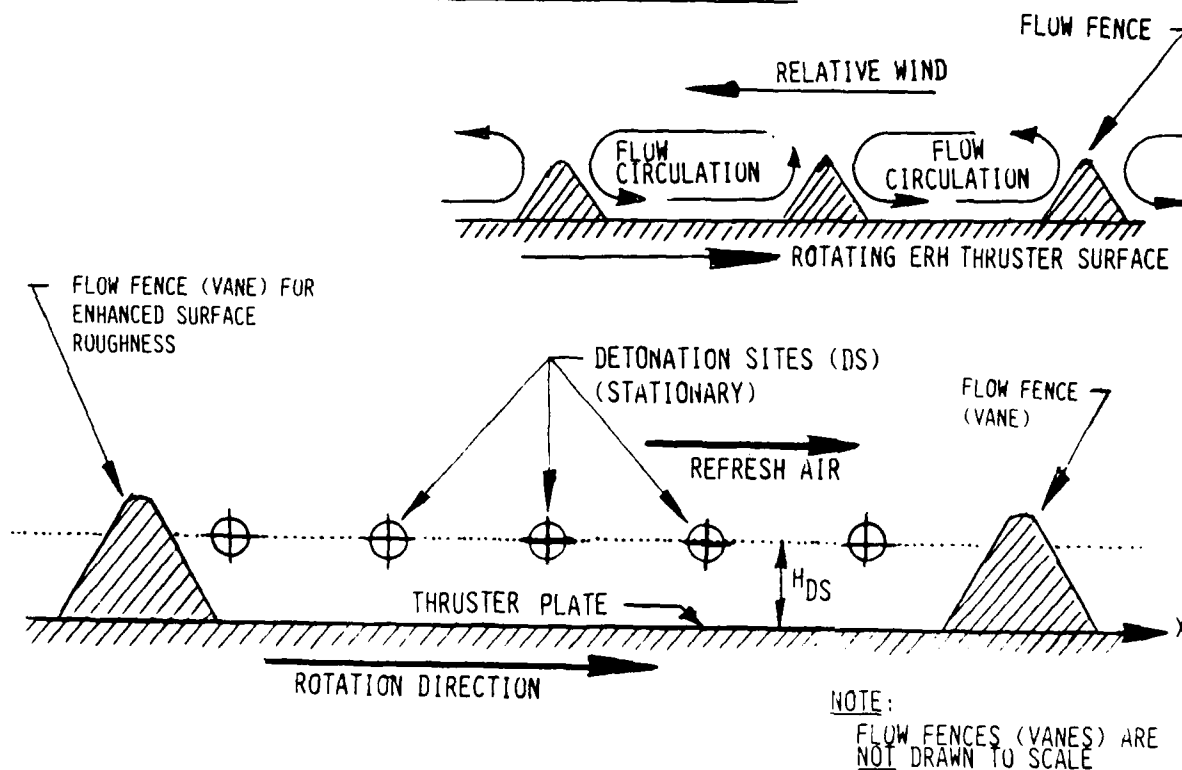
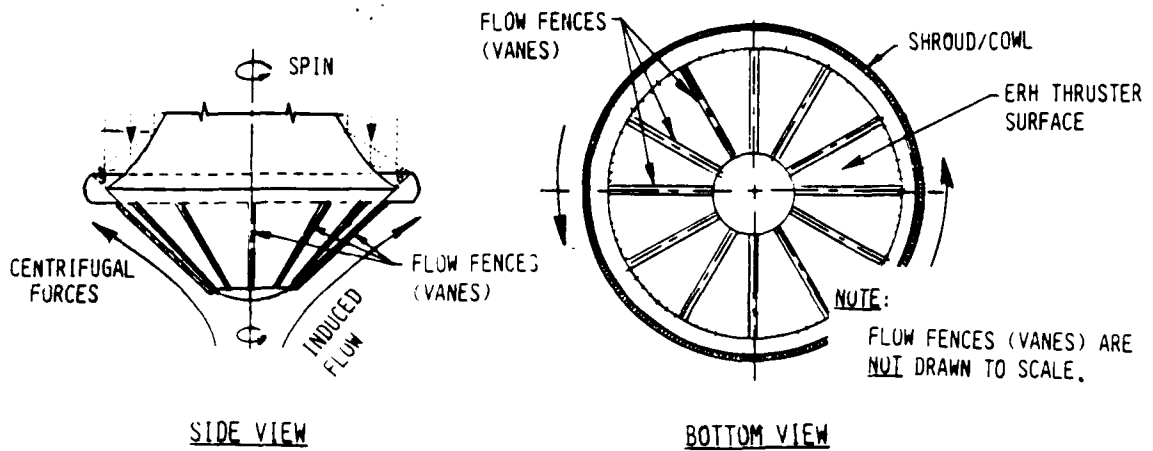


Figure II-24 Mechanisms for active refresh enhancement, cont'd.

G. CENTRIFUGAL FORCES ON BOUNDARY LAYER FLOWS (HOVER CONDITION)



H. AXIAL FAN-DRIVEN "REFRESH" AIR:

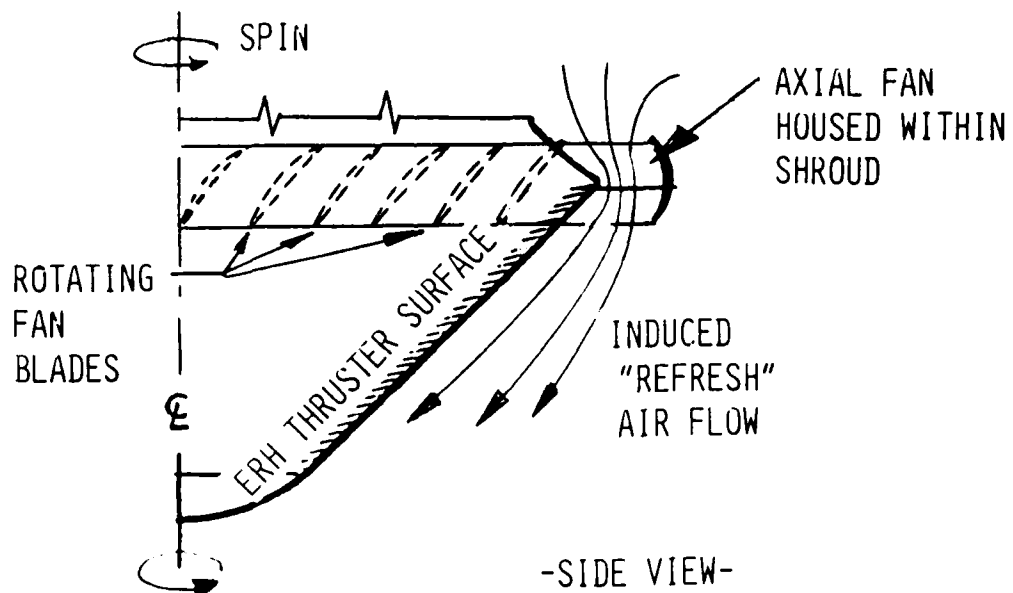


Figure II-24 Mechanisms for active refresh enhancement, cont'd.

spin up the engine, storing much rotational energy in the available mass - while exerting a reaction force against the ground. During the spin-up process, the variable-pitch fan would be set at zero pitch to minimize input power requirements and aerodynamic drag.

At liftoff, the pitch would suddenly be increased, accelerating refresh air across the ERH thruster plug. Efficient axial refresh would probably not occur until the ducted air velocity turned supersonic. Even though the rate of decrease in engine/vehicle rotation would significantly exceed that for the "rotating plate" mechanism in Fig. II-24e, it still might provide sufficient axial refresh flow for the 20 - 30 seconds duration of ERH thruster boost. (After Mach 3 or so, the fan blades would be feathered and the propulsion role would transition from the ERH thruster to other airbreathing modes.)

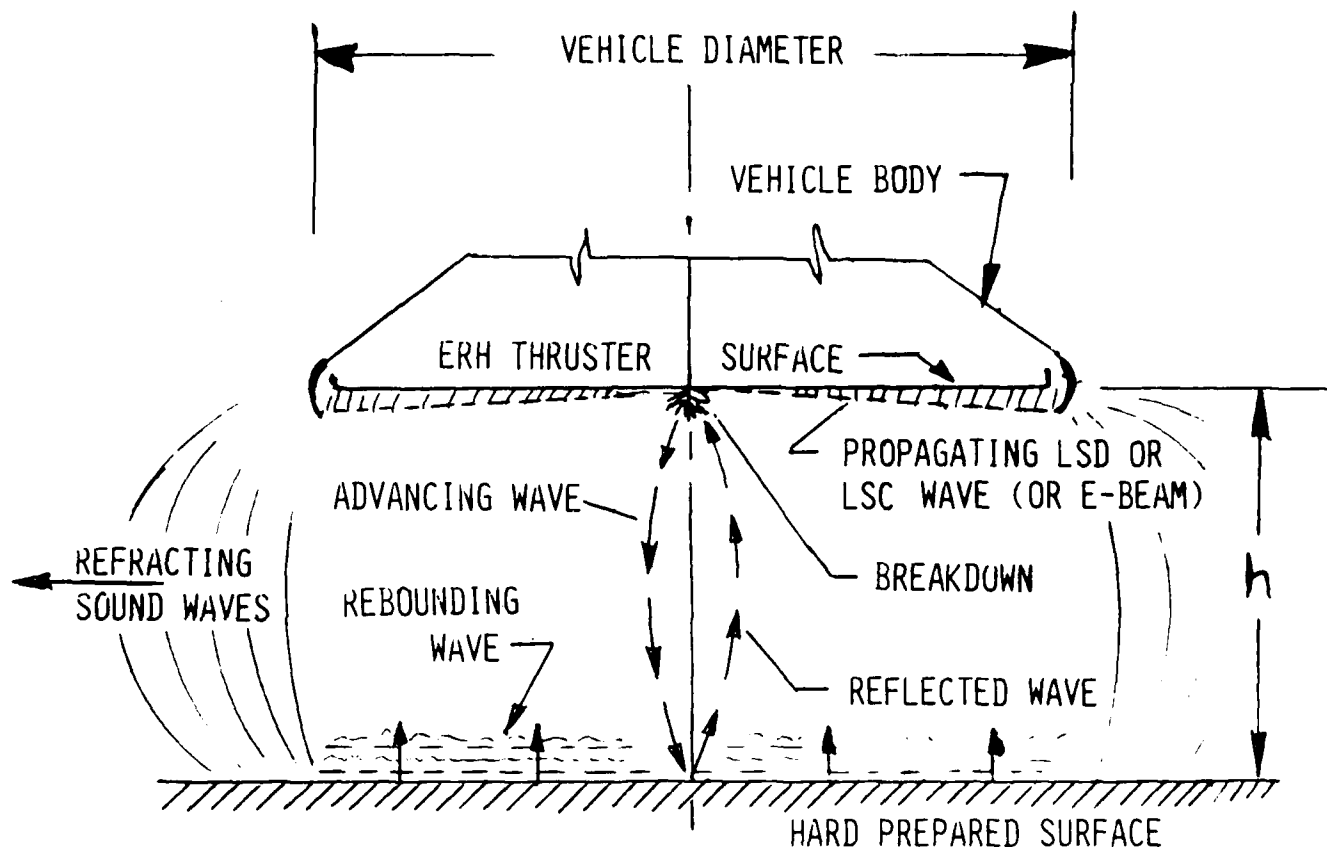
h) Ground resonance: infrasonic levitation

Figure II-25 illustrates another potential refresh-related mechanism which is worthy of note. In operation, it can be likened to the "ground effect" mechanism which all winged vehicles experience at very low altitudes. The effect is associated with a reduced flight power requirement and a region of pressurized air being momentarily "trapped" between the wing and ground plane.

In this scheme, the ERH thruster would act as a directional sonic generator to establish a standing wave system between the vehicle lower surface and a ground-fixed reflector (ideally a hard, smooth prepared surface). As indicated in Fig. II-25, nodes would be enforced at the ground plane and the vehicle underside surface. Then, by simple phase modulation, the pressure nodal planes could be made to shift, elevating the vehicle into the atmosphere - to any height still within ground-effect. In flight, the engine would rebound small "elastic" air masses which move at high velocity (up to Mach 1) between the vehicle and the ground. Sub-audible pulse repetition frequencies could be employed to transfer sufficient momentum for hovering flight.

In essence, the vehicle would be levitated within the standing wave system at an upper node. For example, a five meter diameter engine could hover at 5 meters altitude or one-half wavelength, with an ultrasonic frequency of 33.14 Hz - as shown in Fig. II-26. (This calculation assumes a cold 0° C day when the sound speed is 331.4 m/s.) If sufficient thrust exists, the 5 m vehicle could also hover at 10 meters altitude (one wavelength) at the same sub-audible frequency.

The goal here is to produce a time-averaged overpressure across the engine/vehicle lower surface, sufficient to support the gross takeoff weight. For the 5 m diameter, 5555 kg reference platform, this equates to an overpressure of 0.02737 atm. Whether it is accomplished by bouncing planar shock waves, subsonic aerodynamic "ring vortices", or any other mechanism involving an "elastic" air mass, the resultant effect is a simple momentum exchange with a massive immovable



- ADVANTAGE: REDUCED ERH THRUSTER POWER DURING HOVER
- CONDITION FOR GOOD EFFICIENCY: $h \leq$ VEHICLE DIAMETER

Figure II-25 Infra-sound levitation: ground effect

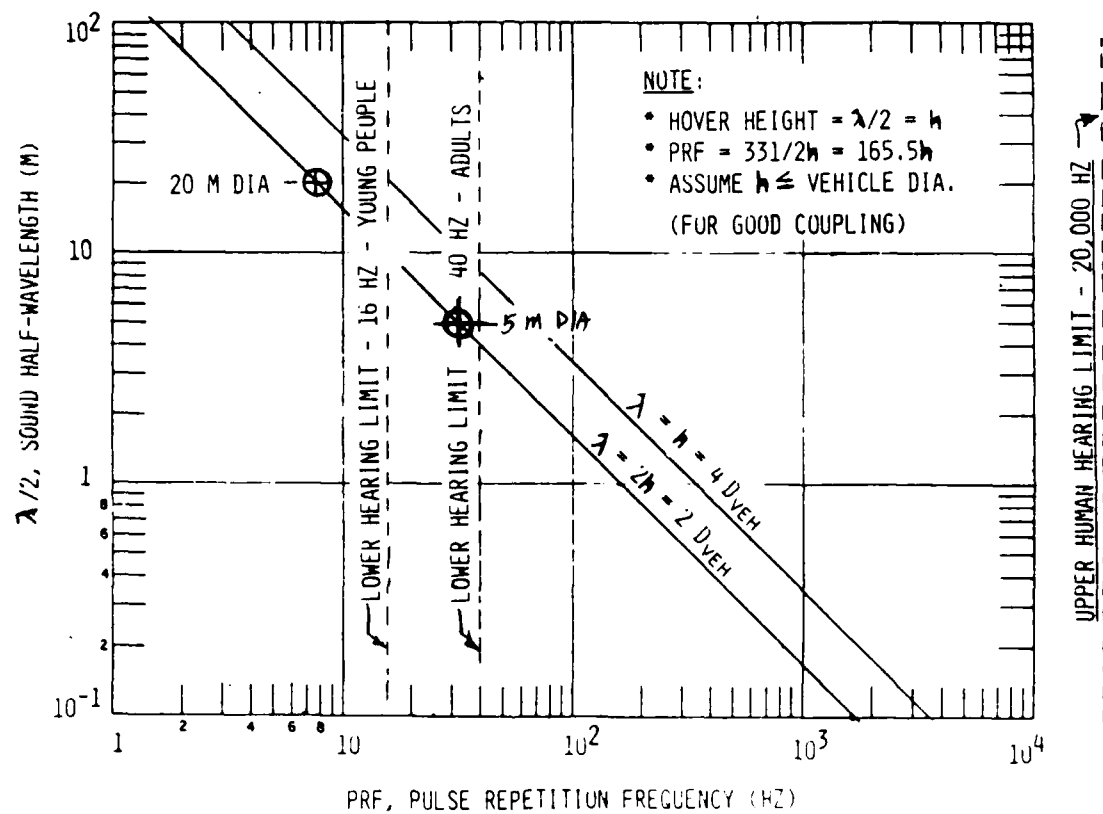


Figure II-26 PRF vs. Vehicle diameter and Hover height

object: the Earth.

In order to generate appropriate infra-sound radiation patterns, ERH thrusters may require specially-shaped surfaces, perhaps even flat-bottomed plugs (i.e., $\alpha = 0$). Note also that the reference ERH thruster utilized LSD-wave sources with kilohertz "excitation" frequencies. In order to efficiently "pump" the 33 Hz standing wave system with LSD waves, unusual amplitude-shaped macropulses (see Fig. II-27) might be required. On the other hand, the substantially lower "excitation" frequencies which are expected from microwave-supported "deflagration" waves, may couple well enough without macro-pulse-amplitude-shaping.

In summary, by establishing a standing wave system between an ERH thruster plug and the Earth's surface, a "ground resonance" effect can be created. The standing wave system may aid in convecting "spent" gases out of the active "detonation" regions and sweeping fresh gases back in. When operating in ground effect, ERH thruster "impulse coupling" efficiency should increase, causing a net reduction in propulsive power required for hover flight. If the laser macro-pulse energy is preserved (e.g., 1.6 MJ for the 12-finger ref. source), this lower beam power level could appear as a diminished pulse repetition frequency (e.g., a reduction

C) Analysis of Primary Receptive Optics Area

This section analyzes the relationship of specific engine/vehicle parameters to the primary optics area available for collecting beamed power. The analysis applies only to the reference vehicle configuration which receives the beam from an orbiting relay satellite, onto a primary optical surface. This parabolic reflecting lens is intimately integrated with an external compression inlet that closely resembles an isentropic spike. To avoid the requirement for a needle-fine inlet spike tip (i.e., an extension of the parabolic PO mirror), an annular laser beam is chosen; hence, for simplicity, a non-focusing conical tip is selected for the reference design.

The general layout of the engine/optics/vehicle configuration is depicted in Fig. II-28. The present analysis applies only to simple PO/SO optical trains; the use of tertiary optics requires a different set of model input assumptions. Note that the angle α sets the ERH thruster apex angle, and determines the maximum diameter of the engine/vehicle centerbody; also, a sharp flow turning angle exists inside the shroud - created by the intersection of PO and conical nozzle afterbody surfaces. This shrouded duct would function well only with supersonic air flow velocities; in practice, the sharp edge would probably be rounded off to some minimum radius - to prevent flow separation at subsonic and low supersonic flight speeds.

A major emphasis of this analysis was to compute the amount of power which may be

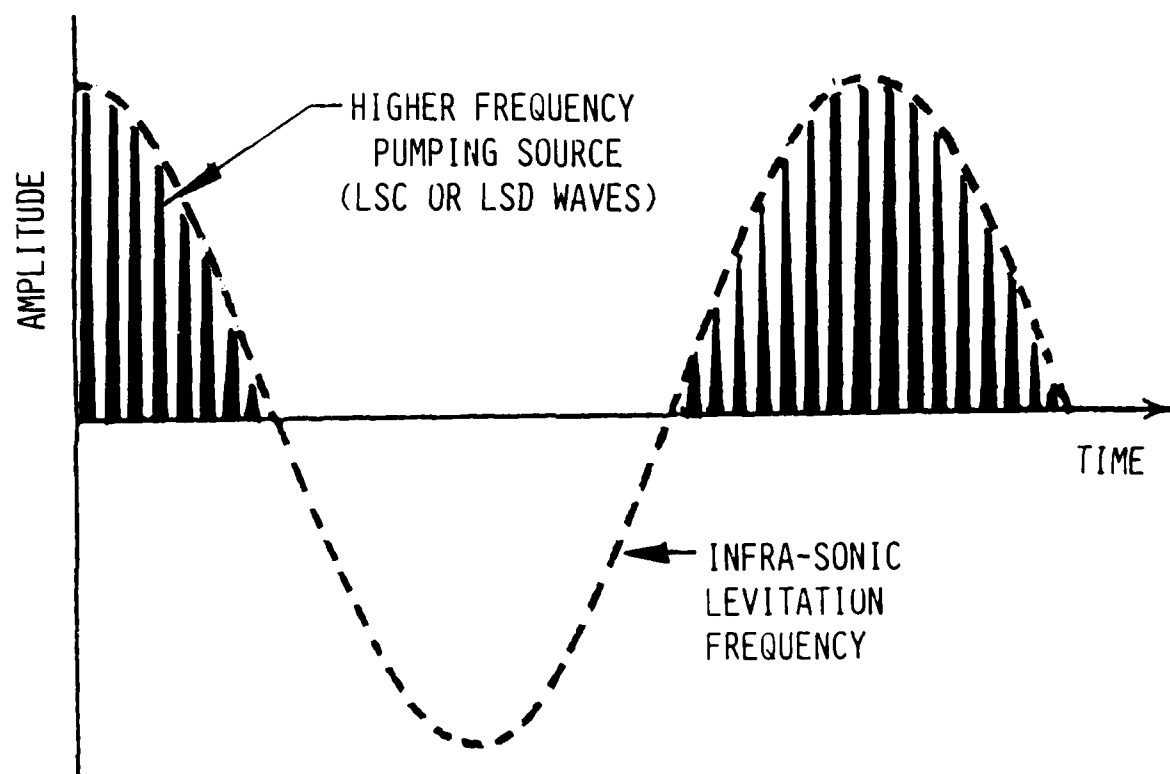
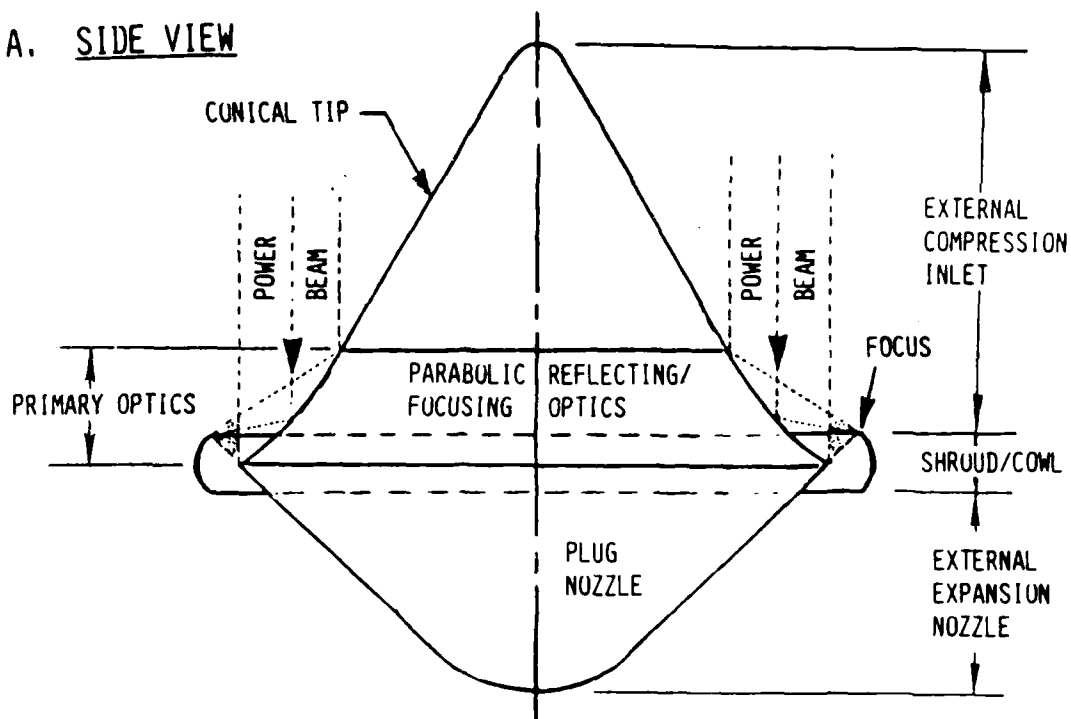


Figure II-27 Amplitude-shaped macro-pulses

A. SIDE VIEW



B. TOP VIEW

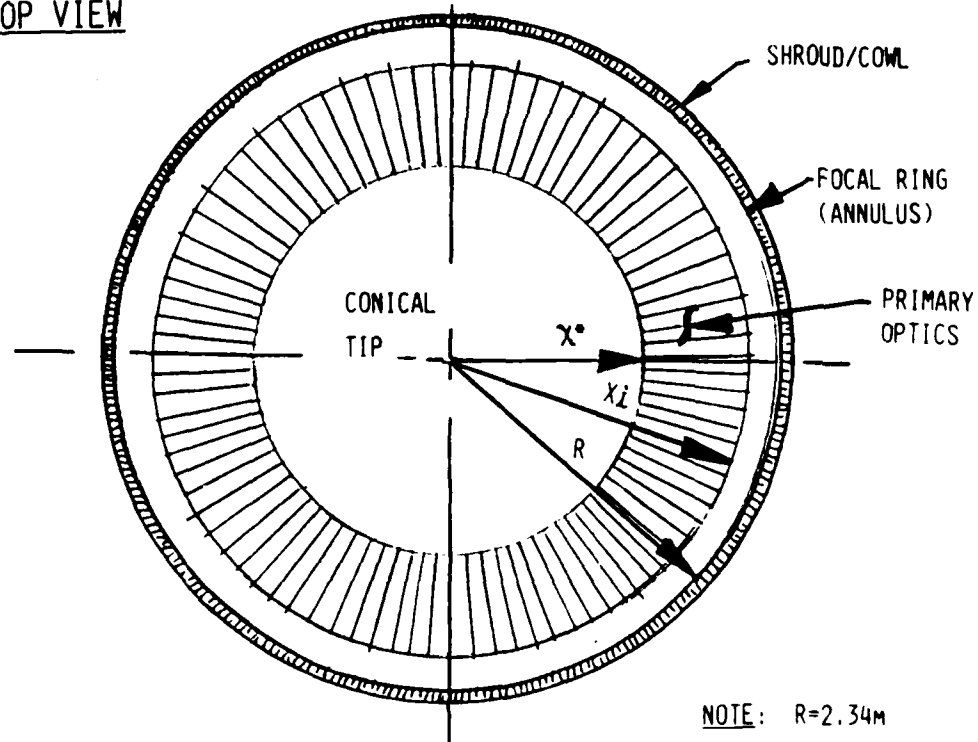


Figure II-28 General layout of Engine/Optics/Vehicle configuration

received by the craft. This peak power level is directly proportional to the area of the receiving optics and the beam wavelength. Note that throughout this treatment, "optics" refers to the primary aperture area and is independent of the power beam wavelength. The fraction of inlet spike frontal area available for collecting and focusing the beam is defined as the "active area fraction". This active-area fraction varies with cone tip angle and the desired focus location relative to the conical bow shock wave (produced by the external compression inlet tip). The analysis assumes that the conical bow shock angle is unaffected by the curvature of the primary optics (which would act as an additional compression surface).

1. Analysis

The basic geometry of the optical trains and the key variables used in the analysis are shown in Fig. II-29. The vertical distance, Z_2 , measured from the PO optics base to the conical shock wave is computed from inviscid shock data. The bow shock wave is assumed to attach to the cowl lip in order to minimize "spillage" drag; thus, Z_2 also represents the cowl lip location. The vertical distance from the PO optics base to the parabola focus is denoted by "F". The quantity D is the difference between Z_2 and F. In the calculations, D was set equal to zero, requiring the parabola focus to coincide with the cowl leading edge. This situation would not be possible if the shroud has a leading-edge flap, because the SO ring would have to be moved aft within the shroud. The equations presented below are generalized for any value of D.

The active area fraction was calculated from Eqn. II-1, with the terms defined in Fig. II-29. The expression which describes the parabolic reflecting surface is given below in Eqn. II-2 [1].

$$\text{Fraction active area} = \left| \frac{\pi \chi_1^2 - \pi (\chi^*)^2}{\pi R^2} \right| \quad (\text{II} - 1)$$

$$y = \frac{(z - R)^2}{4F} \quad (\text{II} - 2)$$

In order to make the inlet spike a continuous surface (i.e., without 'drag-increasing' discontinuities) the contours of the conical tip and parabolic reflecting surface must be matched by equating the first derivatives of the governing equations (i.e., the slopes). The slope of the cone surface is given in Eqn. II-3, and that of the parabola in Eqn. II-4. The dimensions of the cone base x^* and parabola height y^* were then found using Eqns. II-5 and II-6, in terms of the parabola focus location.

$$\text{Cone; } \frac{dy}{dx} = -\frac{1}{\tan \sigma} \quad (\text{II} - 3)$$

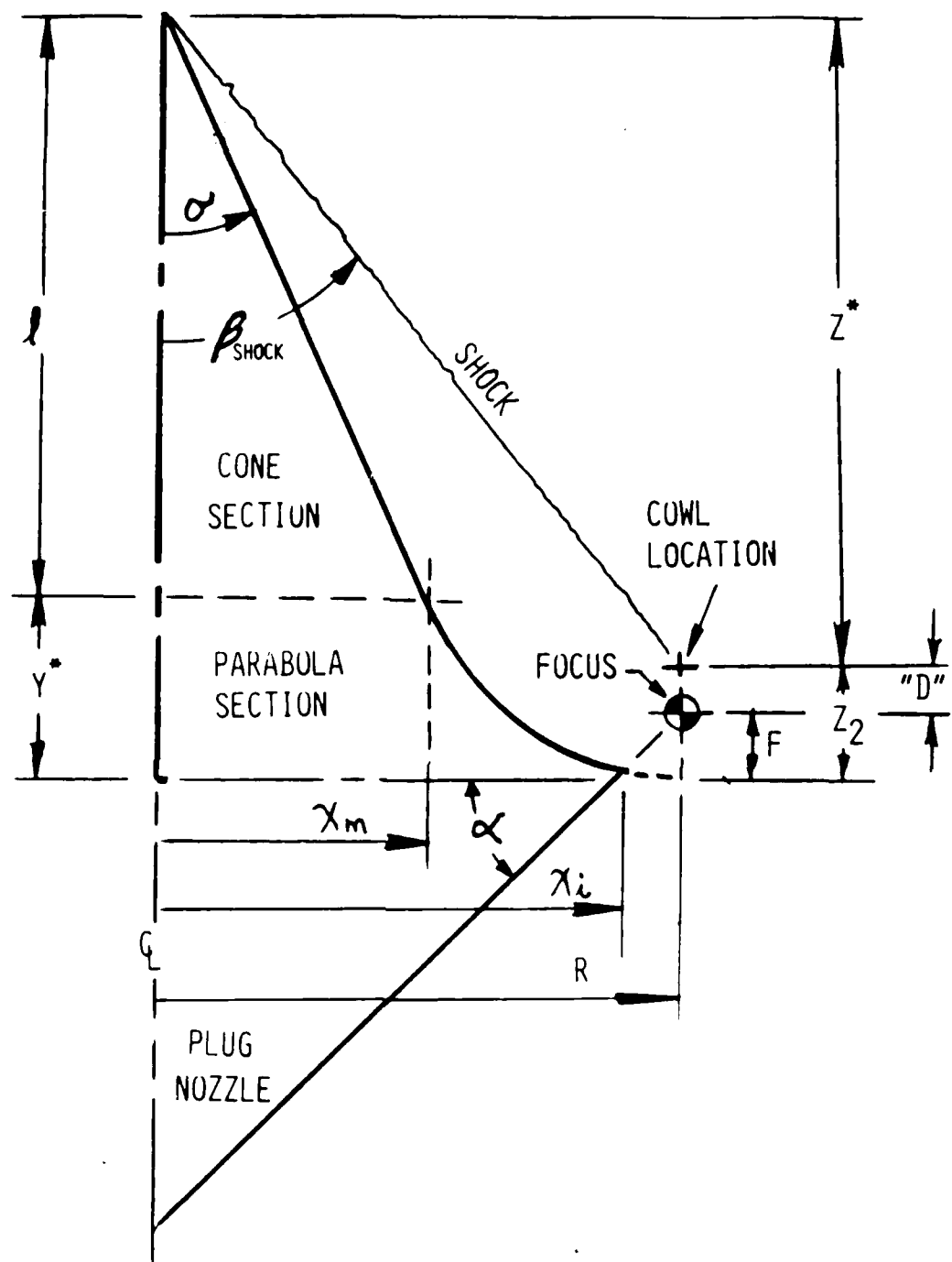


Figure II-29 Geometry for receptive optics

$$\text{Parabola; } \frac{dy}{dx} = \frac{X - R}{2F} \quad (II - 4)$$

$$z^* = R - \frac{2F}{\tan \sigma} \quad (II - 5)$$

$$y^* = \frac{F}{\tan^2 \sigma} \quad (II - 6)$$

The parameters z^* and l were then found from Eqns. II-7 and II-8 with the quantity D given by Eqn. II-9.

$$z^* = \frac{R}{\tan \beta} \quad (II - 7)$$

$$L = \frac{-2F}{\tan^2 \sigma} + \frac{R}{\tan \sigma} \quad (II - 8)$$

$$D = F(-1 - \frac{1}{\tan^2 \sigma}) + R(\frac{1}{\tan \sigma} - \frac{1}{\tan \beta}) \quad (II - 9)$$

At this point, the quantity "D" (measured from the focus to the cowl) can be specified. As mentioned above, D was set equal to zero for this analysis; thus, Eqn. II-9 could be solved for F (the focus location), given a cone half-angle and resultant bow shock wave angle (determined by the flight Mach number), and a maximum optics radius R . The resulting expression is given below.

$$F = \frac{R(\frac{1}{\tan \sigma} - \frac{1}{\tan \beta})}{(1 + \frac{1}{\tan^2 \sigma})} \quad (II - 10)$$

After obtaining F and z^* from Eqn. II-5, z_i must be found by solving for the intersection of the line through points (R, F) and $(R-X, 0)$, and the parabola (Eqn. II-2). The line location is specified by Eqn. II-11, with X calculated by Eqn. II-12. The angle α is that of the afterbody plug nozzle, as defined in Fig. II-29. The intersection point z_i was then found by equating Eqns. II-2 and II-11, resulting in Eqn. II-13 to be solved using the quadratic formula. The root of interest is negative due to the choice of coordinate system.

$$\text{Line; } y = \frac{F}{X}x + F(1 - \frac{R}{X}) \quad (II - 11)$$

$$X = F \tan \alpha \quad (II - 12)$$

$$x_i^2 + (-2R - \frac{4F^2}{X})x_i + (R^2 - 4F^2(1 - \frac{R}{X})) = 0 \quad (II - 13)$$

In the case of $\alpha = 90^\circ$, the equation of the line is given by Eqn. II-14, and the quadratic can be solved for x_i by using Eqn. II-15. The negative root is again the one of interest.

$$y = F \quad (II - 14)$$

$$x_i^2 + (-2R)x_i + (R^2 - 4F^2) = 0 \quad (II - 15)$$

Using x_i obtained from Eqns. II-13 or II-15, the active area fraction can then be calculated from Eqn. II-1.

2. Results

The active area fractions were calculated for cone semi-vertex angles ranging from 16 to 36 degrees, with afterbody angles α of 0, 30, 45, 60 and 90 degrees, at flight Mach numbers of 3, 4, 6, 10 and 20. Tabulated values for the shock wave angle, β , used in the analysis were taken from Ref. [2]. Plots of the active-area vs. cone angle and Mach number are displayed in Figs. II-30 - II-34.

The results presented here are for point designs having a specific cone half-angle, afterbody angle and flight Mach number. These results assume that the focus of the primary optics moves with the cowl to catch the shock at each condition: thus, every point represents a different optical design and inlet geometry. The temptation to associate cowl translation to the values of focal distance presented in the data tables must be avoided.

Also, the present analysis assumed $D = 0$ so that the optical ring focus coincides with the cowl leading edge; however, for proper operation, the focus should actually be slightly outside the shroud such that secondary optics could then intercept and reproject the beam across the nozzle/afterbody as shown in Fig. II-36. The desired D value used in Eqn. II-9 would have to be updated to include this effect.

From the results in Figs. II-30 to II-34, it is apparent that larger cone angles yield lower active areas, as does operation at high Mach numbers. A design Mach number of 3 and 50 % active optics area was selected for the reference point design.

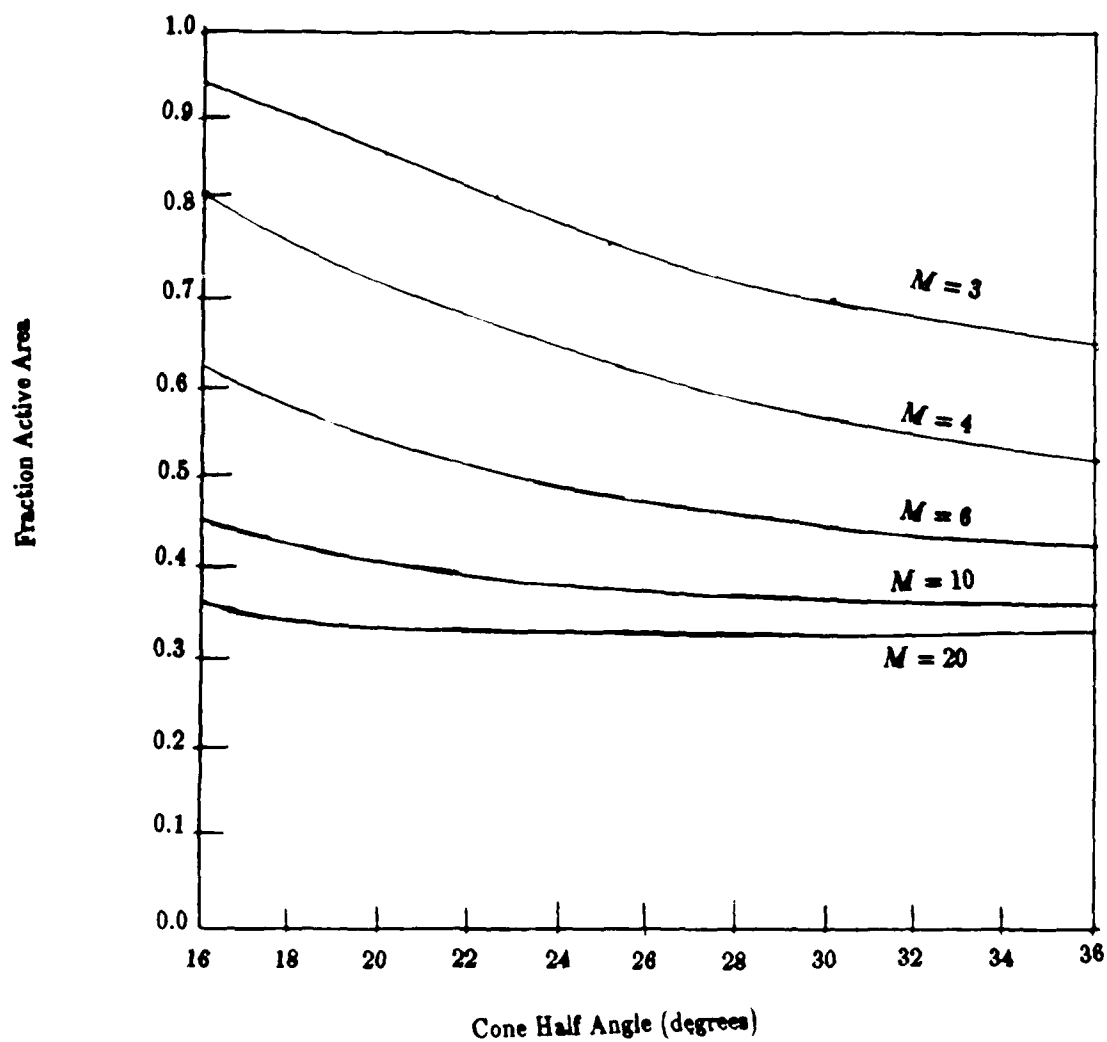


Figure II-30 Active area fraction vs. nose cone angle ($\alpha = 0^\circ$)

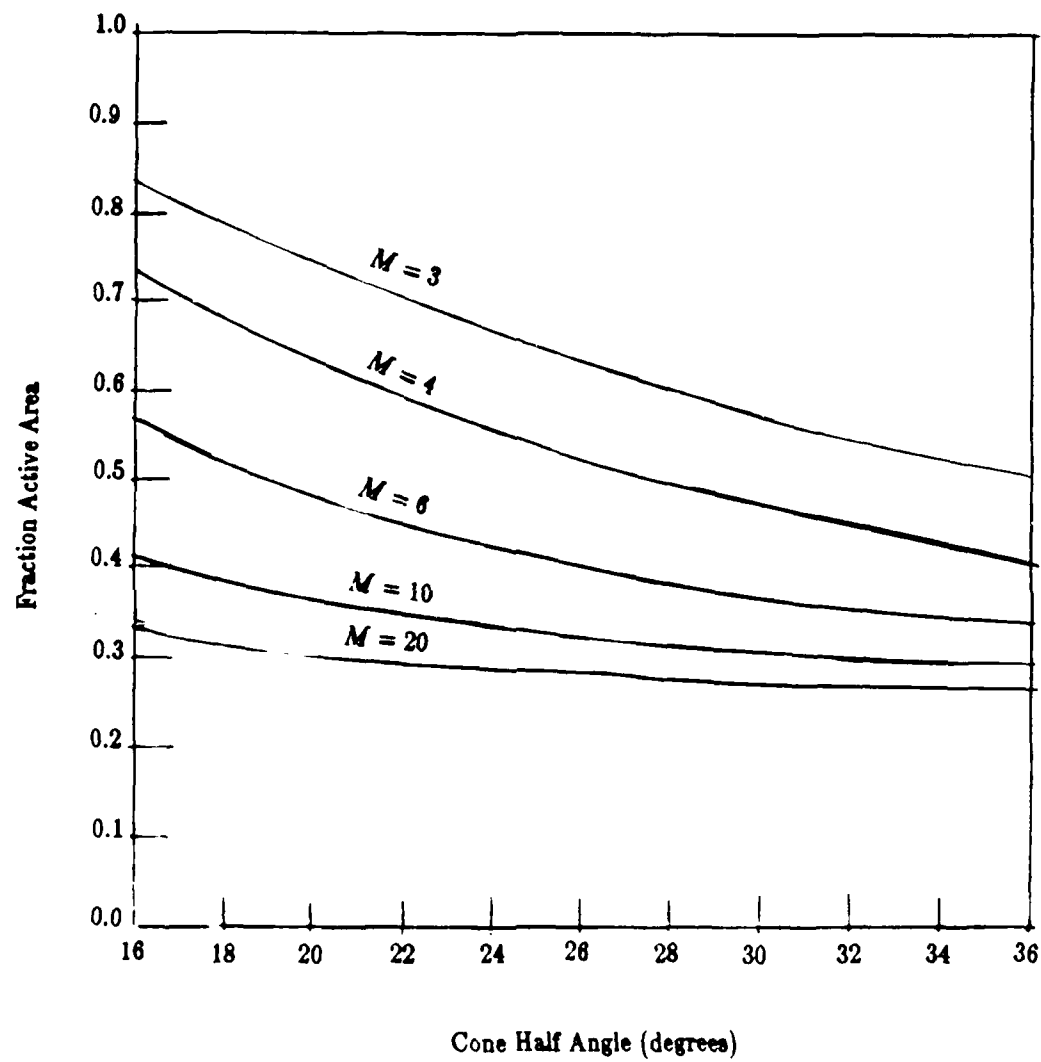


Figure II-31 Active area fraction vs. nose cone angle ($\alpha = 30^\circ$)

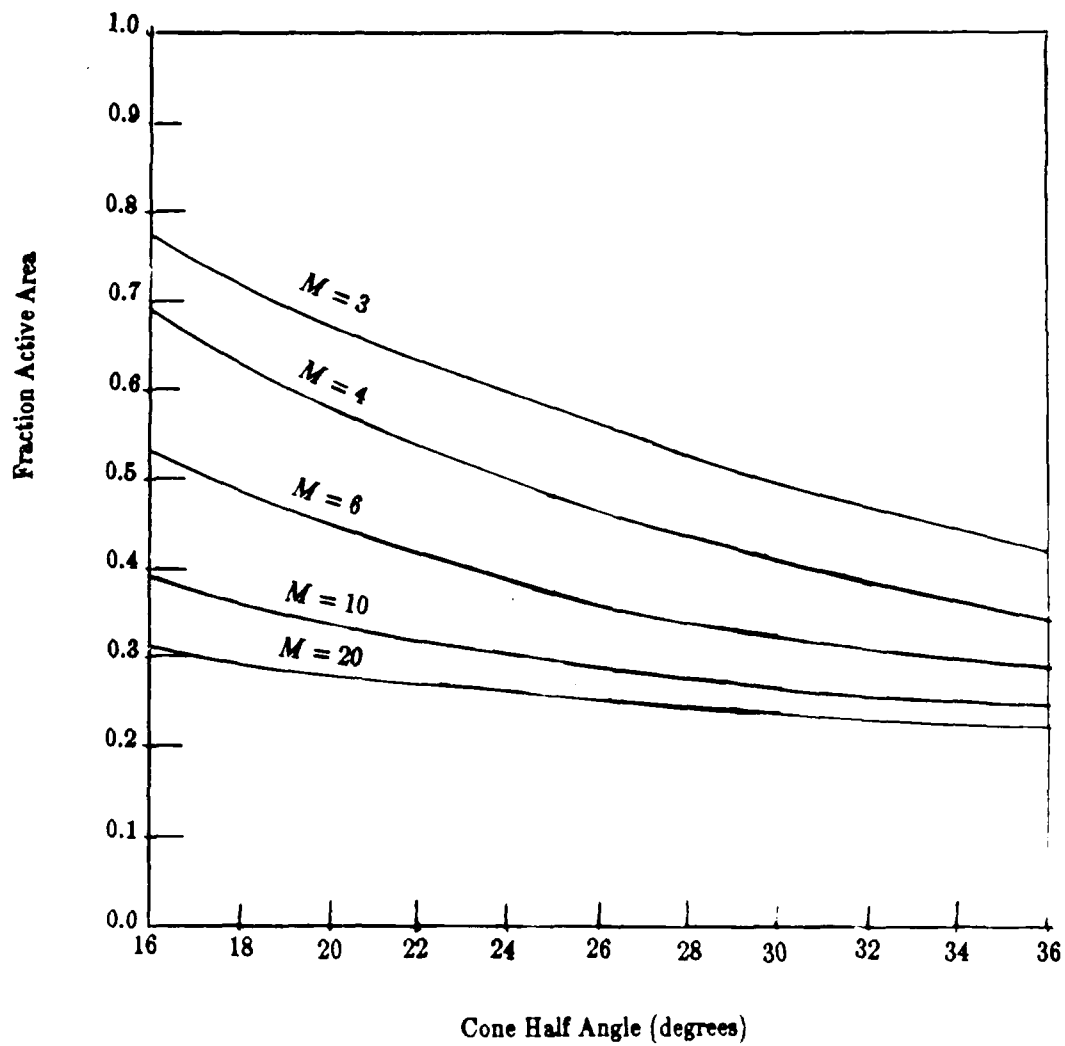


Figure II-32 Active area fraction vs. nose cone angle ($\alpha = 45^\circ$)

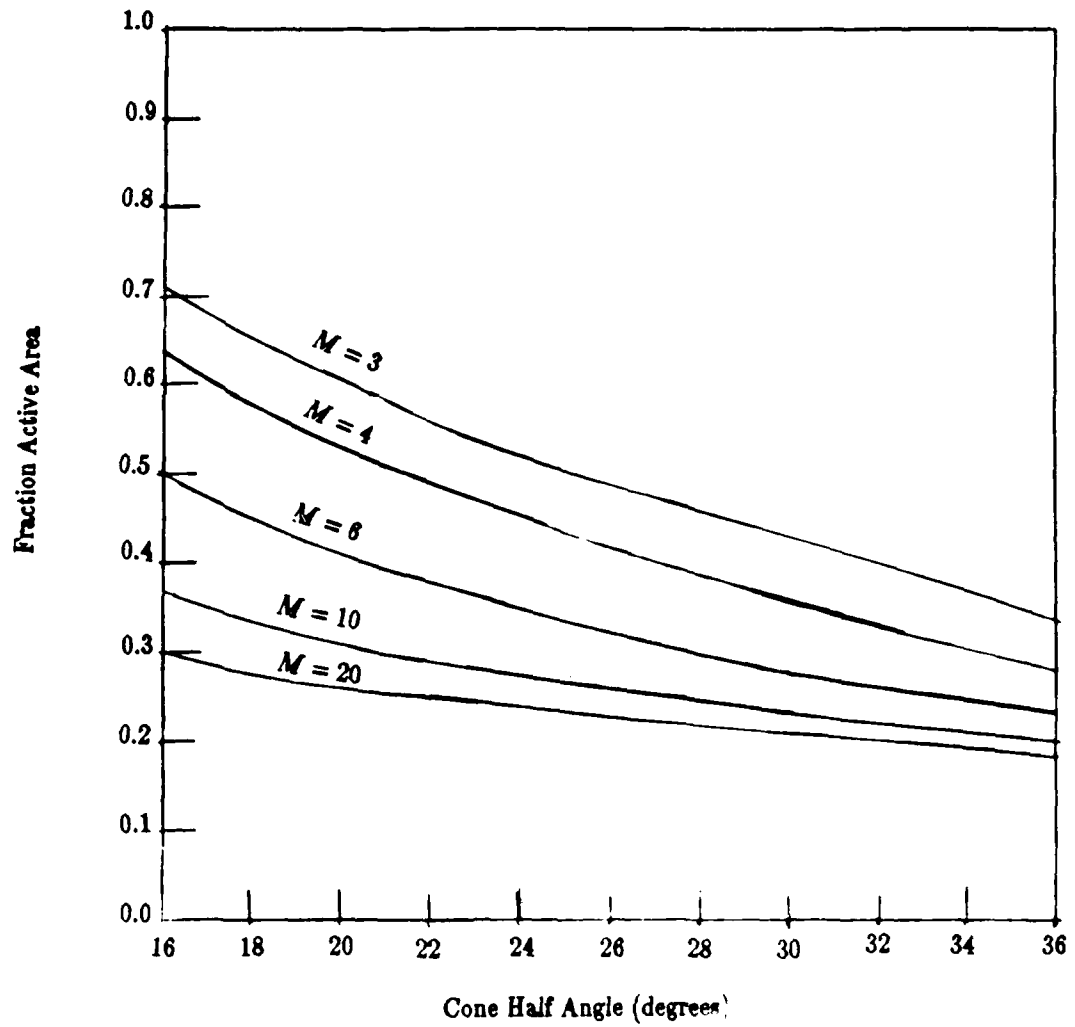


Figure II-33 Active area fraction vs. nose cone angle ($\alpha = 60^\circ$)

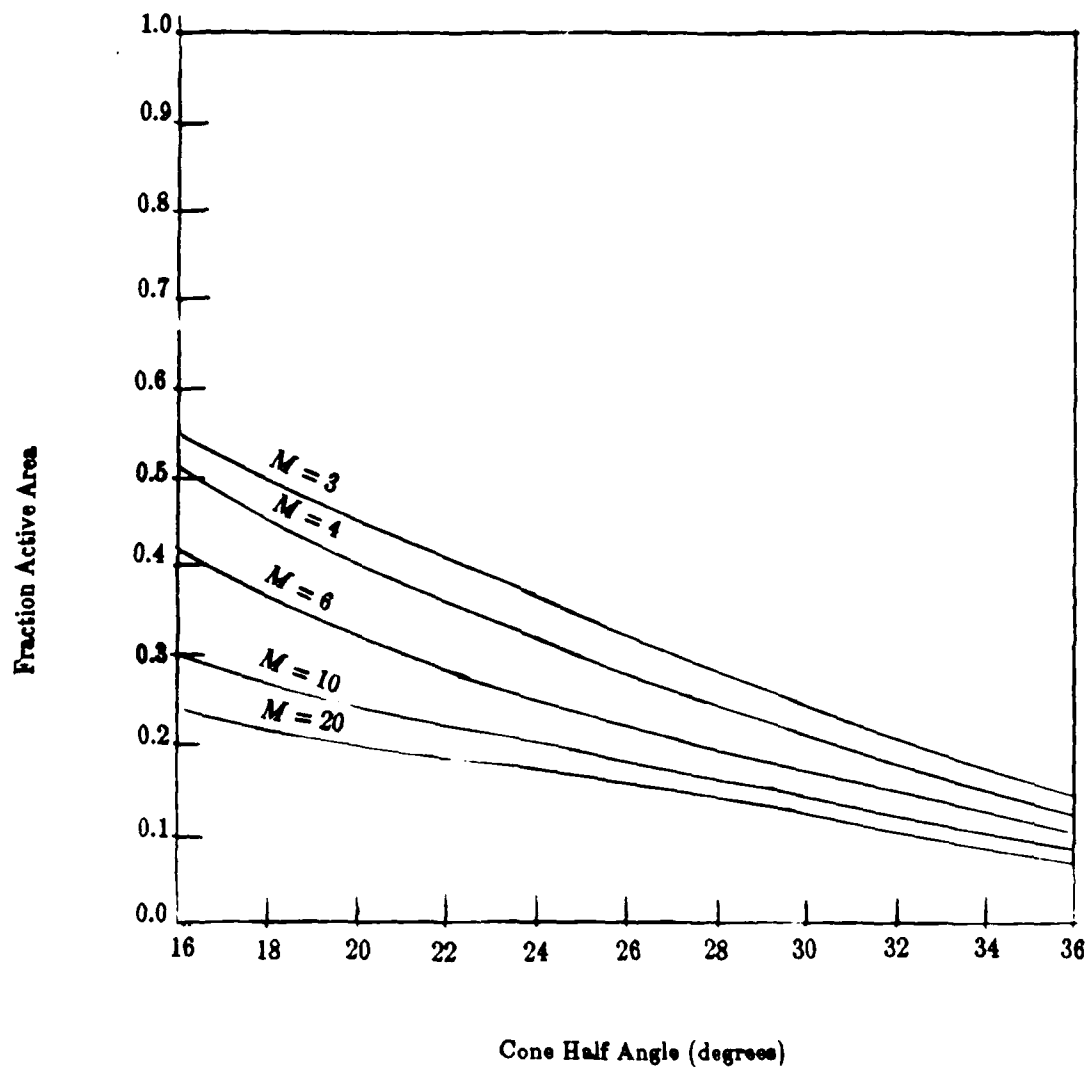


Figure II-34 Active area fraction vs. nose cone angle ($\alpha = 90^\circ$)

CHAPTER III

LASER ENERGY ABSORPTION INTO GASES

A) Introduction

Much of the earlier work on laser impulse generation has been found pertinent to this study of the ERH thruster concept. Yet, there are significant differences which should be mentioned. Many of these earlier studies are founded on slightly different assumptions, and reach different conclusions. This fact has been noted by Boni *et al.* [2].

Figure III-1 shows a typical "perpendicular beam/surface" geometry and the resultant blast wave structure. Most studies also included a direct interaction between the laser and the surface in their analyses, i.e., a direct 'burning' of the surface by the laser. The nature of the resultant absorption wave is then dependent on the type of surface upon which the beam is incident. The surface itself is participating in the overall radiative interaction with the surrounding gas and can contribute some mass, via ablation, to the blast wave. The latter, however, is known to have a negligible effect.*

Pirri[15] Reilly *et al.* [21] and Raizer [17,18], are among those researchers who have attempted analyses which consider the interaction between the laser and the gas as the principal reason for the impulsive and thermal coupling with the surface. Heating of the surface is by radiation and convection from the gas, rather than by direct radiative heating of the surface by the laser. The latter does occur but is considered negligible compared to the former. Note that once the plasma has been created, its absorption of the laser radiation is so great that the surface may be considered as being covered by an optically thick gas and thus, does not "see" the laser beam. Radiation is also considered to be the dominant heat transfer mechanism by which the high temperature plasma heats the surface (i.e., rather than convection). The process of the surface heating will not be discussed further here.

B) Earlier Models of LSD Wave Propagation

Most prior analyses begin with the gas dynamic equations to describe the motion of the ab-

* Most of these earlier studies are in fact largely concerned with enhancing the impulse and thermal coupling of the wave with the surface for destructive applications. Advanced cooling methods, stronger materials and transversely incident pulsed laser beam, can perhaps prevent serious damage to the ERH thruster surface. In fact, some research has indicated that 'laser countermeasures' to the destructive aspects may be easy to develop. This matter is not discussed further here.

sorption wave. Viscous and thermal losses are usually neglected. This is understandable considering that the absorption wave pressure may be greater than these effects, even at very high propagation Mach numbers.

Raizer [18], explains the process of igniting an LSD wave (in air) at the point focus of a laser beam, as follows. First, a strong shock wave is generated in the focal region where the laser energy is deposited in the gas. This shock travels through the gas, heating and ionizing it, further enhancing the absorption of more laser radiation. Radiative energy is deposited in successive layers of gas adjoining the shock front, and these layers in turn act as heat 'sources' which maintain the wave.

The wave, thus, moves along an 'optical channel' towards the laser source and is maintained by the beam. The wave would continue to travel up the beam as a planar wave moving within a cylindrical region, at constant strength, if not for its inevitable lateral expansion. However, most researchers believe this lateral motion is negligibly smaller than the axial, and have ignored it until the end of the laser pulse.

Raizer [17,18], derived specific equations for the velocity and pressure of the LSD wavefront from the integral form of the gas-dynamic equations using a control volume drawn about the wave (see Figure III-2). Raizer obtains Equations III-1 as given below. In deriving these relations, he apparently assumes that the wave moves steadily, at constant strength and without any losses, immediately after its initiation.

$$\begin{aligned}\rho_0 V_{LSD} &= \rho u \\ p_0 + \rho_0 V_{LSD}^2 &= p + \rho u^2 \\ e + \frac{p_0}{\rho_0} + \frac{V_{LSD}^2}{2} + \frac{\Phi}{\rho_0 V_{LSD}} &= e + \frac{p}{\rho} + \frac{u^2}{2}\end{aligned}\quad (III-1)$$

where V_{LSD} is the LSD wavefront velocity, u , p and ρ , the velocity, pressure and density of the plasma behind the wave, respectively. The subscript '0' denotes the ambient values of these last three quantities. Φ is the laser beam intensity. The internal energy of the gas is defined as $e = RT/(\gamma - 1) = p/[(\gamma - 1)\rho]$, where R is the gas constant and T is the temperature.

From these equations, Raizer next obtains an expression for the shock adiabat as:

$$e - e_0 = \frac{(p - p_0)(\frac{1}{\rho_0} - \frac{1}{\rho})}{2} + \Phi \sqrt{(\frac{1}{\rho_0} - \frac{1}{\rho})(p - p_0)} \quad (III-2)$$

This equation may be combined with the equation of state of the gas ($p = \rho RT$), to obtain an explicit expression for the shock adiabat, $p(\rho)$, for the supersonic wave, as:

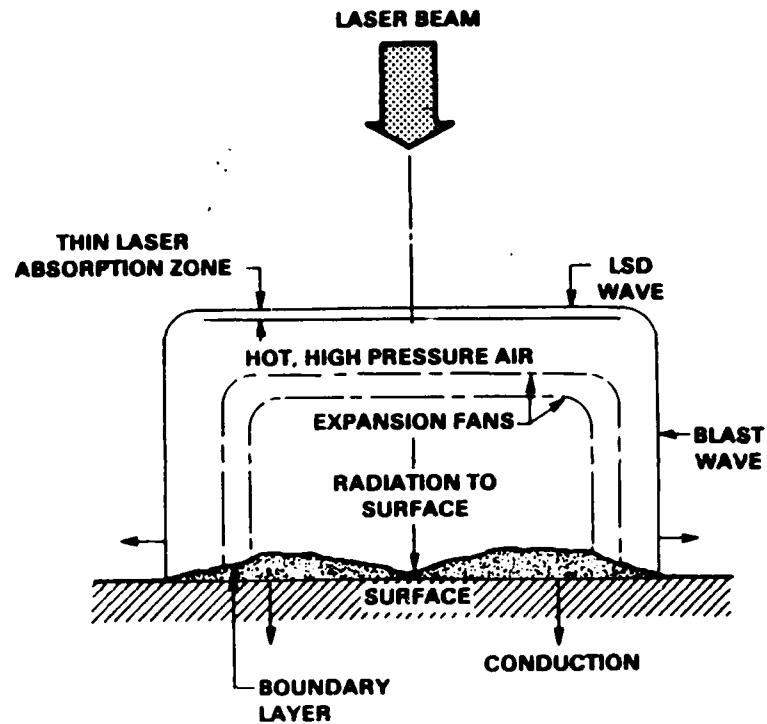


Figure III-1 The LSD wave for the case in point
(After Pirri, Root and Wu, Ref. 36)

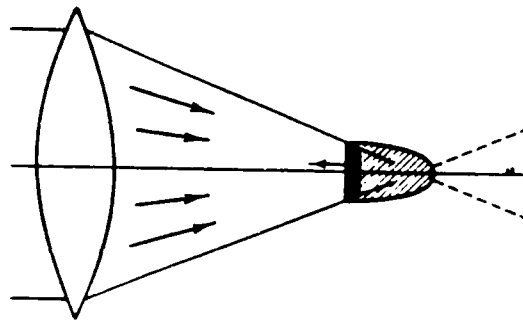


Figure III-2 The LSD wave geometry considered by Raiser (see ref. [18])

$$p = \left\{ \frac{2\sqrt{1 - \frac{E_0}{p}} \Phi \rho^{\frac{1}{2}}}{\left[\frac{\gamma+1}{\gamma-1} \right] \left[\frac{E_0}{p} - 1 \right]} \right\}^{\frac{1}{2}} \quad (III-3)$$

Raizer [18], graphically represents this shock adiabat as shown in Figure III-3. Note the limiting points on this curve. Wave velocity increases from the initial state 'O', along a straight line tangent to the shock adiabat at point 'J', The Chapman-Jouguet point. Point 'A' represents the maximum possible heating and compression of the gas in the detonation regime, with the assumption of zero ambient pressure. Raizer claims that the shock-wave ionized gas obtains additional energy from the absorption of the radiation, and expands along the line AJ until it reaches point J at the end of the energy release. This action, he believes, occurs within the wave front, which he treats as a discontinuity. Raizer admits that this conclusion requires verification by a more detailed theory of the internal wavefront structure. The points 'C' and 'D' represent the possible final states of a 'superdetonation' wave. Raizer implies that, unlike chemical detonation, this superdetonation may not be sustainable with laser energy.

Using Equations (III-1), Raizer shows that the minimum velocity of a supersonic wave in the detonation regime is given by:

$$V_{LSD} = \left[2(\gamma^2 - 1) \frac{\Phi}{\rho_0} \right]^{\frac{1}{2}} \quad (III-4)$$

Some experimental results have supported this finding (e.g., see Ferriter *et al.* [16]).

The pressure behind the wave front is given by:

$$p_{DW} = \frac{\rho_0 V_{LSD}^2}{\gamma + 1} \quad (III-5)$$

Raizer's analysis was not concerned with the internal structure and temporal evolution of the wave. This information is important in obtaining any relationship for the impulse generated. Thus, one must utilize the inviscid gas dynamics equations in their differential forms, in axi-symmetric cylindrical coordinates:

$$\frac{\partial \rho}{\partial t} + \frac{\partial \rho u}{\partial z} + \frac{1}{r} \frac{\partial \rho v}{\partial r} = 0 \quad (III-6)$$

$$\frac{\partial u}{\partial t} + \frac{u \partial u}{\partial z} + \frac{v \partial u}{\partial r} = -\frac{1}{\rho} \frac{\partial p}{\partial r} \quad (III-7)$$

$$\frac{\partial v}{\partial t} + \frac{u \partial v}{\partial z} + \frac{v \partial v}{\partial r} = -\frac{1}{\rho} \frac{\partial p}{\partial r} \quad (III-8)$$

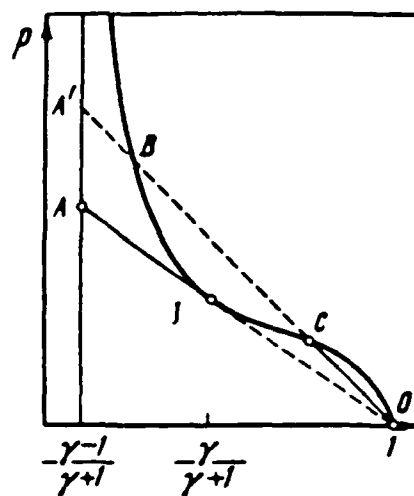


Figure III-3 Shock adiabat of a laser energy absorption wave (see ref. [18])

where u is the axial velocity, v , radial velocity, p , pressure and, ρ , the density. The previous analyses did not consider the energy equation in detail. Holmes *et al* [8], used a polytropic state equation, (assuming a polytropic gas), given by:

$$\frac{p}{\rho^\gamma} = \text{Const.} \quad (III - 9)$$

where the γ used has a value of 1.2 behind the wavefront. They assumed that the LSD wave propagates in the following manner.

1. The wave starts out at the strength and speed given by Raizer.
2. It propagates up the beam with decreasing strength, due to the axial and radial rarefaction fans moving inwards from the outer shock boundaries.
3. When the wave reaches a height equal to its diameter (which is assumed to be about equal to the beam's diameter if the wave speed is constant), the expansion of the wave, presumably, becomes two-dimensional or three-dimensional, i.e., the wavefront geometry is either cylindrical or spherical. This point in time has been denoted by t_{2D} , which is the time required for an axial rarefaction fan to reach the surface.

The rarefaction fans travel at the local speed of sound, c_s , which is not constant. But, using an average c_s , t_{2D} is defined as:

$$t_{2D} = \frac{r_s}{c_s} \quad (III - 10)$$

where r_s is the laser spot radius. Different definitions of t_{2D} have been used in the past, but they are all about equal to the one which uses:

$$c_s = \frac{V_{DW}}{2} \quad (III - 11)$$

Holmes *et al* [8], assume that the radial expansion fans are an effect of the wave's decay and hence consider only the radial gas dynamic equations:

$$\frac{\partial \rho}{\partial t} + \frac{\partial \rho v}{\partial r} + \frac{\rho v}{r} = 0 \quad (III - 12)$$

$$\frac{\partial v}{\partial t} + v \frac{\partial v}{\partial r} = -\frac{1}{\rho} \frac{\partial p}{\partial r} \quad (III - 13)$$

along with the polytropic state equation. Raizer similarly assumes that lateral losses are largely responsible for the wave decay after the pulse has terminated.

Holmes *et al* [8], then neglect the $1/r$ term in considering wave propagation far from the centerline.* This assumption then renders the equation completely one-dimensional. Thus, some

* For the spherical case, a $2/r$ term appears instead of $1/r$.

characteristic solutions may be obtained for the gas pressure and the particle, fan and wave velocities. Because the $1/r$ term is neglected, Equations III-12 and III-13 are not valid at $r = 0$, the centerline. The solutions of these equations say that straight rarefaction fans propagate radially inwards at the local, non-constant, speed of sound. Holmes *et al.* [8], describe the wave decay process based on the motion of each rarefaction coming in, beginning when the first one reaches the centerline.

Applying the boundary condition of zero velocity at the surface, the characteristic solutions yield a surface pressure of:

$$p_{LSD} = \left[\frac{\gamma + 1}{2\gamma} \right]^{\frac{\gamma}{\gamma - 1}} p_{DW} \quad (III - 14)$$

Table III-1-Sedov's Scaling Laws, (See Sedov [22])

	<u>UNPOWERED</u>	<u>POWERED</u>
<u>PLANAR</u>	$p/p_{ref} = (t/t_{ref})^{-2/3}$	$p/p_{ref} = \text{const}$
	$z/z_{ref} = (t/t_{ref})^{2/3}$	$z/z_{ref} = (t/t_{ref})$
<u>CYLINDRICAL</u>	$p/p_{ref} = (t/t_{ref})^{-1}$	$p/p_{ref} = (t/t_{ref})^{-1/2}$
	$r/r_{ref} = (t/t_{ref})^{1/2}$	$r/r_{ref} = (t/t_{ref})^{3/4}$
<u>SPHERICAL</u>	$p/p_{ref} = (t/t_{ref})^{-6/5}$	$p/p_{ref} = (t/t_{ref})^{-4/5}$
	$r/r_{ref} = (t/t_{ref})^{2/5}$	$r/r_{ref} = (t/t_{ref})^{3/5}$

Holmes *et al.* [8], then calculate the impulse for every rarefaction, within the time it takes each one to reach the centerline, using the characteristic pressure behind each rarefaction - until a radius of three times the spot radius is reached. Next, they apply the self-similar solutions of the gasdynamic equations given by Sedov [22], to give the pressure decay to the ambient value. These 'Scaling Laws' are presented in Table III-1.

C) Results of the Earlier Models

The unpowered scaling laws were originally derived by Sedov from dimensional analysis techniques. The powered scaling laws were supplemented to Sedov's by assuming a linear energy deposition (i.e., substituting an energy varying linearly with time in Sedov's original form of these relations). These similarity relations are not without their problems. One of them is that they present a singularity at $t = 0$ and a zero value of absolute pressure as t approaches infinity.

Pirri uses Sedov's self-similar solutions of the gasdynamic equations without considering the motion of the rarefactions. Indeed these equations appear to be complete and valid solutions of the much simplified gasdynamic equations (with the $1/r$ term).

In Pirri's analysis, the wave is assumed to be of constant strength while the laser is on, then decays according to the planar scaling laws until the time t_{2D} (if t_{2D} is greater than t_p). The wave then decays according to the unpowered cylindrical scaling laws until ambient pressure is reached. If $t_p > t_{2D}$, he applies the powered cylindrical scaling laws before going to the unpowered.

Reilly *et al.* [21], use what appears to be a mixture of the above analyses. A rarefaction fan is said to be radially approaching the centerline (from its starting point at the spot radius), at the average local speed of sound c_s . The surface pressure within this rarefaction is defined to be the rarefaction pressure from shock tube analysis. They assume that p_{LSD} is felt across the surface from the centerline to the radial location of the rarefaction at time t . The impulse is then calculated with these pressures assumed constant over these areas until t_{2D} . Next, they apply either of Sedov's scaling laws depending on how t_p compares with the time required for an axial rarefaction fan to reach the surface (t_{2D}), and the time for a radial fan to reach the centerline.

Ferriter *et al.* [6], and Edwards *et al.* [4], have used a computer code called LASNEX to compute the impulse including the interaction between the laser and the surface in their calculation. They claim to have obtained results that agreed with each of the above models. Holmes *et al.* [11], did an experimental simulation of LSD wave propagation, using explosive strips, and claim adequate agreement with their theory. They all however, admit that more sophisticated modeling needs to be done.

Each of these analyses appears to be based on dissimilar physical assumptions but that is not entirely the case. All yield similar results for small radii, for which t_{2D} is also small. Although the characteristic solutions are not valid for small r , they are used by Holmes *et al.* [8], and Reilly *et al.* [21] to give a better description of the wave structure (particularly in its transition to a three-dimensional geometry) than Sedov's solutions supposedly could in that region. But if r is small, the additional assumptions made by Holmes *et al.* [8] and Reilly *et al.* [21] will not be advantageous

because the rarefaction fans will not be of well enough defined structure to make any difference. Hence, the characteristic analysis is not all that advantageous and Sedov's scaling laws can provide adequate information on the wave.

D) Summary

This chapter has presented some of the assumptions behind the earlier analyses on laser impulse generation for beams which are perpendicularly incident to a surface. The following chapter will introduce another analytical model for laser impulse generation, one which applies to LSD waves which propagate parallel (but not necessarily in contact with) the impulse surface.

CHAPTER IV

INSTANTANEOUS "LINE SOURCE" ERH THRUSTER MODEL (STATIC)

A. Impulse Generation Model for LSD Waves Propagating Parallel to a Surface

When an LSD wave propagates parallel to a surface, the type of boundary conditions imposed on the plasma expansion differ from the case of the previous section. As the wave races up the laser beam, it is constrained from expanding in a fully cylindrical geometry by the close proximity of an adjacent surface (see Figure IV-1). However, this does not necessarily remove axi-symmetry from the problem. The wave front within the spot radius may remain as in Figure III-1 or Figure III-2, and the blast wave could still be hemi-cylindrical (or partly spherical). Whatever the case, the details of the LSD propagation the blast wave expansion are more complicated than the for previous case.

1. Initial "Line Source" Conditions Resulting From Rapid LSD Wave Heating of Air

That the parallel beam/surface geometry is a more complicated case is evident from an examination of Figures III-1, III-2 and IV-1. Thermal and viscous losses are certainly of greater importance due to the LSD wave propagating so close to the surface. The wave front velocity can then be reduced by the presence of the surface. It has been shown that viscous effects can reduce the strength of a shock wave, or make it more oblique. Reflections of rarefaction fans shed off the LSD wave front edge may even be absorbed within the air/surface boundary layer.

Therefore, the terms representing these losses have to be included in Equations III-6 - III-8. However, the reasons for neglecting them before could still apply. If the intensity of the incident laser radiation is sufficiently high, the velocity at which the LSD wave front propagates across the plate would be hypersonic. Yet, it is still possible for the losses to be negligible compared to the high pressures that are generated. To simplify the following analysis, these same assumptions will be made here.

Figure IV-1 shows a side view of the parallelly propagating LSD wave's structure. Note the rarefaction fans reflecting back and forth off the plate and the shock boundaries. As indicated, the wave is quite a bit more complicated in its axial propagation geometry than in the perpendicularly-incident-beam case. This implies that the axial dependence of the gasdynamic equations may no longer be as negligible as in the analysis of Holmes *et al.* [8]. However, if, again, the velocity of the

LSD wave across the plate is hypersonic, then the rarefaction fan reflections may not be 'felt' in the time required for the LSD wave to cross the surface (i.e., the laser pulse duration).

In the case of the normally-incident beam, the LSD wave velocity was assumed to be much higher than the radial expansion velocity. This may also be adopted here for the same reasons. The LSD wave propagation and the blast wave expansion may then be considered as axially independent. Hence, the blast wave expansion may be assumed to stem from a thin 'line source' of energy.

2. Modeling of the Cylindrical Blast Wave Expansion Process

The thin line source model of the cylindrical blast wave expansion, according to the assumptions made above, practically neglects the axial propagation time, t_L , of the wave across the surface. Clearly this thin line has a finite diameter (equal to the beam diameter) and the actual LSD wavefront requires a finite amount of time to traverse the length, L , of the surface. Hence, the validity of this model rests mainly on this time, t_L , being very small relative to the expansion time, t_0 .

The time t_L is also equal to the pulse time of the laser, t_p , since it would make no sense to continue the LSD wave off the surface - where no suitable impulse may be obtained. Nevertheless, the plasma "leftover" after the termination of laser pulse might still continue off the surface boundaries if it is not suitably constrained. At present, this effect is not thought to be a significant loss factor in the impulse generation process; yet, it could limit how small t_p , (or L) could be. Bear in mind that the line source model requires a 'long line' and a short energy deposition time to match the implicit assumptions of an infinitely long and thin line with an infinitely small energy deposition time of Sedov's equations[22]. These requirements can be met with a high LSD wave propagation velocity.

When the laser pulse is terminated (i.e., at $t = t_p$), the cylindrical air plasma is not likely to have a radius much larger than the spot radius, r_s , which has been used in the past. The LSD wave velocity across the surface will in general be very high compared to the lateral expansion velocity. Hence, the radius of the cylindrical blast wave at $t = t_p$ may be set equal to r_s .

It is assumed that the laser pulse shape, (i.e., the laser beam intensity vs. time, for $t \leq t_p$), is such that the LSD wave sees a 'fairly constant' laser flux after the beam has passed through the optical train to the thruster surface. Also, for simplicity, it is assumed that the beam cross-section is held somewhat semi-circular immediately adjacent to the thruster surface (see Figure IV-2). This ensures a plasma expansion process with a cylindrical geometry.

As a result of the line source assumptions, the problem becomes virtually one-dimensional.

AD-A187 336

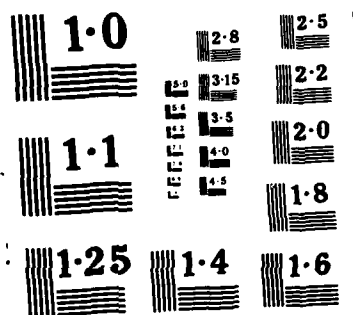
ADVANCED ENERGY CONVERSION CONCEPT FOR BEAMED-ENERGY
PROPULSION(U) RENSSLAER POLYTECHNIC INST TROY NY DEPT
OF MECHANICAL ENGINE L N HYMANO 21 AUG 87

2/3

UNCLASSIFIED

RPI-5-24170 AFOSR-YN-87-1387 AFOSR-84-0361 F/C 9/3

NL





87

axi-symmetrical. Neglecting losses, the wave then could still travel along the surface with a velocity, V_{LSD} , as given by Raizer.

$$V_{LSD} = [2(\gamma^2 - 1) \frac{\Phi}{\rho_0}]^{\frac{1}{2}} \quad (IV - 1)$$

Then the time $t_p = t_L$, can be defined as:

$$t_p = \frac{L}{V_{LSD}} \quad (IV - 2)$$

This definition satisfies the requirements of the line source model as previously mentioned, if the laser intensity, Φ , is large.

The equations are basically the same as the equations used in the previous analyses (p being radially dependent only). Equations III-1 can be applied, without modification, to the line source helping to link the model to the fact that the blast wave is born of laser energy deposition. This further justifies the applicability of Equation III-1 to the line source model. The boundary conditions of zero surface velocity, used to obtain the surface pressure from the gasdynamic equations, are also the same since the blast wave is also radially dependent only.* Since t_p is small, it is assumed that the surface virtually 'feels' this same pressure, p_{LSD} , at the end of the laser pulse.

$$p_{LSD} = \left[\frac{\gamma + 1}{2\gamma} \right]^{\frac{2\gamma}{\gamma - 1}} p_{PDW} \quad (IV - 3)$$

Note that p_{LSD} is the pressure with which the unpowered cylindrical decay is assumed to begin. Figure IV-3 displays p_{LSD} as a function of laser intensity, Φ , for several altitudes of interest. The Φ dependence helps to incorporate the fact that the blast wave is based on laser energy deposition into the line source model. However, the incremental impulse generated during the transit of the LSD wave ($t \leq t_p$), is assumed to be negligible even though the initial pressure may be quite large. This assumption is made because the LSD wave is propagating parallel to the surface and hence, perpendicular to the thrust direction.

At time, t_{2D} , a rarefaction fan propagates radially to the centerline of the blast wave while it is at the radius, r_s , assumed. Then, the blast wave expansion process assumes a cylindrical geometry after the time t_{2D} (this time might be better defined as t , but is kept as such because it turns out to be the same as that defined in the previous analyses).

$$t_{2D} = \frac{r_s}{c_s} \quad (IV - 4)$$

* Because this is not an infinite line source, the non-ideal 3-D effects that perturb the axi-symmetry of the problem may actually alter the surface pressure.

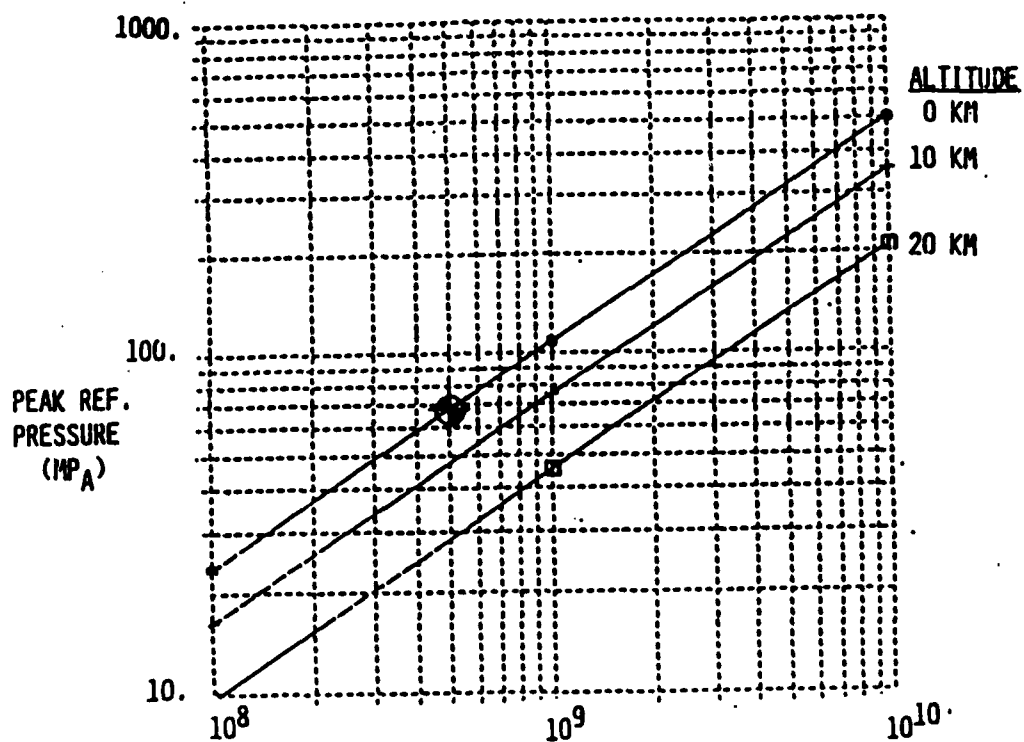


Figure IV-3 Peak surface (reference) pressure, p_{LSD} , vs. Incident laser intensity

where c_s again has an average value of:

$$c_s = \frac{V_{DW}}{2} \quad (IV - 5)$$

Hence, the wave has a structure and temporal history that is largely self-similar (see Figures VI.4).

3. Computation of Impulse Coupling to the Surface

The impulse on the surface is defined as:

$$I = \int_0^{t_p} \int_0^{r(t)} [p(t) - p_0] dA dt \quad (IV - 6)$$

where $dA = L dr$. The pressure history used in this model from Table 1, is displayed in Figures IV-4. By the previously mentioned assumptions and this equation, from $t = 0$ to $t = t_{2D}$, *the surface feels the impulse of a 'planar powered wave' defined by:

$$I_{pp} = 2r_s L p L S D t_{2D} \quad (IV - 7)$$

During this time, the decremental ambient contribution is:

$$I_{ppa} = -2r_s L p_0 t_{2D} \quad (IV - 8)$$

From t_{2D} to t_0 , the unpowered cylindrical scaling law gives:

$$I_{ua} = 4r_s L p L S D t_{2D} \left[\sqrt{\frac{t_0}{t_{2D}}} - 1 \right] \quad (IV - 9)$$

and for the ambient term:

$$I_{aaa} = -\frac{4}{3} r_s L p_0 t_{2D} \left[\left(\frac{t_0}{t_{2D}} \right)^{\frac{3}{2}} - 1 \right] \quad (IV - 10)$$

The sum of these terms defines the total impulse, I .

From the unpowered cylindrical scaling law, the decay time may be calculated as:

$$t_0 = \frac{t_{2D}^2 p L S D}{p_0} \quad (IV - 11)$$

It may be assumed that the blast zone can be refreshed with unheated air, moving radially inwards with the last rarefaction fan as the wave collapses, as t_0 is approached. Then, the plasma

* t_p is not used as the reference time here because it was assumed that there was no contribution to the impulse beforehand.

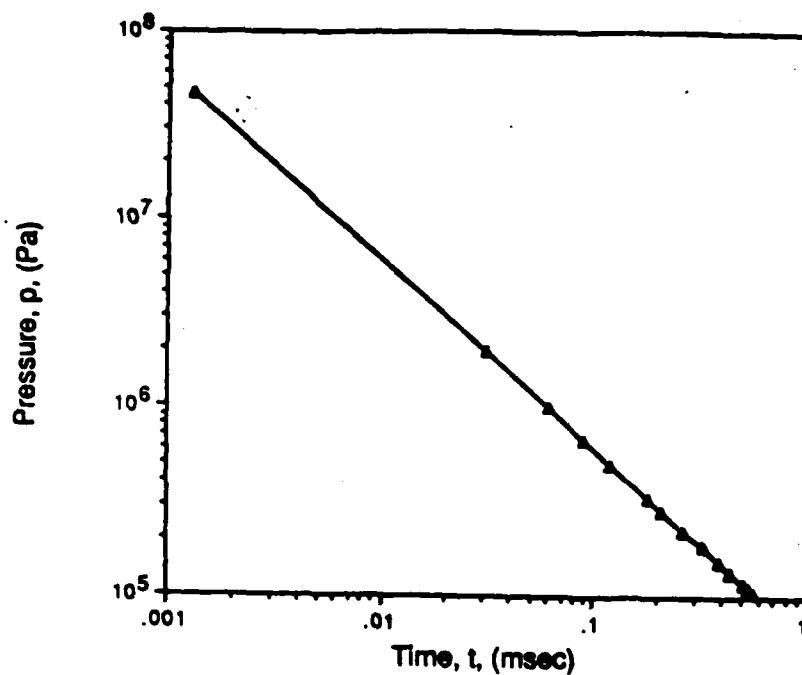


Figure IV-4a Cylindrical blast wave surface pressure vs. time, $p(t)$

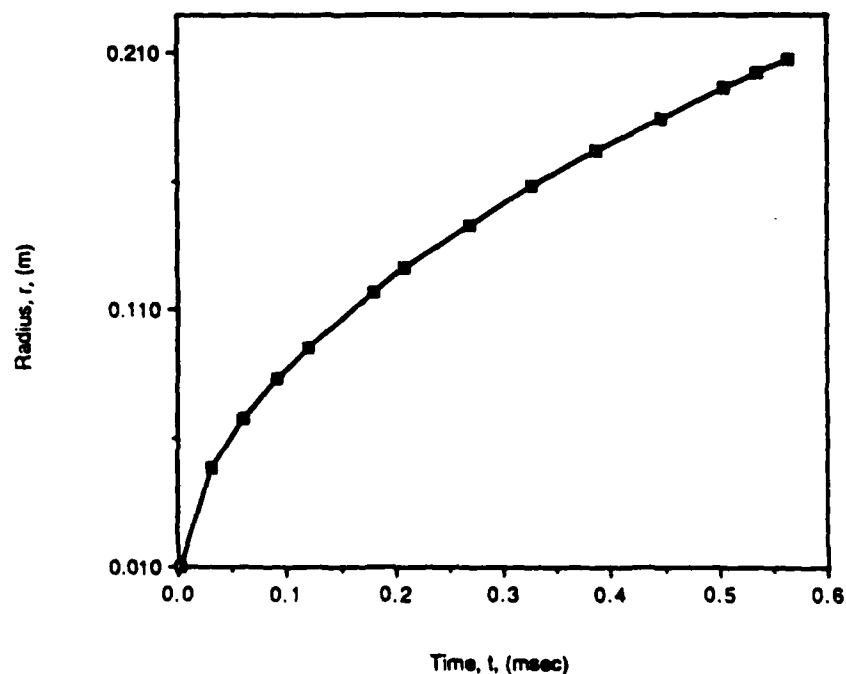


Figure IV-4b Cylindrical blast wave radius vs time, $r(t)$

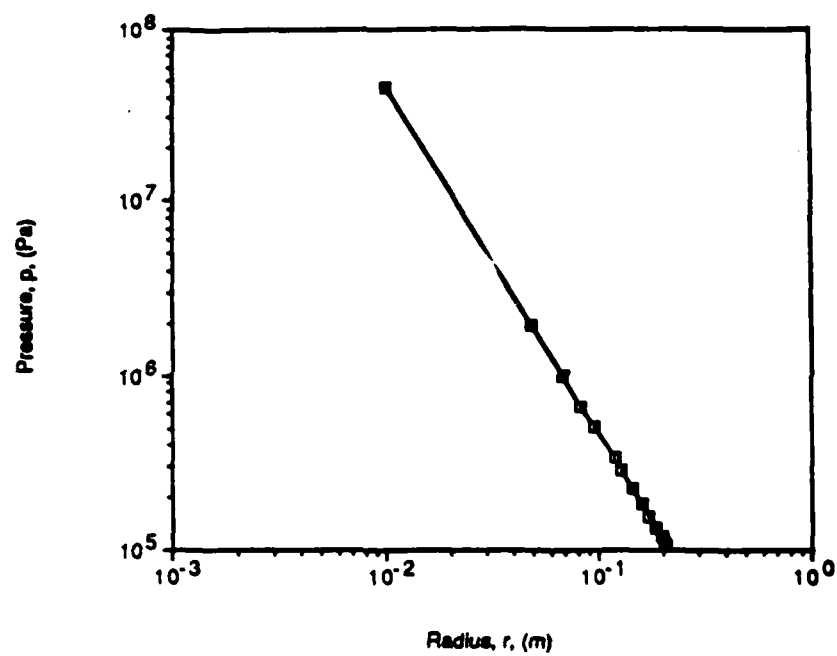


Figure IV-4c Cylindrical blast wave pressure-radius relationship, $p(r)$

decay and the impulse generation cycle end at $t = t_0$. With $t_{refresh}$ essentially zero, the maximum pulse repetition frequency, PRF, of the laser is then defined as:

$$PRF = \frac{1}{t_0} \quad (IV - 12)$$

The peak input power during a laser pulse is given by:

$$P = \frac{\pi}{2} r_s^2 \Phi \quad (IV - 13)$$

and the laser pulse energy is:

$$E_p = P t_p \quad (IV - 14)$$

Note that this definition of the laser pulse energy also helps to incorporate the fact that the blast wave is obtained from a linear, laser energy deposition over a time, t_p . The duty factor of the cycle is

$$DF = t_p PRF \quad (IV - 15)$$

From this, the time-averaged laser power deposited into the gas over the impulse generation cycles may be calculated as $\bar{P} = P \times DF$. The time-averaged thrust over the cycle is defined as:

$$T = I \times PRF \quad (IV - 16)$$

A measure of the impulse delivery efficiency is given by

$$\alpha = \frac{I}{E_p} = \frac{T}{\bar{P}} \quad (IV - 17)$$

which is the definition of the coupling coefficient, CC. From the unpowered cylindrical scaling law, the final radius of the wave may be calculated as:

$$r_0 = r_s \sqrt{\frac{P_{LSD}}{P_0}} \quad (IV - 18)$$

The final width of the cylindrical blast wave is twice this value, and should not approach the length L , or the assumption of axi-symmetry is violated. Also, the plasma must not expand beyond the finite width of the plate during t . Otherwise, a spherical development of the blast wave must be invoked.

A computer program is used to calculate the above variables for an interesting range of beam intensities and atmospheric conditions. The laser radius is set at 1 cm and the surface length, 2.5 m. A value of 1.2 is used for α as in earlier analyses. The results are discussed in the next chapter.

B) Results of the line source model

The main concern of this analysis is the efficiency of impulse delivery to the thruster surface. Critical parameters were varied to observe and understand their effect. The results of the line source calculations are discussed below. The single-pulse impulse is plotted in Figure IV-5. Note that more impulse is imparted to the surface by increasing the laser intensity. This is of course an advantage which can be exploited by the ERH thruster concept. Also note that the impulse decreases with increasing altitude. This is generally true for all airbreathing propulsion systems. This decrease occurs because less air is available for static thrust generation as the air density and pressure decrease with altitude. The time-averaged thrust, displayed in Figure IV-6, also has these same trends.

The peak laser pulse energy and power absorbed by the LSD wave are shown in Figures IV-7 and IV-8. They more or less agree with Reilly's observation that a reduction in the laser intensity is required to generate LSD waves at higher altitudes [20]. Figure IV-9 shows the average power going into a cycle as a function of incident laser intensity. This figure helps to demonstrate how the input laser power is distributed throughout the cycle.

However, the best measure of the impulse delivery's efficiency is the coupling coefficient. This has been plotted in Figure IV-10 against the laser intensity. As indicated, coupling coefficients are quite promising, being on the order of 1000 N/MW. Note also that the thruster efficiency increases with altitude and laser intensity. The increases imply a more efficient absorption and application of laser energy by the air at higher altitudes.

Apparently, the coupling coefficient levels off at the higher intensities and altitudes. This may occur because the air is approaching a limit in its ability to absorb more laser energy; a condition which can be linked to use of Equation III-9 which originates from the entropy equation (i.e., the second law of thermodynamics, see Holmes *et al.* [8]). As derived, the coupling coefficient really depends only on the gas properties and the laser beam intensity. This point is also mirrored by the LSD wave pressure (shown in Figure IV-3) which is a stronger function of laser intensity than altitude. The variations with altitude and intensity is also displayed in the maximum blast wave expansion radius, r_c in Figure IV-11. Note that r_c is also more sensitive to increases in beam intensity than those in altitude. The maximum plasma radius is directly proportional to the square root of the LSD wave pressure and inversely proportional to the ambient pressure.

The parameter r_0 also defines the radius over which the impulse and the mean thrust are delivered. However, these two quantities do not appear to be as sensitive to the area increase. This may be because the other variables they depend on (like p and t), are not very sensitive to the

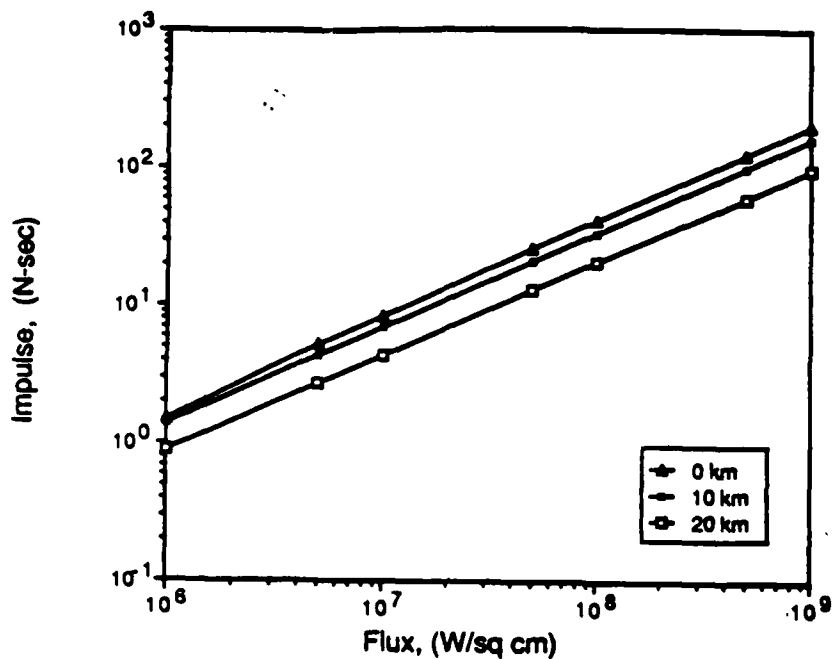


Figure IV-5 Single pulse impulse, I , imparted to the plate

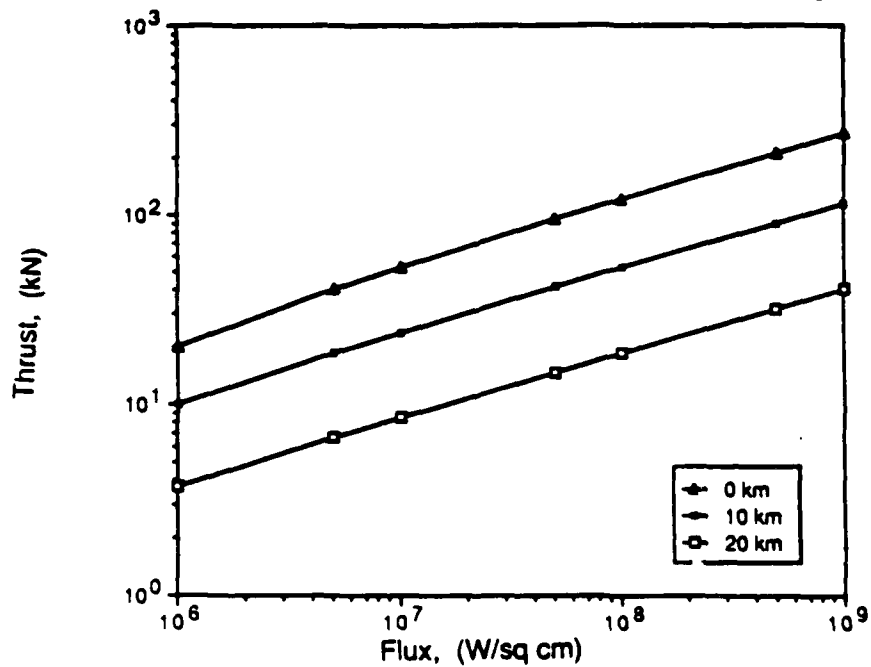


Figure IV-6 Time-averaged thrust, T , applied to the plate

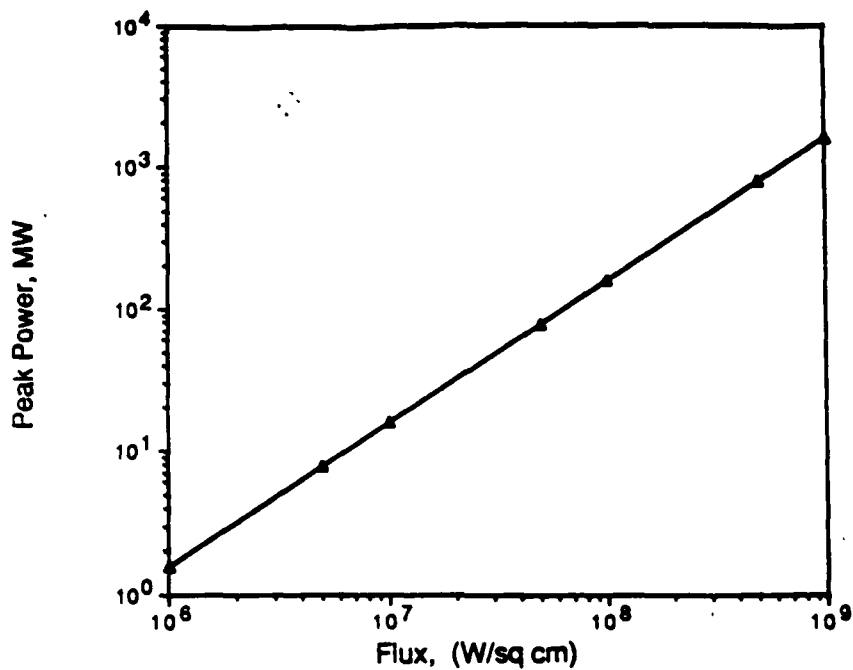


Figure IV-7 Peak laser power supplied to the LSD wave for the plasma

generation

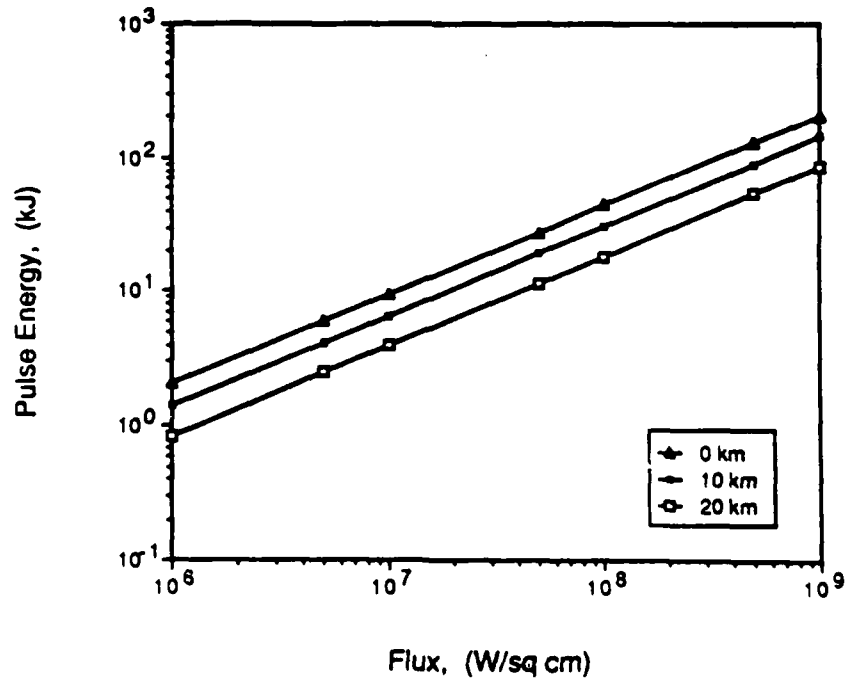


Figure IV-8 Laser pulse energy supplied to generate the line source

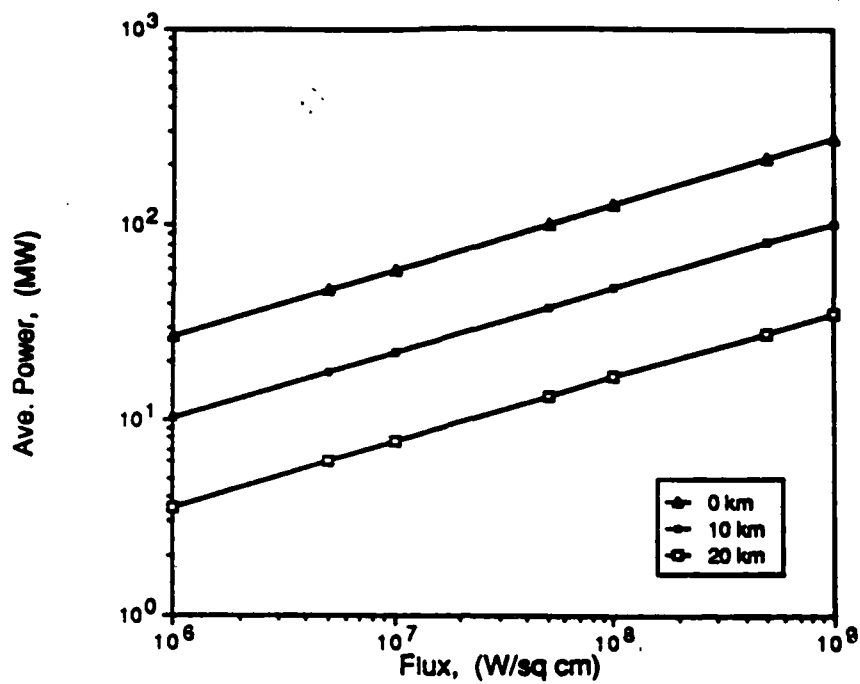


Figure IV-9 Maximum time-averaged power, \bar{P} , vs. incident laser flux

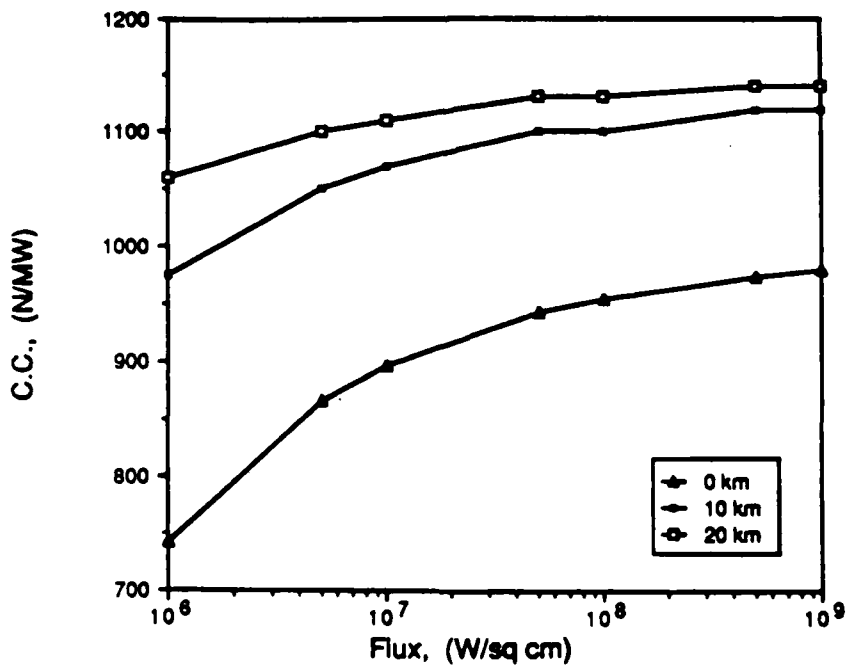


Figure IV-10 Coupling efficiency of the impulse exchange between the blast wave and the plate

altitude effects and thus, counterbalance the area increase. Another parameter on which the mean thrust and the impulse depend is the pulse repetition frequency, PRF, which is shown in Figure IV-12, to decrease with increasing beam intensity, as well as altitude. Evidently, the less dense air at higher altitude takes more time to decay from p_{LSD} to p_0 , and clearly, has the immediate effect of decreasing PRF, since $PRF = 1/t_0$.

Largely because of the necessity for low duty factors (i.e., $DF = t_p/t_0$), the impulse model is valid for intensities greater than about $5 \times 10^7 W/cm^2$. Note in Figure IV.10 that the LSC/LSD transition region for 10.6 micron laser radiation lies between $10^6 - 10^7 W/cm^2$. At the shortest wavelengths of interest (e.g., 0.35 micron) this transition will scale to $4.64 \times 10^7 W/cm^2$ at the upper limit. (Recall that LSC waves have subsonic velocities, and that the model treated here, applies only to LSD waves.) Low duty factors (i.e., about 0.1) require high LSD wave velocities, which goes back to the need for elevated laser intensities to secure short laser pulse times (see Figure IV.13).

At the highest feasible intensities, for 10.6 micron radiation, performance is limited by the breakdown condition to $1 - 2 \times 10^9 W/cm^2$. However, the breakdown threshold can be extended to higher intensities, since this limit scales as wavelength to the 3/2 power (see Reilly). For example, this could permit operation at flux levels as high as $10^{11} W/cm^2$ with 0.5 micron radiation; however, severe demands would be placed on the secondary optics.

It is obvious from the above analytical results, that the static performance predicted for the 'line-source' ERH thruster is exceptionally promising. An exemplary application for this advanced propulsion concept is discussed in the following chapter.

C) Summary

In retrospect, it must be stated that the assumption of a line source was somewhat restrictive to the analysis. As shown above in section B, the validity of the model is confined to a rather narrow range of intensities ranging from $0.5 - 1 \times 10^9 W/cm^2$ at the low end, to $1 - 2 \times 10^9 W/cm^2$ at the breakdown limit, for 10.6 micron radiation. However, the breakdown threshold scales as wavelength to the 3/2 power, so this upper limit could easily be shifted upward by one or two orders of magnitude - simply by invoking higher laser frequencies (e.g., 0.35 to 0.5 microns). Thus, a larger range of validity for the model and for operation of the ERH thruster is possible.

The final set of the gasdynamic equations imply that the LSD wave propagation velocity is independent of wavelength, but this is, in fact, misleading. The exact physics of the laser energy deposition is not fully taken into account in the model. A more rigorous solution would incorporate the laser radiation as a source term in the energy equations, and include re-radiation heat transfer

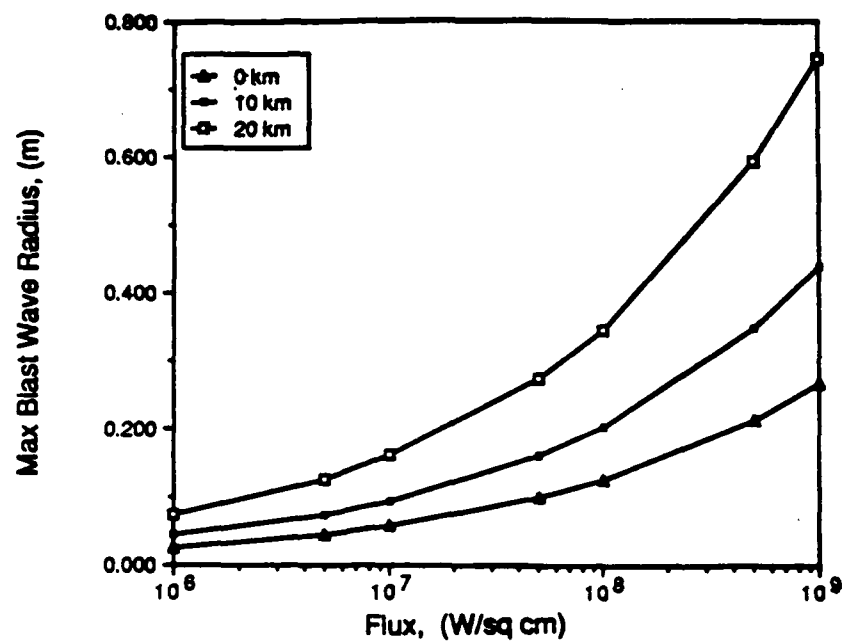


Figure IV-11 Maximum cylindrical blast wave radius, r_0

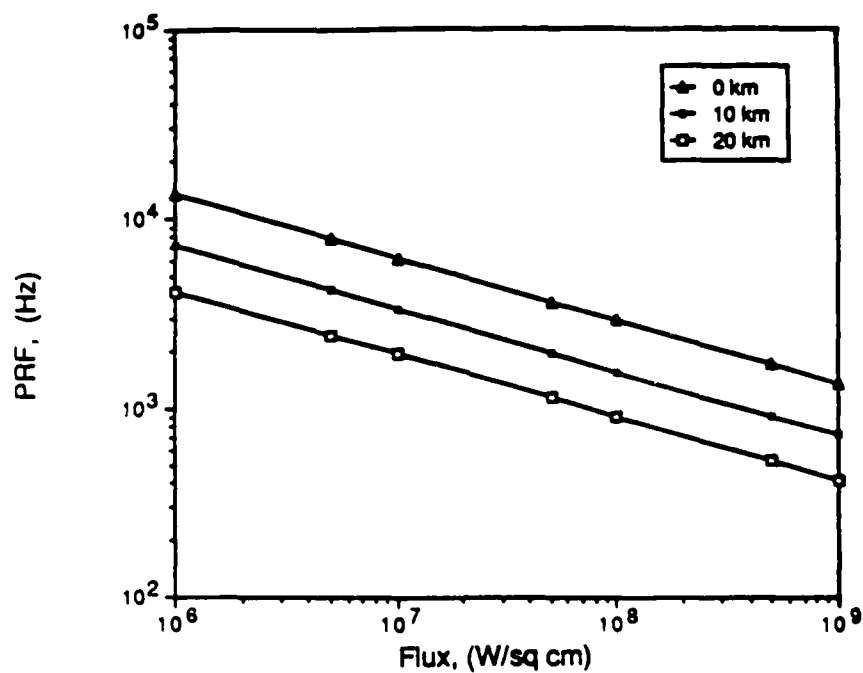


Figure IV.12 Pulse Repetition Frequency, PRF, vs. flux level

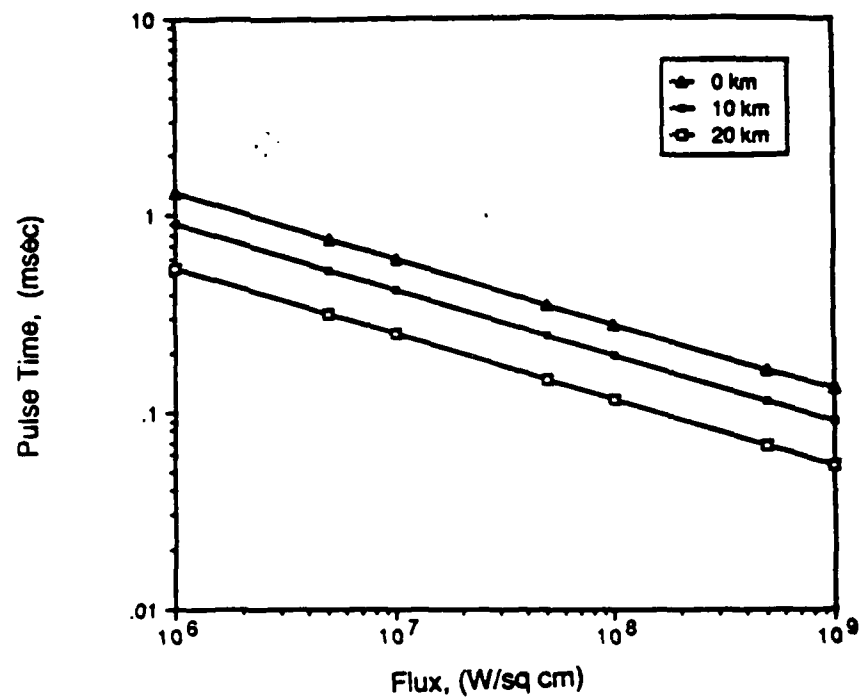


Figure IV.13 Laser pulse duration, t_p , vs. flux level

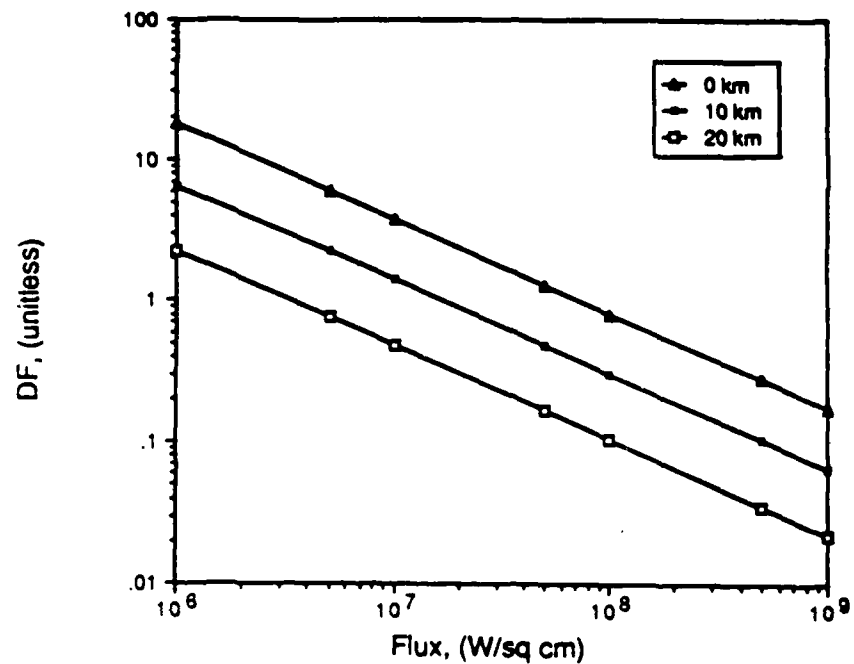


Figure IV.14 Duty factor, DF , vs lased flux

to the immediate surroundings. Jackson and Nielsen [9], and Su and Boni [26] investigated the effects of radiation for LSC waves, but a similar analysis for LSD waves has yet to be performed.

Such effects were also ignored in prior laser impulse studies (by others), with LSD waves. These researchers used the blast wave scaling laws and a polytropic equation of state to include the radiation effects.

Despite the many assumptions, earlier analyses have found good agreement with laser impulse experiments. These experiments were generally performed with 10.6 micron laser radiation (see Holmes *et al.* [8] and Ferriter *et al.* [5]). More experimental work is undoubtedly needed to verify performance projections for the line source models.

Because of the model's simplicity, further improvements in the theoretical model is also in order - to include a more complete representation of the physics. A more elaborate model which could include the breakdown process and the actual dynamics of the LSD wave propagation along the plate would be significantly better. The following chapter includes the latter in an alternate approach.

CHAPTER V

PROPAGATING LSD-WAVE ERH THRUSTER MODEL

In the previous chapter, laser energy deposition into the working fluid was assumed to be instantaneous, resulting in an infinite-length cylindrical blast wave. Actually, energy absorption follows the moving shock front and creates a propagating near-cylindrical blast wave. Here in Chapter V, ERH thruster models, which attempt to incorporate this dynamic behavior are detailed. Two models are developed, one for a hovering flight platform (subsonic velocities), the other for supersonic flight velocities. These are referred to as the "static" and "dynamic" ERH thruster models, respectively.

Both models are applied to a simple engine configuration, consisting only of a lower impulse surface, that is integrated into the lower flight platform surface. As illustrated in Fig. V-1, this thruster surface is assumed to be a circular frustum which comprises the entire aft section of the craft. Also note that an annular cowl wraps about the vehicle midsection, and that the forebody has a conical shape which acts like an external diffuser (at supersonic velocities).

To generate thrust, a series of laser-induced cylindrical blast waves are initiated adjacent to the thruster surface; as these blast waves expand, impulse is delivered to this surface. Before modeling the ERH thruster performance, it is first instructive to examine the laser-induced blast wave phenomenon which is fundamental to actual thruster operation.

A. BASIC OPERATING PRINCIPLES

When a high intensity laser beam is focused in air, a detonation wave is formed; the structure of this wave consists of a shock followed by an absorption zone. Within the absorption zone, laser energy is transferred into the fluid in the form of thermal energy, by the mechanism of inverse bremsstrahlung. This Laser-Supported Detonation (LSD) wave propagates up the laser beam at hypersonic velocities and leaves behind a high temperature, high pressure plasma zone. This, in turn, expands into the ambient air much like a blast wave generated by a conventional chemical explosion. Because LSD waves propagate toward the laser source much faster than the radial expansion of the hot plasma behind the detonation front, the resulting blast wave is cylindrical in shape (i.e., for long laser pulses).

The ERH thruster utilizing LSD blast waves has the following operation. First, several laser beams are projected parallel to the thruster surface, and focused to initiate LSD waves. As these

LSD waves propagate across the thruster plate, high pressure cylindrical blast waves are formed and subsequently expand. The portion of the blast wave in contact with the thruster surface exerts a pressure force upon the surface. This impulsive loading results in thrust. Once the Blast wave pressure decays to the local ambient level, the thruster surface must be cleared of the spent, hot plasma and replaced with ambient air before another set of LSD waves can be initiated. This exchange of the hot plasma with cool, unprocessed air is equivalent to the heat rejection portion of a conventional thermodynamic cycle. In the present analysis, this exchange process is referred to as "surface refresh".

From the above discussion, it is evident that the ERH thruster is a repetitively-pulsed engine, in which its Pulse Repetition Frequency (PRF) is governed essentially by the blast wave decay time and the thruster surface refresh time; the total cycle time is dependent on the local ambient air pressure and density. This implies that thruster performance varies with altitude and flight velocity. Before the ERH thruster performance is analyzed, the structure of the LSD wave is investigated and a static model for the ERH thruster is developed.

B. LSD BLAST WAVE ANALYSIS

A laser supported detonation (LSD) wave can be analyzed as if it were a chemical detonation; the chemical heat of reaction is replaced by the absorbed laser heat flux. Therefore, the ZND detonation wave model, developed by Zel'dovich, Von Newman, and Döring for chemical detonations, can be adapted and used to analyze the LSD wave structure. In the ZND model, chemical detonation wave structure is modeled as a one-dimensional shock front followed by a high speed deflagation; for LSD waves the deflagation is replaced by a thin absorption zone. In LSD waves there is a coupling between the fluid dynamics and the absorption kinetics. The leading shock ionizes the air thereby allowing the formation of the absorption zone, and likewise, the laser energy absorbed within this zone drives the shock. Because of this coupling, the detonation wave structure occurs only when laser intensities are above $10^6 - 10^7 \text{ W/CM}^2$ (for $10.6 \mu\text{m}$ radiation). Raizer[17], using the ZND wave structure, was able to derive the following wave velocity expression for a LSD wave propagating into quiescent gas.

$$V_D = [2(\gamma^2 - 1) \frac{Q}{\rho_0}]^{1/3} \quad (V - 1)$$

This velocity, is the rate at which the detonation front travels with respect to a stationary observer, or from laboratory coordinates.

During the derivation of Eqn. V-1, the detonation wave has been viewed from an Eulerian frame of reference. It is, however, generally easier to examine the detonation wave structure from a

Lagrangian frame. In the Lagrangian frame, the observer is assumed to be traveling on the shock front, typically referred to as shock coordinates. To convert from Eulerian coordinates to shock coordinates the following transformation is applied:

$$u = u' - V_D \quad (V - 2)$$

In Fig. V-2 the structure of the LSD wave is shown in shock coordinates. Observe that a radial rarefaction fan begins to propagate inward toward the blast wave center directly behind the absorption zone. Also note, that regions of steady pressure and expansion velocity exist ahead and behind the rarefaction fan. In an actual blast wave, the converging expansion fan is reflected at wave's centerline and forms a second rarefaction wave which propagates outward from the wave's center.

In this analysis, only the first rarefaction wave will be of interest. Once the first fan reaches the centerline, at location X' in Figure V-2, the blast wave decay is approximated using self-similar theory. Previous investigators [8,15] have successfully applied self-similar blast wave theory away from the LSD detonation front. Here, the blast wave will be analyzed in two sections: first, using the method of characteristics in the region between the absorption front and the plane where the first fan reaches the center line; and thereafter, using self-similar blast wave theory.

In this model, axial relaxation of the LSD blast wave is neglected, and radial expansion is assumed to dominate the pressure decay process. Also, the axial velocity is assumed small when viewed from the Eulerian reference frame. These assumptions permit the use of the following one-dimensional unsteady flow equations to describe the blast wave expansion:

$$\frac{\partial \rho}{\partial t} + u \frac{\partial \rho}{\partial r} + \rho \frac{\partial u}{\partial r} + \frac{\rho u}{r} = 0 \quad (V - 3a)$$

$$\rho \left(\frac{\partial u}{\partial t} + u \frac{\partial u}{\partial r} \right) + \frac{\partial P}{\partial r} = 0 \quad (V - 3b)$$

$$\frac{\partial S}{\partial t} + u \frac{\partial S}{\partial r} = 0 \quad (V - 3c)$$

For the present development, the last term of the continuity equation is dropped. Using an order of magnitude analysis, it can be shown, that the error introduced by neglecting this term is small; its removal simplifies the development of the characteristic equations. Using the method of characteristics, the above system of partial differential equations are recast into ordinary differential equations, such that the fluid properties are described along some characteristic path. Hence, the continuity and momentum equations can be combined and manipulated to give the following result:

$$u + \frac{2C}{\gamma - 1} = J^+ = \text{Const.} \quad (V - 4a)$$

$$u - \frac{2C}{\gamma - 1} = J^- = \text{Const.} \quad (V - 4b)$$

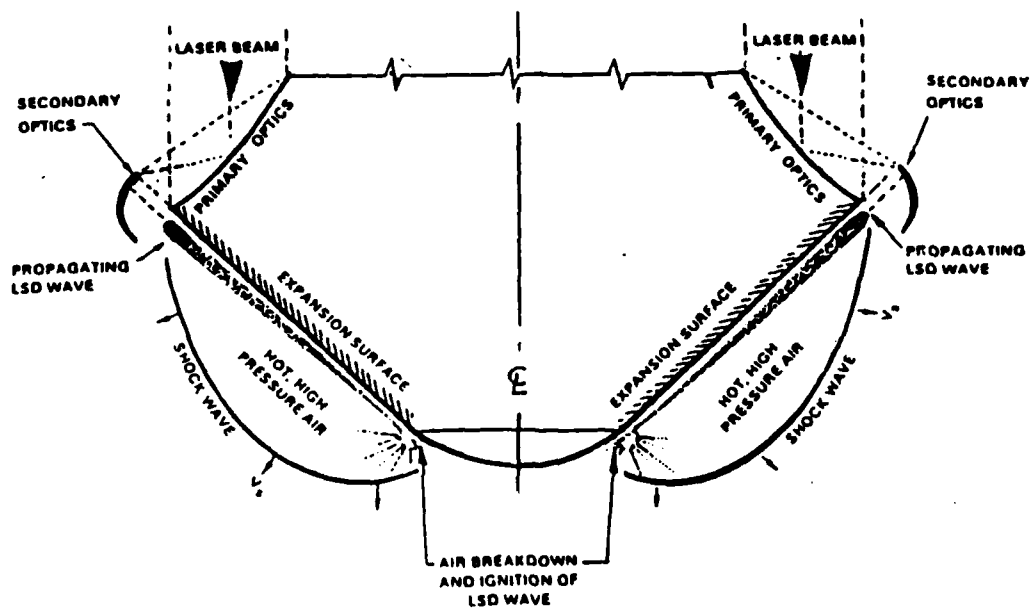


Figure V-1 ERH Thruster Engine Configuration

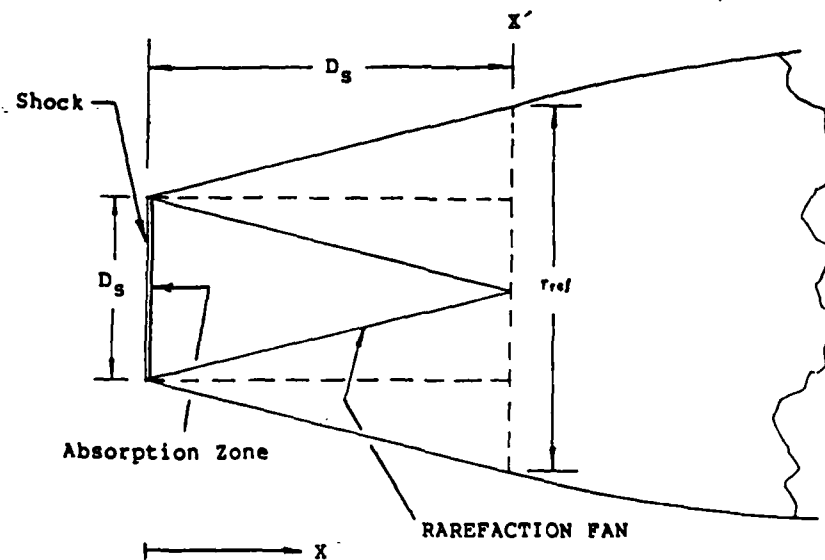


Figure V-2 LSD Wave-Lagrangian View

These equations are the well known Riemann invariants which are valid along the following paths in the length-time plane.

$$\frac{\partial r}{\partial t} = u + C; C^+ \text{ Characteristic} \quad (V - 5a)$$

$$\frac{\partial r}{\partial t} = u - C; C^- \text{ Characteristic} \quad (V - 5b)$$

The above four expressions are fundamental to the analysis of LSD blast waves near the detonation front.

As previously mentioned, the pressure decay process for the rest of the blast wave is approximated using self-similar cylindrical blast wave theory. Expressions predicting this type of wave decay are easily derived from dimensional analysis.

Assume that the column of high pressure plasma generated by a LSD wave can be approximated by a cylindrical blast wave resulting from an intense line source explosion. See Fig. V-3. The dependent variables of this blast wave expansion are velocity (U), pressure (P), and density (ρ), while the independent variables are blast wave radius (R), and time (t). The physical constants of this decay problem are the energy released during the explosion, as well as, the initial density and pressure. The dimensions of these variables are:

$$\{E\} = \frac{KM}{s^2} \quad (V - 6a)$$

$$\{r\} = M \quad (V - 6b)$$

$$\{\rho\} = \frac{K}{M^3} \quad (V - 6c)$$

$$\{t\} = s \quad (V - 6d)$$

It can be shown, that the initial pressure is not important in strong shock waves; thus, the only parameter constants are the energy released and the initial air density. The objective of dimensional analysis is to form nondimensional parameter groups. Observe that the two independent variables can be combined to form the following similarity parameter:

$$\eta_0 = \frac{r}{\left(\frac{E}{\rho_0}\right)^{1/4} t^{1/2}} = \text{Const.} \quad (V - 7)$$

Hence, r is proportional to $t^{-1/2}$. Using the strong shock assumption, following expression can be obtained:

$$P = \left(\frac{2}{\gamma + 1}\right) \rho_0 u^2 \quad (V - 8)$$

Differentiating Eqn. V-7 and substituting it into the above expression results in an expression for pressure:

$$P = \frac{1}{2} \left[\frac{\eta_0^2}{\gamma + 1} \rho_0 \left(\frac{E}{\rho_0} \right)^{1/4} \right] t^{-1} \quad (V - 9)$$

In the above equation the bracketed terms are constant and it is possible to form the following ratio:

$$\frac{P}{P_{ref}} = \left(\frac{t}{t_{ref}}\right)^{-1} \quad (V-10)$$

An additional ratio, can be derived, using Eqn. V-7:

$$\frac{r}{r_{ref}} = \left(\frac{t}{t_{ref}}\right)^{\frac{1}{2}} \quad (V-11)$$

Hence, if blast wave conditions are known for a given time, then the above expressions determine subsequent blast wave pressure decay.

To determine the fluid conditions directly behind the absorption zone, in the Chapman-Jouguet plane, the following equations developed for the ZND model can be used:

$$u_{CJ} = \frac{V_D}{\gamma + 1} \quad (V-12a)$$

$$C_{CJ} = \left(\frac{\gamma}{\gamma + 1}\right)V_D \quad (V-12b)$$

$$C_{CJ} = \gamma u_{CJ} \quad (V-12c)$$

Recall that the Chapman-Jouguet plane is located just behind the reaction zone; in the case of LSD waves it is behind the absorption zone. Chapman-Jouguet theory predicts that stable detonation waves exist only when the relative velocity of the flow in the Chapman-Jouguet plane, with respect to the wave front, is equal to the local sound speed; therefore:

$$V_D - u_{CJ} = C_{CJ} = \left[\frac{\gamma P_{CJ}}{\rho_{CJ}}\right]^{\frac{1}{2}} \quad (V-13)$$

Combining the definition of the ideal gas sound speed, the expression for polytropic expansion and Eqns. V-12c and V-13 the pressure behind the detonation is given by:

$$P_{CJ} = \frac{\rho_0 V_D^2}{\gamma + 1} = \frac{[2(\gamma^2 - 1)]^{\frac{1}{2}}}{\gamma + 1} \rho_0^{\frac{1}{2}} V_D^{\frac{3}{2}} \quad (V-14)$$

Assuming that the axial velocity is zero, the initial impulse pressure and sound speed are given by the following expressions, respectively:

$$P_1 = P_{CJ} \left(\frac{\gamma + 1}{2\gamma}\right)^{\frac{2}{\gamma - 1}} \quad (V-15)$$

$$C_1 = \frac{V_D}{2} \quad (V-16)$$

Using the above results, the Riemann invariants and the self-similar expansion expressions, it is now possible to determine the expansion of the blast wave and subsequent thrust generation. The pressure decay near the detonation front is now examined.

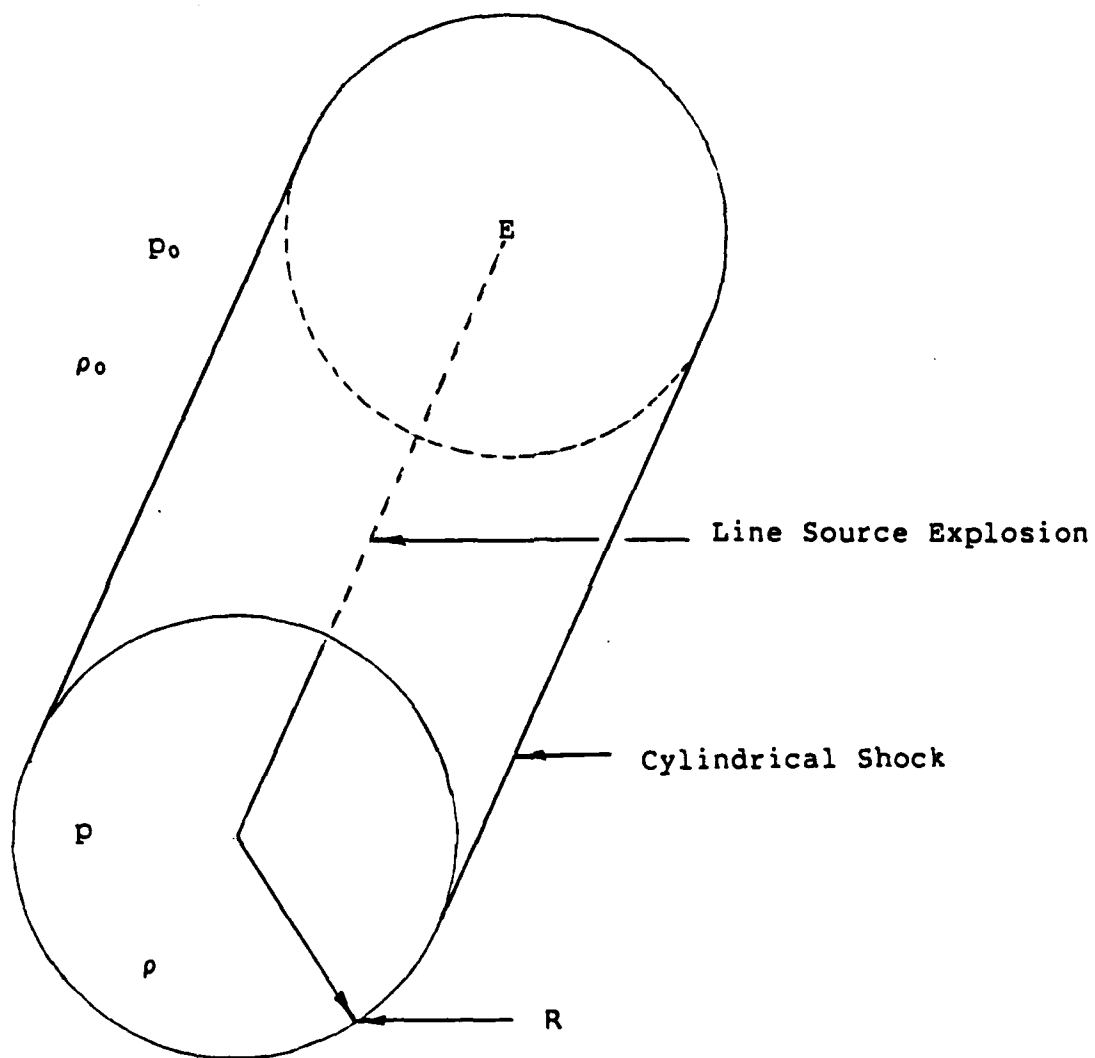


Figure V-3 Cylindrical Blast Wave Geometry

From Fig. V-4 it is seen that the first rarefaction fan is a simple backward facing wave; thus, flow conditions behind it can be calculated using the invariant along the C^+ characteristic. Because the radial velocity ahead of the expansion fan is equal to zero, the invariant is written as:

$$\frac{2}{\gamma-1}C_1 = u_2 + \frac{2}{\gamma-1}C_2 \quad (V-17)$$

Combining this with the perfect gas relations, the above equation can be written as:

$$u_2 = \frac{2}{\gamma-1}(C_1 - C_2) \quad (V-18a)$$

$$u_2 = \frac{2}{\gamma-1} \left[\left(\frac{\gamma P_1}{\rho_1} \right)^{\frac{1}{2}} - \left(\frac{\gamma P_2}{\rho_1} \right)^{\frac{1}{2}} \left(\frac{P_1}{P_2} \right)^{\frac{\gamma-1}{2\gamma}} \right] \quad (V-18b)$$

$$u_2 = \frac{2}{\gamma-1} \left(\frac{\gamma P_1}{\rho_1} \right)^{\frac{1}{2}} \left\{ 1 - \left(\frac{P_1}{P_2} \right)^{\frac{\gamma-1}{2\gamma}} \right\} \quad (V-18c)$$

This expression can then be solved numerically with the following well established shock tube result, to determine the pressure behind the rarefaction fan (P_{r1}).

$$u_2 = \left(\frac{\gamma_0 P_0}{\rho_0} \right)^{\frac{1}{2}} \left[\frac{P_2}{P_0} - 1 \right] \left[\frac{\frac{2}{\gamma_0}}{(\gamma_0 + 1) \frac{P_2}{P_0} + (\gamma_0 - 1)} \right]^{\frac{1}{2}} \quad (V-19)$$

Substituting this result into equation 18c, the particle velocity behind the refraction fan can be determined. Knowing the particle velocity, it is now possible to find the location of the radial shock front. At X' , the radius of the blast wave is defined as R_{ref} . This reference radius is used to start the self-similar analysis.

C. STATIC THRUST MODEL

The impulse loading on the thruster surface due to an expanding cylindrical plasma blast wave, is given by the integral relation:

$$I = \int \int P dA dt \quad (V-20)$$

Using the above expression, the impulse delivered to the thruster plate can now be found.

To determine the impulse contribution of Region 1 (see Fig V-2) note that its geometry remains fixed as the LSD wave propagates over the thruster surface. The location of X' can be determined by integrating Eqn. V-5b, solving for the integration constant and multiplying the result by V_D .

$$X' = 2R_0 \quad (V-21)$$

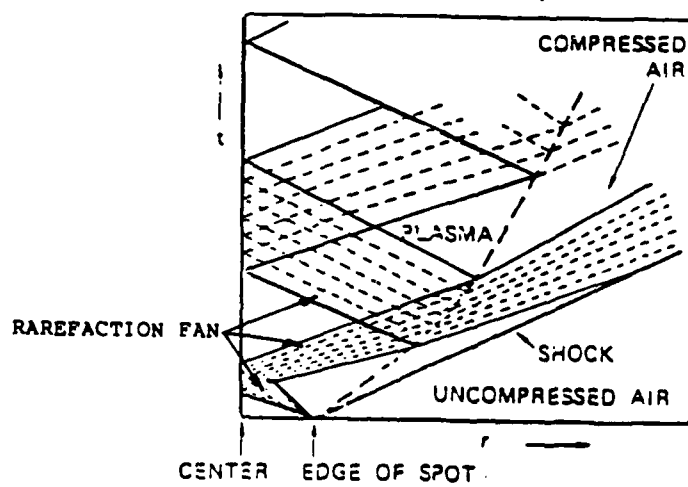
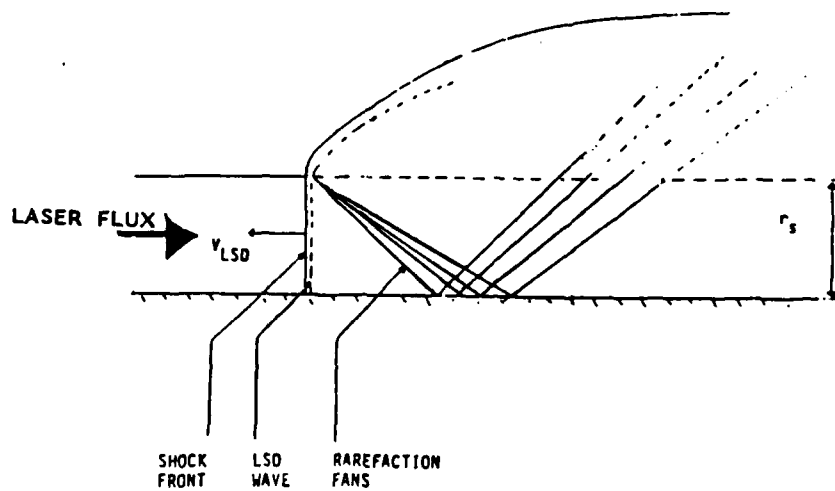


Figure V-4 LSD/Blast Wave Expansion (from Ref. 8)

Therefore the impulse contribution of this region is simply:

$$I_1 = 2r_o(r_o P_1 + r_{ref} P_2)t \quad (V - 22)$$

where the t is equal to the time necessary for the detonation front to propagate across the thruster surface. Since the laser pulse is terminated when the detonation front reaches the end of the thruster plate, t is equal to the laser pulse duration time t_p .

The impulse contribution for the region $X > X'$ in Fig. V-2, can be determined from Eqs. 10, 11 and 20, which are combined to give:

$$I_2 = r_{ref} P_{ref} \Delta x_i \int_{t_{ref}}^{t_0} \left(\frac{t}{t_{ref}}\right)^{-\frac{1}{2}} dt = 2r_{ref} P_{ref} t_{ref} \left[\left(\frac{t_0}{t_{ref}}\right)^{\frac{1}{2}} - 1\right] \Delta x_i \quad (V - 23)$$

where t_0 is the time necessary for the blast wave to decay to the local ambient pressure, and t_{ref} is the time required for the first rarefaction fan to reach the blast wave center. To account for varying flow properties along the plug nozzle, the impulse in the radial expansions regime is numerically integrated over the thruster surface, using a given step size of delta x . Thus, the total impulse generated by the LSD wave is the sum of the contributions from the two expansion regimes, as given below:

$$I_{TOTAL} = I_1 + \sum_{i=1}^N I_i \quad (V - 24)$$

Note that the impulse force acts along the thruster's surface normal. For the ERH thruster engine configuration examined, all of the impulse loading predicted by the above expression does not contribute to engine thrust; only the impulse vector component aligned with the vehicle flight direction. Thus, magnitude of the impulse component resulting in upward thrust is:

$$I_{USABLE} = I_{TOTAL} \cos \alpha \quad (V - 25)$$

where α is the base angle of the truncated conical plug.

In trajectory calculations is convenient to use time averaged thrust. This mean thrust is defined as:

$$T = \frac{1}{t_{CYCLE}} \int_t^{t+t_{CYCLE}} I dt = \frac{I_{TOTAL}}{t_{CYCLE}} \quad (V - 26)$$

where I is the impulse delivered per laser pulse, and T_{CYCLE} is the blast wave period. The blast wave period is simply the total expansion time of the LSD blast wave, plus the refresh time; as given by:

$$t_{CYCLE} = \frac{1}{PRF} = t_0 + t_{REFRESH} \quad (V - 27)$$

The refresh time is the time necessary for the hot expanded gas to clear the thruster surface and be replaced by the ambient air. Currently, an adequate model for the refresh process does not exist and in this analysis the refresh time is set equal to zero.

Input energy per laser pulse is evaluated as follows:

$$E_P = \frac{\pi R_L^2}{2} \phi t_p \quad (V - 28)$$

In the derivation of this equation it is assumed that the laser beam has a semicircular shape and uniform intensity. Recall that the laser energy is absorbed in a thin region behind the detonation front. Thus, t_p is the time required for this LSD wave to transverse the ERH thruster plate. To convert the pulse energy to time average laser power the following equation is used:

$$P_{AVE} = \frac{E_P}{t_{CYCLE}} \quad (V - 29)$$

Finally, an important measure of thruster efficiency is the coupling coefficient, which is the ratio of usable single-pulse impulse to laser input energy per pulse. Therefore, the coupling coefficient is defined by:

$$CC = \frac{I_{USABLE}}{E_P} = \frac{T}{P_{AVE}} \quad (V - 30)$$

D. DYNAMIC THRUSTER MODEL

The above analytical model does not consider the effects of flight platform velocity on ERH thruster performance. This model is sufficient for static and low subsonic flight velocities, but when flight velocities are supersonic, ram drag, compressibility effects and flow expansion over the aft plug nozzle (the thruster surface) become important. For an airbreathing engine net thrust is the force resulting from the addition of all pressure and viscous forces, excluding the external drag forces; that is, gross thrust minus ram drag. Note external drag forces caused by the "installed" engine are typically included with vehicle drag. As a result, it was necessary to develop a dynamic model for ERH thruster performance.

In supersonic flight, an attached oblique shock forms at the conical spike tip. The air is compressed after passing through this oblique shock, and it is turned to flow tangent to the forebody surface; the entire forebody of the flight platform is essentially an isentropic spike inlet. The annular cowl, which circumscribes the craft's midsection, then redirects the flow parallel to the thruster surface. In the ERH thruster operation, the cowl only turns the flow, and does not decelerate or accelerate it. Additionally, the cowl is assumed to have a sufficiently large capture area such that no spillage occurs beyond the design mach number of three. With these cowl characteristics, no normal shock forms at the cowl entrance and the exit mach number is equal to that at the cowl entrance. Upon leaving the cowl, the ducted air expands along the thruster surface as if it were emerging from a free expansion type plug nozzle.

Therefore the only stagnation significant pressure loss occurs as the air passes through the oblique shock. To calculate such losses, an experimentally determined pressure recovery inlet schedule developed by Marquardt[29] for the XRJ59-MA-3 inlet was used. In the present analysis, it is also assumed that the air flow through the cowl remains undisturbed by the LSD wave propagation and subsequent blast wave expansion. Such an assumption appears to be justified, when the maximum expansion of the blast wave is small compared to cross sectional flow area of the cowl.

In supersonic flight, pressure variations along the thruster surface become pronounced and must be considered when calculating the LSD blast wave expansion. When calculating this pressure variation, it is assumed that the compressed air flow leaving the cowl expands as shown in Fig. V-5. To calculate the pressure for a given thruster surface location (s) it is necessary to determine the local cross sectional area of the expanding gases.

Typically, for a non-truncated plug nozzle, the pressure at the end of the plug is always equal to P_0 , the ambient pressure. Using this condition and assuming isentropic flow over the plug the following expression can be solved for the mach number at the plug end (M_e).

$$\frac{P_{T_{oe}}}{P_0} = (1 + \frac{\gamma-1}{2} M_e^2)^{\frac{\gamma}{\gamma-1}} \quad (V-31)$$

where $P_{T_{oe}}$ denotes the stagnation pressure at the cowl exit. As previously mentioned this is determined using the Marquardt inlet data. Once M_e is known, the cross-sectional flow area, A_e , can be obtained using:

$$\frac{A_{oe}}{A_e} = \frac{M_e}{M_{oe}} \left[\frac{2 + (\gamma-1)M_{oe}^2}{2 + (\gamma-1)M_e^2} \right]^{\frac{\gamma+1}{2(\gamma-1)}} \quad (V-32)$$

where A_{oe} and M_{oe} are the cross-sectional flow area and the mach number at the cowl exit respectively.

From the nozzle's geometry:

$$R_e = \sqrt{\frac{A_e}{\pi}} \quad (V-33)$$

If the cross-sectional flow area is assumed to vary linearly along the thruster surface, then:

$$A = \pi [R_e^2 - (\frac{s}{\cos \alpha})] \quad (V-34)$$

In this equation, α is the plug base angle and s denotes an arbitrary position along the plug surface. For a given s, the corresponding mach number can be found implicitly using:

$$M(s) = \frac{A_e M_e}{A(s)} \left[\frac{2 + \frac{\gamma-1}{2} M_e^2}{1 + \frac{\gamma-1}{2} M(s)^2} \right]^{\frac{\gamma+1}{2(\gamma-1)}} \quad (V-35)$$

Now the local expansion pressure can be calculated from:

$$P(s) = \frac{P_{T_{oe}}}{(1 + \frac{\gamma-1}{2} M(s)^2)^{\frac{\gamma}{\gamma-1}}} \quad (V-36)$$

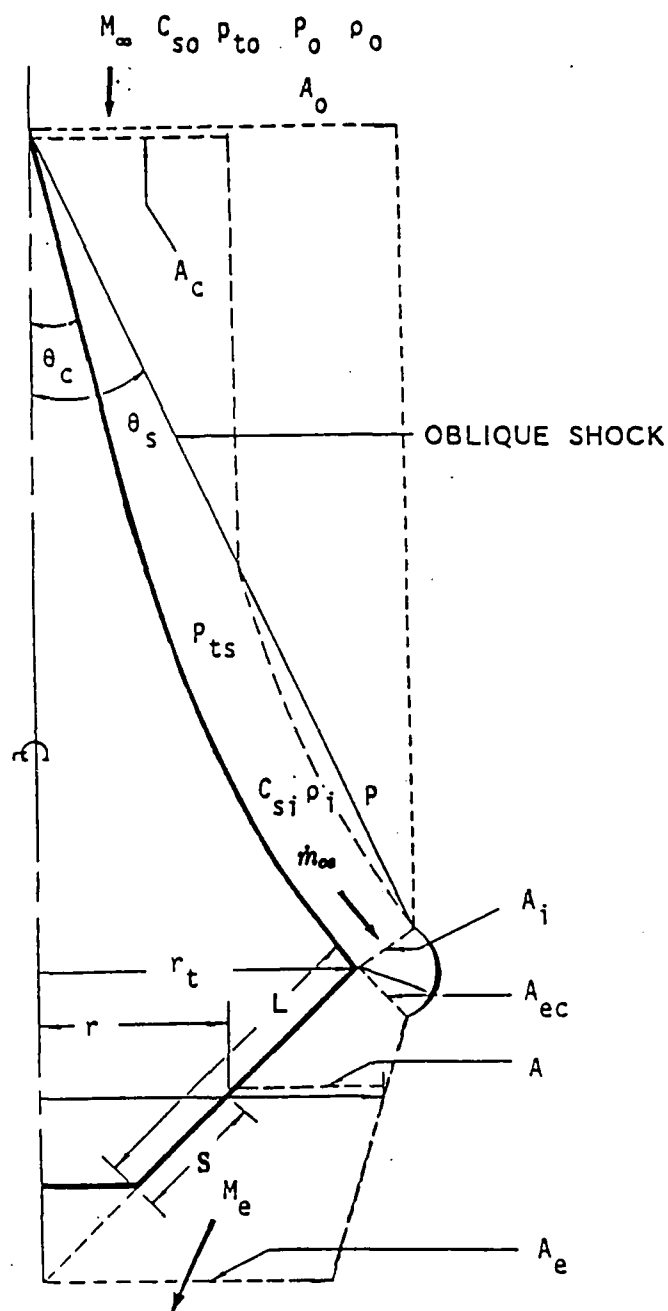


Figure V-5 Supersonic Air Expansion Over Thruster Plate

In the dynamic model, the LSD blast waves must expand to this pressure.

To calculate the net thrust, a control volume is constructed as shown in Fig. V-6. By choosing the control volume boundary adjacent to ERH thruster surface, the complex flow conditions due to the interaction between the blast wave expansion and the air flow directed by the cowl can be neglected; this simplifies the drag analysis.

Recall that in the development of the LSD blast wave model, the ambient pressure was already subtracted from the integrated impulse, hence it is necessary only to consider the pressure difference across the cowl. The verticle force due to this pressure difference is given by:

$$\text{Pressure Drag} = (P_0 - P_{\infty})A_{\text{cs}} \sin \alpha \quad (V - 37)$$

Note that there is a force due to the momentum change of the incoming air flow is redirected to convect over the thruster surface. This force is calculated using the following expression:

$$\text{Cowl Drag} = \dot{m}_{\text{cs}} V_{\infty} \sin \alpha \quad (V - 38)$$

Therefore the net thrust is given by:

$$T_{\text{net}} = T - \text{Pressure Drag} - \text{Cowl Drag} \quad (V - 39)$$

E. RESULTS

Performance maps for the ERH thruster engine were generated by incorporating the preceding static and dynamic models into a comprehensive computer simulation. Using this computer model, the effects of flight mach number and altitude on net engine thrust, as well as several other performance parameters was investigated.

As previously mentioned, the reference ERH thruster surface configuration, is a truncated conical plug which comprises the entire aft section of the vehicle. This plug has a semi-vertex angle of 45 degrees, and numerous LSD waves are ignited, equally spaced, around the circumference of the plug. The exact number of LSD waves which were studied ranged from 12 to 48. In each case, the laser spot diameter was varied, such that the peak laser power supplied to the ERH thruster remained constant. For this analysis, the beam intensity used to initiate the LSD waves was held constant at $5 \times 10^8 \text{ W/cm}^2$, over the semi-circular spot of 0.5 cm or 1.0 cm for the 48 and 12 line systems, respectively.

Before time average performance parameters can be calculated, it is first necessary to determine the total thruster cycle time. Because the refresh time has been neglected, the total cycle time

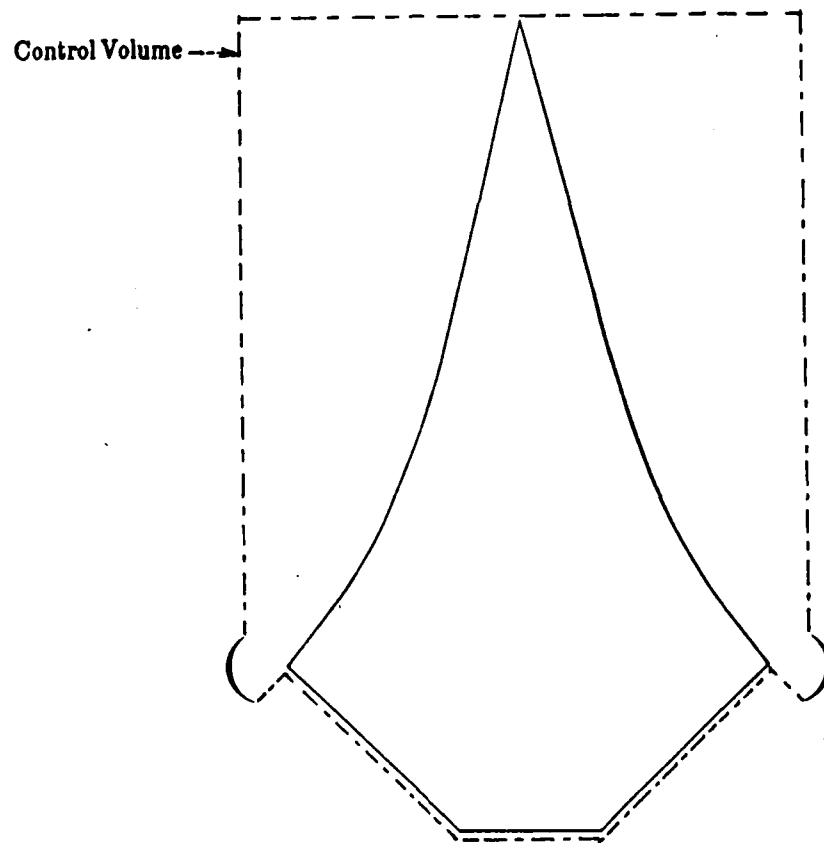


Figure V-6 Dynamic Model Control Volume

is determined by the maximum expansion time; i.e., the time necessary for the entire blast wave to expand to ambient pressure. At low flight velocities, the local pressure over the conical nozzle (the thruster surface) is roughly uniform, and the blast wave expansion time remains constant over the entire thruster area. For supersonic flight velocities, however, high pressure air is convected from the cowl across the thruster surface. Therefore, the local ambient pressure at the base of the conical thruster surface is greater than that at its truncated tip. If the difference in the blast wave expansion times between the base and tip of the conical plug is greater than the transit time of the LSD wave front (this is always the case), the max expansion time is expected to occur at the lower thruster/nozzle end (where the LSD waves are initiated). Fig. V-7 shows the max expansion time and expansion radius for a thruster at an altitude of 10km and a flight mach number of 3. Notice that the max expansion time occurs near the lower end of the plug nozzle.

In Fig. V-8 net thrust variation is presented as a function of flight mach number and altitude for the 48 beam ERH thruster configuration. Recall that net thrust is the time-averaged thrust minus ram drag. For a given altitude, observe that thrust drops off at some critical mach number. This is due, in part, to the increased ram drag experienced by the ERH thruster engine at higher mach numbers.

Fig. V-8 also shows that mean thrust decreases with increasing altitude. This result is not unexpected since at higher altitudes atmospheric pressure and density decrease. The ERH thruster, like other airbreathing engines, relies on momentum transfer of incoming ambient air to generate thrust; therefore, as the density decreases, so does engine thrust.

Another factor which causes a reduction in net thrust, for this ERH engine configuration, is illustrated in Fig V-9: the maximum pulse repetition frequency (PRF). Note that PRF decreases with increasing altitude. During ERH thruster operation, LSD blast wave pressure must expand to local ambient levels before the thruster surface can be refreshed and new LSD waves initiated. At higher altitudes, the local static pressure is lower, so the blast wave expansion time (t_0) is generally longer. Since the high internal pressure of the plasma blast wave decreases rapidly as the wave expands, most of the engine thrust is generated during the initial blast wave decay. Therefore, an increase in the LSD blast wave expansion time (t_0) does not greatly increase impulse delivery to the thruster plate, and time-averaged thrust must decrease.

Closely related to the PRF is the time-averaged laser power; its variation with altitude and flight mach number can be seen in Fig. V-10. Also, in Fig. V-11, the predicted coupling coefficient (cc) performance is plotted, with the dotted line indicating the theoretical limit for airbreathing engines. Since the calculated coefficients at high altitudes (e.g., 30km) so closely approach the theoretical limit, it is suspected that this first order analysis of ERH engine performance may be

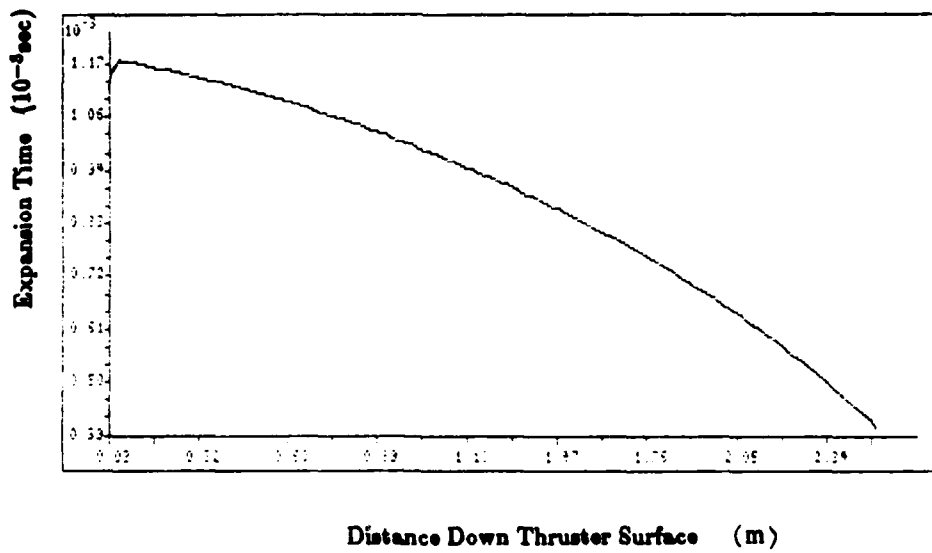
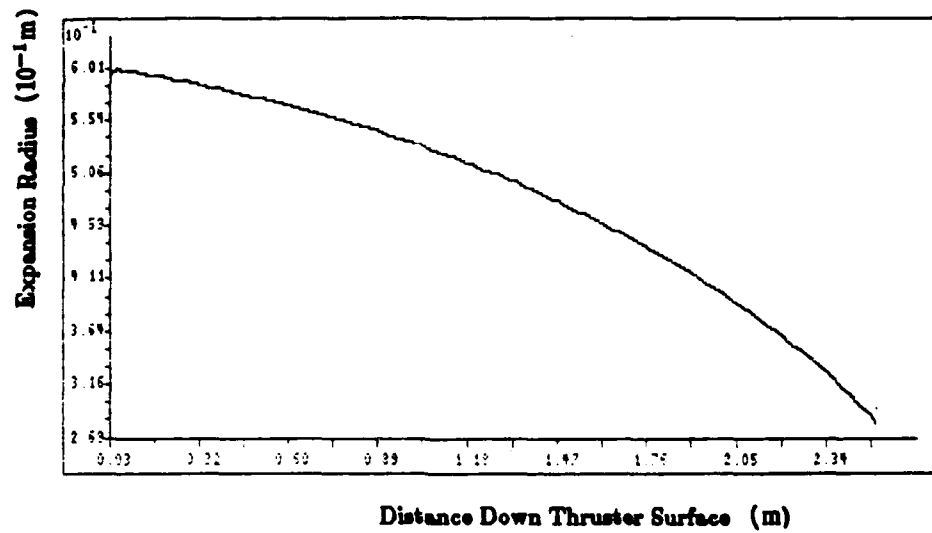


Figure V-7 Max Expansion Time-10km, Mach 3

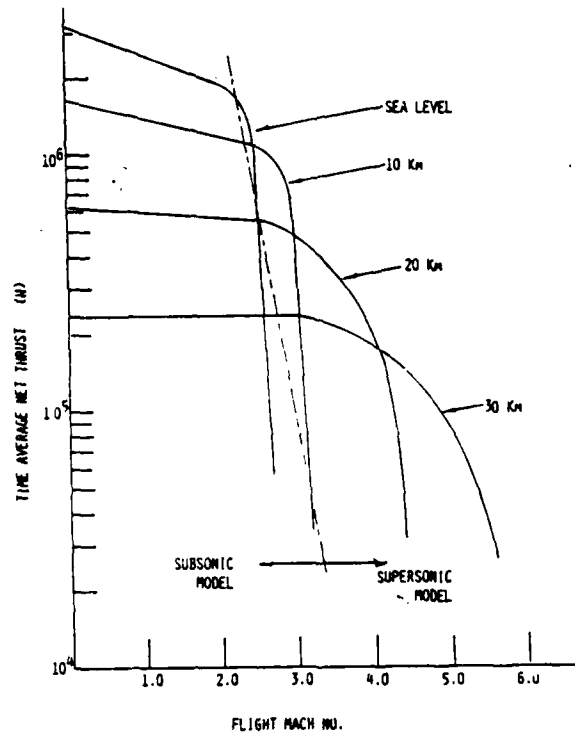


Figure V-8 Time Average Thrust-48 Beams

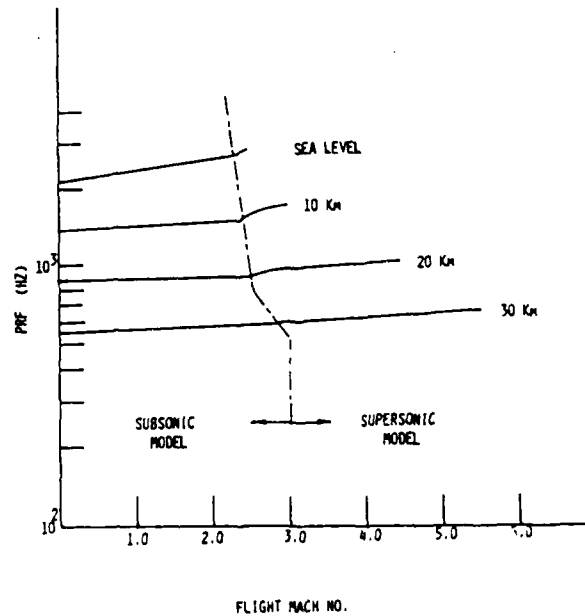


Figure V-9 PRF-48 Beams

overly optimistic.

The performance maps presented heretofore are for the 48 beam ERH thruster configuration. Comparison of these with those for a 12 beam thruster configuration (Figs. V-12, 13, 14 and 15) shows that for a given operating condition, the 48 beam configuration gives better thrust and its PRF is greater. Therefore, while the laser energy per pulse is the same in both configurations, the time-averaged power for the 12 beam configuration is less. Higher time-average power produces increased thrust for the 48 beam ERH thruster. Although, time-averaged thrust increases with number of beams for this engine concept, there obviously is a limit to the minimum beam diameter, e.g., as set by optical parameters. This trend should not be generalized to all ERH thruster configurations at this point. Each thruster configuration should be analyzed as a separate entity.

E. Future Extensions

There are a number of reasons for the high values of predicted performance for the ERH thruster. In the current model, as mentioned above, the refresh time (t_{refresh}) is set to zero. In an actual engine, t_{refresh} would have some finite value, which would cause a decrease in the PRF and hence, the time averaged thrust. A second model simplification, which probably contributes to producing optimistic results, is the omission of axial rarefaction waves within the LSD blast wave simulation. Inclusion of axial expansion effects in this blast wave model, would result in a reduction in the impulse delivery to the thruster surface. At the present time, the combined effects of these simplifications on ERH thruster performance have yet to be quantified. Future development of these ERH thruster models should address the above deficiencies.

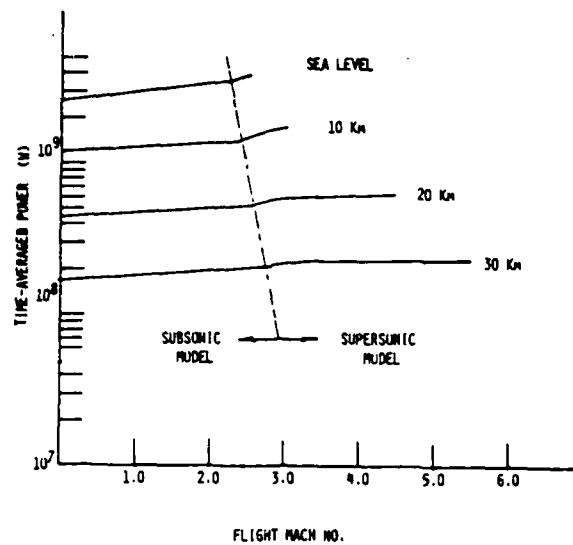


Figure V-10 Time Average Power-48 beams

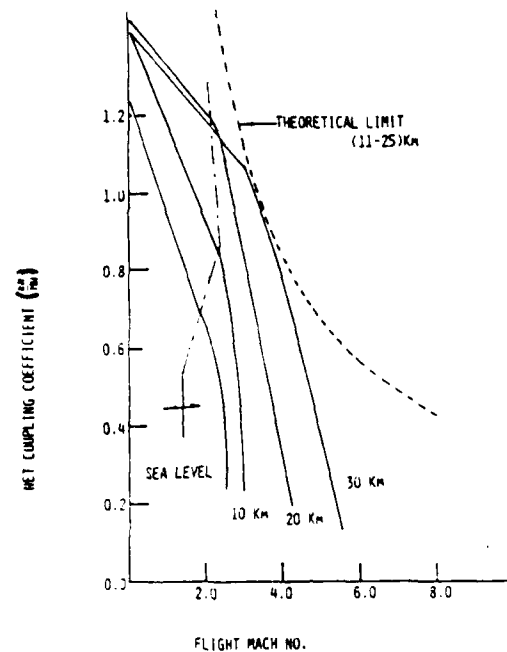


Figure V-11 Coupling Coefficient-48 Beams

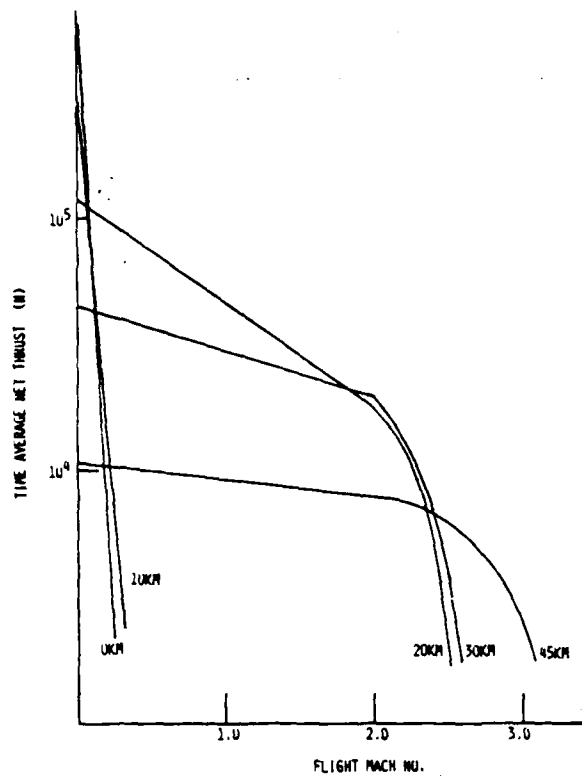


Figure V-12 Time Average Thrust-13 Beams

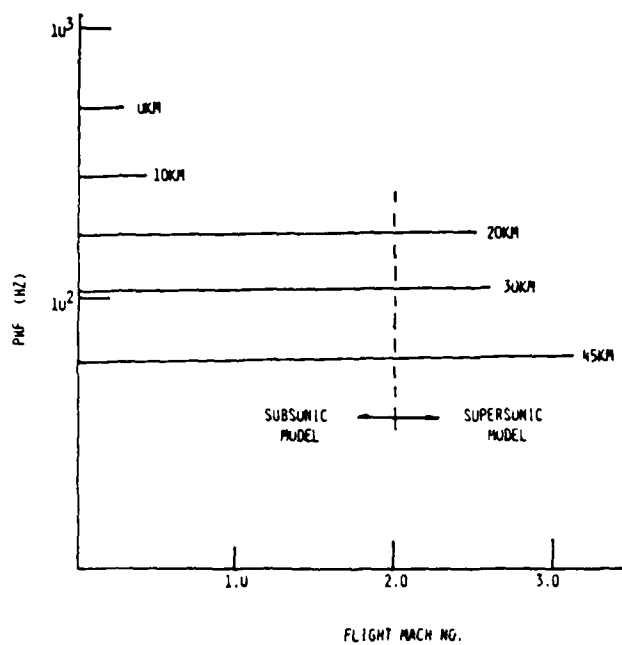


Figure V-13 PRF-13 Beams

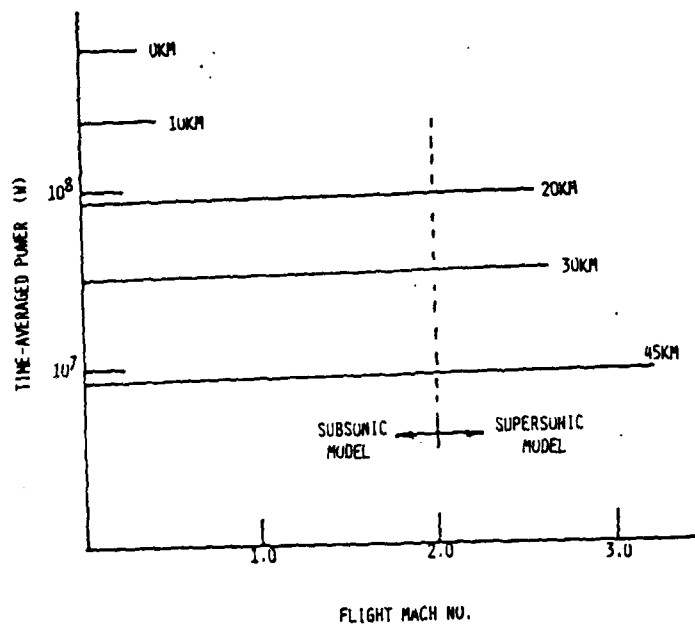


Figure V-14 Time Average Power-12 beams

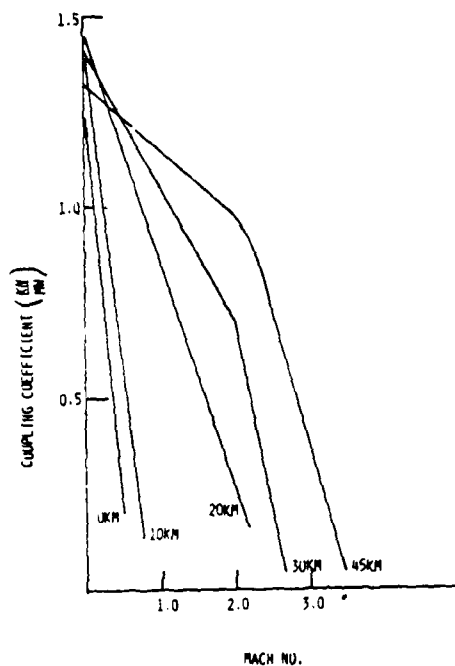


Figure V-15 Coupling Coefficient-12 Beams

CHAPTER VI

LSC WAVE ERH THRUSTER MODEL (STATIC)

A pulsed LSC wave, specific to ERH thruster impulse generation, is characterized by high plasma temperatures $O(11000\text{ K})$ and moderate pressures (according to the intensity), and low to moderate propagation velocities. The high pressures are somewhat un-characteristic of the usual combustion process. The term Laser Supported Detonation (LSD) wave is used because it has the characteristic high pressures of the upper end of a pressure vs. specific volume (inverse of density) plot known as a Chapman-Jouguet (CJ) diagram based on their combustion theory (e.g., see Holmes et al.)[8].

This point is an upper C-J point, the term LSC implies a lower pressure, weaker wave, i.e., a deflagration wave which it really isn't. C-J theory assumes instantaneous energy deposition, not continuous to some finite pulse time which known LSC wave theories assume. These may be why some prefer the term Laser Sustained Plasma (LSP) instead of LSD or LSC.

An LSC wave exists between laser intensities of about 2.5×10^4 to $7 \times 10^6\text{ W/cm}^2$ at a wavelength of 10.6 microns. The low end of this range represents the threshold for air plasma generation with a laser wavelength of 10.6 microns, whereas the upper limit is the transition region between LSC and LSD wave propagation for that same wavelength. The lower intensity required for LSC wave generation makes it more attractive than the LSD wave from the standpoint of reduced noise during hover and VTOL operations.

The basic elements of an LSC wave are a hot plasma zone, the moving rarefaction fans produced in the plasma zone, and the shock outside of the plasma (Fig. VI-1). The physics of LSC are not as well understood as that of LSD. An attempt was made to use Sedov's blast wave scaling laws to model the time history of the LSC wave pressure and physical dimensions (e.g. plasma zone radius) in predicting its effectiveness for low-altitude ERH thruster propulsion. Sedov's theory is also meant for instantaneous energy deposition. It has been used in a modified form to include some cases of linear energy deposition (with time) which is the form used for a wave powered by a laser, while its original form is used when the laser pulse has ended (i.e., unpowered).

An LSC wave, being a laser generated and sustained plasma, should supposedly be optically thin so that the laser radiation diffuses throughout the plasma for its initiation, growth and support by the laser energy. It has yet to be verified, however.

A. Description of the Model

In the first instant of the process, laser light is focused at the center of the craft's lower surface, forming a cylindrical plasma zone which is assumed to expand radially at a velocity, V_{LSC} , given by the following expression:

$$V_{LSD} = (W + 1) \left[\frac{2(\gamma - 1)(\gamma_0 - D\Phi)}{(\gamma_0 + 1)(\gamma + W)(\gamma_0 - 1 - 2W)} \right]^{\frac{1}{2}} \quad (VI - 1)$$

where γ and γ_0 are the ratios of specific heats in the plasma and the ambient air respectively, Φ is the received laser intensity (assumed 85air, and W is the percentage difference between the wave velocity above and the particle velocity through the LSC wave. Pirri et. al. give 0.04 as a good value for W . $\gamma_0 = 1.4$ and $\gamma = 1.2$ are taken for these respective parameters. The average radius of the cylinder may be approximated by multiplying this velocity by the time:

$$R = V_{LSC}t \quad (VI - 2)$$

During this phase, the impulse delivered to the craft is due to the pressure inside of the plasma zone. The initial plasma zone pressure is given by:

$$p_{LSC} = \left[1 - \frac{2W}{\gamma_0 - 1} \right] \left[\frac{\gamma_0 + 1}{2} \rho_0 \right]^{\frac{1}{2}} \left[\frac{(\gamma - 1)(\gamma_0 - 1)\Phi}{(\gamma + W)(\gamma_0 - 1 - 2W)} \right]^{\frac{1}{2}} \quad (VI - 3)$$

This LSC pressure equation was first derived by Pirri et al.[15] and has been assumed for this analysis. However, it was derived for the case of a laser beam perpendicularly incident to a surface, not transversely. This equation (plotted in Fig. VI-2), gives rather large values of the pressure at the higher intensities which as previously stated may be the nature of an LSC wave and/or possibly indicative of the transition to an LSD wave or because of the different boundary conditions.

As the transition occurs, the value of W should increase to that for an LSD wave, according to Pirri et al.. These LSC/LSD transition effects are not considered in this analysis. However, higher intensity calculations have been made, despite this, to observe the effect.

This LSC pressure is the reference pressure used initially in the appropriate scaling law for the changes in the internal plasma pressure in this analysis. Once the LSC wave is initiated, a rarefaction fan travels from the top of the plasma zone to the surface of the craft at the plasma sound speed given by:

$$c_s = \left(\frac{\gamma p_{LSC}}{\rho_0} \right)^{\frac{1}{2}} \left[\left(\frac{W + 1}{W} \right) \left(\frac{\gamma_0 - 1}{\gamma_0 + 1} \right) \right]^{\frac{1}{2}} \quad (VI - 4)$$

Once the rarefaction fan has reached the surface, the pressure inside of the plasma zone begins to decrease rapidly even with the laser on. It was concluded that the best usage of laser power would result by setting the laser pulse time, t_p , equal to the plasma zone height divided by plasma sound speed. Hence:

Note: $6\text{ cm} \leq H \leq 50\text{ cm}$

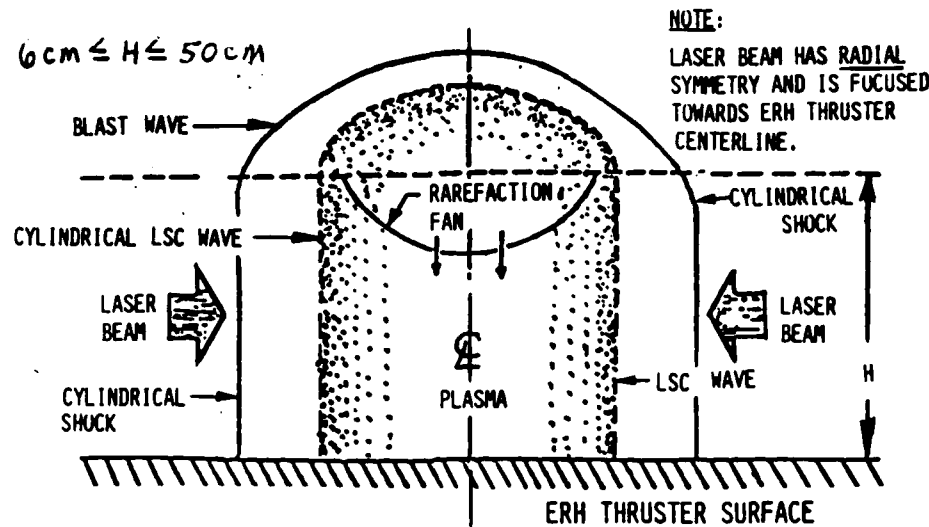


Figure VI-1 Sketch of LSC wave structure

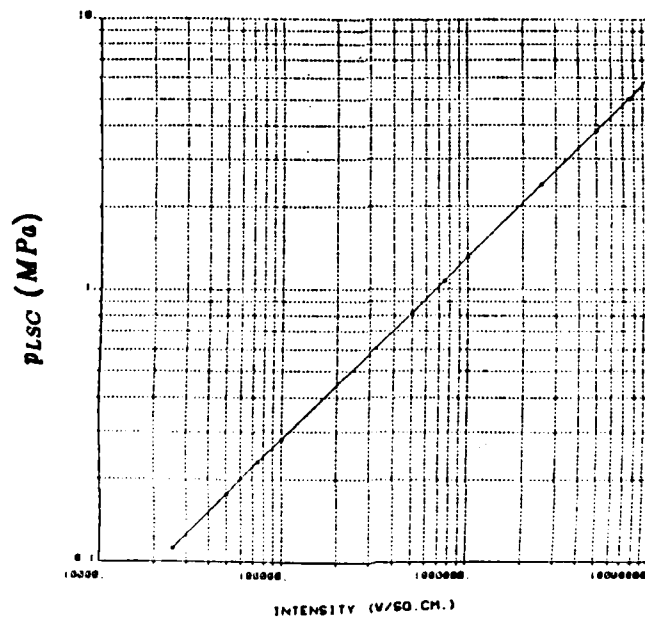


Figure VI-2 Surface pressure due to LSC wave, p_{LSD} , vs. intensity

$$t_p = \frac{H}{c_s} \quad (IV - 5)$$

This would increase the laser pulse repetition rate and improve the propulsion system's coupling coefficient (i.e. thrust per input power).

The cases studied utilized cylinder heights of 6, 12.5, 25, 50, and 100 cm. The air inside of the cylindrical plasma zone can reach temperatures in excess of 15,000 K, well beyond the temperature limit of any known materials. Because of the short pulse duration, it was assumed that the surface (either by active or passive cooling) can maintain its structural integrity throughout all operational modes. The following section describes the various scaling laws used and the physical significance of each one.

During the pulse time, the pressure inside of the plasma zone is constantly changing with time due to the rarefaction wave and the plasma zone's radial expansion. The scaling laws as presented by Sedov were used to account for this behavior. Because of the actual physical geometry of the plasma region, the unpowered cylindrical scaling law was used with all reference parameters taken at the end of the pulse duration (i.e., $t_{ref} = t_p$, $p_{ref} = p_{LSC}$). This is given by:

$$\frac{p}{p_{ref}} = \left(\frac{t}{t_{ref}} \right)^{-\frac{1}{2}} \quad (VI - 6)$$

Thus, once the rarefaction wave reaches the surface and the laser beam is shut off. The plasma zone then decays in a manner described by the following relationship:

$$\frac{R}{R_{ref}} = \left(\frac{t}{t_{ref}} \right)^{\frac{1}{2}} \quad (VI - 7)$$

Two conditions were examined. The first condition assumed that the plasma zone would continue to expand in a manner which could still be modeled with the unpowered cylindrical scaling. The expansion occurs to ambient pressure with the reference radius smaller than the plasma zone height.

In the second condition, the plasma zone needs to further expand even when its radial dimension is equal to its height. Because of the physical geometry involved (fig. VI-1), unpowered cylindrical scaling would not be an appropriate scaling law. The additional expansion is described by the unpowered spherical scaling law.

$$\frac{p}{p_{ref}} = \left(\frac{t}{t_{ref}} \right)^{-\frac{1}{2}}; \quad \frac{R}{R_{ref}} = \left(\frac{t}{t_{ref}} \right)^{\frac{1}{3}} \quad (VI - 8)$$

Full expansion to ambient is described with this law. Once the plasma zone has expanded to ambient (by either condition), air is assumed to refresh the lower surface at about perhaps the

craft speed. Once new air is in place, the cycle is ready to begin again.

A computer program was written to model the proposed cycle. Laser intensity and zone height are entered into the computer: velocities, pressures and time scales are all computed. Ambient data were all taken for sea level conditions. The program checks whether condition one or condition two will prevail and run through the appropriate scaling laws. Reference values are also generated by the computer program. The program calculates the total impulse delivered to the craft by the equation:

$$I = \int_0^{t_0} \int_{A(t)} [p(t) - p_0] dA dt \quad (VI-9)$$

where t_0 is the time it takes for the pressure to decay to the ambient value p_0 . t_0 and R_{max} are calculated by the scaling laws. The program calculates impulse by dividing the integral into domains of separate scaling laws and then adds these domains to obtain the total impulse.

The impulse for each phase (or domain) and each condition is then:

unpowered cylindrical:

$$I = \pi (V_{LSC} t_p)^2 [P_{LSC} (t_r - t_p) - \frac{1}{2} \frac{p_0 (t_R^2 - t_p^2)}{t_p}] \quad (VI-10)$$

or unpowered spherical:

$$I = \frac{5}{3} \pi R_R^2 p_R t_R^{\frac{1}{2}} (t_0^{\frac{3}{2}} - t_R^{\frac{3}{2}}) - \frac{5}{9} p_0 t_R^{-\frac{1}{2}} (t_0^{\frac{3}{2}} - t_R^{\frac{3}{2}}) \quad (VI-11)$$

$$\text{where: } R_R = V_{LSC} t_p \left(\frac{t_R}{t_p} \right)^{\frac{1}{2}}$$

$$p_R = p_{LSC} \left(\frac{t_R}{t_p} \right)^{-\frac{1}{2}}$$

$$t_0 = \left(\frac{p_0}{p_R} \right)^{-\frac{1}{2}} t_R$$

$$t_R = \left(\frac{H}{V_{LSC} t_p} \right)^2 t_p$$

The total cycle period is equal to t_0 plus the refresh time if any significant refresh time exists. This period is used to get the maximum repetition rate of the laser pulse:

$$PRF = \frac{1}{t_0} \quad (VI-12)$$

Then the mean thrust may be calculated by:

$$T = I \times PRF \quad (VI-13)$$

Time-averaged power is calculated by multiplying the incident laser intensity by the average pulsed-time LSC wave surface area.

$$P = 2\pi R(t_0)\Phi \quad (VI-14)$$

The pulse energy is calculated as:

$$E_p = 2\pi \int_0^{t_p} \Phi V_{LSC} t H dt = \pi V_{LSC} t_p^2 H \Phi \quad (VI-15)$$

The coupling coefficient is calculated in the usual manner by dividing the impulse by this energy.

$$\alpha = \frac{I}{E_p} \quad (VI-16)$$

B. Analytical Results

The results obtained from the LSC wave computer model are illustrated in Figures VI-3 through VI-10. Figure VI-3 plots mean-thrust versus intensity, with 5 curves corresponding to 5 different plasma zone cylinder heights. The mean thrust increases with the height and the intensity. As might be expected, a larger plasma zone height means that the larger amount of energy being deposited into the thruster is thus producing a larger thrust.

As shown in Figure VI-4, the PRF decreases with increasing intensity at a given plasma zone height. At a given intensity, the PRF decreases with increasing plasma zone height, since the time required for the rarefaction wave to traverse from top to bottom is longer, and the velocity of the wave remains unchanged. It is noted that the PRF represented here may be the fastest allowable cycle time if the refresh time was negligible. By rotating the thruster surface or the incident laser fluxes maintaining a constant supply of fresh air and area for the LSC wave, the cycle could be quickly be initiated again as soon as ambient conditions are reached.

The plot of coupling coefficient versus intensity shown in figure VI-5 reveals some interesting features. It does display an extremum, which locates an optimal coupling coefficient at about $10^6 W/cm^2$. the step in the curve occurs as the program transitions from condition 1 to condition 2. This dip along with other sudden changes in C.C., PRF, T and r_0 , may be appearing because the transition to LSD conditions, which is a complicated process, is occurring. The implication is that condition 2 is being chosen at this intensity because the wave is stronger and is reaching H sooner. This effect appears at later time in the cycle implying that more time is needed for full wave expansion. This may support the above hypothesis. This verifies that the higher intensities produces higher coupling coefficients due to a longer thrust schedule.

Figure VI-6 shows how much energy is being accepted by the LSC wave from the amount being dumped into it. It also increases with height and intensity.

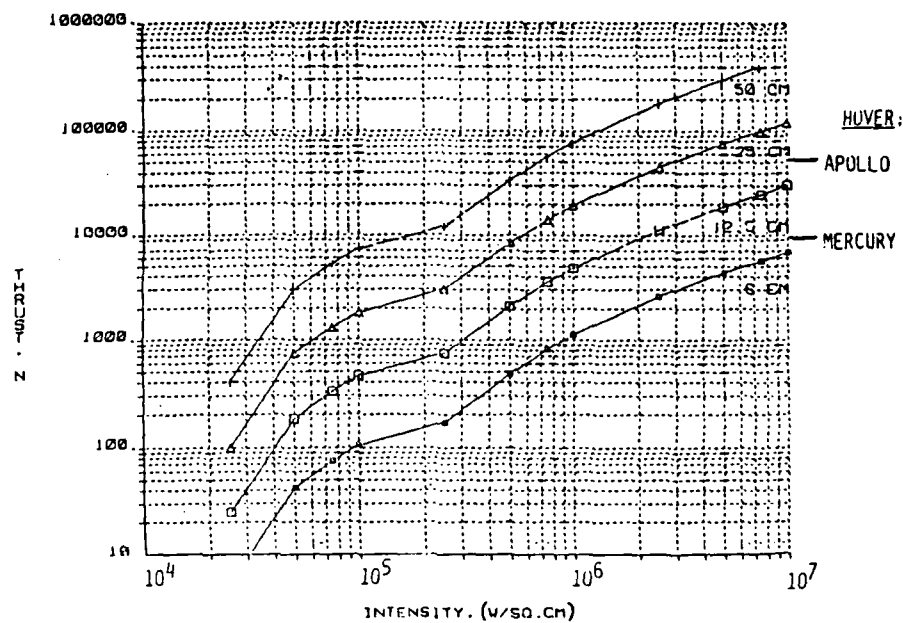


Figure VI-3 Time-averaged thrust vs. Intensity for the LSC wave based-ERH-thruster

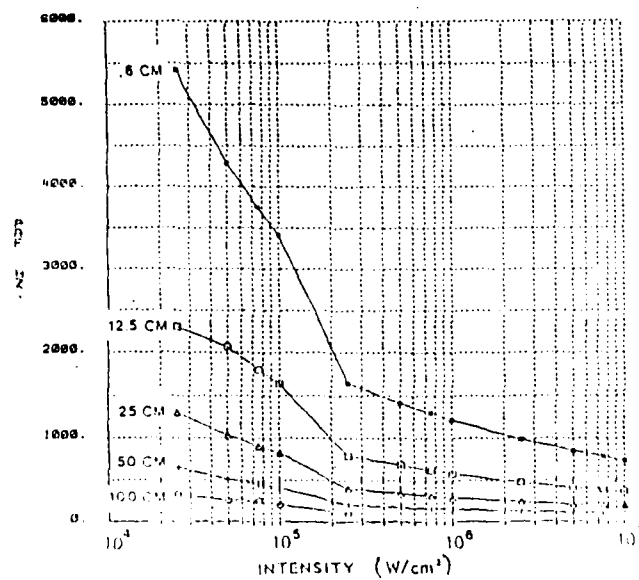


Figure VI-4 PRF vs. intensity for the LSC wave based-ERH-thruster

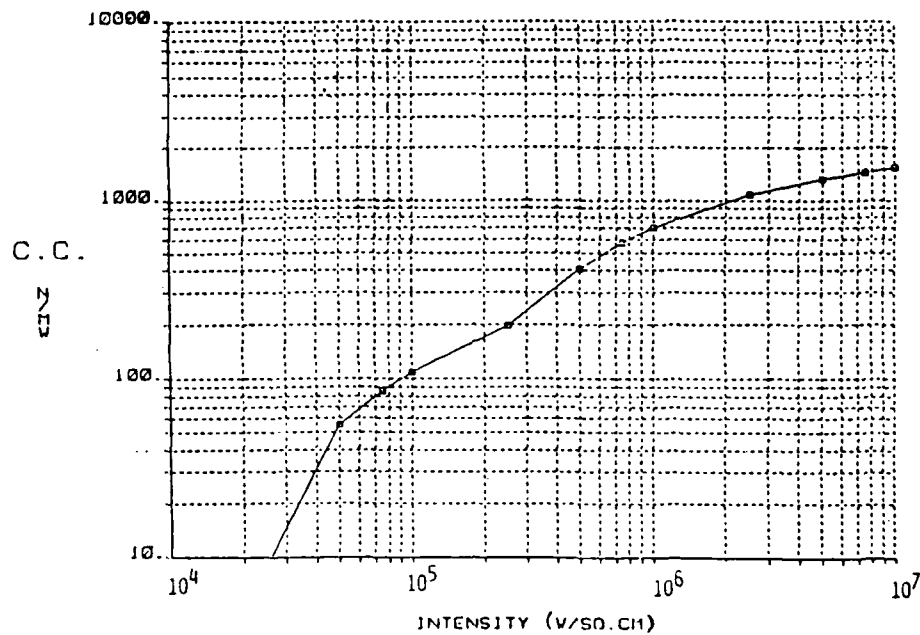


Figure VI-5 Coupling coefficient vs. intensity for the LSC wave based-ERH-thruster

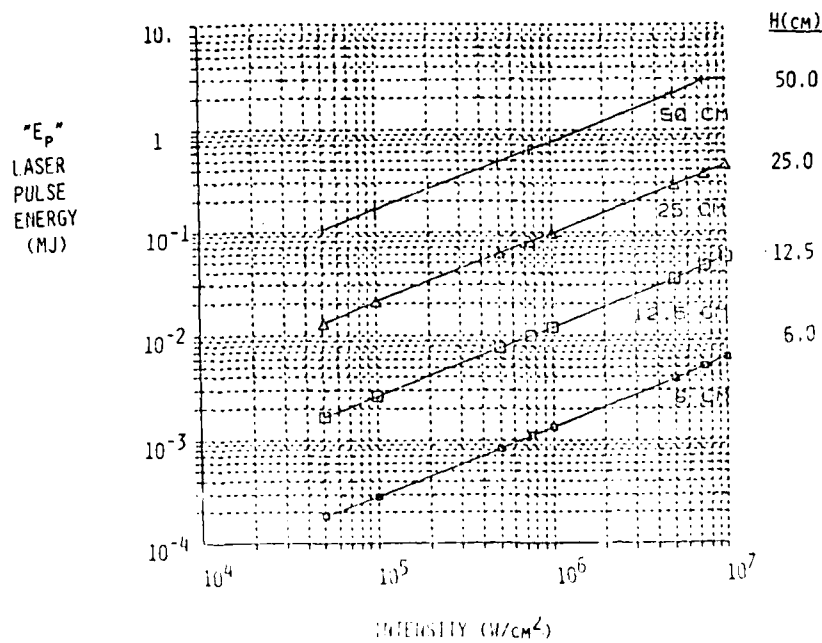


Figure VI-6 Laser pulse energy, E_p

The time averaged power should show a similar trend if there are no losses in the cycle. However, around 10^6 W/cm^2 , figure VI-7 shows a dip in the power required by the wave for the cycle.

Figure VI-8 simply shows that as more energy is being deposited into the wave, it takes less time for the wave to grow, hence the decrease of the pulse time with the intensity. Figure VI-9 shows the growth of the LSC wave within that time. It depends on the gas properties and not the flux because they should be the ultimate constraint on the gas geometry. This is a nature of the gas dynamics reflected in the equations (mainly Sedov's) and in these results.

Figure VI-10 shows the total growth of the wave and displays the effect mentioned earlier as it appears in the complete wave expansion.

C. Summary

This analysis was the result of a simple model of an LSC wave to be used in an ERH thruster. The results appear promising. A considerable amount of thrust seems achievable for hovering and more. The ERH thruster itself appears to compare very well with known engines (compare figure VI-5 with the 40 N/MW capability of existing ion thrusters). However some of the assumptions made impose some restrictions on these results. The size, shape and strength of the wave may not agree with the use of Sedov's scaling laws. It is apparent that Sedov's scaling laws are questionable at $r=0$ and infinity. For the low velocities of the LSC wave and its high temperatures, thermal and viscous losses may be very important and would have to be considered in further analyses.

The geometry of the LSC wave itself may even be more complicated than it has been imagined to actually be in figure VI-1. The model used in this analysis did not fully acknowledge the complexities of figure VI-1, though it is believed to be adequate in this first investigation.

Pirri's pressure and velocity equations were derived for a 1-D model and was good to start with, but their compatibility with the boundary conditions of this configuration should be re-analyzed in the future. Pirri had also assumed that a strong shock existed in front of the LSC wave. This simplified his analysis but yielded those rather high pressures for the wave.

An acoustical analysis appears to be the next best step in the development of any future models. It would be even better if a numerical model could be developed using finite difference methods.

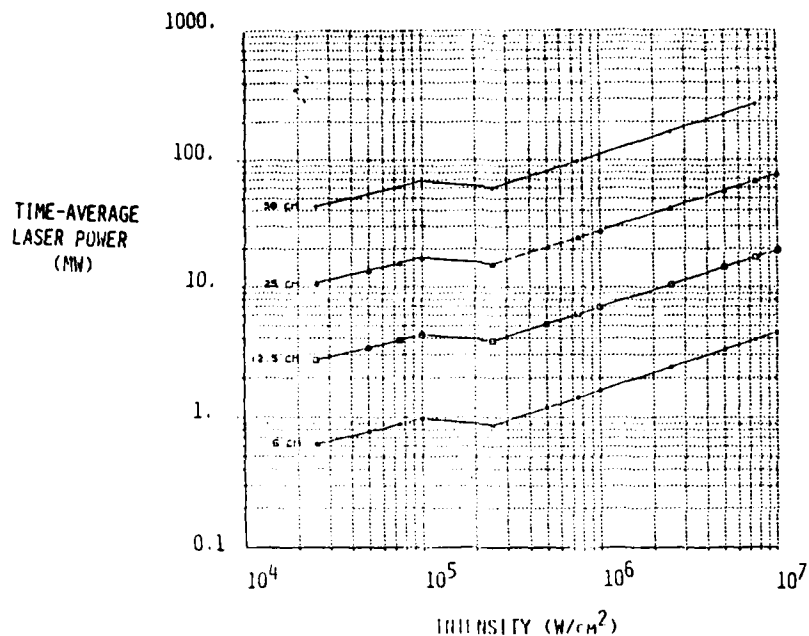


Figure VI-7 Time-averaged laser power required by the LSC-wave-based ERH thruster

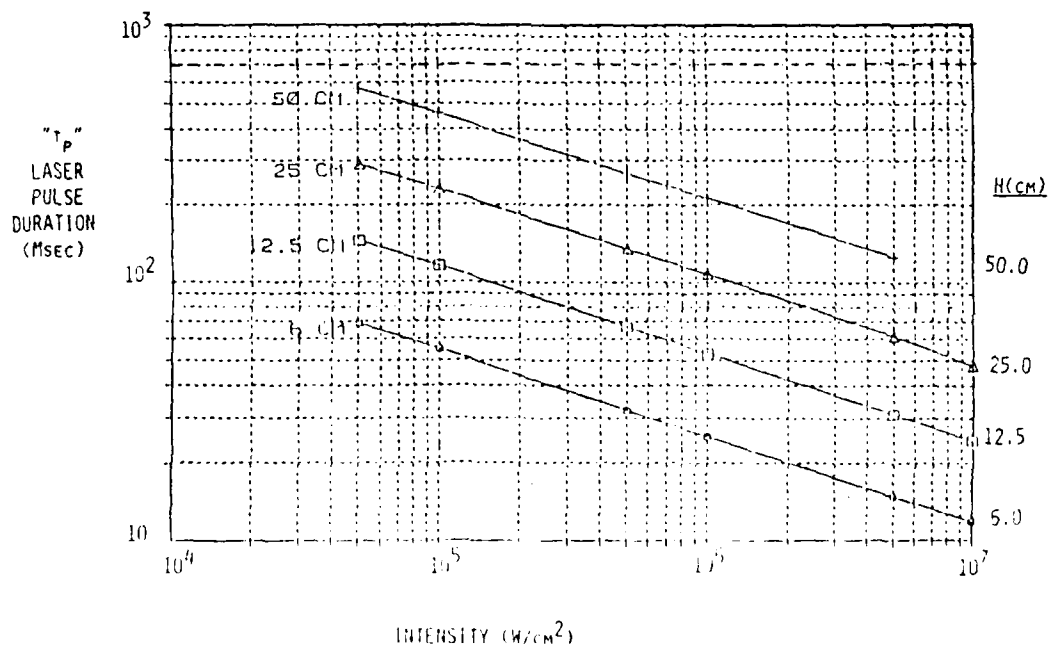


Figure VI-8 Laser pulse duration, t_p

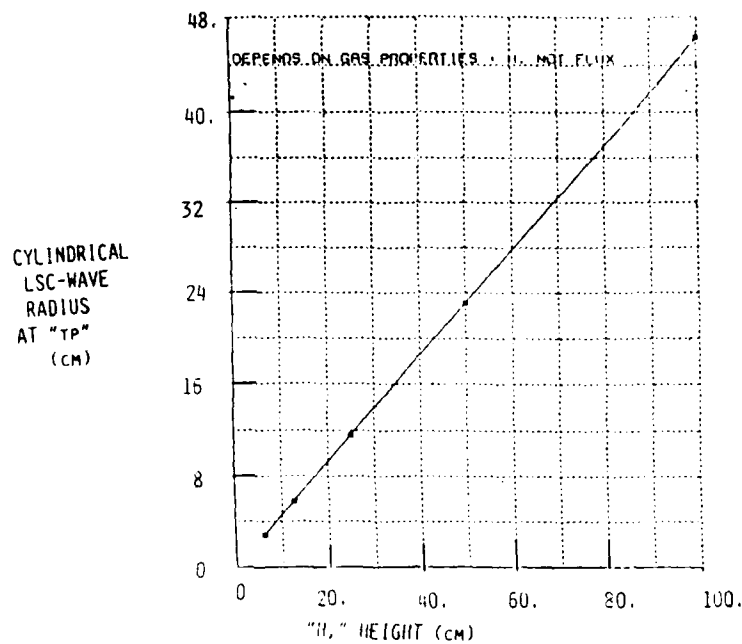


Figure VI-9 Cylindrical LSC wave's radius at time t_p

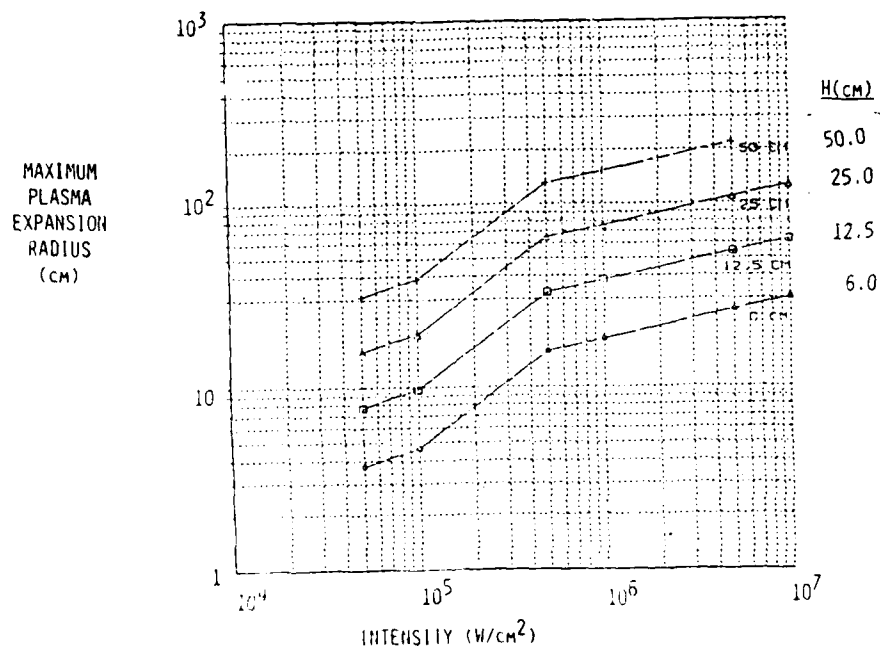


Figure VI-10 Radius of the wave at the end of the expansion

CHAPTER VII

TEMPERATURE HISTORY OF AN ERH THRUSTER SURFACE

An ERH thruster surface that is exposed to a laser-supported combustion (LSC) wave can experience high temperature due to radiative heat transfer between the wave and the surface. As the wave propagates periodically over the surface, the surface temperatures increase on each cycle. An initially cool surface will, after a time, attain the maximum allowable temperature for the surface material. The time to maximum temperature can be estimated by calculating the net radiative heat transfer to the surface coupled with the transient thermal response of the surface.

The vehicle configuration examined in this study utilizes an ERH thruster, which is sketched in Fig. VII-1 [10]. The base of the vehicle is a disk of radius 1.25 m. Energy is supplied to the LSC wave by a laser beam that is projected inward from the edges of the disk (around the entire circumference). The LSC wave propagates radially outwards towards the edge of the disk. At the edge, the beam is extinguished, and a new wave is initiated at the disk center. This process continues periodically until adequate thrust is achieved or until maximum temperatures are exceeded. This chapter analyzes the static "hover" or subsonic flight condition only, where forced convective cooling of the ERH thruster surface cannot be invoked. Forced convective heating of the surface was not analyzed.

Figure VII-2 shows an alternate view of the propagating LSC wave. As the wave expands outward, a rarefaction wave propagates inside the LSC wave cylinder. The pressure difference between the back of the rarefaction wave and the lower vehicle surface produces the flight propulsive thrust. The physical size of the two LSC wave configurations which are examined in this analysis were determined by the hovering thrust which is required by a vehicle the size of a Mercury capsule. The two LSC waves have the requisite heights and pulse rate frequencies to produce identical thrust. The difference between these two configurations arises from the assumed emissivity of the ERH thruster surface. The first LSC wave propagates over a surface with an emissivity of 0.1 while the second has an emissivity of 0.6. Note that both ERH thruster surfaces are basically horizontal (i.e., a flat-bottomed vehicle).

A. Radiation Model

The LSC wave is essentially a thin layer of absorbing and emitting gas at an elevated temperature. In the present study, the LSC wave is assumed to be gray and isotropic with respect

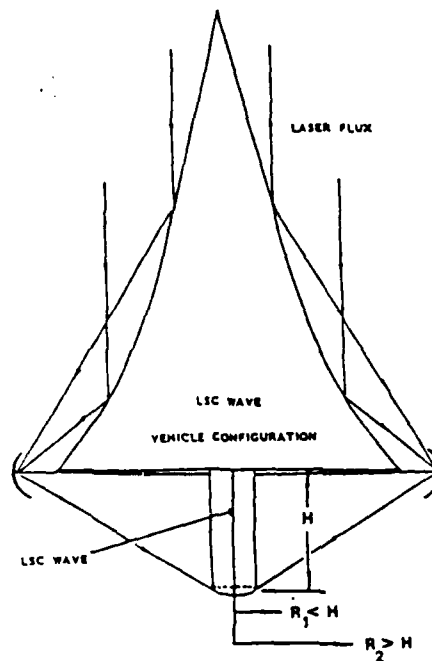


Figure VII-1 ERH Thruster Configuration

Note: $6\text{ cm} \leq H \leq 50\text{ cm}$

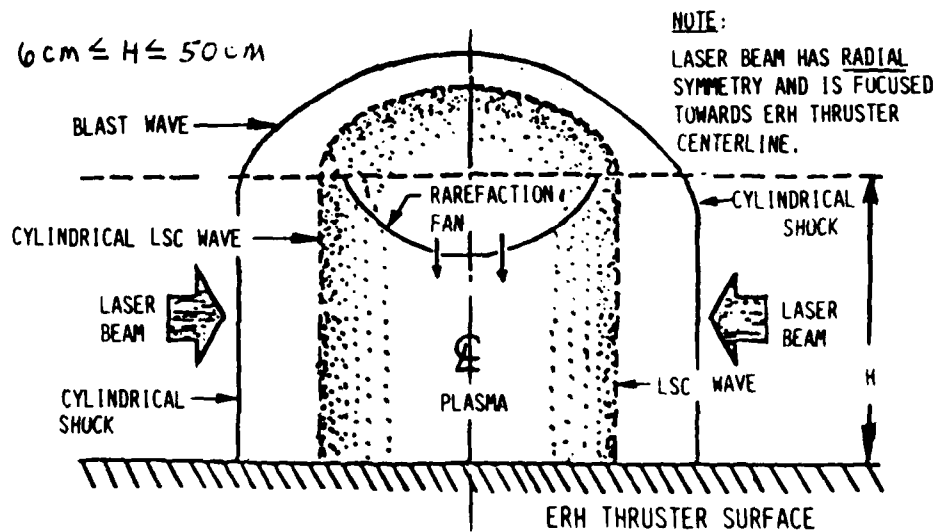


Figure VII-2 LSC-Wave Expansion

to temperature, pressure and radiative properties. No scattering of radiation is considered. The thickness of the LSC wave is small relative to the diameter of the ERH thruster surface and the height of the wave. This fact allows a significant simplification in the radiation modeling. Energy emitted from the LSC wave that arrives at a point on the thruster surface will, in general, have passed through a short path in the LSC wave and a long path in the transparent medium (air) between the LSC wave and the surface. If all the radiation emitted by the LSC wave is assumed to originate at a plane in the center of the wave, the total path length and orientation of the emitted radiation will not be greatly in error. The LSC wave can then be replaced by an infinitesimally thin *LSC surface* which emits the same total radiative flux as the actual LSC wave. To determine the radiative flux emitted by the LSC wave, a mean beam length analysis[23] was used. The mean beam length for two infinite parallel planes (the inner and outer diameter of the LSC wave),

$$L_e = -\frac{1}{a_p} \ln[2E_3(a_p D)] \quad (VII-1)$$

where a_p is the Planck mean absorption coefficient, D is the thickness of the LSC wave, and E_3 is an exponential integral. The quantity $a_p D$ is the optical thickness of the LSC wave. For the cases investigated here, the LSC temperature is 16,000 K, the pressure is 3 atm, and the thickness, D , is 1.5 cm. This corresponds to a laser intensity of 10^5 W/m^2 . The Planck mean absorption coefficient for these conditions, from[32], is $a_p = 0.01 \text{ cm}$, and the corresponding optical thickness is 0.015. The mean beam length can be used to determine the total emittance of the LSC wave by:

$$\epsilon = [1 - \exp(-a_p L_e)] \quad (VII-2)$$

In the present study, the value of the total emittance was 0.03. The purpose of the present analysis is to predict temperatures on the thruster surface. This will be accomplished by solving energy balance equations at the thruster surface. The present analysis does not attempt to specify a correct energy balance for the LSC wave. The temperature of the LSC wave is regarded as given from gas dynamic considerations. With these stipulations, it is possible to replace the actual LSC wave with an equivalent black surface. The black LSC surface emits the same total energy as the actual LSC wave. Since the actual LSC wave has an emittance of 0.03 and a black surface has an emittance of 1.0, the black surface must have a lower equivalent temperature, specified by

$$\sigma T_e^4 = \epsilon \sigma T_{LSC}^4 \quad (VII-3)$$

where T_e is the equivalent temperature and T_{LSC} is the actual temperature of the LSC wave. The calculated equivalent temperature of the black LSC surface is 6660 K.

This equivalent black surface will produce the correct incident radiation on the ERH thruster surface. Radiative energy that originates at the thruster surface and is incident on the actual LSC

wave will either be transmitted through the wave or be absorbed by the wave. There is no scattering in the LSC wave, so energy originating at the vehicle surface will not be scattered back to the vehicle. This is the reason that the equivalent LSC surface must be black, so that no energy leaving the vehicle surface will be reflected back to the vehicle surface. From the point of view of the vehicle surface, the actual LSC wave looks exactly like a black surface.

Since the equivalent LSC wave surface has a lower temperature, the spectrum of emitted radiation will be shifted to longer wavelengths than exist in the actual case. This is not a matter of concern, because the thruster surface will be assumed to be gray, and only the magnitude of the incident flux and not the spectral distribution of energy will affect the thruster surface energy balance.

Replacing the actual LSC wave with an equivalent black surface will not lead to a correct energy balance for net radiation from the LSC wave. As mentioned earlier, this analysis does not attempt to model the behavior of the LSC wave, and our only concern is that the net radiation to the thruster surface can be modeled using enclosure theory for diffuse gray surfaces[23]. The view factors needed in the radiation analysis can be obtained analytically by using the results of Ref[19], and applying configuration factor algebra.

B. Conduction Model

The radiation to the thruster surface is coupled with conduction in the surface. Initially the thruster surface is at atmospheric temperature. An LSC wave is initiated at the center of this disk-shaped surface, and propagates outward to the edges. The time of propagation to the edge is short compared to the thermal time constant for the thruster surface; therefore, the surface temperature is assumed to remain constant during the cycle. After the first cycle, the net radiative flux to the surface during the cycle is calculated as a function of radial position. This radiative flux is then used as input to a transient conduction analysis of the surface. The result of the conduction analysis is an estimate of the thruster surface temperature rise during the first cycle. This temperature may vary with radial position.

The process is then repeated for the next cycle. The radiative flux to the surface during the second cycle is calculated as a function of the new surface temperature distribution. At the end of the second cycle, the conduction analysis is repeated with a new initial temperature and heat flux distribution. This process of solving radiation and conduction alternately is continued in each succeeding cycle. It is possible to solve coupled radiation and conduction in this way without iterating on the surface temperatures because of the very short cycle time, and the resulting relatively

slow rise in surface temperature. Using values of temperature from a previous time step instead of current values does not result in a significant error in heat flux rates.

To compute the radiative flux to the thruster surface, the surface is divided into numerous concentric isothermal rings. At the beginning of the cycle, the LSC surface is located at the boundary between the innermost ring (which is actually a disk) and the second concentric ring. The LSC surface resembles a very thin-walled hollow cylinder. During the cycle, the LSC surface steps toward the disk perimeter, with its location always being between concentric rings. The time which the LSC wave remains at each location is determined by the velocity of the LSC wave, the laser pulse duration, and the incremental radial dimension. At each location of the cylinder, the configuration factors must be recalculated, and the equations for radiative energy balance in an enclosure solved again.

Conduction in the ERH thruster surface will be assumed to be one-dimensional, with no conduction in the radial or circumferential directions. Since the problem is axisymmetric, there is no temperature variation circumferentially; however, a temperature gradient can exist in the radial direction due to the radiation. The one-dimensional assumption is justified because the temperature gradients into the surface are expected to be much larger than the radial temperature gradients.

The one-dimensional transient heat conduction equation was solved for each isothermal ring on the vehicle surface. The conduction equation was discretized using an explicit finite-difference method[13]. The explicit method was superior to an implicit method in this case because of the very short time steps involved. The numerical solution was compared to the analytical solution for conduction in a semi-infinite solid with a constant surface heat flux, and agreed well.

C. Analytical Results

Two LSC wave ERH thruster configurations were analyzed. Both thrusters utilize a LSC wave which is extinguished after traveling over the inner part of the surface. The LSC wave effective temperature is also the same for both designs. The difference between the two thrusters arises from the different values for the emissivity of the vehicle surfaces. The parameters utilized for input to the numerical solution are shown in Table VII-1.

A short time exists between the extinction of one LSC wave and the initiation of the new wave at the thruster center. This time interval is represented by the difference between the thrust duration and the laser pulse time in Table 1. The thruster surface material for the second case was graphite, with emissivity of 0.6. For the first case, the assumed surface emissivity was 0.1. This lower emissivity value could possibly be produced by coating the graphite (or other base material)

Table VII - 1
Parameters Utilized for Input into Numerical Solution

	Both LSC Cases	Metallic Surface	Dielectric surface
Surface Emissivity		0.1	0.6
LSC Wave Height	0.5m		
Radius of Vehicle Surface	1.25m		
Radius of Propagation	0.23cm		
Laser Pulse Time	0.36msec		
Thrust Pulse Time	0.40msec		
LSC Wave Thickness	1.5cm		
LSC Wave Pressure	3Atm.		
LSC Wave Temperature	16000K		
LSC Effective Temperature	6660K		

with a thin layer of another substance with this radiative property value. The base material for the first case was also graphite.

For an operating time of approximately 0.3 seconds, the average surface temperature for the lower emissivity case reached 28°C . The average temperature for the higher emissivity case for the same operating time was approximately 66°C . Longer operating times were not investigated due to the large computation times which were required. Nevertheless, it is seen that this design shows promise for staying within permissible temperature limits for a total time of a second or more.

The radial distribution of the surface temperature for the two emissivity cases at various times are given in Figs. VII-3a and VII-3b, respectively. As expected, the temperature has a maximum value near the thruster geometric center, and tends to decline near the outer periphery of the disk. The relatively flat temperature profiles which exist over most of the disk surface provide justification for the one-dimensional conduction analysis. The maximum temperature after 70 cycles (0.3 seconds) for both designs occurs at the center. For the first design, the center temperature reached a maximum value of 176°C . The second design, which has a higher emissivity, had a center temperature of 955°C . If two-dimensional conduction effects were accounted for in the thruster surface, the center temperature would be somewhat lower. Based on the difference in the maximum values of the two center temperatures of the first and second cases, the first case is the more promising configuration.

For the conduction analysis, the thruster surface was assumed to be a semi-infinite solid. The penetration depth of the temperature field into the surface is shown in Figs. VII-4a and VII-4b for the first and second cases, respectively. Below this depth, there is no significant rise in the vehicle temperature. At the largest time studied, the penetration depth was about 2 cm for both designs.

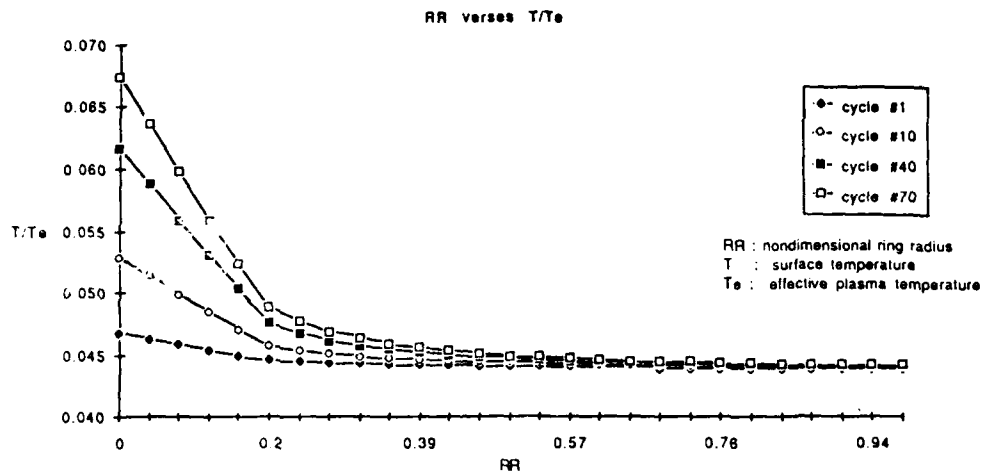


Figure VII-3a RR Verses T/T_e , Surface Emissivity of 0.1

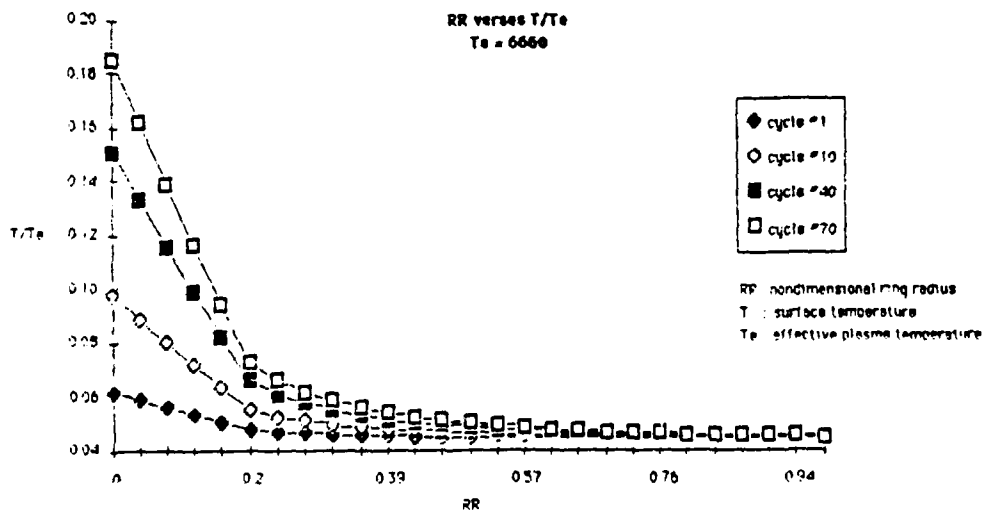


Figure VII-3b RR Verses T/T_e , Surface Emissivity of 0.6

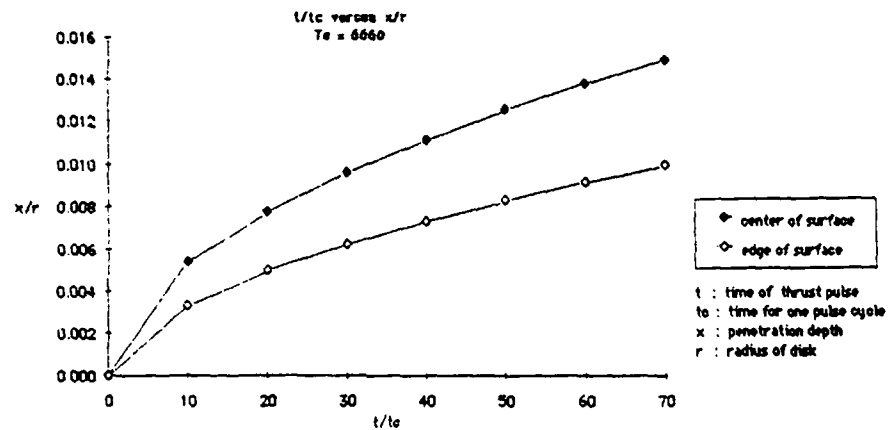


Figure VII-4a t/t_c Verses x/r , Surface Emissivity of 0.1

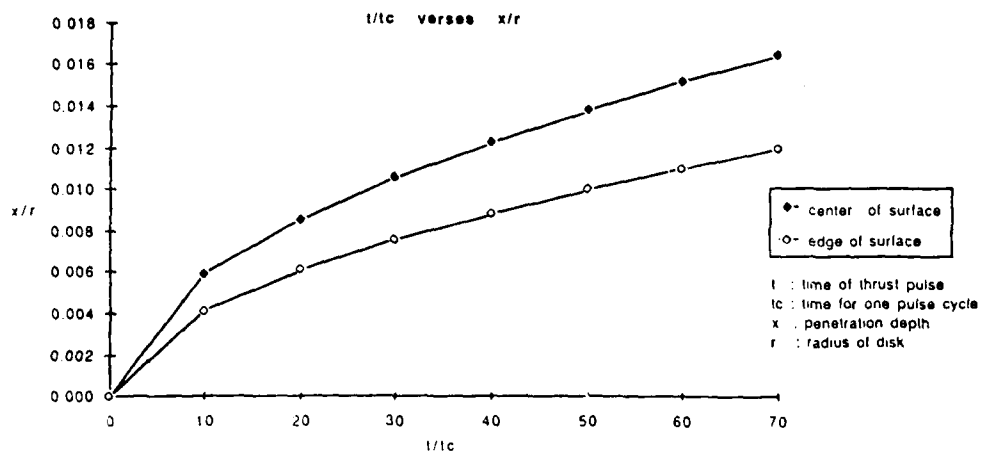


Figure VII-4b t/t_c Verses x/r , Surface Emissivity of 0.6

Two positions on the surface, the center and the edge, are the locations of maximum and minimum temperature, respectively. Figures VII-5a and VII-5b represent the surface temperature time history of these two locations for the low and high emissivity cases. In both of these figures, the line which represents the center temperature is decreasing with time. This fact shows that the net heat flux to the surface is decreasing with time as the surface temperature increases. The surface temperature for both cases may reach an equilibrium value if the computational time is increased. These two figures again show that the lower emissivity case holds more promise of surviving a greater number of LSC wave cycles.

It should be noted that the final thruster surface temperature is rather sensitive to the assumed values of LSC wave temperature, pressure, and thickness. Since the LSC wave is not truly isothermal and the thickness is not sharply defined, it is difficult to specify these parameters exactly. Relatively small changes in the assumed average values of these parameters can have a large effect on the final results.

D. Future Extensions

Three main refinements to the present analysis will be made in the future. The refinements to be considered are: 1) relaxation of the assumption that the absorptivity and emissivity of the thruster surface are equal, 2) two-dimensional conduction effects in the thruster surface (conduction in the radial direction), and 3) convective heat transfer effects between the plasma and thruster surface.

The radiation analysis refinement will allow the thruster surface to have different absorptivity and emissivity coefficients. The absorptivity coefficient will be in the high temperature solar range, while the emissivity coefficient will be in the lower temperature infrared range. This improvement in the analysis will allow the surface to be chosen on its selective radiative characteristics.

Two dimensional conduction effects will be utilized in the future to better approximate the conduction in the thruster surface. The inclusion of conduction in the radial direction will lower the center temperature and allow a longer total thrust time. The convective heat transfer effects will also be included in the future when the gas dynamics of the moving LSC wave are better understood.

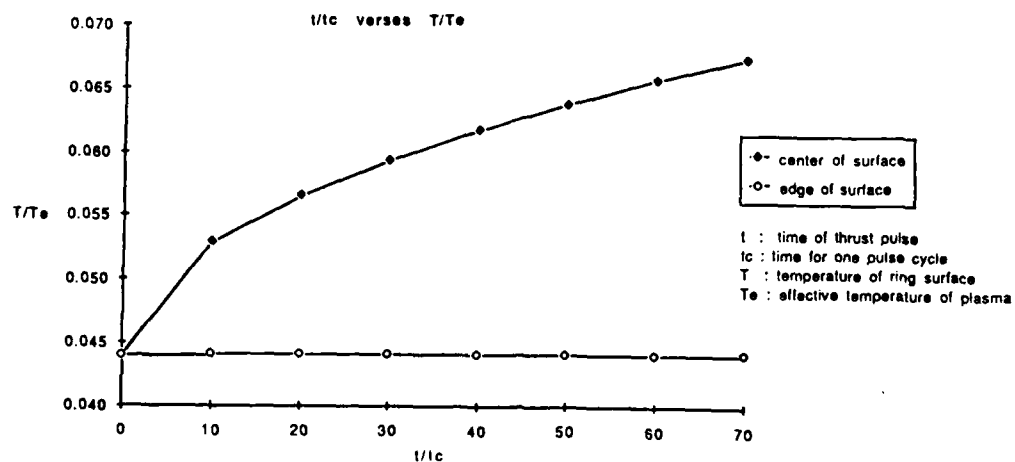


Figure VII-5a t/t_c Verses T/T_e , Surface Emissivity of 0.1

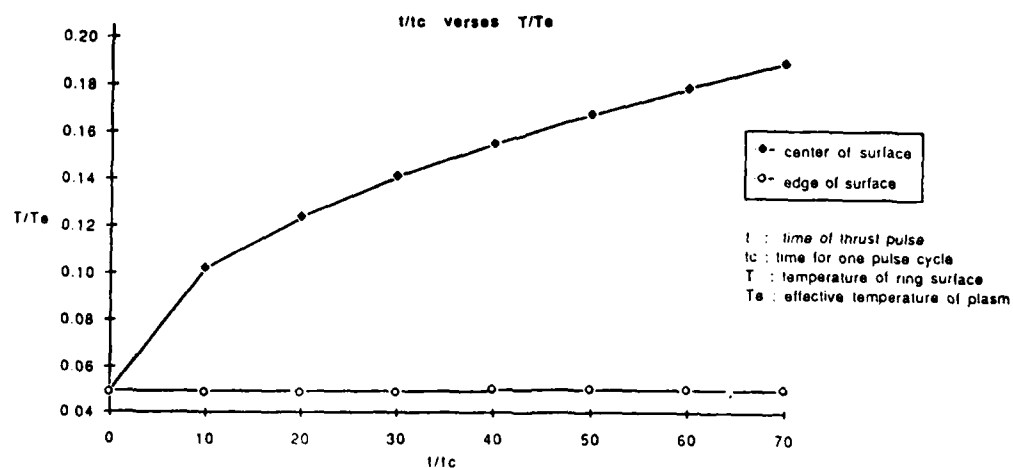


Figure VII-5b t/t_c Verses T/T_e , Surface Emissivity of 0.6

CHAPTER VIII

FAR-FIELD SOUND LEVELS PRODUCED BY ERH THRUSTER

A. Introduction

The continuous series of laser-induced impulses used as a means of propulsion in vehicles powered by External Radiation Heated (ERH) thrusters, will generate high sound pressure levels in the vicinity of the launch site. A rough estimate of these levels can be made under the assumption that the ERH thruster-propelled vehicle can be approximated (for acoustical purposes) as a uniformly radiating spherical source whose diameter equals that of the vehicle. The sound pressure level at the surface of this hypothetical source will be assumed to have an amplitude equal to the average pressure exerted on the vehicle surface by the laser-induced explosions.

For the two types of vehicles considered in this study - a 5555-kg vehicle 5 m in diameter (Apollo Lightcraft) and a 900-kg vehicle 2.5 m in diameter (Mercury Lightcraft)- the average pressures are 2.775 kPa and 1.799 kPa. These correspond to sound pressure levels (re. 20 μ Pa) of 162.8 and 159.1 dB, respectively, in the immediate vicinity of the vehicles. (Sound pressure levels (SPL) in decibels (dB) are given by

$$SPL = 20 \log \left[\frac{\text{Sound Pressure in Pascals}}{20 \mu\text{Pa}} \right] \quad (VIII - 1)$$

on this scale the faintest sound that can be heard has a SPL of 0 dB, while the threshold of pain is at 120 dB.)

The SPL of sound emanating from a spherical source in the absence of boundaries will decrease with distance r from the source as $20 \log(r/R)$, where R is the radius of the source (2.5 m in the case of the 5555-kg vehicle and 1.25 m in the case of the 900-kg vehicle). Therefore the SPL as a function of distance can be represented by

$$SPL = 162.8 - 20 \log \frac{r}{2.5}$$

$$SPL = 170.8 - 20 \log r \quad (VIII - 2)$$

for the 5555-kg vehicle, and

$$SPL = 159.1 - 20 \log \frac{r}{1.25}$$

$$SPL = 161.0 - 20 \log r \quad (VIII - 3)$$

for the 900-kg vehicle. These expressions hold for average pressure levels generated when the vehicles are hovering; if they are accelerating at the designed maximum rate of 33 gs, the SPLs will increase

by $20 \log 33 = 30.4 \text{ dB}$ at any noise measurement location. The following Table shows the noise levels predicted by the above equations at distances ranging from 20 m to 20 km during hover: These figures will be increased by 30.4 dB when the respective vehicles accelerate at the design maximum of 33 g.

Table VIII-1 — Predicted noise Levels (dB)

Distance r	spl (5555-kg vehicle)	spl (900-kg vehicle)
20 m	144.8	135.0
50 m	136.8	127.0
100 m	130.8	121.0
200 m	124.8	115.0
500 m	116.8	107.0
1 km	110.8	101.0
2 km	104.8	95.0
5 km	96.8	87.0
10 km	90.8	81.0
20 km	84.8	75.0

By way of comparison, the SATURN V launch vehicle used in the APOLLO program was known (see, e.g., Peterson and Gross, 1974) to produce SPL's well in excess of 90 dB at a distance of 20 km from the launch site. Table VII-1 shows that the SPL's produced by the ERH thruster vehicles in hover will not exceed those of the SATURN V. The additional 30.4 dB produced when the vehicles accelerate at 33 g could raise the SPL's above those produced by the SATURN V, however.

The simplified picture of the noise problem posed by ERH thrusters in the above discussion is rather too crude to be used as a basis for a definitive estimate of the noise levels to be expected during hover and acceleration. A more refined picture will be developed below from which such an estimate can be obtained. The simplified picture is useful, nonetheless, because it demonstrates that the magnitude of the noise problem posed by the launch of ERH thruster propelled vehicles is not so small that it can be dismissed out of hand.

B. BLAST WAVE CHARACTERISTICS

A realistic acoustic model of an ERH thruster vehicle must incorporate the nonlinear characteristics of blast waves, whose attenuation with distance are significantly different from those of ordinary linear acoustic waves. In the discussion that follows, the spherically expanding blast wave will form the basis for such a model, notwithstanding the fact that the laser-induced explosions

which propel the vehicle maybe linear rather than spherical. This approach is justified because of the fact that the explosions are of finite length and occur in close proximity to a finite baffle (the lower vehicle surface). The results of a more detailed analysis incorporating both a cylindrical near-field blast wave and a spherical far-field blast wave would, to some extent, modify the results of the simplified analysis performed below, but would not materially affect the conclusions drawn from it.

The instantaneous spatial pressure distribution is shown qualitatively in Fig. VIII-1 for four increasing values of elapsed time following an explosion (Kinney & Graham, 1985)[11]. Analysis of the blast wave responsible for such a pressure distribution was performed originally in order to predict the characteristics of nuclear explosions (Taylor, 1950)[27]. The equivalent analysis of a cylindrical wave was performed by Lin (1954)[12]. Both analyses introduced the assumptions of self-similar behavior inherent in the scaling laws invoked by Reilly et al. (1979)[21] in their study of momentum transfer arising from laser-induced explosions near non-ablating surfaces.

Some results of Taylor's analysis which are particularly appropriate here are: (a) Blast wave profiles consist of a strong shock front behind which pressure, temperature, and density rapidly decrease; (b) Pressure profiles at any instant in time are self-similar - that is, similar if the pressure is normalized with respect to the peak pressure immediately behind the shock, and distance is normalized with respect to the shock radius; (c) Peak pressure behind the shock front declines with the inverse cube of the shock radius; and (d) Speed of the shock front declines as the inverse $3/2$ power of the shock radius. Analogous results hold (except that the respective powers of the shock radius are different) in the case of cylindrical shocks.

The similarity rules governing blast waves cannot hold far from an explosion because: (a) Small-amplitude (acoustic) waves decline inversely with the first power of the radius of the wave front (the equivalent of the shock front in the case of blast waves); and (b) The wave profile does not change shape with time or distance - i.e. the wave is non-dispersive. Attention must therefore be paid to those circumstances which prevail while an explosion-induced disturbance undergoes the transition from blast wave to sound wave.

C. BLAST WAVE APPROXIMATION

Some insight can be obtained from an examination of Fig. VIII-2, in which the solid line is a plot of data obtained from page 92 of Kinney & Graham (1985)[11]. The ratio of blast overpressure ΔP to the ambient reference pressure P_0 is represented on the abscissa, while the ratio of shock radius R to a reference radius R_0 is represented on the ordinate (the reference radius R_0 has arbitrarily been defined as the value of R at which ΔP equals $100P_0$). The point corresponding to the actual

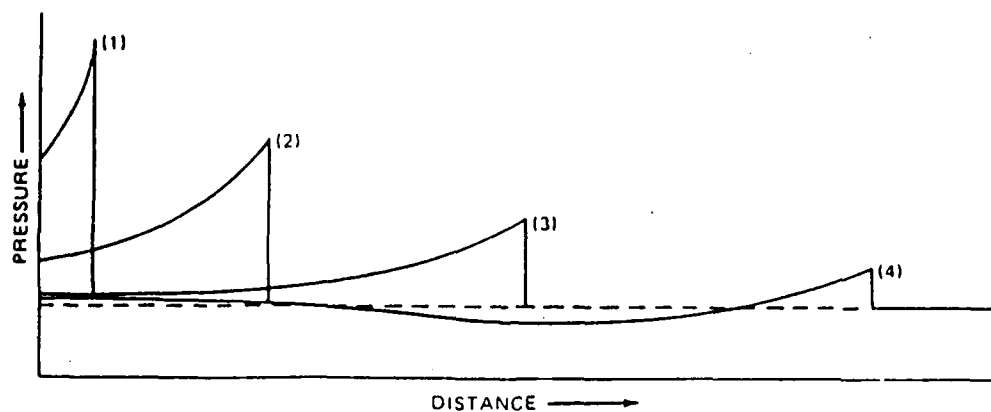


Figure VIII-1 Typical Pressure for Successive Times After Explosion

location and magnitude of peak overpressure at a given value of time after the explosion will move along the solid line from right to left as time increases. Because of this behavior, which is indicated in Fig. VIII-2 by the arrow labeled DIRECTION OF WAVE PROPAGATION, a plot of peak pressure versus location will hereafter be referred to as a *Pressure-Distance Trajectory (PDT)*.

The dashed line tangent to the left end of the solid line has the slope corresponding to the $1/R$ pressure variation of linear acoustic waves, while the dashed line tangent to the right end of the solid line has the slope corresponding to the $1/R^3$ pressure variation of strong blast waves. Therefore the right-hand extremity of the solid line lies in the blast wave regime while the left-hand extremity lies in the acoustic regime. Inspection of Fig. VIII-2 reveals that, when viewed on a logarithmic rather than a linear scale, the transition of an explosion-induced disturbance from a nonlinear blast wave to a linear acoustic wave is centered in the neighborhood of the point B, which is the closest point on the solid line to the point A where the two tangent lines cross.

This suggests that the actual PDT can be approximated by the left-hand tangent line for linear acoustic waves, and by the right-hand tangent line for blast waves, with transition occurring at the single point A. Analysis would begin with formulation of blast wave conditions near the source explosion, and the blast wave scaling laws would then be used to determine the pressure signature corresponding to point A. This would then be used to establish the acoustic far-field signature for large values of R . An estimate of the error likely to be incurred by utilizing the approximate PDT can be made by noting that the ratio of the overpressure at the actual midpoint B of transition in Fig. VIII-2 to that at point A is about $4/3$ corresponding to an under-estimation of $20 \log(4/3) \approx 2, 5dB$.

D. BLAST WAVE SPECTRUM

Inspection of Fig. VIII-1 reveals that a single blast wave profile displays, at a given instant in time, an approximately exponential variation of pressure with distance from the blast center, at least in the neighborhood of the shock front. This suggests that, to a first approximation, the pressure-time signature observed at a stationary observation point as the blast wave passes by it will exhibit a sharp rise (due to the passage of the shock front) followed by an initially (at least) exponential pressure drop with time due to the passage of the (spatially) exponentially varying self-similar pressure profile behind the shock front. The validity of this approximation was proved by Taylor (1950)[27] for spherical blast waves.

The ERH thruster will be powered not by a single laser-induced explosion, however, but by a series of explosions occurring at a prescribed Pulse Repetition Frequency (PRF). Therefore the resulting pressure signature will appear, as shown in Fig. VIII-3, in the form of a steady-periodic

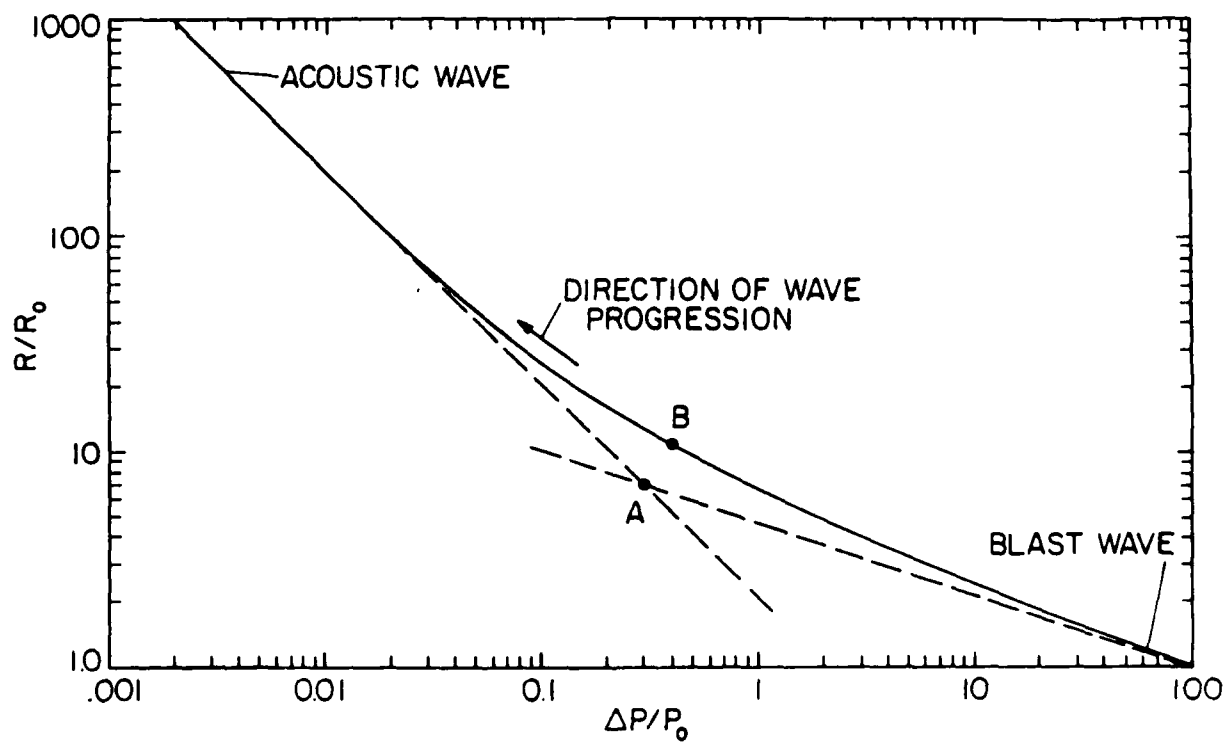


Figure VIII-2 Plot of Peak Blast Wave Pressure vs. Distance from the Source.

oscillation each cycle of which consists of a step-function rise followed by an exponential decay, the period T of the cycle being equal to $1/\text{PRF}$.

The pressure-time signature $p(t)$, being periodic, can be represented as a Fourier series:

$$p(t) = \sum_{q=0}^{\infty} a_q e^{j - jn\omega_0 t} \quad (\text{VIII} - 2)$$

where t is the time, $j = \sqrt{-1}$, $\omega_0 = 2\pi\text{PRF}$, and

$$a_q = \frac{\omega_0}{2\pi} \int_{-\pi/\omega_0}^{\pi/\omega_0} p(t) e^{-jn\omega_0 t} dt \quad (\text{VIII} - 3)$$

The pressure-time signature during one cycle ($t = -\pi/\omega_0$ to π/ω_0) is given by

$$p(t) = p_1 e^{1 - b(t + \frac{\pi}{\omega_0})} \quad (\text{VIII} - 4)$$

where p_1 is the maximum pressure at the shock front. If the indicated integration is carried out we obtain, after some rearrangement,

$$p(t) = p_1 \left[1 - \exp\left(\frac{-2\pi b}{\omega_0}\right) \right] \frac{\omega_0}{\pi} \left[\frac{1}{2b} + \sum_{n=1}^{\infty} (-1)^n (b^2 + n^2 \omega_0^2)^{-\frac{1}{2}} \sin(n\omega_0 t + \phi_n) \right] \quad (\text{VIII} - 5)$$

where $\phi_n = \tan^{-1} \frac{b}{n\omega_0}$.

In order to obtain spectral components of $p(t)$ the constants p and b must be evaluated. In carrying out the evaluation, it is important to note that $p(t)$ in Eqn. VIII-4 is the total absolute pressure, not the overpressure ΔP of Fig. VIII-2. In terms of the notation of that figure, $p_1 = \Delta P + P_0$. The ambient reference pressure P_0 is (at least in the acoustic far-field) the time-average value of $p(t)$ in Eqn. VIII-5 - i.e.

$$P_0 = p_1 \left[1 - e^{\left(\frac{-2\pi b}{\omega_0}\right)} \right] \frac{\omega_0}{2\pi b} \quad (\text{VIII} - 6)$$

At point A in Fig. VIII-2, $\Delta P/P_0$ is about 0.3, so that $p_1 = P_0 + \Delta P = 1.3P_0$. If we substitute this relation for p_1 into Eqn. VIII-6 while defining the variable $X = \frac{2\pi b}{\omega_0}$ in order to simplify the resulting expression, we get the following transcendental equation:

$$P_0 = 1.3P_0 [1 - e^{-X}] / X \quad (\text{VIII} - 7)$$

This equation will be satisfied by $X \approx 0.55$, and therefore b will have a range of values for the smaller vehicle (900-kg, 2.5 m diameter) from 8.85 s^{-1} under hovering conditions ($\text{PRF} = 16.1 \text{ Hz}$) to 292 s^{-1} under maximum (33 g) acceleration ($\text{PRF} = 531 \text{ Hz}$). For the larger vehicle (5555-kg, 5 m diameter) the corresponding range of values is 20.2 s^{-1} under hovering conditions (PRF

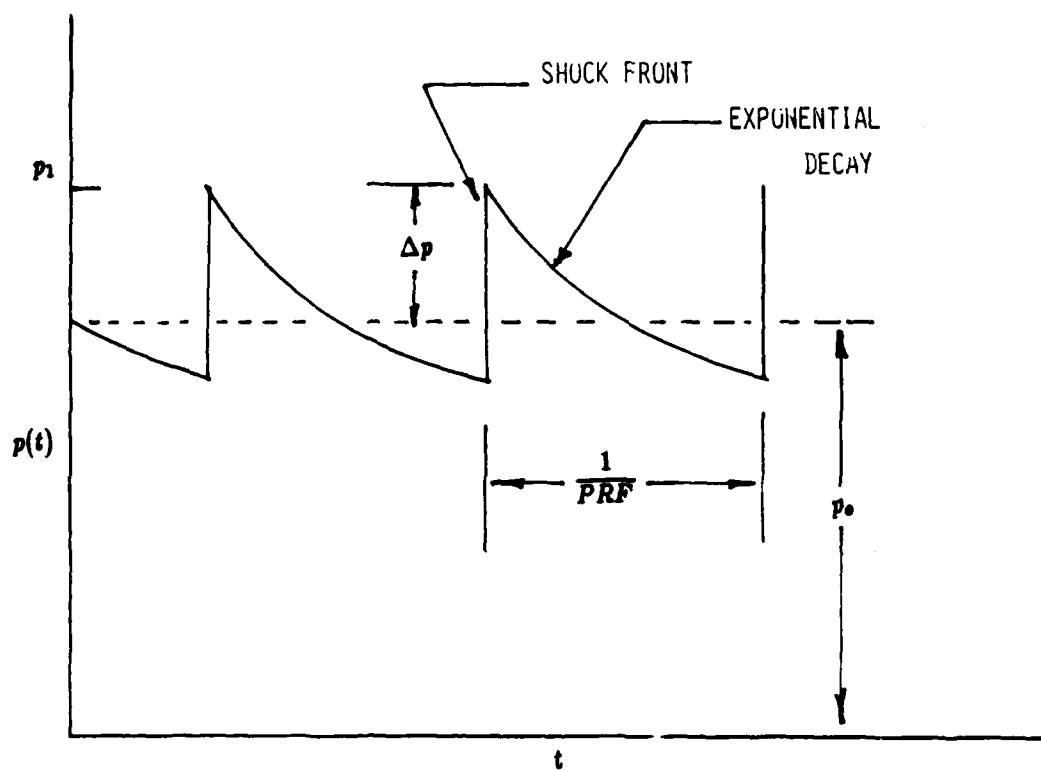


Figure VIII - 3. Pressure Signature of ERH Thruster

= 36.8 Hz) to 668 s⁻¹ under maximum (33 g) acceleration (1214 Hz). The variable X can also be substituted into Eqn. VIII-5, thereby simplifying the form:

$$p(t) = \frac{p_1[1 - \exp(-X)]}{X} \left[\frac{1}{2} + \sum_{n=1}^{\infty} (-1)^n \left(1 + \frac{\pi^2 n^2}{X^2}\right)^{-\frac{1}{2}} \sin(n\omega_0 t + \phi_n) \right] \quad (VIII-8)$$

where $\phi_n = \tan^{-1} \frac{X}{\pi n}$.

The RMS amplitudes p_n of the Fourier components of the pressure signature will therefore be

$$p_n = \frac{p_1}{\sqrt{2}} [1 - \exp(-X)] \left(1 + \frac{\pi^2 n^2}{X^2}\right)^{-\frac{1}{2}} \quad (VIII-9)$$

The sound pressure levels (SPL_n) due to these amplitudes at point A in Fig. VIII-2 (which can be defined as

$$SPL_n = 20 \log(p_n / P_{ref}) \quad (VIII-10)$$

where P_{ref} is the reference sound pressure, 20 Pa) will have the form

$$SPL_n = 20 \log \left\{ \frac{P_1}{\sqrt{2} P_{ref}} [1 - e^{-X}] \left(1 + \frac{\pi^2 n^2}{X^2}\right)^{-1/2} \right\} \quad (VIII-11)$$

as a consequence of this result.

In the present problem, P_0 is 1 atmosphere (about 101 kPa) so that $p_1 = 1.3P_0 = 131.3 \text{ kPa}$. If this value, together with the previously determined value of 0.55 for X, is substituted into Eqn. VIII-11 the values of the SPL_n can be calculated. The following Table lists the values for the first 10 spectral components:

Table VIII-2—SPL Values for the First Ten Spectral Components

n	$SPL_n(\text{db})$	n	$SPL_n(\text{db})$
1	170.6	6	155.2
2	174.7	7	153.8
3	161.2	8	152.7
4	158.7	9	151.6
5	156.7	10	150.7

For values of n greater than 10, SPL_n can be obtained from the approximate equation

$$SPL_n = 170.7 - 20 \log n \quad (VIII-12)$$

Note that the magnitudes of the spectral components are independent of the PRF. Note also that if an error of 0.1 dB is acceptable, then Eqn. VIII-12 can be used to predict the values of the spectral

components for n in the range from 1 to 10. As free-field measurements rarely are observed to exhibit repeatability within a tolerance of 0.1 dB, it is reasonable to regard Eqn. VIII-12 as being an adequate approximation (i.e. within the limits of experimental error) of the spectral components at a distance corresponding to point A in Fig. VIII-2.

E. FAR-FIELD SOUND SPECTRUM LEVEL

Estimation of far-field sound levels of the spectral components requires that the distance R from the blast center corresponding to point A in Fig. VIII-2 be determined. For the 5555-kg vehicle at sea level conditions the maximum expansion of a typical plasma column is about 0.4 meters in diameter and 2.5m in length, enclosing a volume of about $0.16m^3$. This volume is achieved assuming an expansion to ambient pressure of plasma in a half cylindrical column with maximum plasma pressure varying inversely with the square of the column diameter. This same expansion, when it has occurred only to the extent where the pressure is 130 percent of ambient (the condition at point A in Fig. VIII-2) will occupy a volume of only $0.12m^3$.

If we now assume that, for acoustical purposes only, the plasma column is equivalent to a spherical blast of such a magnitude that, when it has expanded to reach point A in Fig. VIII-2 the volume enclosed by the shock front equals the previously calculated value of $0.12m^3$, then a formula for the far-field levels of the spectral components can be readily obtained. The radius of a $0.12m^3$ sphere is about 0.3 m so that, because sound pressure levels vary as ten times the logarithm of the square of the ratio of the distance R from the blast center to the sphere radius R_0 , a factor

$$10 \log(R/0.3)^2 = 10.3 + 20 \log R \quad (VIII - 13)$$

must be subtracted from the components in Eqn. VIII-12. Therefore the far-field levels of the spectral components will be given by

$$SPL_q = 170.7 - 20 \log n - (10.3 + 20 \log R)$$

$$SPL_q = 160.4 - 20 \log n - 20 \log R \quad (VIII - 14)$$

where r is in meters.

This result holds for the 5555-kg vehicle, but can also be applied to the 900-kg vehicle if 2 dB is subtracted. The need for the correction arises from the fact that in the case of the smaller vehicle the radius of the cylindrical shock corresponding to a 30% overpressure is approximately the same as that in the larger vehicle, but the shock length, and therefore the shock volume used to calculate radius of the equivalent spherical blast, is half the previous value. This means that R_0 is

reduced by the factor $2\frac{1}{2}$, twenty times the logarithm of which is 2 dB. In addition, the proximity of the vehicle surface enhances the sound pressure levels achieved for the same reason that a baffle enhances the sound level of a loudspeaker driver. The enhancement is directional, with the greatest intensity being achieved underneath the vehicle.

A conservative estimate of the enhancement can be obtained by assuming that the vehicle surface functions as an infinite plane baffle, with a resulting enhancement of 6 dB. Adding this amount to the spectral components obtained above yields

$$SPL_n = 166.4 - 20 \log n - 20 \log R \quad (VIII - 15)$$

for the spectral components produced by the 5555-kg vehicle. The 6 dB enhancement is partially negated, in the case of the 900-kg vehicle, by the 2 dB scale reduction effect noted above, so that for this vehicle

$$SPL_n = 160.4 - 20 \log n - 20 \log R \quad (VIII - 16)$$

At large distances the value of R will be essentially equal to r , the distance between the vehicle and the point at which the noise level is evaluated. This fact will be utilized in the following discussion of overall noise level.

F. OVERALL FAR-FIELD SOUND LEVEL

The overall sound pressure level (SPL) is obtained by the formula

$$SPL = 10 \log \sum_{n=1}^{\infty} 10^{SPL_n/10} \quad (VIII - 17)$$

where SPL_n is as given in Eqn. VIII-15 and VIII-16. After substitution of these equations into VIII-17 followed by some rearrangement, one obtains

$$SPL = 166.4 + 10 \log \sum_{n=1}^{\infty} \frac{1}{n^2} - 20 \log R \quad (VIII - 18)$$

for the 5555-kg vehicle and

$$SPL = 160.4 + 10 \log \sum_{n=1}^{\infty} \frac{1}{n^2} - 20 \log R \quad (VIII - 19)$$

for the 900-kg vehicle. The value of the infinite sum is $\frac{\pi^2}{6}$, so that

$$10 \log \sum_{n=1}^{\infty} \frac{1}{n^2} = 10 \log \frac{\pi^2}{6} = 2.2 \quad (VIII - 20)$$

and this, in turn yields

$$SPL = 168.6 - 20 \log R \quad (VIII - 21)$$

for the 5555-kg vehicle and

$$SPL = 165.6 - 20 \log R \quad (VIII - 22)$$

for the 900-kg vehicle.

These last equations permit the construction of a somewhat more reliable table of SPL versus distance r than Table VIII-1 (q.v.):

Table VIII-3—SPL vs. Distance From Vehicle

Distance r	spl (5555-kg vehicle)	spl (900-kg vehicle)
20 m	142.6	140.6
50 m	134.6	132.6
100 m	128.6	126.6
200 m	122.6	120.6
500 m	114.6	112.6
1 km	108.6	106.6
2 km	102.6	100.6
5 km	94.6	92.6
10 km	88.6	86.6
20 km	82.6	80.6

If this set of data is compared with that in Table VIII-1 it is seen that a more detailed analysis results in a 5.6 dB increase in predicted overall noise level above that given by Eqn. VIII-3 for the 900-kg vehicle, and a 2.2 dB decrease in predicted overall noise level below that given by Eqn. VIII-2 for the 5555-kg vehicle. Note that these results hold only if laser-induced explosions occur only one at a time. If $m > 1$ explosions occur at one time, distributed over the surface of the vehicle, then the quantity $20 \log m$ must be added to the data in Table VIII-3. Therefore minimum noise is likely to be achieved when only one explosion at a time takes place.

G. SUMMARY

The preceding sections show that the employment of a crude, simple-source type acoustical model of an ERH thruster propelled vehicle in hover yields approximately the same results (to within a few decibels) as a more detailed model employing concepts from the theory of blast waves in the derivation of a sound spectrum. While the assumptions invoked in formulating the latter model are

admittedly conservative, it is unlikely that results obtained from the analysis of a more elaborate, less conservative model would differ from those obtained here except in detail.

In particular, the above results suggest that the overall noise level produced by ERH thruster propelled vehicles under uniform, non-dissipative atmospheric conditions in the absence of ground proximity effects can be considerable. The mitigating effects (if any) of atmospheric and ground absorption are too complicated and uncertain to be included within the scope of the present work, but should be considered in future efforts.

In one respect the blast wave model does produce a substantial reduction in predicted noise level in comparison with the earlier simple-source model. It was observed previously that this model predicted an increase in overall noise with vehicle acceleration, the augmentation reaching 30.4 dB under 33 g acceleration. The more accurate blast wave model, on the other hand, predicts no augmentation whatsoever with acceleration. This is because thrust increases required for acceleration are achieved by increasing the PRF rather than the blast intensity. The model also suggests that one way to minimize the overall noise level is to avoid having more than one laser-induced explosion occur at a time (i.e., the rotary detonation wave engine approach).

The effect of vehicle acceleration on perceived loudness (the subjective level of noise) is another matter, however, because this quantity is frequency dependent. In general we can expect increasing PRF to achieve acceleration to increase the perceived noise level because of the increase of sensitivity with frequency of the the human ear in the range 0-2 kHz. The actual increase in perceived noise level realized at large distances from the vehicle, where frequency-dependent atmospheric and ground absorption effects cannot be ignored, are beyond the scope of the present work and should be considered later.

We therefore recommend that the work begun here be continued in pursuit of two objectives: (a) Assessment of the noise spectrum far from the vehicle including frequency-dependent atmospheric and ground absorption effects. (b) Assessment of perceived noise levels far from the vehicle under conditions ranging from hover to maximum acceleration. As an aid to verifying these results we recommend that a digitally synthesized simulation of the anticipated noise signature be made. Such a simulation can be accomplished using equipment in the Laboratory for Noise and Vibration Control Research (LNVCR). Finally, we recommend that additional work be carried out to develop an acoustical model for predicting the noise level and lift enhancement achieved when operating an ERH thruster vehicle very close to the ground.

Documented in the following Chapter is a n account of progress made, to date, and the digitally synthesized simulation of these anticipated noise signatures.

CHAPTER IX

SIMULATION OF ERH THRUSTER NOISE SIGNATURES

A. Introduction

The purpose of the effort described here in Chapt. 9 is to produce acoustic signatures which approximate those that would be perceived by a stationary ground-based observer during various flight maneuvers of the reference vehicle (Apollo Lightcraft). Several assumptions are made in order to simplify both the analysis of the engine/vehicle as an acoustic source, and the creation of the synthesized signatures:

1. The engine/vehicle is considered to be a point acoustical source. Directivity effects are ignored.
2. Only the direct acoustic signature is modeled; no attempt is made to include effects due to reverberation (from the atmospheric and ground surface).
3. The speed of sound in air is assumed to be constant and not a function of altitude.
4. No attempt is made to include sonic booms caused by the vehicle exceeding Mach 1.

This project essentially combines a model of the acoustic response of the Apollo Lightcraft ERH thrusters to a laser pulse (i.e. the acoustic impulse response) with various sets of vehicle trajectory and laser pulsing (i.e. forcing function) data. The acoustic impulse response model is presented in Chapter 9, and the vehicle trajectory/forcing function model is reviewed below in Section G of this chapter.

B. Model Description

The computer program links the acoustic impulse response model, which was developed for a stationary source/stationary observer, to the trajectory/forcing function data—in order to generate acoustic signatures for a traveling source/stationary observer. The effects of Doppler shifting and amplitude attenuation of the observed source signature are incorporated as a function of the vehicle dynamics. The resulting expressions for the traveling source/stationary observer signatures form the basis of a computer program which generates a sequence of numbers that represents digitized samples of the analog signatures. Next, these digitized samples are processed by a digital-to-analog converter (DAC), then low pass filtered to remove harmonics of the sampling frequency produced by the DAC, and finally recorded on magnetic tape. The instrumentation setup is shown schematically

in Fig. IX-1.

The overall process is regarded as a cascade of two processes, as illustrated in Fig. IX-2. The first process H_1 describes the static acoustic impulse response $Y_s(t)$ of the ERH thruster to a laser pulse, where both the vehicle and the observer are stationary. The acoustic impulse response H_1 is a function of PRF only. Figure IX-3(a) qualitatively shows the static acoustic response of the thruster to a 500 Hz PRF pulse train, while Fig. IX-3(b) shows the response to an 1135 Hz PRF pulse train. Process H_2 describes the time-varying nature of the transmission path from the moving thruster/vehicle to the fixed observer; it combines the output $Y_s(t)$ from the static model H_1 together with relative distance data $x(t)$ and relative velocity data $v(t)$ to yield the dynamic acoustic response $Y_0(t)$ for a moving source and fixed observer.

C. Model Implementation

The decision to implement the synthesis using a digital system was based largely upon three considerations:

1. The acoustic impulse response does not represent one of the standard signal types available on hard-wired analog function generators;
2. The acoustic impulse response changes with frequency;
3. Precise control of the signature amplitude and frequency is required to reflect changes in the acoustic transmission path due to vehicle dynamics.

The natural choice for such arbitrary waveform generation capability is a digital computer-based system. This approach does, however, introduce several additional considerations which must be addressed in order to achieve the desired result. A brief discussion of these considerations is presented here. The goal is to provide motivation for, as well as describe in detail, the approach used to digitally synthesize the acoustic signature.

Figure IX-3 depicts the nature of the theoretical static acoustic impulse response $Y_s(t)$ of the Apollo Lightcraft. The figure was generated by using a digital computer to calculate $Y_s(t)$ for a number of different values of time t . Enough values were calculated so that when the corresponding points were plotted and connected with straight line segments, the resulting figure closely approximates a graphical representation of the actual analog signal. This is essentially the approach used to generate an analog signal from a set of discrete data where a DAC is used as the output device instead of a plotter. The main problem is to determine how many data points are required to produce a satisfactory approximation to the actual analog acoustic response signature $Y_s(t)$.

If the discrete data is sent to a DAC instead of a plotter, an analog signal will result. There

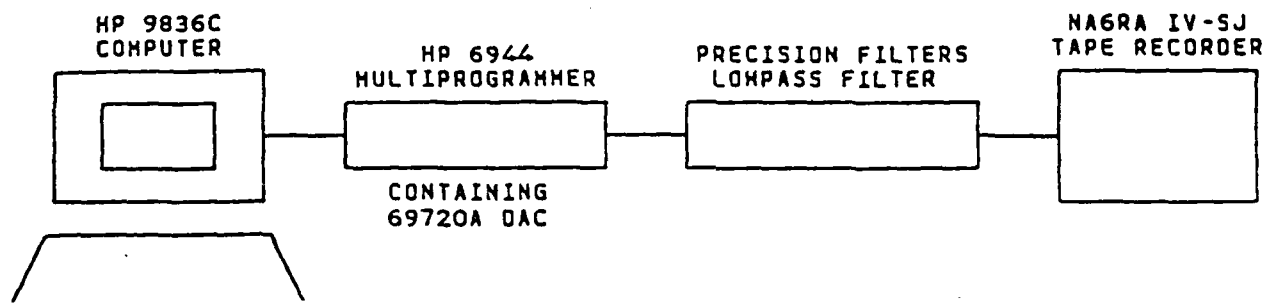


Figure IX-1. Instrumentation Setup

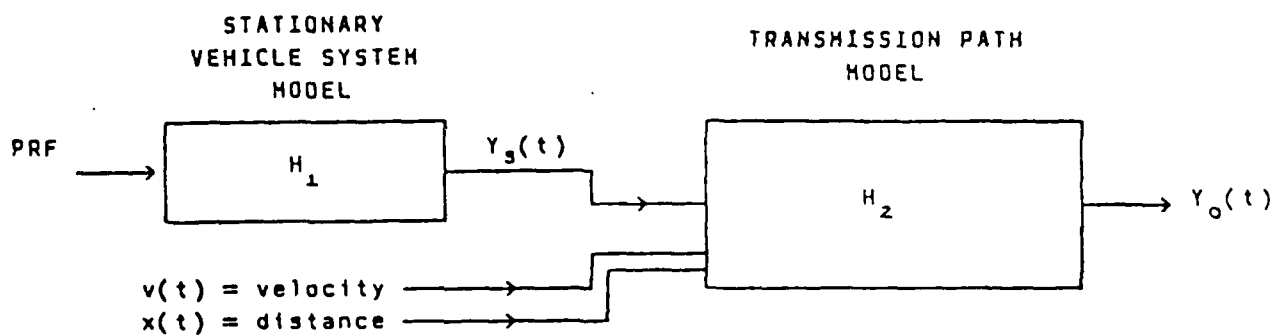


Figure IX-2. Computer Code Flowchart



Figure IX-3(a). Theoretical Acoustic Impulse Response- $PRF \approx 500H_s$



Figure IX-3(b). Theoretical Acoustic Impulse Response- $PRF = 1135$

are a number of different varieties of DAC available, but the most common is the zero order hold voltage DAC. The resolution of the DAC is defined to be the magnitude of the smallest change in output voltage that can be attained under program control, divided by the magnitude of the largest change in output voltage that can be attained under program control, expressed in per cent. The 69720A DAC is a 12-bit, zero order hold voltage DAC with a resolution of $(1/2^{12}) \times 100 = 0.024\%$. The term zero order hold refers to the fact that if a data value representing a voltage V_1 is written to the DAC, the output of the DAC will change (almost) instantaneously to V_1 and will remain constant until a new data value is written.

As one might expect, the approximation of a given analog signal by a digitally synthesized signal generally improved as the frequency Ω , at which the analog signal is sampled increases. Two factors tend to limit the choice of Ω , and hence limit the accuracy of the approximation:

1. Each digital to analog conversion requires a finite length of time to occur.
2. Finite machine memory limits the number of data values which can be stored prior to being sent to the DAC.

The 69720A DAC can process data at a rate of up to 30 kHz real time during disk to DAC transfers. The 236C computer system has approximately 15 Mbyte of free disk space to hold data for the DAC. We describe next how these constraints impose restrictions on the class of signals that can be satisfactorily synthesized.

D. Digital Simulation Constraints

Refer to Fig. IX-4(a) where several cycles of the function $f_1(t) = \sin 0.8\pi t$ are plotted. This function is periodic with a period of $2\pi/0.8\pi = 2.5$ seconds. Suppose $f_1(t)$ is sampled at one second intervals, which is equivalent to saying that the sampling frequency ω_s is two and one half times the frequency of $f_1(t)$ evaluated at $t = n$, $n = 0, 1, 2, \dots$. These are the values of $f(t)$ indicated by the tic marks in Fig. IX-4(a). If this sequence is subsequently sent to a zero order hold DAC, the resulting analog waveform will appear as in Fig. IX-4(b).

Next consider Fig. IX-4(c), where several cycles of $f_2(t) = \sin 2.8\pi t$ are shown. If $f_2(t)$ is sampled at one second intervals and the resulting sequence is sent to the DAC, the output is as shown in Fig. IX-4(d). Notice that the output from the DAC is the same for both $f_1(t)$ and $f_2(t)$. This phenomenon is called aliasing of $f_2(t)$, and occurs whenever a periodic function is sampled at less than (or precisely at) twice its frequency. The signal in Fig. IX-4(b) may be a rather crude approximation to the original signal in Fig. IX-4(a), but at least it tends to track $f_1(t)$ as it oscillates. This is clearly not the case for Figs. IX-4(c) and IX-4(d). Consideration of this phenomenon provides

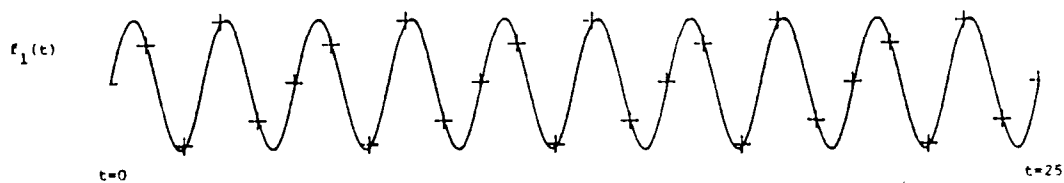


Figure IX-4(a). Aliasing and Sampling-Induced Modulation—(analog signal)

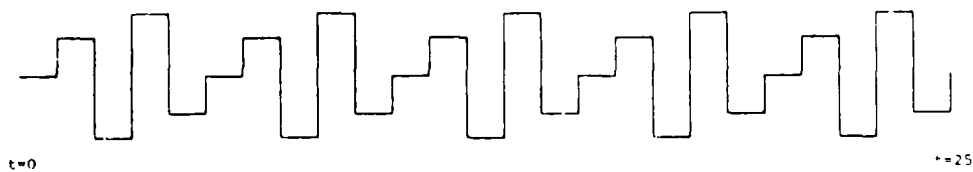


Figure IX-4(b). Aliasing and Sampling-Induced Modulation—(sampling $f_1(t)$ at a rate of 1 sample/sec)

motivation for the following criterion:

Nyquist Criterion. In order to uniquely recover a band-limited signal from its sample sequence, the signal must be sampled at a rate of greater than twice the frequency of any constituent components.

Notice that if the original function is not band-limited, it is, strictly speaking, impossible to recover it exactly from its sample sequence. Because the 69720A DAC has a maximum sampling rate of 30,000 samples per second, the Nyquist criterion demands that the input data to the DAC represent samples obtained from an original signature having a bandwidth of less than 15 kHz. This represents one important constraint on the class of signatures that can be accurately synthesized. The second constraint, to be discussed next, is even more severe.

Refer once again to Fig. IX-4(b). Although $f(t)$ is sampled in accordance with the Nyquist Criterion, the signal produced by the DAC exhibits an amplitude modulation which is not present in the original signal. For the purposes of synthesizing signatures from sampled data, this modulation represents an unwanted artifact. Sampling of a cosinusoid of frequency ω_1 , using a sampling frequency such as $\omega_s = (r/s)\omega_1$, where the numbers r and s are relatively prime, results in a periodic sample sequence of period $T_{A.M.} = s/\omega_1 = r/\omega_s$. For instance, Fig. IX-4(b) shows the result of sampling $f_1(t)$, which has frequency $\omega_1 = 0.8\pi/\text{sec}$, at a sampling frequency of $\omega_s = 2\pi/\text{sec}$. Then

$$\omega_s = \left(\frac{2\pi}{1 \text{ sec}}\right)\left(\frac{0.8\pi}{\text{sec}}\right) \quad (IX-1)$$

$$\omega_s = \frac{2}{0.8}\omega_1 = \frac{5}{2}\omega_1 \quad (IX-2)$$

$$T_{A.M.} = \frac{2}{\omega_1} = \frac{5}{\omega_s} \quad (IX-3)$$

Hence the resulting amplitude modulated sample sequence should have a period

$$T_{A.M.} = 2T_1 = \frac{2}{\omega_1} = \frac{5}{\omega_s} = 5T_s \quad (IX-4)$$

and this is verified in Fig. IX-4(b).

It can be shown that the frequency spectrum of a carrier signal of frequency ω_s modulated by a waveform of frequency ω_m will contain a component at ω_s , a component at $\omega_s + \omega_m$, and a component at $\omega_s - \omega_m$. The latter two components are referred to as sidebands. The presence of sidebands is a consequence of modulation caused by sampling and elimination of the sidebands requires removal of the modulation.

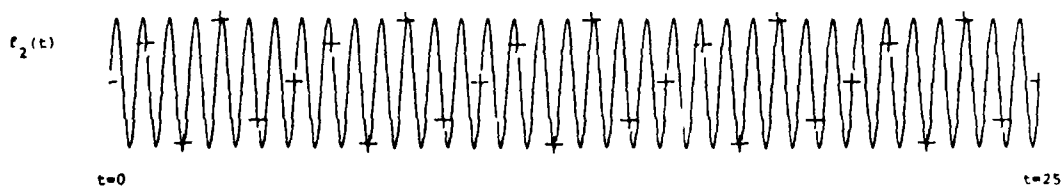


Figure IX-4(c) Aliasing and Sampling--(analog signal $\sin(2.8\pi t)$)

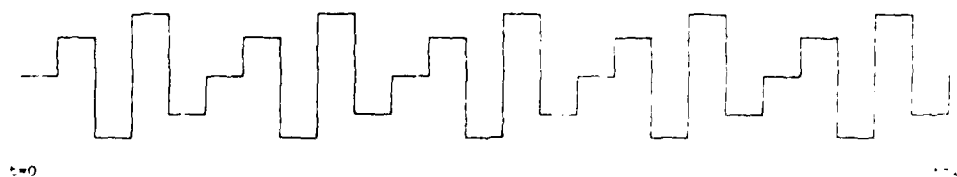


Figure IX-4(d) Aliasing and Sampling-Induced Modulation--(sampling $f_2(t)$ at a rate of 1 sample/sec)

E. Reduction of Undesired Modulation Effects

Modulation of the original signal by the sampling function signal will always occur to some extent when the sampling frequency is a non-integer multiple of the fundamental frequency of the original periodic signal. The only recourse is to reduce its effect to an acceptable level, if possible. Two means of accomplishing this are:

1. If the signal is band-limited, increasing the sampling frequency will reduce the amplitude of the modulation, and hence the amplitude of the sidebands. It can be shown that the amplitude of modulation of a cosinusoid $f(t) = \cos \omega t$ produced by sampling at a frequency $\omega_s = \alpha \omega_1$, $\alpha > 2$, must satisfy

$$\text{A.M.} \leq \cos(0) - \cos\left(\frac{2\pi}{\alpha}\right) \quad (\text{IX} - 5)$$

or

$$\text{A.M.} \leq 1 - \cos\left(\frac{2\pi}{10}\right) \quad (\text{IX} - 6)$$

For example, if $f(t) = \cos \omega_1 t$ is sampled at a rate of $\omega_s = 10\omega_1$, the maximum possible amplitude modulation due to sampling is

$$\begin{aligned} \text{Maximum A.M.} &= 1 - \cos\left(\frac{2\pi}{10}\right) \\ &= 0.191 \\ &= 19.1\% \text{ modulation} \\ &= -14\text{dB} \end{aligned} \quad (\text{IX} - 7)$$

Given no other constraints, it would seem that a sampling rate should be chosen to ensure a sampling-induced modulation of less than -120 dB for any frequency component in the acoustic signature, since this represents the dynamic range of the typical human ear. Not only would this be impractical given the limitations on the sampling frequency of the 69720A DAC, but it is unnecessary because the dynamic range of a 12 bit DAC such as the 69720A is only 72 dB. The ratio of sampling frequency required to ensure a modulation of amplitude of less than -72 dB is found as follows:

$$\begin{aligned} -72\text{dB} &= 20 \log\left[1 - \cos\left(\frac{2\pi}{\alpha}\right)\right] \\ -3.6 &= \log\left[1 - \cos\left(\frac{2\pi}{\alpha}\right)\right] \\ 2.51 \times 10^{-4} &= 1 - \cos\left(\frac{2\pi}{\alpha}\right) \end{aligned} \quad (\text{IX} - 8)$$

$$\cos\left(\frac{2\pi}{\alpha}\right) = 0.999749$$

$$\frac{2\pi}{\alpha} = 0.0224$$

$$\alpha = 28$$

This results motivates the adoption of a second sampling criterion.

Sampling Criterion 2. In order to suppress sampling-induced amplitude modulation of the synthesized signature, and hence to suppress the associated sidebands, the analog acoustic impulse response signature must be sampled at a rate of at least 28 times ω_f , where ω_f is the frequency of the highest frequency component in the signature.

Note that this is a conservative criteria; this criteria may be relaxed if additional information regarding the frequency content of the analog signature is available.

2. A second means of dealing with the objectionable sidebands is simply to mask them by adding white noise at a level which is sufficient to interfere with the sidebands, but not to interfere appreciably with the carrier tone. This is known as dithering.

A number of preliminary signatures have been synthesized where the criteria described above were violated. In all but one case (that of a very low PRF), the difference tones are clearly audible. On one very high frequency trace, the signature is aliased from inaudible frequencies down to the audible range. An updated version of the software is being generated which adheres to the criteria that have been discussed here. This updated software will utilize a truncated Fourier series approximation to the ideal static acoustic impulse response signature to assure adherence to the criteria outlined above. In addition, the least significant bit of the DAC will be dithered.

The 6944/69720A DAC system only supports continuous digital to analog conversions at a rate of 30 kHz. However, it is possible to achieve an effective sampling rate of 250 kHz. In order to achieve an effective sampling rate of 250 kHz, the data is sampled by the DAC at a rate of 25 kHz and recorded on the Nagra IV-SJ tape recorder which has a 10:1 ratio of recording speeds. When the data is recorded at 1.5 inch/second, the effective 250 kHz sampling rate is achieved. This approach was used to generate several of the preliminary traces, and it will be used for all future work. Note that the high sampling rate achievable with this approach enables us to retain more terms of the Fourier approximation to the ideal acoustic impulse response than would be allowed by the sampling criteria for a 30 kHz sampling rate. Hence a closer approximation to the ideal impulse response is obtained.

Having described the major considerations for constructing the system model for H_1 , the static acoustic impulse response of the Apollo Lightcraft, the process of modeling H_2 , the acoustic transmission path, is outlined next.

F. Model for Acoustic Transmission Path H_2

The moving source/stationary observer formula for calculating Doppler shift of a pure tone frequency source f_s is given by

$$f_r = \left[\frac{1}{1 - \frac{v(t)}{c}} \right] f_s \quad (IX - 9)$$

where:

f_s =actual frequency of the source (Hz),

$v(t)$ =the radial component of the velocity of the source relative to a fixed observer (ft/sec), where velocity toward the observer is considered positive.

c =the speed of sound in air (ft/sec)

f_r =the Doppler shifted source frequency (Hz).

Although the formula above is written for a source which produces a single frequency $f_s(t)$, the formula is valid for complex tone sources as well. If a source signature is written as a Fourier series, each component of the series is shifted as indicated above.

The amplitude of the observed signature is calculated using

$$A_r = A_{s0} \left[\frac{X_0}{X(t)} \right] \quad (IX - 10)$$

where:

A_{s0} =the peak amplitude of the acoustic pressure observed at a distance X from the acoustic source

X_0 =the distance in feet between the source and the observer at which A is measured

$X(t)$ =the actual radial distance in feet between the source and the observer

It should be noted that for the purposes of simulating the acoustic signature, the sole criterion for selecting a reference pressure $A_{s0}X_0$ is to utilize the maximum dynamic range of the 12 bit 69720A DAC. The actual sound pressure level of the synthesized signature is a function of the gain (volume) on the equipment used to play back the recorded signatures.

The parameters $f_s(t)$, $v(t)$, and $x(t)$ used in these formulas describe the PRF and vehicle dynamics and are, with the possible exception of $f_s(t)$ in certain cases, continuous functions of

time. In order to implement computer algorithms to calculate the Doppler shift and attenuation it is necessary to choose discrete times at which to evaluate the parameters $f_s(t)$, $v(t)$, and $x(t)$. We define the parameter sampling period T to be the time interval in seconds between successive evaluations of the parameters $f_s(t)$, $v(t)$, and $x(t)$. We define the parameter sampling frequency Ω_p to be the inverse of the parameter sampling period.

Experience has shown that the value of Ω_p must be chosen carefully to reduce quantization effects to an unacceptable level. A number of signatures were processed for various sets of vehicle flight data utilizing a parameter update frequency of 30 parameter samples per second. In no case were amplitude quantization effects audibly detectable; however, frequency quantization was clearly audible for signatures having time rates of change of frequency of greater than roughly 800 Hz/sec. Research has demonstrated that, over a broad frequency range, an average person can discriminate pitch changes of roughly 0.5%, whereas amplitude discrimination is only 12%^[1]. This implies that both frequency and amplitude quantization can be reduced to inaudible levels by choosing a parameter sampling frequency such that

$$0.005 \leq \frac{1f_r(t) - f_r(t - T_p)}{f_r(t)} \quad (IX - 11)$$

where

$f_r(t)$ = the Doppler shifted source frequency in Hertz,
evaluated at time t seconds

T_p = the parameter sampling period in seconds.

This will ensure that, for any given time step T , the observed frequency change by no more than 0.5%.

G) Single Relay Satellite Trajectory Simulation

Simulation of an accurate lift-off trajectory for the Apollo Lightcraft is an important first step in generating the acoustic signature representative of those which would be heard by a stationary, ground-based listener. A number of simplifying assumptions were made to constrain the variety of trajectories possible for a given set of initial conditions and vehicle flight characteristics. These assumptions are given below:

1. The Lightcraft is powered directly from a single relay satellite. All laser power is relayed from this satellite.

2. The lower relay satellite is in a circular equatorial orbit at 100 miles (162.2 km) altitude. This fairly low altitude was considered to be a lower bound for viable relay station orbits.
3. The Lightcraft must always point towards the relay satellite, and thus moves up the beam emanating from it.
4. The Lightcraft lifts off with a specific initial zenith angle, which is determined by the type of trajectory to be flown. An initial zenith angle of zero degrees means a vertical lift-off; an initial zenith angle of seventy degrees implies a nearly horizontal lift-off. For the trajectory simulations, initial zenith angles of 0 and 45 degrees were used.
5. The vehicle flies either with a constant acceleration (as felt by the pilot), or a constant thrust. In the constant acceleration cases thrust must vary due to the changing drag forces on the vehicle (i.e., with flight speed).
6. The coefficient of drag, C_D , for the Apollo Lightcraft was calculated as a function of flight mach number only. The drag coefficient data used in the simulation is displayed in Fig. IX-5.
7. The liftoff engine is an ERH thruster, with either a rotating line source, or twelve simultaneous line sources. If the line sources are simultaneous, the PRF (Pulse Repetition Frequency) of the vehicle is reduced by 12 x.

Although a large number of trajectories were "flown", only three representative cases are reported here: 1) Horizontal, constant thrust fly by, 2) Vertical takeoff at 3G's acceleration, 3) 45° (initial) takeoff at 3 G's acceleration. A cassette tape recording of these three noise signatures is included with this final report.

1) Horizontal, Constant-thrust Flyby

The constant altitude, constant velocity flyby is one of the simplest trajectory/forcing function that can be used to generate acoustic signatures for a traveling source/stationary observer. It was the first case to be simulated, and hence served to help "debug" the system.

Figure IX-6 portrays the geometry for this case. The vehicle is assumed to fly over the observer at an altitude of 50 ft, and a velocity of 100 MPH—much like a helicopter. The ERH thruster develops a constant level of thrust at a pulse repetition frequency (PRF) of 41.67 Hz. This is somewhat higher than that required for "stationary hover" (i.e., 37.8 Hz). As indicated in Fig IX-6, the thrust vector is tilted slightly forward (in the direction of flight) to counteract aerodynamic drag forces (~ 5670lbs).

The trajectory simulation routine computes the line-of-sight distance from the vehicle to the

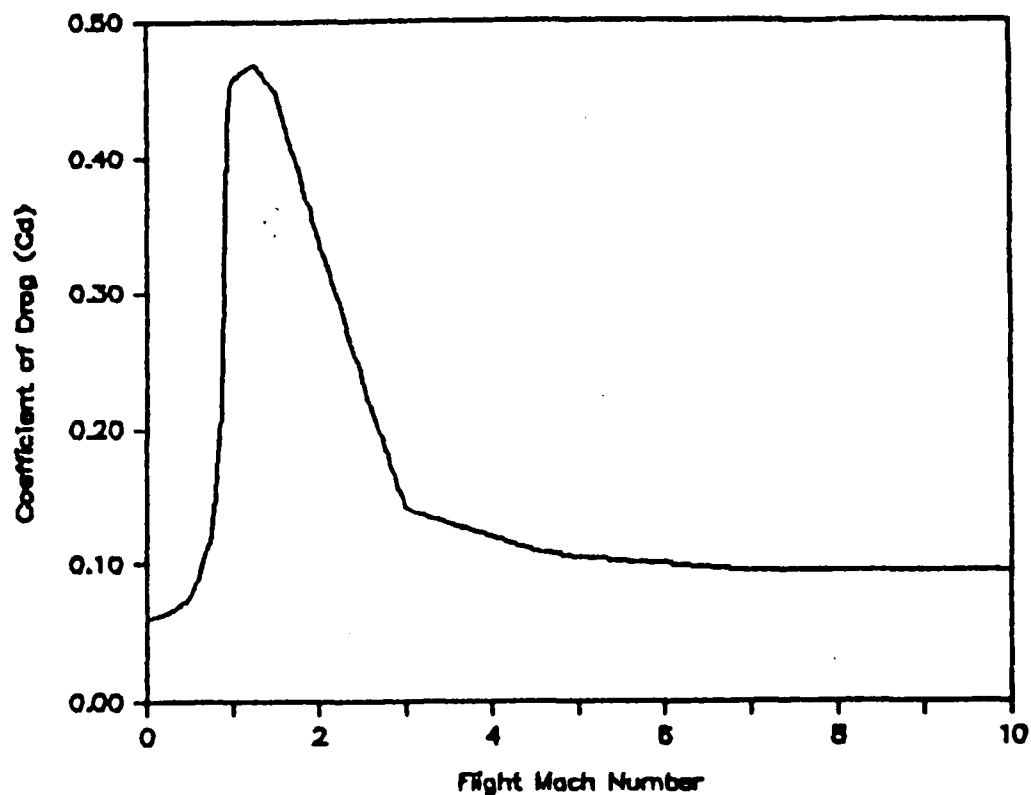


Figure IX-5 Drag Coefficient vs Flight Mach Number

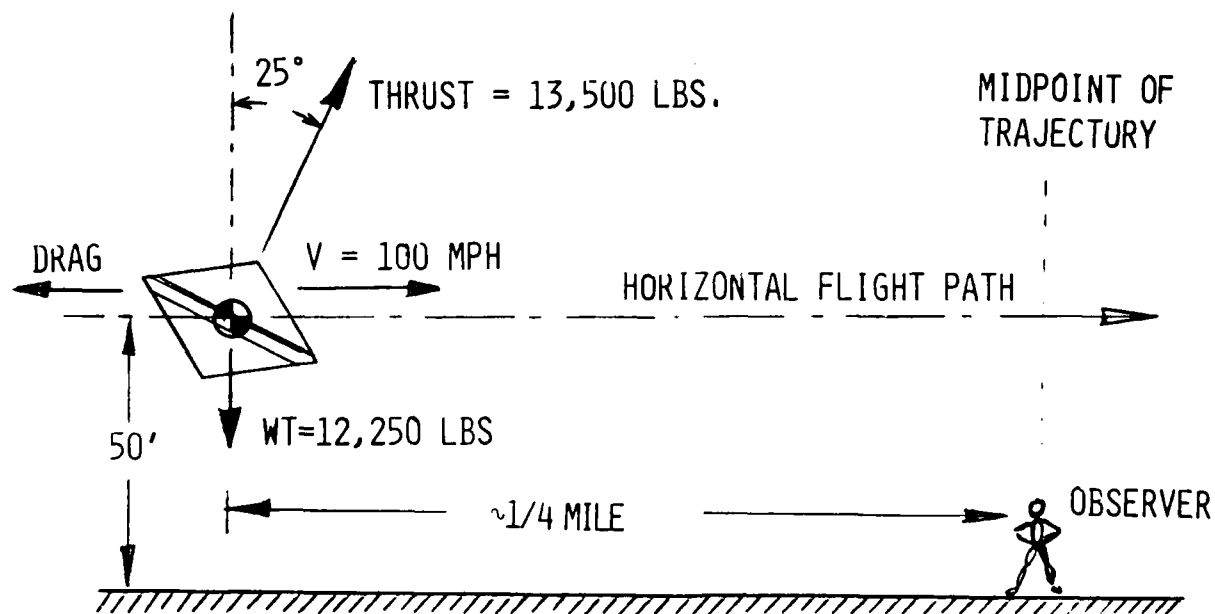


Figure IX-6 Geometry for Horizontal Fly-by at constant thrust, 50 ft altitude, 100 MPH and 41.67 Hz PRF.

observer, and the vehicle velocity component radial to the observer. The PRF in this case is held constant at 41.67 Hz. The simulation begins when the vehicle is just over 1/4 mile (1467 ft) away from the observer.

The acoustic signature for this case is displayed in Fig. IX-7. As indicated, the pulse frequency is doppler-shifted from 48 to 36.75 Hz upon passage of the vehicle. Also the normalized real amplitude of the ERH thruster increases to a maximum at the point of closest approach.

This "test" case assumed no change in vehicle pointing throughout the entire 20 second duration of the simulation; i.e., the relay satellite would have to be at a very high altitude. For the following two cases, all the afore-mentioned input assumptions are applied—such that the vehicle must chase the low altitude relay satellite into orbit.

2) Vertical liftoff at 3 G's acceleration

To calculate the location and flight direction of the Apollo Lightcraft, it is necessary to determine four parameters which exactly describe the launch trajectory. These four parameters are:

- (i) vehicle altitude - "h"
- (ii) zenith angle - " ϕ "
- (iii) satellite angle - " θ "
- (iv) vehicle angle - " δ "
- (v) vehicle to satellite distance - " β "

The relationship of these key trajectory model parameters is displayed in Fig. IX-8, which also indicates the location of vehicle take-off. Note the current positions of the vehicle and relay satellite in relation to the point of liftoff.

The initial conditions must be specified, of course, before the trajectory can be analyzed. Figure IX-9 portrays the initial liftoff geometry, for which the vehicle altitude, h, is set to zero. For the case at hand, the zenith angle ϕ_0 is also set to zero, for the 3 G constant acceleration launch. The observer is assumed to reside at the launch site.

Calculation of the pulse repetition frequency, PRF, depends on the ERH thruster mode and the level of thrust it is generating. For the "simultaneous twelve-line-source" model for the ERH thruster, a PRF of 37.8 Hz is required to hover the Apollo Lightcraft. This frequency generates about 12,250 lbs. of thrust; hence, the PRF for a specific thrust output is

$$PRF_{SL} = 37.8 \left[\frac{T}{12,250} \right] \quad (IX - 12)$$

where T is the desired thrust in pounds.

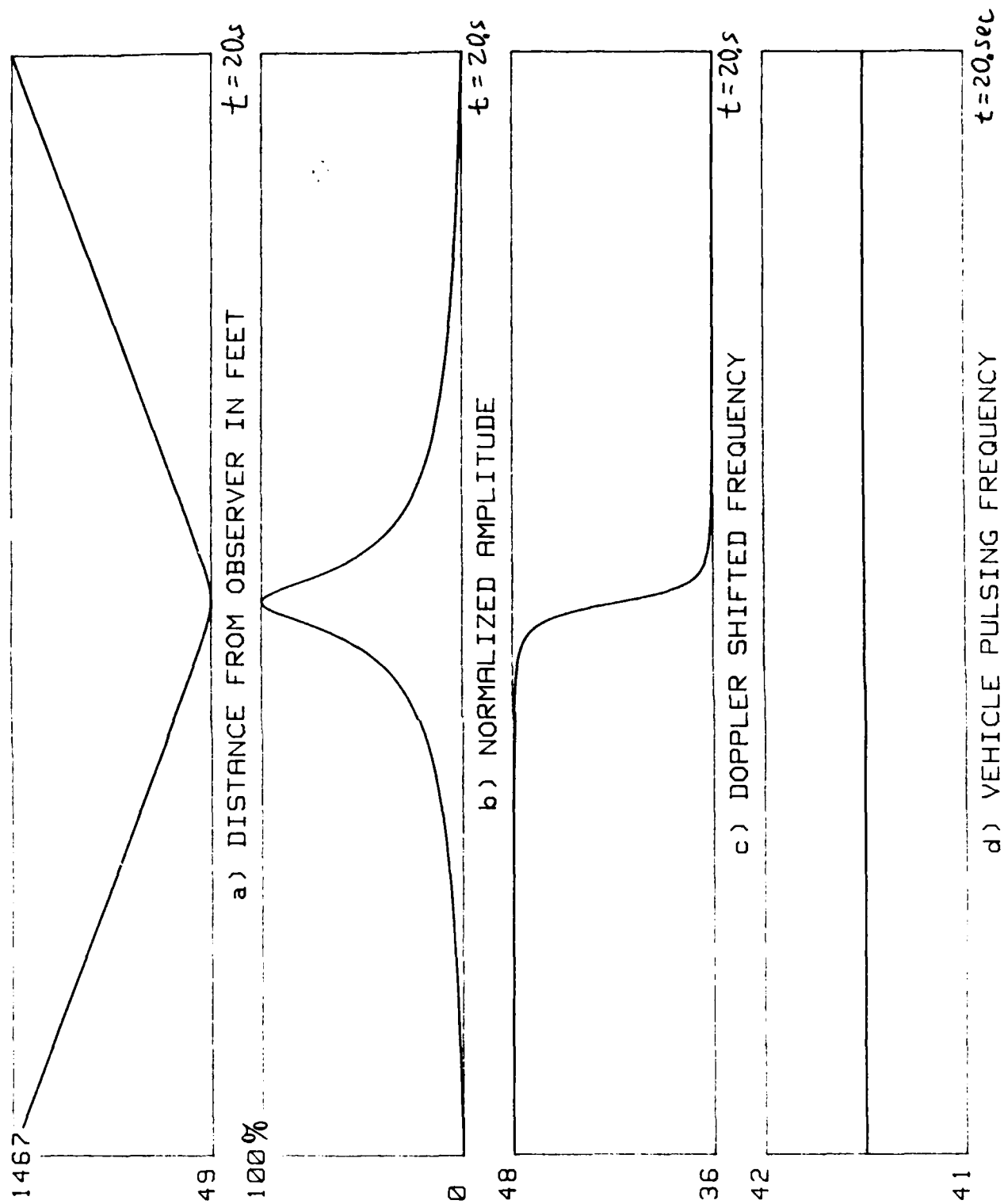


Figure IX-7 Acoustic Signature for 100 MPH Flyby at 50 ft.

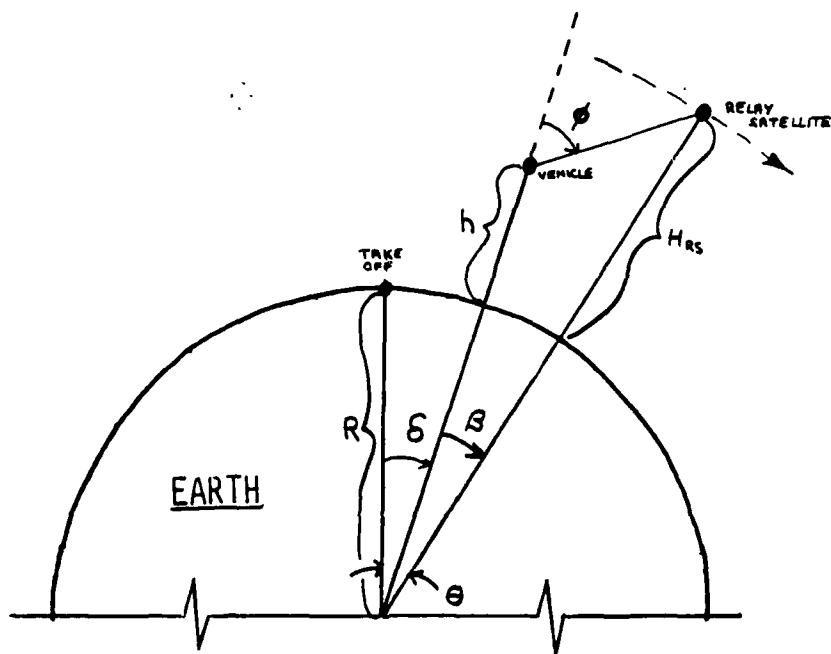


Figure IX-8 Key Trajectory Parameters

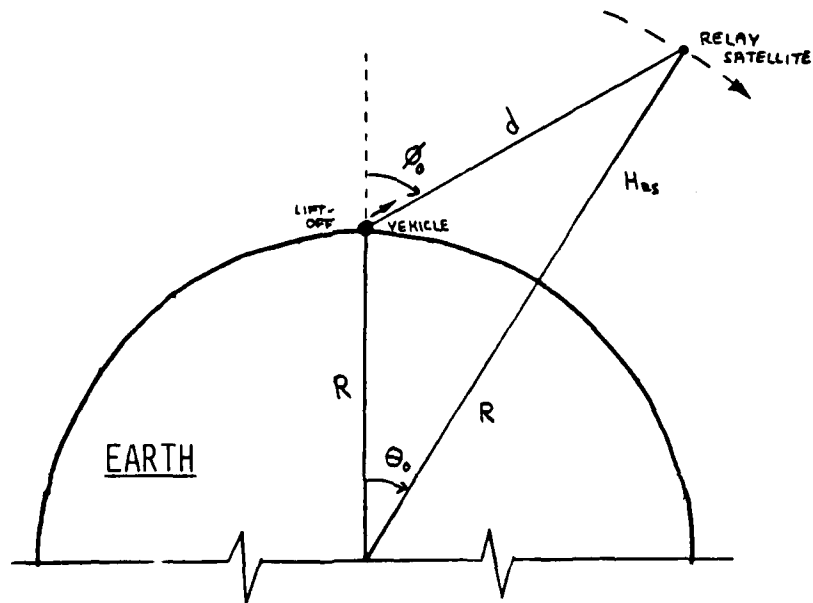


Figure IX-9 Initial Liftoff Geometry

For a "rotating line source" model, the PRF is increased by a factor of twelve. Each line source is pulsed in sequence. This has the effect of multiplying the PRF by 12 x:

$$PRF_{RL} = 454 \left[\frac{T}{12,250} \right] \quad (IX - 13)$$

The last two 3 G simulations assume the use of this rotating-line-source mode for ERH thruster operation.

Figure IX-10 gives the trajectory/forcing function data for the constant 3 G launch from an initial zenith angle of zero degrees. Figure IX-10a gives the altitude vs. downrange distance; Fig. IX-10b, the flight Mach number vs. time; Fig. IX-10c, the zenith angle vs. time; and Fig. IX-10d, the PRF vs. time. Note that the PRF must increase from 1360 Hz at liftoff to roughly 4800 Hz when "punching-through" Mach 1; at 20 seconds into the simulation, PRF has reached 6500 Hz.

The acoustic signature for this case is given in Fig. IX-11. As indicated, the maximum vehicle distance from the source is 13,000 ft. or about 2.5 miles altitude. The doppler-shifted frequency hits a low of 1043 Hz and a high of 3070 Hz.

3) 45° Liftoff at 3 G's acceleration

The initial conditions for this trajectory simulation are identical to the previous one with two exceptions. First, the vehicle is launched at a zenith angle of 45°, instead of 0°. Second, the observer is placed one half mile downrange of the vehicle launch site, instead of coincident.

The trajectory/forcing function data for the 45° zenith angle case is presented in Fig. IX-12, and the resulting acoustic signature in Fig. IX-13. Note that the temporal patterns for normalized amplitude and doppler-shifted frequency are very different from the previous case. The differences become especially pronounced when heard on the audio cassette.

H) Summary

The acoustic simulations are technically interesting in their own right and give a firm tactile understanding of what this new class of airbreathing thrusters will sound like. However, one additional noteworthy realization came almost as a by-product of the study. During stationary hover, when simultaneously pulsed with big energies and low frequencies, the ERH thruster can be designed to be inaudible - in the infrasonic regime. Alternately, when accelerating at high G levels in the rotating-line-source mode, the ERH thruster can be engineered to produce ultrasonic noise -

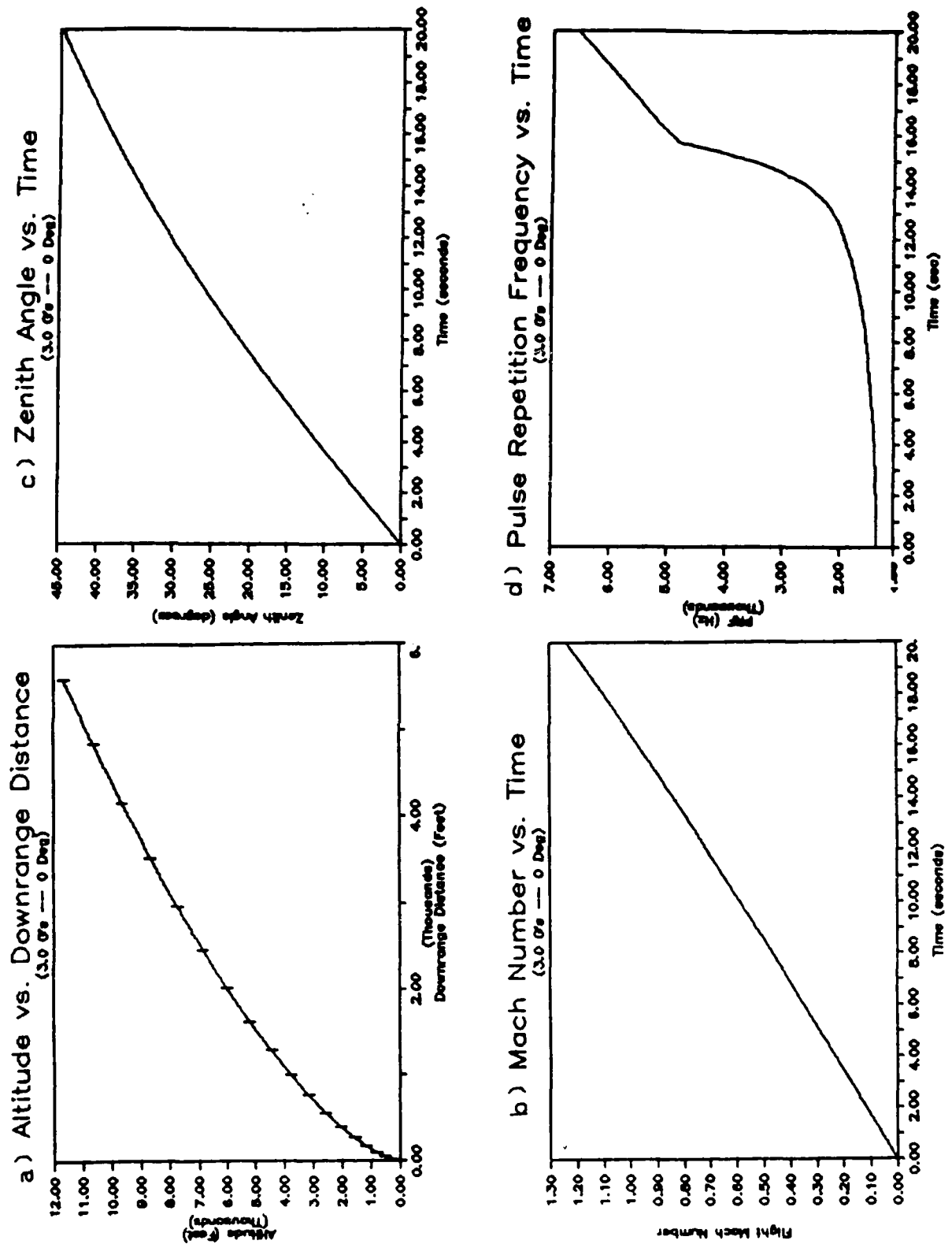


Figure IX-10 Trajectory Forcing Function for Constant 3 G Launch from 0° Initial Zenith Angle

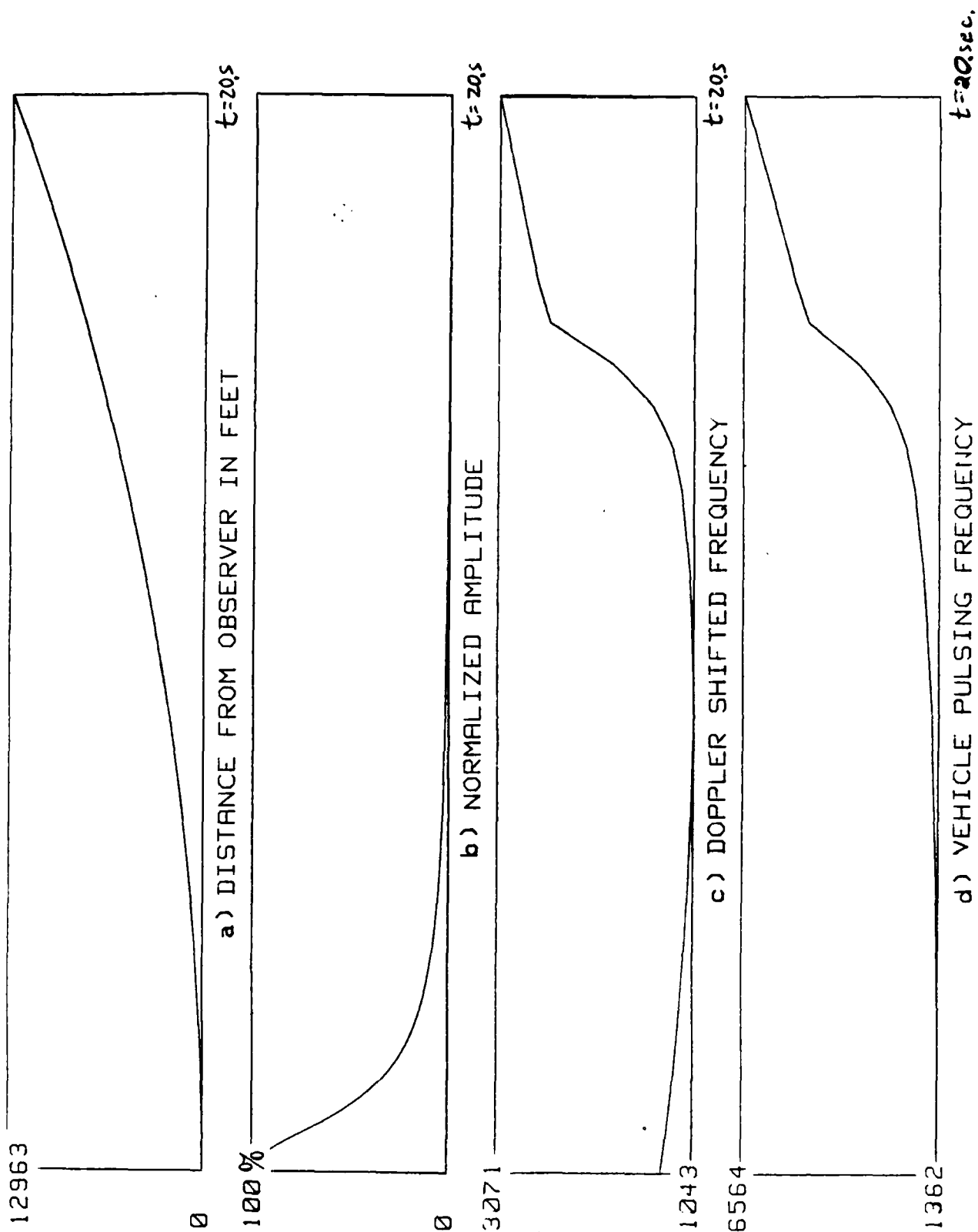


Figure IX-11 Acoustic Signature for Constant 3 G Launch from 0° Initial Zenith Angle

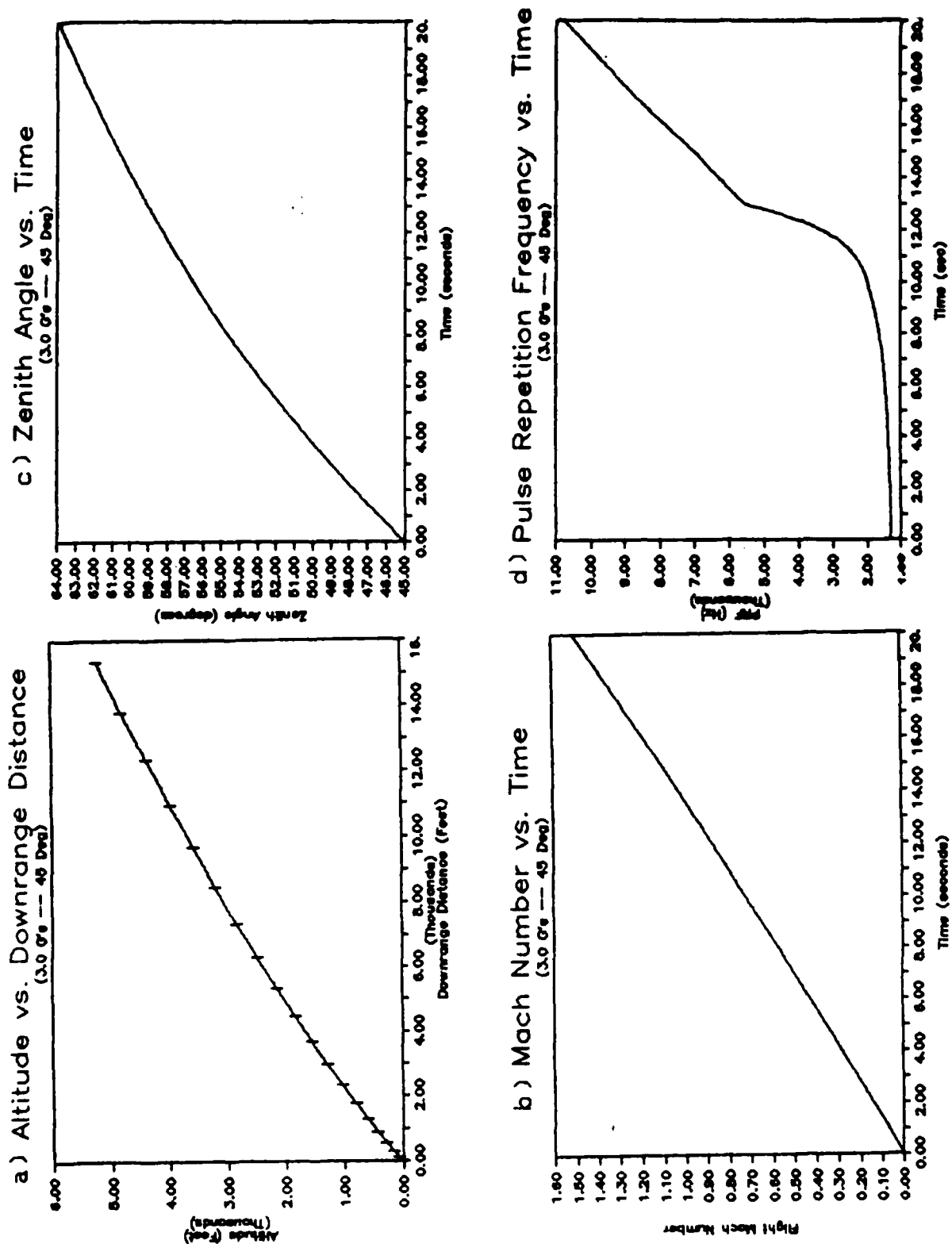


Figure IX-12 Trajectory/Forcing Function for Constant 3 G Launch from 45° Initial Zenith Angle.

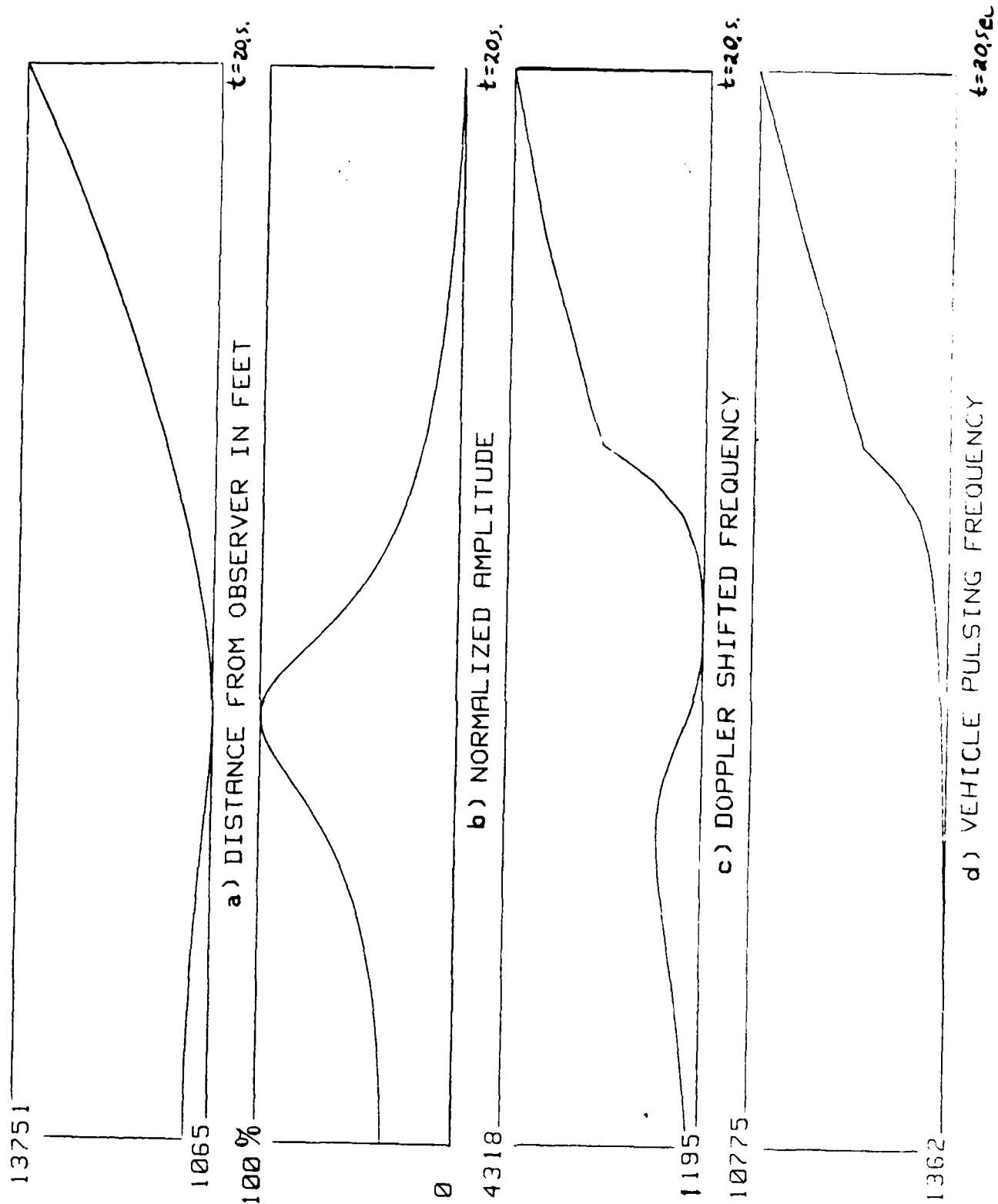


Figure IX-13 Acoustic Signature for Constant 3 G Launch from 45° Initial Zenith Angle.

also beyond the range of human hearing. For example, assume that the 1.6 MJ pulse energy shared by the 12 line source is set off sequentially; then beyond Mach 1 (with a constant 3 G launch), the ERH thruster PRF will exceed 15 kHz, which is inaudible by most of the population.

Through proper engineering, these ERH thrusters hold good potential for effectively "silent" operation - although sound pressure levels will still reach dangerous levels at close proximity to the vehicle.

CHAPTER X

CONCLUSIONS

Preliminary investigations of the ERH thruster concept have demonstrated that this advanced airbreathing beam-powered engine has great potential for application in future SSTO shuttlecraft. The level of thrust produced by this engine, given a certain level of input thermal power, falls roughly between the non-afterburning turbojet and the turbofan. However, the acceleration performance can be astounding. Thrust-to-weight ratios for the ERH thruster can exceed 30, whereas conventional turbomachinery lies in the range of 5 and 15.

Although the current study concludes that the ERH thruster has great promise, further theoretical and experimental work is needed. Such proof-of-concept research should investigate the (i) "refresh" process (i.e., exhaust/intake cycles), (ii) real gas effects, (iii) wavelength scaling effects (incl. the potential for microwave frequencies), (iv) LSD wave ignition energy losses, (v) radiation heat transfer (i.e., energy losses out of the plasma), and (vi) flight dynamic performance vs. quasi-static (hover and subsonic) capability.

Clearly, there can be no substitute for experimental verification of these basic research issues. Several pulsed lasers with adequate characteristics (e.g., kiloJoule-level pulses, at roughly 10 μ sec duration) currently exist at AVCO Everett Research Laboratory, and elsewhere. Such lasers would be ideal for small proof-of-concept experiments.

In summary, the ERH thruster concept has survived this first critical examination into the propulsive physics. However, further substantial increases in the state of knowledge can only come with a well conceived program involving both theoretical and experimental elements - pushed simultaneously.

REFERENCES

1. Billig, F. S., "External Burning in Supersonic Streams", Technical Memorandum TG-912, John Hopkins University, Applied Physics Laboratory, Silver Spring, Maryland, May 1967.
2. Boni, A. A., Su, F. Y., Thomas, P. D. and Musal, H. M., "Theoretical Study of Laser Target Interaction", Final Report No. SAI 77-567LJ, Science Applications, Inc., La Jolla, Cal., May 1977.
3. Courant, R., Super Sonic Flow and Shock Waves, Springer-Verlag, NY, 1976.
4. Edwards, A., Ferriter, N., Fleck Jr., J. A. and Winslow, A. M., "A Theoretical Description of the Interaction of a Pulsed Laser and a Target in an Air Environment", UCRL-51489, Lawrence Livermore Lab., U. of Cal., Cal., Nov. 1973.
5. Ferriter, N., Maiden, D. E., Winslow, A. M. and Fleck Jr., J. A., "Laser-Supported Detonation Waves", UCRL-51836, Lawrence Livermore Lab., U. of Cal., Cal., June 1975.
6. Graham, A. R., "NASA Plug Nozzle Handbook", Contract NAS 9-3748, General Electric Co. for the New York State Atomic and Space Development Authority.
7. Hill, P. and Peterson, C., Mechanics and Thermodynamics of Propulsion, Addison-Wesley Publishing, 1965.
8. Holmes, B., "The Mechanical Loads from LSD Waves and Their Simulation- Vol 1", Stanford Research Inst., Report AFWL-TR-75-285, 1976.
9. Jackson, J. P. and Nielsen, P. E., "Role of Radiative Transport in the Propagation of Laser-Supported Combustion Waves", AIAA Jou., Vol. 12, No. 11, Nov. 1974, p. 1498.
10. Kaminski, D. A., Editor, GE Heat Transfer Data Book.
11. Kinney, G. F. and Graham, K. J., Explosive Shocks in Air (2nd. ed.), New York, Springer Verlag Inc. 1985.
12. Lin, S. C., "Cylindrical Waves Produced by Instantaneous Energy Release", J. A. P., 25, 1974, 54-57.
13. Myers, G. L., Analytical Methods in Conduction Heat Transfer, McGraw H.
14. Myrabo, L. and Ing, D., The Future of Flight, New York, Baen Enterprises, 1985.
15. Pirri, A., "Theory for Momentum Transfer to a Surface with a High-Speed Flow", Fluids, Vol. 16, No. 9, Sept. 1973.
16. Powers, M. V., Zaretzky, C. and Myrabo, L., The Future of Flight, New York, Baen Enterprises, 1985.

AD-A187 336

ADVANCED ENERGY CONVERSION CONCEPT FOR BEAMED-ENERGY
PROPULSION(U) RENSSELAER POLYTECHNIC INST TROY NY DEPT
OF MECHANICAL ENGINE. L N MYRABO 21 AUG 87

3/3

UNCLASSIFIED

RPI-3-24170 AFOSR-YR-87-1387 AFOSR-84-8361 F/C 9/3

NL

END

DATE

FILED

8



1.0



1.1



1.25

1.5
1.6
1.8
2.0
2.2
2.5
2.8
3.15
3.6
4.0
4.5
5.0
5.6
6.3
7.1
8.0
9.0
10
11
12.5
14
16
18
20
22.5
25
28
31.5
36
40
45
50
56
63
71
80
90
100

2.8

3.15

3.6

4.0

4.5

2.5

2.2

2.0

1.8



1.4



1.6

- Performance", AIAA-86-1761.
17. Raizer, Y. P., "Heating of a Gas by a Powerful Light Pulse", Soviet Phys. JETP, Vol. 21, No. 5, Nov. 1965.
 18. Raizer, Y. P., Laser Induced Discharge Phenomena, Consultants Bureau (Div. of Plenum Publishing), N.Y., 1977.
 19. Rea, S. M., "Rapid Method For Determining Concentric Cylinder Radiation View Factors", AIAA Journal, Vol. 12, No. 8, p. 1122-1123.
 20. Reilly, J. P., "Propagation of High Power Microwave Beams," Unpublished Report, W. J. Schafer Associates, Inc., Wakefield, Mass., Aug. 1979.
 21. Reilly, J. P., Ballantyne, A., Woodroffe, J. A., "Modeling of Momentum Transfer to a Surface by Laser-Supported Absorption Waves", AIAA Jour., Vol. 17, No. 10, Oct. 1979, p. 1098.
 22. Sedov, L. I., Similarity and Dimensional Methods in Mechanics, 4th Russian ed., Academic Press, Inc., N.Y., 1959.
 23. Siegel, R. and Howell, J. R., Thermal Radiation Heat Transfer, McGraw-Hill, 1984.
 24. Sims, J. L., "Tables for Supersonic Flow Around Right Circular Cones at Zero Angle of Attack", NASA Report SP-3004, 1963.
 25. Strayer, T. D., Bossard, J. A., Richard, J. C., Gallimore, A. D. and Myrabo, L. N., "Investigation of Beamed-Energy ERH Thruster Performance", AIAA-86-1760, 1986.
 26. Su, F. Y. and Boni, A. A., "Non-linear Model of Laser-Supported Deflagration Waves", Phys. of Fluids, Vol. 19, No. 7, July 1976, p. 960.
 27. Taylor, Sir G. I., "The Formation of a Blast Wave by a very Intense Explosion; I. Theoretical Discussion", Proc. Roy. Soc., A201, 1950, 159-174.
 28. Thomas and Finney, Calculus and Analytic Geometry, Addison-Wesley Publishing Co., 5th ed., 1980.
 29. Unpublished data from Marquardt Corporation, Van Nuys, Cal., 1958.
 30. Watson, K. N. and Kroll, N., "Theoretical Study of Ionization of Air by Intense Laser Pulses", Phys. Rev. A., Vol. 5, No. 4, April 1972.
 31. White, F., Viscous Fluid Flow, McGraw-Hill, N.Y., 1974, pp. 637-645.
 32. Yoshikawa, K. K. and Chapman, D. R., "Radiative Heat Transfer and Absorption Behind A Hypersonic Normal Shock Wave", NASA TN D-1424.
 33. Zel'dovich B., Theory of Detonation, Academic Press, NY, 1960.

34. Zang, C. J. and Micci, M. M., "Thermal Analysis of a Magnetic Induction Thruster", Journal of Propulsion, Vol. 2, No. 1, Jan. - Feb. 1986, pp. 50 - 56.
35. Broch, J. T., Application of B and K Equipment to ACOUSTIC NOISE MEASUREMENTS, 2nd. Ed., Larsen and Son, Soborg, Denmark, Jan. 1971, p. 35.
36. Pirri, A. N., Root, R. G. and Wu, P. K. S., "Plasma Energy Transfer to Metal Surfaces Irradiated by Pulsed Lasers", AIAA Paper No. 77-658, AIAA 10th Fluid and Plasmadynamics Conference, Albuquerque, N. Mex., 27 - 29 June, 1977
37. Schlier, R. E., Pirri, A. M. and Reilly, D. J., "Air Breakdown Studies", Technical Report No. AFWL-TR-72-74, Avco Everett Research Laboratory, Everett, MA., February 1973.
38. Lencioni, D. E., "Real Air Breakdown", presented at HELREG Propagation Subpanel Meeting, Mitre Corp., Bedford, MA., November 1975.
39. Lencioni, D. E. *et al.*, "The Effect of Dust on 10.6 μ m Laser-Induced Air Breakdown", LPT-20, MIT Lincoln Laboratory, Lexington, MA., April 1973.

TECHNICAL MEETINGS (Conference Paper)

T.D. Strayer, J.A. Bossard, J.C. Richard, A.D. Gallimore and L.N. Myrabo, "Investigation of Beamed-Energy ERH Thruster Performance", Paper No. AIAA-86-1760, AIAA/SAE/ASME/ASEE 22nd Joint Propulsion Conference, Huntsville, Alabama, June 16-18, 1986.

WORKSHOPS (Proceedings)

L.N. Myrabo, "The Mercury Lightcraft Concept", Proceedings of the SDIO/DARPA Workshop on Laser Propulsion, Volume 2-Contributed Papers, J.T. Kare (Technical Ed.), Lawrence Livermore National Laboratory, Livermore, CA, 7-18 July 1986, pp. 13-21.

Presentations

L.N. Myrabo, "The Apollo Lightcraft Project," Laser Propulsion Workshop, Lawrence Livermore National Laboratory, Livermore, California, 7-18 July 1986.

L.N. Myrabo, "Riding the Light Fantastic: A Prophecy on the Future of Flight," Experimental Aircraft Association, 1986 Convention, Oshkosh, Wisconsin, August 4, 1986.

L.N. Myrabo, "Super Advanced Propulsion Concepts," NASA Marshall Space Flight Center, MSFC, Alabama, 29 August 1986.

L.N. Myrabo, "Advanced Airbreathing Propulsion for Future Aerospace Vehicles," Aero Propulsion Laboratory, Air Force Wright Aeronautical Laboratories, WPAFB, Ohio, 29 September 1986.

L.N. Myrabo, "Beam Power for Aero and Spacecraft," Invited Lecture, NASA Lewis Research Center, Cleveland, Ohio, November 12, 1986.

L.N. Myrabo, "The Apollo Lightcraft Design Project at RPI," USRA/NASA Advanced Aeronautics Design Program: December Review, Morro Bay, California, 1-4 December 1986.

L.N. Myrabo, "Advanced Combined-Cycle Engines for Transatmospheric Propulsion," Invited Lecture for UTSI Short Course on Scramjet Technology, R.A. Crawford (Organizer), The University of Tennessee Space Institute, Tullahoma, TN, March 30 - April 3, 1987.

ATE
LMED
8